

HARVARD UNIVERSITY
Graduate School of Arts and Sciences



DISSERTATION ACCEPTANCE CERTIFICATE

The undersigned, appointed by the

Harvard John A. Paulson School of Engineering and Applied Sciences
have examined a dissertation entitled:

“Flexible Mechanical Metamaterials: Solitary Waves and Phase Transitions”

presented by: Bolei Deng

A handwritten signature in black ink that reads "Bolei Deng".

Signature _____

A handwritten signature in black ink that reads "K. Bertoldi".

Typed name: Professor K. Bertoldi

Signature _____

A handwritten signature in blue ink that reads "Z. Suo".

Typed name: Professor Z. Suo

Signature _____

A handwritten signature in black ink that reads "C. Rycroft".

Typed name: Professor C. Rycroft

Signature _____

A handwritten signature in blue ink that reads "J. Vlassak".

Typed name: Professor J. Vlassak

August 26, 2021

Flexible Mechanical Metamaterials: Solitary Waves and Phase Transitions

A DISSERTATION PRESENTED
BY
BOLEI DENG
TO
THE SCHOOL OF ENGINEERING AND APPLIED SCIENCES

IN PARTIAL FULFILLMENT OF THE REQUIREMENTS
FOR THE DEGREE OF
DOCTOR OF PHILOSOPHY
IN THE SUBJECT OF
MATERIALS SCIENCE AND MECHANICAL ENGINEERING

HARVARD UNIVERSITY
CAMBRIDGE, MASSACHUSETTS
AUGUST 2021

©2021 – Bolei Deng
ALL RIGHTS RESERVED.

Flexible Mechanical Metamaterials: Solitary Waves and Phase Transitions

Over the last two decades, metamaterials — materials whose properties are defined by their structure rather than their composition — have been a magnet for scientists, generating significant interest in the research community. In this dissertation, I explore the nonlinear mechanics of flexible mechanical metamaterials (flexMMs) focusing on: (i) the propagation of solitary waves, and (ii) structural phase transitions.

I first investigate the nonlinear dynamic behavior of flexMMs based on the *rotating squares mechanism*. I experimentally and numerically demonstrate that this system supports the propagation of *elastic vector solitons* and construct a theoretical framework to capture them.

Next, I investigate the formation of multiple phases in the rotating squares systems and the evolution of domain walls between these phases. I derive an analytical solution that captures the profiles and locations of such domain walls and exploits it to guide the design of flexMMs with new functionalities.

Finally, I explore topological phase transitions in micrometer-scale cellular flexMMs. I present a two-tiered strategy based on swelling that is able to fast, reversibly, and robustly change the fundamental topology of cellular lattices, e.g., connectivity and number of the nodes. I then harness these topological changes to design active surfaces with tunable properties and functionalities.

Contents

1	Introduction	1
1.1	Flexible mechanical metamaterials	2
1.2	Solitary waves	3
1.3	Phase Transitions	4
1.4	Dissertation Overview	6
2	Metamaterials with Amplitude Gaps for Elastic Solitons	9
2.1	Abstract	10
2.2	Introduction	10
2.3	Metamaterial Design and Characterization	11
2.4	Discrete and Continuum Models	14
2.5	Amplitude Gaps for Solitons	15
2.6	Enhanced Tunability via Symmetry Breaking	17
2.7	Functional Devices Based on Amplitude Gaps	19
2.8	Discussion	24
3	Anomalous Collisions of Elastic Vector Solitons in Mechanical Metamaterials	25
3.1	Abstract	26
3.2	Introduction	26
3.3	Elastic Vector Solitons	28
3.4	Anomalous Collisions Between Vector Solitons	29
3.5	Amplitude Gap Theory with Frozen Solitons	34
3.6	Applications	36
4	Characterization, Stability and Application of Domain Walls in Flexible Mechanical Metamaterials	39
4.1	Abstract	40
4.2	Significance Statement	40
4.3	Introduction	41
4.4	Flexible Mechanical Metamaterial Based on the Rotating-squares Mechanism	42
4.5	Phase-inducing Defects and Domain Walls	47
4.6	Pinning Defects and Stable Domain Walls	51
4.7	Domain Walls with Arbitrary Orientations	52
4.8	Applications	55

4.9	Conclusions	58
5	Liquid-induced Topological Transformations of Cellular Microstructures	59
5.1	Abstract	60
5.2	Introduction	61
5.3	A Two-tiered Dynamic Strategy	62
5.4	Liquid-induced Topological Transformations	66
5.5	Reverse Transformations and Modular Control	68
5.6	Generalization of the strategy	69
5.7	Applications	70
5.8	Conclusions	74
6	Conclusions	75
Appendix A	Supplementary Information: Metamaterials with Amplitude Gaps for Elastic Solitons	78
A.1	Fabrication	79
A.2	Testing	82
A.3	Discrete Model	86
A.4	Continuum Model	95
A.5	Amplitude Gaps for Solitons	100
A.6	Solution for the Aligned Chain	105
A.7	Solitons Excited by Pulling	107
A.8	Energy Carried by Solitons	110
A.9	Dispersion Relation	112
A.10	Additional Results for Splitter	118
A.10.1	Experimental results	118
A.10.2	Numerical results	119
A.11	Additional Results for Diode	124
A.11.1	Experimental results	124
A.11.2	Numerical results	125
Appendix B	Supplementary Information: Anomalous Collisions of Elastic Vector Solitons in Mechanical Metamaterials	128
B.1	Fabrication	129
B.2	Testing	131
B.3	Mathematical Models	133
B.3.1	Discrete model	133
B.3.2	Analytical solution for a single pulse	135
B.4	Numerical Simulations	140
B.5	Additional Results	143
Appendix C	Supplementary Information: Characterization, Stability and Application of Domain Walls in Flexible Mechanical Metamaterials	147
C.1	Fabrication	148

C.2	Testing	152
C.3	Discrete Model	155
C.3.1	Governing equations	155
C.3.2	Defects	158
C.3.3	Total energy of the structure	159
C.3.4	Uniaxial compression of a structure without defects	160
C.3.5	Parameter identification	162
C.3.6	Propagation of linear waves	164
C.3.7	Additional numerical results	168
C.4	Continuum Model	176
C.4.1	Analytical solution	178
C.4.2	Position ζ_0 and orientation φ of the domain walls	183
C.4.3	Stress-strain curves	187
C.4.4	Additional analytical results	189

Appendix D	Supplementary Information: Liquid-induced Topological Transformations of Cellular Microstructures	190
D.1	Materials and Methods	191
D.1.1	Materials	191
D.1.2	Methods	192
D.2	Theoretical Model	197
D.2.1	Critical Young's modulus	197
D.2.2	Verification of the critical Young's modulus	201
D.2.3	Critical adhesion energy	204
D.3	Supplemental Results & Figures	205
D.3.1	Cellular structures of low Young's modulus materials	205
D.3.2	3.2 Synthesis of liquid crystalline polymer (LCP) microstructures	205
D.3.3	Characterization of material properties	207
D.3.3.1	Swelling and trapping of an LCP microplate	207
D.3.3.2	Glass transition temperature of LCP in the dry and wet states	207
D.3.3.3	Young's moduli of LCP in the dry and wet states	208
D.3.3.4	Systematic study of the swelling behavior of LCP with different liquids	208
D.3.4	Characterization of the topological transformation	210
D.3.4.1	3D topography of the cellular structures	211
D.3.4.2	Assembly process: symmetry breaking and phase boundaries	212
D.3.4.3	Stability of the assembled microstructures under harsh conditions	213
D.3.4.4	Reversibility and fatigue test	214
D.3.4.5	Hysteresis test	215
D.3.5	Generalization of the topological transformation	215
D.3.5.1	Other lattice geometries	215
D.3.5.2	Other structural dimensions	218
D.3.5.3	Other materials	218
D.3.6	Free-standing cellular structures	220

D.3.7	Local transformations with small droplets	221
D.3.8	Phase design	223
	D.3.8.1 Geometrical perturbations	223
	D.3.8.2 Phase boundary design	225
	References	238
	List of Publications	239

Listing of figures

1.1	Deformation of an elastomeric block with an array of circular holes subjected to uniaxial compression ^[1]	2
1.2	Recreation of a solitary wave on the Scott Russell Aqueduct on the Union Canal ^[2]	4
1.3	Strategies to reconfigure mechanical metamaterials at different scales using (a) swelling ^[3] , (b) heating ^[4] and (c) electric field ^[5]	5
2.1	Propagation of elastic vector solitons in a chain with all horizontal hinges aligned. (a) Few units of our sample (Scale bar: 2 cm). (b) Schematics of our testing setup. (c) Evolution of the rotation and longitudinal displacement of the second and fortieth units as a function of time during two different experiments. (d) Schematic of the system. (e) Measured transmission, A_{40}/A_2 , as a function of the amplitude of the input signal, A_2 . (f) Measured cross-correlation of $\theta_2(t)$ and $\theta_{40}(t)$ as a function of the amplitude of the input signal, A_2 . (g) Evolution of the pulse velocity c as a function of its amplitude. The grey region in (e)-(g) highlights the amplitude gap as predicted by the continuum model. The error bars in (g) show the 95% confident interval of the measured velocities and amplitudes of solitons in experiments. The corresponding error bars for simulation results are too small to show.	13
2.2	Propagation of elastic vector solitons in a chain with vertically shifted neighboring horizontal hinges. (a) Schematic of the system. Neighboring horizontal hinges are shifted by $a \tan \varphi_0$ in vertical direction. (b) Evolution of the amplitude gap as a function of the angle φ_0 . (c) Few units of our sample characterized by $\varphi_0 = 5^\circ$ (Scale bar: 2 cm). (d) Measured transmission, A_{40}/A_2 , as a function of the amplitude of the input signal, A_2 . (e) Measured cross-correlation of $\theta_2(t)$ and $\theta_{40}(t)$ as a function of the amplitude of the input signal, A_2 . (f) Evolution of the pulse velocity c as a function of its amplitude. The grey region in (b) and (d)-(f) highlights the amplitude gap as predicted by the continuum model. The error bars in (f) show the 95% confident interval of the measured velocities and amplitudes of solitons in experiments. The corresponding error bars for simulation results are too small to show.	18

2.3	Soliton splitter. (a) Schematics of our soliton splitter. A pair of stiffer hinges (with stiffness K_s^d and K_θ^d) is introduced to connect the 24th and the 25th pairs of crosses. (b) Rotation of the pairs of crosses during the propagation of the pulse, as recorded with our high-speed camera. The location of the stiff pair of hinges is indicated by the dashed red line. (c and d) Simulations corresponding to the experiments shown in B. The numerical analysis are conducted on a 2×1000 chain with symmetric crosses characterized by $\varphi_0 = 0^\circ$ and a pair of stiffer hinges placed between the 500th and the 501st units. (e and f) Numerical results for a 2×1000 chain with asymmetric crosses characterized by $\varphi_0 = 5^\circ$ and a pair of stiffer hinges placed between the 500th and the 501st units.	20
2.4	Mechanical diode. (a) Schematics of our mechanical diode. (b) Optical images showing the propagation of a solitary wave excited at the left end of the chain. (c) Rotation of the pairs of crosses induced by a pulse excited at the left of the chain. (d) Optical images showing the propagation of a solitary wave excited at the right end of the chain. (e) Rotation of the pairs of crosses induced by a pulse excited at the right of the chain. (f) Schematic highlighting the working principles of our mechanical diode. (g) Measured transmission, $ A_{40}/A_{10} $, as a function of the input amplitude, $ A_{10} $, for pulses excited at the left end of the chain. (h) Measured transmission, $ A_{10}/A_{40} $, as a function of the input amplitude, $ A_{40} $, for pulses excited at the right end of the chain.	22
3.1	Experiments on collisions between elastic vector solitons. (a) Schematic of the system. (b)-(c) Schematics of the impactors used to excite (b) positive and (c) negative rotations. (d) Schematic of our first experiment. (e)-(f) Rotation of the pairs of crosses during the propagation of the pulses, as recorded during our first test in (e) experiments and (f) numerical simulations. (g) Schematic of our second experiment. (h)-(i) Rotation of the pairs of crosses during the propagation of the pulses, as recorded during our second test in (h) experiments and (i) numerical simulations.	31
3.2	Numerical simulations and complete phase diagram of vector soliton collisions. (a) Cross-correlation between $\theta_{10}(t < t_c)$ and $\theta_{N-10}(t > t_c)$ as a function of A_{left} for $A_{\text{right}} = 0.2$. Triangular markers correspond to experimental data, while the black line is generated using numerical simulations. (b) Numerically obtained cross-correlation between $\theta_{10}(t < t_c)$ and $\theta_{N-10}(t > t_c)$ as a function of A_{left} and A_{right} . (c) Complete picture of the collision dynamic between the pulses supported by the system. (d)-(e) Rotations of the pairs of crosses during the propagation of the pulses as found in numerical simulations for (d) $(A_{\text{left}}, A_{\text{right}}) = (-0.3, 0.22)$ and (e) $(0.08, 0.3)$	32
3.3	Interaction between propagating solitons and a frozen soliton. (a) A $N = 500$ chain with a frozen soliton placed in the middle of it. (b)-(c) Numerically obtained cross-correlation between $\theta_{10}(t)$ and $\theta_{N-10}(t)$ as a function of A_{left} and A_f with frozen solitons of width defined by (b) W_f and (c) W_f^{eff}	35

- 3.4 Other types of collisions and potential applications.** (a)-(b) Rotations of the pairs of crosses as numerically found when considering two solitons of amplitude $A_{\text{left},1}$ and $A_{\text{left},2}$ initiated at the left end at time $t_1 = 0$ and $t_2 = 0.3\text{s}$. ($A_{\text{left},1}, A_{\text{left},2} = (0.4, 0.3)$ in (a) and $(0.4, -0.3)$ in (b). (c) A soliton with amplitude $A_{\text{right}} = -0.18$ is excited from the right end as a probing soliton to detect the rotation direction of the main soliton of amplitude $A_{\text{left}} = 0.4$. (d) An amplitude $A_{\text{left}} = 0.4$ soliton is destroyed by six small solitons of amplitude $A_{\text{right},k} = -0.2$, (with $k = 1, \dots, 6$). 37
- 4.1 The rotating square system.** (a) The system consists of a network of 21×21 square domains connected by thin ligaments. The positive direction of rotation alternates for neighboring squares: a counter clockwise rotation of the $[i, j]^{\text{th}}$ square (the square located on the i^{th} row and j^{th} column) is defined positive if $i + j$ is an even number and negative if $i + j$ is odd. (b) Deformation of the sample when subjected to $\varepsilon_{\text{applied}}^{yy} = -4\%$. The color indicates the rotation of the squares. (c) We model the system as an array of rigid squares connected at their vertices by elastic springs. (d) Evolution of θ_{st} as a function of ε_{st}^{yy} as predicted (solid lines) and measured in our experiment (markers). 43
- 4.2 Uniaxial compression of the rotating-square structure with phase inducing defects.** (a) Deformation at $\varepsilon_{\text{applied}}^{yy} = -4\%$ of a sample with 8 phase-inducing defects arranged to induce nucleation of *phase+*. (b)-(c) Deformation at (b) $\varepsilon_{\text{applied}}^{yy} = -4\%$ and (c) $\varepsilon_{\text{applied}}^{yy} = -6\%$ of a sample with 8 phase-inducing defects arranged to induce nucleation of *phase+* near to the bottom boundary and *phase-* near the top one. Experimental and numerical snapshots are shown on top and bottom, respectively. The color corresponds to the rotation of the squares. Zoom-ins of the defects are also shown. (d) Comparison between analytically predicted (solid lines) and experimentally extracted (circular markers) evolution of the squares' rotation θ across the sample for different values of applied strain. (e) Analytically predicted evolution of the total energy of the structure as a function of domain wall position y_0 for different values of applied strain. (f) Evolution of the domain wall position y_0 as a function of the applied strain $\varepsilon_{\text{applied}}^{yy}$ as predicted by theory (continuous line), numerical simulations (dashed line) and extracted from experiments (markers). (g) Evolution of the energy barrier ΔE as a function of applied strain $\varepsilon_{\text{applied}}^{yy}$. 44
- 4.3 The effects of pinning defects.** (a) Deformation at $\varepsilon_{\text{applied}}^{yy} = -6\%$ of a sample with 4 pinning defects and 8 phase-inducing defects. Experimental and numerical snapshots are shown on left and right, respectively. The color corresponds to the rotation of the squares. A zoom-in of a pinning defect is also shown. (b) Analytically predicted evolution of the total energy of the structure as a function of domain wall position y_0 for different values of applied strain. (c) Numerically predicted deformation at $\varepsilon_{\text{applied}}^{yy} = -6\%$ of structures comprising 21×60 squares with pinning defect separated by 10 holes. The domain wall becomes wavy for large enough values of applied compression. 52

4.4	Domain walls at different orientations. (a) Deformation at $\varepsilon_{\text{applied}}^{yy} = -4\%$ of a sample with 8 phase-inducing defects arranged along two lines that form an angle $\varphi_d = \arctan(1/2)$ and $\pi/4$ with the horizontal axis. (b) Analytically predicted evolution of E_{total} at $\varepsilon_{\text{applied}}^{yy} = -4\%$ as a function of ζ_0 and φ . The triangular marker corresponds to the configuration of the experimentally observed domain wall. (c) Deformation at $\varepsilon_{\text{applied}}^{yy} = -4\%$ of a sample with 4 pinning defects in addition to 8 phase-inducing defects arranged as in A. (d) Analytically predicted evolution of E_{total} at $\varepsilon_{\text{applied}}^{yy} = -4\%$ as a function of domain wall position ζ_0 and orientation φ . The triangular marker corresponds to the configuration of the experimentally observed domain wall. (e) Numerically predicted deformation at $\varepsilon_{\text{applied}}^{yy} = -4\%$ for 51×51 structures with the pinning defects arranged along complex paths (in addition to phase-inducing defects to initiate <i>phase+</i> and <i>phase-</i> at desired locations). The color in all snapshots corresponds to the rotation of the squares.	53
4.5	Potential applications of domain walls in mechanical metamaterials. (a) Experimentally measured (markers), numerically calculated (dashed lines) and theoretically predicted (solid lines) stress-strain curves for 21×21 structures without domain wall and with a horizontal domain wall. Note that the numerical and analytical predictions for the structure without domain wall match perfectly, so that the green solid and dashed lines overlap. (b) Numerically calculated stress-strain curve for 21×21 structures with two vertical domain walls (blue line) and two perpendicular domain walls at $\varphi = \pi/4$ (red line). The corresponding deformations are shown as insets. (c) Dispersion relations for planar elastic waves in the undeformed ($\theta = 0$) and compressed ($\theta = 0.4$) configurations. (d) Evolution of the band gap frequency, f , as a function of the squares rotation θ . (e) Evolution of θ along the y -direction for a 21×21 sample with an horizontal domain wall at $\varepsilon_{\text{applied}}^{yy} = 0\%$, -4% and -8% . (f) Modal displacement fields at $\varepsilon_{\text{applied}}^{yy} = 0\%$ ($f = 2811$ Hz), -4% ($f = 2812$ Hz) and -8% ($f = 2779$ Hz).	57

- 5.1** **Strategy for topological transformation of cellular structures.** (a-b), Schematic illustration of topological transformation occurring at the architectural scale during liquid immersion and evaporation (a), and corresponding changes in the polymer network at the molecular scale (b). Since the liquid in the compartments evaporates prior to that inside the polymer network, the capillary forces introduced at the air-liquid interface always act on the softened structure, enabling the structure to deform, and the edges to be zipped together. This results in the formation of new nodes (shown in orange and indicated by orange arrow on the right), and in the disappearance or change in connectivity of the original nodes (shown in red). (c) Schematics of the assembly of two adjacent walls from a cellular structure characterized by angle α , edge length l , thickness b and height h . The walls are stretched and folded by the capillary forces.(d) Contour plot of critical Young's modulus E_{cr} with respect to structural parameters α and (b) while the slenderness ratio is fixed as $l/b = 15$. The star marker denotes the corresponding parameters of the considered structure.(e) A list of commonly used polymeric materials and their Young's moduli in a dry state. In particular, the Young's modulus of a liquid crystalline polymer (LCP) changes reversibly from 23,000 kPa in the dry state to 80kPa in the wet state.(f) Micrographs of an LCP microplate with dimensions $l = 100 \mu\text{m}$, $b = 7 \mu\text{m}$ and $h = 70 \mu\text{m}$ after exposure to acetone.(g) Critical modulus E_{cr} as a function of swelling ratio δ . The star marker represents the swelling ratio of the selected material.

63

5.2 Experimental characterization of the assembly and disassembly of a triangular lattice. (a) Top view of the initial triangular micro-cellular structure imaged by scanning electron microscope (SEM). (b) Top and tilted views of the assembled micro-cellular structure. The initial triangular lattice is transformed to a hexagonal lattice upon application of an acetone droplet. One of the new nodes is marked with an orange circle, and one of the original nodes with a white circle. (c) Profilometer 3D surface topography of the initial (top) and assembled microstructure (bottom). While the top surface of the original structure is planar, the assembled structure contains nodes of two different heights due to the deformation of the walls. (d) Fluorescence confocal (FC) images of the microstructures at different stages of the assembly. Rhodamine B was co-polymerized into the polymer for characterization by FC microscopy. (e) Schematic representation of the generalized mechanism of the disassembly process showing how the mixture of two different liquids decouples the two scales, with one, highly volatile liquid, acting at the molecular scale and another, chemically inert, less volatile liquid, returning the structure to its original state at the micron scale. (f) Fluorescence confocal images of the LCP microstructures at different stages during the disassembly induced by the DCM:ethanol mixture at 2:1 ratio, with DCM swelling the assembled structure significantly to disassociate the assembled walls, and ethanol exerting capillary forces on a stiffened structure after evaporation of DCM. (g) Selective trapping of intermediate stages by tuning the evaporation kinetics (imaged by SEM) using different solvent concentrations and polymer compositions. All the presented structures are transformed from the assembled hexagonal lattice. (h) Partial topological transformation of the initial triangular lattice into a hierarchical triangular lattice with two compartment sizes using a mixture of acetone and ethanol.

67

5.3 Generalization of topological transformation principle. (a) Generalized lattice consists of nodes with different angles. The edges forming the smallest angle will undergo zipping for angle-guided capillary-driven transformations from: i, Circular to square, ii, Rhombitrihexagonal to hybrid hexagonal, iii, Kagome to hexagonal and iv, Rhombus to hexagonal. Note that compared to the triangular-transformed and kagome-transformed hexagonal lattices, which are comprised of nodes connecting three equal double-walls, nodes in the hexagonal lattice assembled from the diamond structure comprise two single walls and one double wall – resulting in additional anisotropy along the horizontal direction. (b) Multi-stimuli deformation of molecularly aligned LCP diamond-shaped cellular structures with director oriented along the z-axis. (c-d), Regional triangular-hexagonal transformations through localized multi-step assembly/disassembly.

71

5.4	Exemplary applications of lattice structures undergoing topological transformations. (a) Information encryption. Heart shape and Harvard shield outlined by the phase boundaries appear upon topological transformation of the triangular lattice. The shape and location of phase boundaries are designed by manipulating the distribution of the initial angular perturbations, with the nodes in the pink regions encrypted to transform to a “Y” shape and nodes in the orange regions to transform to an inverted “Y” (shown schematically on the left). (b) Particle and bubble trapping/releasing through the closed chambers formed by topological transformation. (c) Ball bouncing test to measure the resilience of the surface before and after transformation. Note that the topological transformation is necessary to change the coefficient of restitution, as simply-buckled and undeformed structures show the same resilience. (d) Bandgaps at a particular frequency can be tuned by capillarity-driven assembly for some lattices. Examples for bandgaps in rhombitrihexagonal and Kagome lattices are shown. (e-f), Controlling surface properties upon topological transformations: (e) Wetting;(f) Friction.	73
A.1	Fabrication of the aligned chain. (a) Parts used to fabricate the unit cell. (b) Exploded view of the two pairs of crosses. (c) The chain is realized by putting together a number of unit cells.	80
A.2	Fabrication of the shifted chain. (a) Parts used to fabricate the unit cell. (b) Exploded view of two pairs of crosses. (c) The chain is realized by putting together a number of unit cells.	81
A.3	Experimental setup. (a)-(b) Pictures of our experimental setup showing the sample, the lamp used to illuminate it, the pendulum and the impactor used to excite the pulses and the camera used to monitor the propagation of the pulses. (c) Top-view of the pendulum and the impactor. (d) Side-view of the pendulum and the impactor. (e) Close-up view of the impactor. (f) Close-up view of the end of the pendulum. (g) Friction is minimized by supporting each rigid unit with pins.	83
A.4	Digital image correlation analysis. For each pair of rigid crosses four markers (blue dots) are tracked.	84
A.5	Exciting different rotations in the shifted chain. (a) Energetically favorable rotations are excited by placing a pair of crosses with $\varphi_0 = 0$ at the left end of the chain. (b) Energetically unfavorable rotations are excited by placing a pair of crosses with $\varphi_0 \neq 0$ at the left end of the chain.	85
A.6	Schematics of the system. (a) Configuration in which neighboring horizontal hinges are shifted in vertical direction by $a \sin \varphi_0$. (b) Configuration in the horizontal hinges are all aligned. (c) Chain comprising 2×10 cross-shaped rigid units.	87
A.7	Schematics showing how U_{input} is applied in our discrete simulations. (a) A linear spring with stiffness $K_{input} = 1$ is connected to the mid-point at the left end of the chain. (b) U_{input} is applied to this spring.	90
A.8	(a) Geometry of the rigid unit in our aligned chain. (b) Geometry of the rigid unit in our shifted chain. The back dot represent the center of mass. (c) View of the experimental setup used to estimate k_s and k_l . (d) Picture showing the test conducted to estimate k_s . (e) Picture showing the test conducted to estimate k_l . (f) Picture showing the test conducted to estimate k_θ	91

A.9	Comparison between experimental and numerical results for (a) experiment #1 and (b) experiment #2 shown in Fig. 2.1(c) of the main text. Experimental (solid lines) and numerical (dashed lines) signals recorded at the 2nd (blue lines) and 40th (magenta lines) pairs of crosses are reported as a function of time. In our numerical simulations, we apply the experimental signal recorded at 2nd pair of crosses as boundary conditions.	94
A.10	Numerical results for a chain comprising 2×150 crosses with $\varphi_0 = 0^\circ$. Rotation (left) and normalized displacement (right) profiles are shown at $T = 1050, 1550$, and 2050	94
A.11	(a)-(b) Analytical solution for a structure characterized by $K_s = 0.0185$, $K_\theta = 1.5 \times 10^{-4}$, $\alpha = 1.8$, $c = 0.1$ and $\varphi_0 = 5^\circ$. (c)-(d) Comparison between analytically (lines) and numerically (markers) predicted rotation and normalized displacement profiles at $T = 840$, 1080 , and 1320 . Also in this case we assume that $K_s = 0.0185$, $K_\theta = 1.5 \times 10^{-4}$, $\alpha = 1.8$, $c = 0.1$ and $\varphi_0 = 5^\circ$	99
A.12	(a)-(c) Evolution of the amplitude gap as a function of the angle φ_0 chains characterized by (a) $\alpha=1.8$, $K_\theta=1.5 \times 10^{-4}$ and $K_s=0.02$; (b) $\alpha=1.8$, $K_\theta=1.0 \times 10^{-3}$ and $K_s=0.02$; (c) $\alpha=1.8$, $K_\theta=1.5 \times 10^{-4}$ and $K_s=0.1$. (d) Evolution of φ_0^{cr} as a function of K_s and K_θ , assuming $\alpha = 1.8$. 103	
A.13	(a)-(b) Analytical solution for a structure characterized by $K_s = 0.0185$, $K_\theta = 1.5 \times 10^{-4}$, $\alpha = 1.8$, $c = 0.1$ and $\varphi_0 = 0.0$. (c)-(d) Comparison between analytically (lines) and numerically (markers) predicted rotation and normalized displacement profiles at $T = 840$, 1080 , and 1320 . Also, in this case we assume that $K_s = 0.0185$, $K_\theta = 1.5 \times 10^{-4}$, $\alpha = 1.8$, $c = 0.1$ and $\varphi_0 = 0^\circ$	106
A.14	(a) Evolution of $A_{upper} = -A_{lower}$ as a function of α and K_θ (assuming $K_s = 0.02$). (b) Evolution of $A_{upper} = -A_{lower}$ as a function of α and K_s (assuming $K_\theta = 1.5 \times 10^{-4}$). (c) Evolution of $A_{upper} = -A_{lower}$ as a function of K_θ and K_s (assuming $\alpha = 1.8$).	107
A.15	(a) Region (shaded area) of the φ_0 - K_θ domain in which pulling solitons exist. (b)-(c) Analytical solution for a structure characterized by $K_s = 0.0185$, $K_\theta = 1.5 \times 10^{-4}$, $\alpha = 1.8$, $c = 0.5$ and $\varphi_0 = 8^\circ$. (d)-(e) Comparison between analytically (lines) and numerically (markers) predicted rotation and normalized displacement on the same structure at $T = 226, 294$, and 360 . (f) Relation between pulse velocity and amplitude for pulling solitons propagating in structures characterized by different angles φ_0	109
A.16	A schematic diagram for the analysis of unit cell energy.	110
A.17	Evolution of E_S as a function of the amplitude A for the aligned (blue line) and shifted (purple line) chains.	113
A.18	(a)-(b) Linear dispersion relations for a chain with $\varphi_0 = 0$ and $\varphi_0 = 5^\circ$, respectively. The dispersion curves are color-coded to show the modal ratio of rotation η_θ . (c)-(d) Amplitude transmission coefficients of the two linear modes for a chain with $\varphi_0 = 0$ and $\varphi_0 = 5^\circ$, respectively; (e)-(f) Frequency content of a typical soliton supported by a chain with $\varphi_0 = 0$ and $\varphi_0 = 5^\circ$, respectively. Note that the frequency range is changed in order to show the low frequency dominance in the soliton.	117
A.19	Experimentally measured rotation of the pairs of crosses during the propagation of the pulse for soliton splitters with two stiffer hinges made of (a) polyester sheets with thickness $t_h^d = 0.508$ mm, (b) polyester sheets with thickness $t_h^d = 0.635$ mm and (c) paper clips. The location of the stiff pair of hinges is indicated by the dashed red line	119
A.20	Experimentally measured rotation during the propagation of the pulse for soliton splitters characterized by (a) $\varphi_0 = 0^\circ$ and (b) $\varphi_0 = 5^\circ$. The location of the stiff pair of hinges (made of polyester sheets with thickness $t_h^d = 0.635$ mm) is indicated by the dashed red line	119

A.21 Soliton splitter with a stiff defect ($K_s^d/K_s = K_\theta^d/K_\theta = 30$) between the 500th and 501st rigid crosses . (a)-(d) Numerical results for a 2×1000 chain with symmetric crosses characterized by $\varphi = 0^\circ$. (e)-(h) Numerical results for a 2×1000 chain with asymmetric crosses characterized by $\varphi = 5^\circ$.	121
A.22 Soliton splitter with a softer defect ($K_s^d/K_s = K_\theta^d/K_\theta = 1/30$) between the 500th and 501st rigid crosses . (a)-(d) Numerical results for a 2×1000 chain with symmetric crosses characterized by $\varphi = 0^\circ$. (e)-(h) Numerical results for a 2×1000 chain with asymmetric crosses characterized by $\varphi = 5^\circ$.	122
A.23 Numerical results showing the effect of $K_s^d/K_s = K_\theta^d/K_\theta$ on the amplitude of the transmitted and reflected solitons. Amplitude ratios (a) A_r/A_t and (b) A_t/A_i as a function of $K_s^d/K_s = K_\theta^d/K_\theta$ for different values of A_i . The splitter considered in our simulations comprises a chain of 2×1000 crosses with $\varphi_0 = 0^\circ$, $K_s = 0.02$, $K_\theta = 1.5 \times 10^{-4}$, $\alpha = 1.8$ and $\varphi = 0^\circ$. A pair of stiffer hinges are inserted at the center of the chain with stiffness ratio $K_s^d/K_s = K_\theta^d/K_\theta \in [1, 100]$.	123
A.24 (a) Experimentally measured transmission, $ A_{40} / A_{10} $, as a function of the input amplitude, $ A_{10} $, for pulses excited at the left end of the chain. (b) Experimentally measured transmission, $ A_{10} / A_{40} $, as a function of the input amplitude, $ A_{40} $, for pulses excited at the right end of the chain. (c)-(g) Optical images and corresponding rotation of the pairs of crosses as measured in five different experiments.	125
A.25 Numerical results showing the effect of N_a and φ_0 on the breakdown amplitude A_{br} . (a) Transmission as a function of the amplitude of the input signal for diodes characterized by different numbers N_a of pairs of crosses with $\varphi_0 = 5^\circ$ (while keeping $N=12$). (b) Transmission as a function of the amplitude of the input signal for diodes characterized by $N_a = 3$ and $\varphi_0 = 3^\circ$ and 7° (while keeping $N=12$). (c) Evolution of the breakdown amplitude A_{br} as a function of N_a and φ_0 .	127
B.1 Fabrication of our structure. (A) Parts used to fabricate a 2×2 unit. (B) Exploded view of two pairs of crosses. (C) The chain is realized by putting together a number of 2×2 units.	130
B.2 Experimental setup. (A) Pictures of our experimental setup showing the LEGO chain, the metal bars used to constrain the transverse movement of the chain and the pendulums and impactors used to excite the pulses at both ends. (B) A few units of our sample. (C) The impactor used to initiate solitons that excite positive rotations. (D) The impactor used to initiate solitons that excite negative rotations. (E) Close view of the pendulum consisting of a metal frame and a hammer. (F) Friction is minimized by supporting each rigid unit with pins. (G) Digital image correlation analysis. For each pair of rigid crosses four markers (blue dots) are tracked.	131
B.3 Schematics of the structure considered in this study.	134
B.4 Schematics of the structure considered in this study with a frozen soliton located at its center.	141

B.5	Displacement signal. (A)-(B) Longitudinal displacement of the pairs of crosses during the propagation of the pulses, as recorded in (A) experiments and (B) numerical simulations. The pulses excited at the left and right end are characterized by $A_{\text{left}} = 0.2$ and $A_{\text{right}} = 0.2$, respectively. (C)-(D) Longitudinal displacement of the pairs of crosses during the propagation of the pulses, as recorded in (C) experiments and (D) numerical simulations. The pulses excited at the left and right end are characterized by $A_{\text{left}} = -0.2$ and $A_{\text{right}} = 0.2$, respectively. In (C) and (D) we find that the units near collision point do not move - an indication of anomalous collisional dynamics.	143
B.6	A chain with odd pairs of crosses. (A) We consider a chain with $N = 49$ pair of crosses. To initiate a soliton at the right end that induces negative rotations, we use an impactor that hits the mid-point of the last pair. (B)-(C) Rotation of the pairs of crosses during the propagation of the pulses, as recorded in (B) experiments and (C) numerical simulations. (D)-(E) Longitudinal displacement of the pairs of crosses during the propagation of the pulses, as recorded in (D) experiments and (E) numerical simulations. The pulses excited at the left and right end are characterized by $A_{\text{left}} = 0.2$ and $A_{\text{right}} = -0.2$, respectively. The experiments are conducted on a chain with with 49 pairs of crosses, whereas in the numerical simulations we consider 499 units.	144
B.7	Numerically obtained cross-correlation between $\theta_{10}(t < t_c)$ and $\theta_{N-10}(t > t_c)$ as a function of A_{left} and A_{right}	145
B.8	Anomalous collisions can be exploited to actively manipulate and control the propagation of pulses. (A) Anomalous collisions provide opportunities to remotely induce changes in the propagation velocity of a soliton. To demonstrate this, we consider a left-initiated pulse with $A_{\text{left},1} = 0.4$ and $c = 275$ unit/s and use the interactions with a soliton subsequently excited at the left end to reduce its velocity to $c = 215$ unit/s and with a right-initiated solitary wave to then accelerate it to $c = 255$ unit/s. (B) Anomalous collision can be exploited to block the propagation of a soliton. Specifically, a large propagating soliton can be blocked by sending a sequence of relatively small pulses with opposite rotation direction. As an example, we consider a left-initiated soliton with $A_{\text{left}} = 0.4$ and six right-initiated solitons with $A_{\text{right},k} = -0.2$ (with $k = 1, \dots, 6$). Each of the six collisions results in energy radiation to linear waves or to other small amplitude solitons and reduces the amplitude of the left-initiated pulse, which eventually vanishes as its amplitude falls within the amplitude gap of the structure. Therefore, six small pulses efficiently mitigate and destroy the main left-initiated soliton at $t = 2$ s. (C)-(D) Anomalous collisions can also be exploited to probe the direction of the rotational component of a pulse. To demonstrate this, we consider a main left-initiated soliton with $A_{\text{left}} = \pm 0.4$ and a probing, small right-initiated pulse with $A_{\text{right}} = -0.18$. If $A_{\text{left}} = 0.4$ (C), the "echo" of the probing soliton reaches the right end before the main soliton, indicating that it has been reflected by the main soliton. From this information, we therefore deduce that the main soliton is of positive amplitude. If $A_{\text{left}} = -0.4$ (D), no "echo" is observed, as the probe penetrate the main soliton. From this information, we therefore deduce that the main soliton is of negative amplitude. Finally, it is important to point out that, since the probing soliton carries much less energy than the main one, the latter is almost unaltered by the collision (i.e. its velocity changes from 275unit/s to 272unit/s).	146

C.1	Snapshots of our sample comprising an array of 21×21 squares connected at their vertices by thin hinges.	149
C.2	(a) Magnified view of a phase-inducing defect. (b) Magnified view of a pinning defect.	149
C.3	Distribution of phase-inducing defects within the sample to generate the deformation fields shown in (a) Fig. 4.2A of the main text; (b) Fig. 2B-C of the main text; (c) Fig. 4.4A of the main text ($\varphi_d = \arctan(1/2)$); (d) Fig. 4.4A of the main text ($\varphi_d = \pi/4$).	150
C.4	Distribution of pinning defects within the sample to generate the deformation fields shown in (a) Fig. 4.3A of the main text; (b) Fig. 4.4C of the main text ($\varphi_d = \arctan(1/2)$); (c) Fig. 4.4C of the main text ($\varphi_d = \pi/4$).	151
C.5	Distribution of phase-inducing and pinning defects within the sample to generate the deformation fields shown in (a) Fig. 4.5B of the main text; (b) Fig. 4.5C of the main text.	151
C.6	(a) Top view of the testing setup. (b) Front view of the testing setup. (c) Magnified view of the sample, with plastic stickers on the center of square cells. (d) Magnified view of the setup highlighting the cover and base plates used to prevent out-of-plane deformation.	152
C.7	Procedure for tracking the deformation of our samples.	154
C.8	Discrete model based on rigid units connected at their vertices by springs. (b) Schematic view of the $[i, j]^{\text{th}}$ rigid square unit.	156
C.9	(a) A phase-inducing defect is modelled using one spring. (b) A pinning defect is modelled using two springs.	158
C.10	(a) A snapshot of the experiments where uniaxial compression leads to homogeneous deformation. (b) Matching of the model predicted force-strain relation with the experimental measurements. (c) FEM simulations for the estimation of k_s	163
C.11	Supercell used to calculate the dispersion relation.	167
C.12	Numerically predicted deformation at applied strain $\varepsilon_{\text{applied}}^{\text{yy}} = -2\%, -4\%$ and -8% of structures comprising 21×21 squares (top) and 51×51 squares (bottom) in the absence of intentional defects.	168
C.13	Numerically predicted deformation at applied strain $\varepsilon_{\text{applied}}^{\text{yy}} = -2\%, -4\%$ and -8% of structures comprising 21×21 squares (top) and 51×51 squares (bottom) with phase-inducing defects linearly arranged and angled at $\varphi_d = 0$ to get <i>phase-</i> to propagate from the top boundary and <i>phase+</i> from the bottom one.	168
C.14	Numerically predicted deformation at applied strain $\varepsilon_{\text{applied}}^{\text{yy}} = -2\%, -4\%$ and -8% of structures comprising 21×21 squares (top) and 51×51 squares (bottom) with phase-inducing defects linearly arranged and angled at $\varphi_d = \arctan(1/2)$ to get <i>phase-</i> to propagate from the top-right corner and <i>phase+</i> from the bottom-left one.	169
C.15	Numerically predicted deformation at applied strain $\varepsilon_{\text{applied}}^{\text{yy}} = -2\%, -4\%$ and -8% of structures comprising 21×21 squares (top) and 51×51 squares (bottom) with phase-inducing defects linearly arranged and angled at $\varphi_d = \pi/4$ to get <i>phase-</i> to propagate from the top-right corner and <i>phase+</i> from the bottom-left one.	169
C.16	Numerically predicted deformation at applied strain $\varepsilon_{\text{applied}}^{\text{yy}} = -2\%, -4\%$ and -8% of structures comprising 21×21 squares (top) and 51×51 squares (bottom) with pinning defects equally spaced along a horizontal line spanning their center, in addition to the previous phase-inducing defects arranged as in Fig. C.13.	170

C.17	Numerically predicted deformation at applied strain $\varepsilon_{\text{applied}}^{\text{yy}} = -2\%, -4\% \text{ and } -8\%$ of structures comprising 21×21 squares (top) and 51×51 squares (bottom) with pinning defects equally spaced along a line at $\varphi_d = \arctan(1/2)$, in addition to the previous phase-inducing defects arranged as in Fig. C.14.	170
C.18	Numerically predicted deformation at applied strain $\varepsilon_{\text{applied}}^{\text{yy}} = -2\%, -4\% \text{ and } -8\%$ of structures comprising 21×21 squares (top) and 51×51 squares (bottom) with pinning defects equally spaced along a line at $\varphi_d = \pi/4$, in addition to the previous phase-inducing defects arranged as in Fig. C.15.	171
C.19	Numerically predicted deformation at applied strain $\varepsilon_{\text{applied}}^{\text{yy}} = -6\%$ of structures comprising 21×21 squares and pinning defects equally spaced along horizontal lines located near the top (left) and bottom (right), in addition to the previous phase-inducing defects arranged as in Fig. 4.2B of the main text.	171
C.20	Deformation at $\varepsilon_{\text{applied}}^{\text{yy}} = -6\%$ of a sample with 4 pinning defects and 8 phase-inducing defects arranged as in Fig. 4.2A of the main text. Since the phase-inducing defects induce the formation of a single phase, no domain wall is generated (i.e. pinning defects along can not lead to the formation of domain walls).	172
C.21	(a) Numerically predicted deformation at $\varepsilon_{\text{applied}}^{\text{yy}} = -6\%$ of structures comprising 21×60 squares with pinning defect separated by 5 (top) and 13 (bottom) holes (in addition to phase-inducing defects arranged to generate an horizontal domain wall). (b) Corresponding domain wall profiles extracted at $\varepsilon_{\text{applied}}^{\text{yy}} = -2\%, -4\% \text{ and } -6\%$.	172
C.22	Numerically predicted deformation at $\varepsilon_{\text{applied}}^{\text{yy}} = -4\%$ (top) and -10% (bottom) of structures comprising 21×60 squares with (a) only one pinning defect and (b) two pinning defects at the center (in addition to phase-inducing defects arranged to generate an horizontal domain wall).	173
C.23	Numerically predicted deformation at $\varepsilon_{\text{applied}}^{\text{yy}} = -4\%$ (top) and -6% (bottom) of structures comprising 51×51 squares with four pinning defects arrange at the vertices of a rhombus with edge (a) $5a$ and (b) $8a$. In addition, two phase-inducing defects are located next to the top and bottom boundary to promote <i>phase -</i> . These defects results in the formation of a rhomboid <i>phase +</i> region defined by the pinning defects.	174
C.24	Numerically predicted deformation at $\varepsilon_{\text{applied}}^{\text{yy}} = -6\%$ (left) and -10% (right) of structures comprising 21×21 squares with (a) only one pinning defect and (b) two pinning defects (in addition to phase-inducing defects arranged to generate an horizontal domain wall). Similar wavy pattern are observed for the emerged domain walls as in the wide 21×60 squares sample (see Fig. C.21).	175
C.25	Schematic of a domain wall with an orientation of φ and position ζ_0 .	180
C.26	Analytical predicted evolution of E_{total} as a function of domain wall position y_0 at $\varepsilon_{\text{applied}}^{\text{yy}} = -2\%, -4\%, -6\% \text{ and } -10\%$ for structures with (a) 21×21 squares; (b) 51×51 squares and (c) 201×201 squares and phase-inducing defects arranges to generate an horizontal domain wall. The results indicate that, while in small structures E_{total} gradually turns into a multi-welled landscape with two minima that progressively move towards the horizontal boundaries, in larger structures present E_{total} becomes flat upon compression. As such, we expect the domain walls in large structures to remain at the center even upon compression. In another words, the shifting of domain walls observed in our samples is caused by boundary effects.	184

C.27	Analytically predicted evolution of E_{total} as a function of ζ_0 and φ at $\varepsilon_{\text{applied}}^{yy} = -2\%$, -4% and -8% for structures comprising 21×21 squares and phase-inducing defects arranged as (a) in Fig. 4.2B-C of the main text; (b) in Fig. 4.4A of the main text ($\varphi_d = \arctan(1/2)$) and (c) in Fig. 4.4A of the main text ($\varphi_d = \pi/4$). As the applied compression increases, the local minima of E_{total} move away from the centered line between and shift towards the boundaries. Furthermore, for the cases with $\varphi_d \neq 0$ the domain walls also change their orientation as $\varepsilon_{\text{applied}}^{yy}$ increased. These results nicely explain the experimental results reported in Figs. 4A and 4C.	185
C.28	Analytically predicted evolution of E_{total} at $\varepsilon_{\text{applied}}^{yy} = -2\%$, -4% and -8% for structures comprising 21×21 squares and phase-inducing and pinning defects arranged as (a) in Fig. 4.3A of the main text; (b) in Fig. 4.4C of the main text ($\varphi_d = \arctan(1/2)$) and (c) in Fig. 4.4C of the main text ($\varphi_d = \pi/4$).	186
C.29	Stress-strain curve measured in experiments (markers) and predicted by numerical simulations (dashed lines) and analytical solution (solid lines) for structures with 21×21 squares and (a) no phase-inducing defects; (b-d) phase-inducing and pinning defect arranged along two lines that form an angle (b) $\varphi_d = 0$, (c) $\arctan(1/2)$ and (d) $\pi/4$ with the horizontal axis to generate a domain wall.	188
C.30	(a)-(b) Comparison between analytically predicted (solid lines) and experimentally extracted (circular markers) evolution of the squares rotation θ across the sample at $\varepsilon_{\text{applied}}^{yy} = -4\%$ for a 21×21 structure with defects arranged as in (a) Fig. 4.4A of the main text and (b) Fig. 4.4C of the main text. (c) Contour plot of domain wall width w as a function of φ and θ_{st} as predicted by Eq. (C.53). As observed in experiments, our analytical solution predicts the domain walls to become thinner for increasing compression (i.e. for larger θ_{st}).	189
D.1	Schematic presentation of the structural parameters used for a theoretical model. (a) Pre- and post-assembly configurations of a triangular compartment. (b) Components of wall deformation required for assembly. (c) Pure bending of an initially straight beam. (d) Contour plot of critical Young's modulus E_{cr} with respect to structural parameters "α and b, while the slenderness ratio is set as $l/b = 5, 15$ and 50 . (e) Relation between E_{cr} and the wall thickness b predicted by our theoretical model for triangular lattices with $\alpha = 60^\circ$. The slenderness of the lattice edges remains constant at $l/b = 15$.	198
D.2	Transformation of cellular structures with different wall thicknesses b and angle "α. (a) Top view optical images of the liquid-treated cellular structures with thicknesses $b = 7, 10, 13$ and $16 \mu\text{m}$, respectively. (b) Image processing to track the area of each compartment. (c) Distributions of the compartment areas and the corresponding assembly index R. (d) Critical Young's modulus E_{cr} as a function of wall thickness b. For a fixed material stiffness $E = 80 \text{ kPa}$, we can derive the critical thickness $b_{cr} = 12.6 \mu\text{m}$. (e) Assembly index R with increasing thickness b. The predicted b_{cr} captures the critical thickness where R starts to deviate from 1 (perfect assembly). Cellular structures with different "α after liquid treatment. (f) Square lattice; (g) hexagonal lattice. Scale bars, $100 \mu\text{m}$.	203
D.3	Distorted triangular lattices made of (a), EcoflexTM 00-10, and (b) EcoflexTM 00-50 after being peeled off the silicon master. Scale bar, $100 \mu\text{m}$.	205
D.4	Synthesis of LCP. (a) LCP chemical constituents. (b) Phase diagram of the reactive LC monomer mixture. The heating rate of the differential scanning calorimetry (DSC) was $10^\circ\text{C}/\text{min}$. (c) Schematic of the polymerization setup.	206

D.5	Characterization of material properties of LCP. (a) Phase diagrams of the LCP polymer. Dry LCP polymer and wet LCP polymer swollen with acetone. The heating rate of the differential scanning calorimetry (DSC) was 10 °C/min. (b) Young's modulus characterization of the LCP upon swelling and drying. AFM was applied to measure the Young's moduli of the polymer on a cellular structure in the original dry state, fully swollen state, and dried state after evaporation of the liquid.	209
D.6	Swelling behavior of LCP with different liquids. Snapshots of LCP cellular structures in the initial state, during immersing in liquids, and after evaporation of liquids. (i) Water does not wet the structure. (ii) Ethanol wets the structure but does not swell the LCP noticeably. (iii-iv), isopropanol and hexane wet and swell the structure slightly but are not sufficient to trigger assembly upon evaporation. (v-vi), Dichloromethane and toluene wet the structure, but the swelling ratio is so large that the LCP films rupture and delaminate from the glass substrate. Scale bar, 100 μm .	210
D.7	3D topography of the cellular structures. Top and tilted view of the optical profilometer measurements showing the reconfigured 3D shape of the (a) initial triangular lattice and (b) assembled hexagonal lattice. (c) The height profile of the assembled hexagonal lattice along the dashed line. The newly formed nodes are $\approx 10 \mu\text{m}$ shorter than the original nodes. Furthermore, the inset of (c) shows that the transformed hexagonal structure contains flat bottoms and sharp vertical walls, which indicates that half of the initial triangle compartments are completely closed through the transformation.	211
D.8	Initial instability of the node and domain boundaries formation in a perfect triangular lattice after transformation. (a) A schematic demonstrating the initial instability of a triangular lattice node. (c) Two equally probable ways of transforming initial nodes leading to two different phases. (c) The evaporation line formed during transformation and the unit cells are assembled sequentially from right to left. (d) Phase boundary forms between two phases. Scale bar, 100 μm .	213
D.9	Stability of the assembled microstructures under harsh conditions. Confocal microscopy images of the assembled structure for (a) a triangular-to-hexagonal system and (b) a diamond-to-hexagonal system, at room temperature (left), heated to 130 °C (middle), and cooled to room temperature (right). The structure is locked in a fully assembled configuration throughout the heating and cooling process. (c) Optical microscopy images of the assembled structure after immersion in ethanol for 0 day, 1 day, 2 days, and 10 days post assembly. Scale bar, 100 μm .	214
D.10	Reversibility, fatigue and hysteresis test with LCP (2wt%). (a) Reversibility and fatigue test over ten cycles. (b) Hysteresis test over time breaks of 3, 6, 9 and 18 days.	216
D.11	Topological transformation of complex lattice geometries in large areas. (a) Circular lattice (inset) transformed to a square lattice. (b) Initial kagome lattice (inset) transformed to a hexagonal lattice. (c) Transformation of flower-patterned lattice. Scale bar, 100 μm . (d) Initial isolated rings transformed to an interconnected square lattice. When the top surface is coated with conductive materials, such transformation could be potentially used to alter the conductivity of the cellular structures. Scale bar, 30 μm .	217

D.12	Topological transformation of cellular structures with edge length $l=20 \mu\text{m}$, $b=2 \mu\text{m}$, and $h=10 \mu\text{m}$. (a) Initial triangular lattice and (b) assembled hexagonal lattice. (c) Initial diamond lattice and (d) assembled hexagonal lattice. These results prove that, as predicted by our theoretical model (Fig. D.2), our strategy is applicable to smaller scales. Scale bar, $20 \mu\text{m}$.	218
D.13	Application to different polymeric materials. (a) Topological transformation of a poly(2-hydroxyethyl methacrylate-co-n-butyl-acrylate) PHEMA-co-PBA triangular cellular lattice to a hexagonal one. (b) Schematic of experimental setup and LCP chemical constituents for the synthesis of molecularly aligned nematic LCP.	219
D.14	(a-b) The free-standing triangular cellular mesh with soft deformable substrate: (a) initial structure upon exposure to liquid (acetone); (b) partially assembled structure after the evaporation. (c-d) The free-standing square cellular mesh with soft deformable substrate: (c) initial structure; (d) after the evaporation, the structure assembled chaotically and deformed globally due to the floppy nature of square lattice.	220
D.15	Localized transformation with small droplets. (a-d) Localized transformation of the triangular lattice into a hexagonal lattice with different sizes of the applied droplets. Note that the small droplet applied tends to spread to a hexagonal shape due to the symmetry and connectivity of the initial triangular lattice. (e) Multi-step localized transformation after a sequential assembly (large area)-disassembly (medium area)-assembly (small area) process. (f) Integration of the kinetic trapping effect of buckled walls with the local transformation.	222
D.16	Perturbation design for uniform assembly. (a) The phase selection can be controlled at each initial node by introducing a small difference in the local angles $\Delta\alpha$. (b) A schematic of the experimental design of the node to favor phase I using curved walls. The schematics exaggerate the curvature used in the experiments shown in c-f. (c) Actual structure with slightly perturbed angles $\Delta\alpha = 2.5^\circ$ (imaged by SEM). The inset shows the corresponding CAD design. The initial structure is visually indistinguishable from a perfect triangular lattice. (d) Confocal snapshots of the assembly of a perturbed triangular lattice at different time points. (e-g) Initial triangular lattice with $\Delta\alpha = 2.5^\circ$ is transformed to a perfect hexagonal lattice with a single uniform phase without phase boundaries: (e) top view, (f) tilted view and (g) zoomed-in tilted view. Scale bar, $100 \mu\text{m}$. (h) Large-area uniformed transformed samples ($1.5 \text{ cm} \times 1.5 \text{ cm}$, much larger samples are readily accessible with molding) used for friction and wetting measurement. Homogeneous transformations are observed in every region as illustrated by twelve different regions of sample each containing roughly 20 by 20 compartments (2 mm by 2 mm in size).	224
D.17	Phase boundary design. (a) Schematics of two imperfection designs that lead to phase I and phase II respectively. (b) Design of a phase boundary by controlling the distribution of the two types of angular perturbations. (c) SEM image of the engineered phase boundary: the nodes on the left are designed to favor a different phase than the nodes on the right. Scale bar, $100 \mu\text{m}$. (d) Phase designed heart pattern before and after transformation. Scale bar, $400 \mu\text{m}$. (e) Photos of microstructures with designed phase boundaries before and after capillary reconfiguration. The boundary between the two phases is optically visible in the assembled structures. Scale bar, 5 mm.	226

To my grandparents Xu Deng and Zuoqun Jiang.

献给我的爷爷奶奶

Acknowledgments

To all of the incredible people whom enabled the work presented in this dissertation.

I am grateful to all of the people who have helped, encouraged, guided, mentored, and supported me throughout my Ph.D. career as well as my life. My accomplishments would not have been possible without them. In the following paragraphs, I may only include a small portion of them, but I am equally grateful to the rest.

First and foremost, I would like to thank my advisor, **Prof. Katia Bertoldi**, for her unconditional support. She provides consistent guidance on my research projects and career development while allowing tremendous flexibility and freedom in research directions and working styles. She is always available whenever I need a discussion. None of my research achievements would have been possible without her support.

I am also thankful to other Professors who have mentored me: **Prof. Pai Wang**, **Prof. Vincent Tournat**, **Prof. Jordan R. Raney**, **Prof. Joanna Aizenberg**, and **Prof. Prashant K. Purohit**. They offer me enormous support in research projects and also serve as my role models in academics. Special thanks to **Prof. Pai Wang**, **Prof. Vincent Tournat** for their additional helps and advice as my close friends.

I am grateful to my dissertation committee members **Prof. Zhigang Suo**, **Prof. Joost J. Vlassak**, and **Prof. Chris Rycroft** for their valuable input on my research projects, as well as the exciting courses that they instructed during my Ph.D. years.

I would like to express my deep gratitude to all of my collaborators — **Prof. Pai Wang**, **Qi He**, **Prof. Vincent Tournat**, **Prof. Ahmad Rafsanjani**, **Prof. Jordan R. Raney**, **Dr. Lishuai Jin**, **Dr. Antonio E. Forte**, **Chengyang Mo**, **Liyuan Chen**, **Dr. Donglai Wei**, **Yuning Zhang**, **Siqin Yu**, **Jian Li**, **Prof. Prashant K. Purohit**, **Dr. Nickolaos Vasios**, **Dr. Benjamin Gorissen**, **Dr. Mohamed Zanaty**, **Dr. Alison Grinthal** and **Dr. James C. Weaver** — for their selfless contributions and guidance. I want to especially thank **Shucong Li** and **Dr. Ahmad Zareei** for

proofreading this dissertation.

I want to thank all the colleagues through my years in the Bertoldi group, **Dr. Farhad Javid**, **Dr. Elisa Boatti**, **Prof. Tal Cohen**, **Dr. Fionnuala Connolly**, **Connor McCann**, **Eder Medina**, **Prof. Jochen Muller**, **Catherine Ding**, **Dr. Yunfang Yang**, **Bangyuan Liu**, **Dr. Panos Pantidis**, **Dr. Mehdi Torbati**, **Kausalya Mahadevan**, **Stephanie Vincent**, especially my office mates from Pierce 404, 410 to 327, **Prof. Andrew Gross**, **Dr. Baohong Chen**, **Prof. Johannes T. B. Overvelde**, **Dr. Sahab Babaee**, **Dr. Nickolaos Vasilios**, **Dr. Gabriele Librandi**, **Dr. Bejamin Gorissen** and **David Mélançon**, for making my working days enjoyable. I would like to express my special gratitude to **Dr. Matheus Fernandes** for always being my comrade in classes and for the endless discussions in Pierce 327.

I would like to further thank everyone in the **Harvard School of Engineering and Applied Sciences** and **Harvard Graduate School of Arts and Sciences**, especially the instructors of all the amazing courses at Harvard, **Prof. Lakshminarayanan Mahadevan**, **Prof. Xin Li**, **Prof. David Parkes**, **Prof. Sasha Rush**, **Prof. Pavlos Protopapas**, **Prof. Mark Glickman**, and **Prof. David Sondak**, and the administrators **John Girish**, **Ann Greaney-Williams**, and **Lisa Frazier-Zezze**.

I am blessed to have many close friends at Harvard, **Liyuan Chen**, **Siqin Yu**, **Anqi Chen**, **Siyi Xu**, **Dr. Yuxing Yao**, and **Dr. Yanhao Yu**, as well as old friends outside of my academic circle, **Yiwei Zhao**, **Yidong Zhao**, **Yi Huang**, and **Kun Shang**. They have been exceptionally supportive and encouraged me through every step of my life. Most importantly, I want to thank my beloved girlfriend **Shucong Li** for her extraordinary support in every aspect of my life. She is not only a strong and thoughtful collaborator who offered me the opportunity to publish an article in *Nature* but also a considerate partner who supports me through the difficult times and encourages me to be myself.

My deepest gratitude to my parents **Bei Shi** and **Jiang Deng** for their consistent love that brings me from a little kid in southwest China to a Ph.D. at Harvard University. I am equally thankful to my other relatives, especially my maternal grandparents **Shouliang Shi** and **Keqing Wang** for their unreserved loves and my parental grandparents, **Xu Deng**, **Zhuoqun Jiang**, for taking care of me from the very beginning of my life to the very end of their lives.

Chapter 1

Introduction

1.1 Flexible mechanical metamaterials

Metamaterials — man-made structures with physical properties governed by their geometry rather than compositions — usually consist of periodically arranged building elements that act together to exhibit collective behaviors that surpass those of natural materials^[6–8]. Over the past decades, metamaterials have been designed to achieve exotic and unusual optical^[9], acoustic^[10], electro-magnetic^[7] and thermal^[11] properties and functionalities.

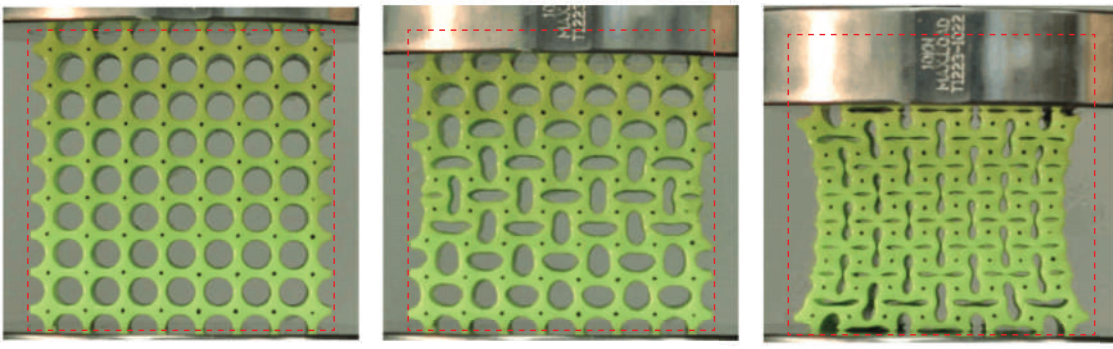


Figure 1.1: Deformation of an elastomeric block with an array of circular holes subjected to uniaxial compression^[1].

More recently, mechanical metamaterials have emerged as an effective platform to control motion, deformations, stresses, and mechanical energy. Mechanical metamaterials have enabled the design of systems with unusual (zero or negative) values for familiar mechanical parameters, such as Poisson's ratio^[12,13], compressibility^[14] and thermal expansion^[15,16]. Further, they also provide opportunities to control linear mechanical waves in unprecedented ways^[17] and to facilitate applications such as nonreciprocal transmission^[18,19], cloaking^[20], and noise reduction^[21–23].

While the field has initially focused on linear properties, more recently it has been shown that non-linearities and instabilities can be exploited to further expand the range of achievable functionalities^[6]. One of the simplest examples of flexible mechanical metamaterials (flexMM) is a

block of elastomer with a square array of circular holes (see Fig. 1.1). When this metamaterial is uniaxially compressed, buckling of the beam-like ligaments triggers a sudden transformation of the holes into a periodic pattern of alternating and mutually orthogonal ellipses, which leads to a negative Poisson's ratio^[13]. Further, flexMM have been designed to realize systems with switchable properties^[13,24] and programmable responses^[25], reconfigurable structures^[26], soft robots^[27] and mechanical logic devices^[28].

In this dissertation, I further explore the nonlinear behavior of flexMMs, focusing on the rich physics of solitary waves and phase transitions.

1.2 Solitary waves

Solitary waves are self-reinforcing wave packets that maintain their shapes and propagate at constant velocities as a result of the balance between nonlinear and dispersive effects in the medium. Solitary waves exhibit three key features^[29]: (i) permanent form, (ii) localized profile, and (iii) shape that does not change through collisions (except for a phase shift). These features led Zabusky and Kruskal^[29] to coin the name *soliton* (after photon, proton, etc) to emphasize the particle-like character of these wave pulses. Solitary waves were first described by John Scott Russell in 1834, where he observed nonlinear water wave packets propagating with stable shape and constant velocity in the Union Canal in Scotland (see Fig. 1.2)^[2,30]. Since then solitary waves have been widely studied in various areas of science and engineering, including optics^[31,32], electronics^[33], plasmonics^[34,35], quantum mechanics^[36], general relativity^[37] and mechanics^[38–40]. In mechanical systems, solitary waves have been mostly studied in granular media, whose nonlinear response originates from Hertz contact between grains^[41,42].



Figure 1.2: Recreation of a solitary wave on the Scott Russell Aqueduct on the Union Canal^[2].

The complex and programmable deformation of flexMMs makes them an ideal platform to engineer and control the propagation of solitary waves. Different from granular media whose nonlinear response is solely determined by contact, the nonlinear response of flexMMs can be tailored by tuning their geometry. By carefully choosing the geometry, a flexMM can be designed to be either monostable or multistable or to support large internal rotations — features that have been shown to result in interesting nonlinear dynamic phenomena.

1.3 Phase Transitions

Many forms of matter can exist in multiple phases with different microstructures and properties, including ferroelectrics^[43–45], ferromagnets^[46,47], ferroelastics^[48,49], shape memory alloys^[49,50], and liquid crystals^[51]. The coexistence of two or more phases inevitably leads to the emergence of domain walls — a narrow region that separates different phases. The existence and movement of such domain walls have been exploited to enable logic operations^[52], racetrack memory^[53]

and line scanners for reading optical memories^[54]. Although phase transitions and domain walls have been mostly studied at the atomic scale, they can also emerge at the macroscopic scale in multistable flexMMs^[5,27,28,55–62], where they can be exploited to control elastic pulses^[28,56,58,62], encrypt information^[5], as well as to design deployable structures^[59] and phase transforming metamaterials^[55,57].

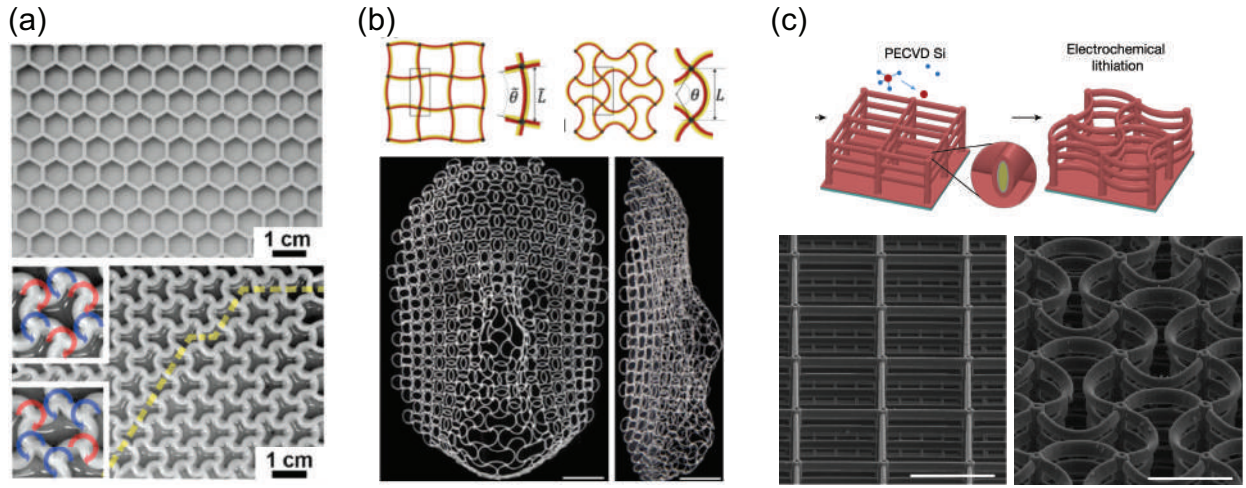


Figure 1.3: Strategies to reconfigure mechanical metamaterials at different scales using (a) swelling^[3], (b) heating^[4] and (c) electric field^[5].

In multiphase materials, different phases usually lead to different physical properties, therefore controllable phase transitions are often explored as a way to switch material properties. In mechanical metamaterials, phase transitions via swelling^[4,63,64], electromagnetic^[5,65] actuation and mechanical instabilities^[24,26,66,67] have been harnessed as effective ways to build active structures with tunable properties and functionalities (see Fig. 1.3). For example, by applying voltage onto a silicon-coated tetragonal micro lattice, it can be transformed from a perfect square lattice to a sinusoidal buckling pattern in a controllable and ‘non-volatile’ way (see Fig. 1.3(c)), successfully altering the dispersion relation of the structure and opening phononic bandgaps upon actuation^[5]. However, it is very hard, if not impossible, for these global field based transformation methods

(e.g., electric, magnetic, and heat fields) to change the fundamental topology of the structures, e.g., location, number and connectivity of nodes and compartments, which would profoundly affect their acoustic^[68–71], electrical^[72], chemical^[73,74], mechanical^[75,76], and optical^[77] properties, as well as heat^[68,78], fluid^[79,80] and particle transport^[81]. To change the topology of the architectures, one needs to reorganize and repack around each individual node, and coordinately bend, stretch and even fold every wall, which requires a sophisticated localized force field. In chapter 5, we present a two-tiered dynamic strategy that can systematically transform the fundamental topology of microscale cellular flexMMs with merely a droplet of liquid. The strategy is widely applicable to different geometries, materials, and dimensions and leads to a variety of functionalities.

1.4 Dissertation Overview

Each chapter of this thesis is based on a first-author or co-first-author article published in a peer-reviewed journal and the corresponding supplementary information is included as Appendices.

First, in chapter 2, I investigate the nonlinear dynamic behavior of a highly nonlinear flexMM based on the rotating squares mechanism and reveal the propagation of *elastic vector solitons*. The coupling between the two components of the vector solitons gives rise to a unique feature: the emergence of amplitude gaps - ranges in amplitude where elastic soliton propagation is forbidden due to the lack of coupling between its two components. We establish a theory that fully captures the propagation of these waves and exploit this theory to control the propagation of large amplitude vibrations in unprecedented ways, as demonstrated by the design of soliton splitters and diodes.

In chapter 3, I study the collisions between such vector solitons and discover anomalous interactions between them. Although solitons are known to emerge unchanged from collisions, the vector

solitons repel each other upon collision if they exhibit different polarization directions. Our analysis reveals that such anomalous collisions are a consequence of the large-amplitude characteristics and the vectorial nature of the solitons, which locally modify the properties of the underlying media. The rich interactions between solitons pave new ways towards the advanced control of large amplitude mechanical pulses enabling remote detection, control, and destruction of high-impact signals.

In chapter 4, I use a combination of experimental, numerical, and theoretical tools to engineer the domain walls in a flexMM based on the rotating squares mechanism. Upon uniaxial compression, the flexMM bifurcates into two buckling-induced phases that we refer to as phase+ and phase-. By introducing defects into the system that locally nucleate one of the two phases, we can controllably guide the system to transition into either phase+ or phase-. Interestingly, when such phase-inducing defects are arranged such that two phases coexist, a domain wall emerges across which the angle of squares switches from one direction of rotation to another. We develop a theoretical model that fully captures the profile and position of a domain wall as a function of applied strain. With the guidance of this theoretical model, we reveal that the flexMM creates long-range interactions between the local defects through domain walls, which ultimately affect the global mechanical properties of the structure and lead to applications such as information encryption, stiffness tuning, and waveguiding.

Finally, in chapter 5, I develop a new strategy to transform the topology of flexMMs at the micro-scale. Our approach only requires exposing the structure to a select liquid. At the molecular scale, the liquid first infiltrates the constitutive material making it three orders of magnitude softer, and then upon evaporation, the remaining liquid forms a network of capillary forces acting at architectural scale (which is micrometer scale in this study) to ‘zip’ the softened edges into a

new topology. The transformed structure then regains its stiffness after full evaporation of the liquid. Compared to existing transformation methods that fail to change the underlying topology, our method enables extremely fast (~ 10 s), robust, and highly reversible topological transformations and is compatible with simple fabrications. We develop a generalized theoretical model that links structural geometries, material properties and capillary forces, which helps the design of more complex structural geometries and the integration with responsive materials. The topological changes can be refined to develop smart surfaces that can encrypt information, trap selective particles, release bubbles at precise positions, change friction, wetting, and resilience proprieties.

This dissertation does not contain all of the papers that I published during my graduate studies at Harvard. A complete list of contributions can be found in the Section ‘*List of Publications*’ at the end of the dissertation.

Chapter 2

Metamaterials with Amplitude Gaps for Elastic Solitons

By: Bolei Deng, Pai Wang, Qi He, Vincent Tournat, Katia Bertoldi. Published in *Nature Communications*, on Aug. 24 2018. [doi:10.1038/s41467-018-05908-9](https://doi.org/10.1038/s41467-018-05908-9)

2.1 Abstract

We combine experimental, numerical and analytical tools to design highly nonlinear mechanical metamaterials that exhibit a new phenomenon: gaps in amplitude for elastic vector solitons (i.e. ranges in amplitude where elastic soliton propagation is forbidden). Such gaps are fundamentally different from the spectral gaps in frequency typically observed in linear phononic crystals and acoustic metamaterials and are induced by the lack of strong coupling between the two polarizations of the vector soliton. We show that the amplitude gaps are a robust feature of our system and that their width can be controlled both by varying the structural properties of the units and by breaking the symmetry in the underlying geometry. Moreover, we demonstrate that amplitude gaps provide new opportunities to manipulate highly nonlinear elastic pulses, as demonstrated by the designed soliton splitters and diodes.

2.2 Introduction

Following John Scott Russell's observation of nonlinear water wave packets propagating with stable shape and constant velocity in the Union Canal in Scotland^[30], the unique properties of solitons have been studied and exploited in many areas of science and engineering^[31,82,83]. Focusing on mechanical systems, granular crystals have been found to provide an effective platform for the propagation of highly nonlinear solitary waves^[83–86] and have enabled the design of impact mitigation layers^[87], lenses^[88], switches^[89] and non-destructive detection techniques^[90]. However, the solitons observed in granular media are of scalar nature and lack of the multiple polarizations typical of elastic waves propagating in solid materials.

Polarization is an important property of vector waves like electromagnetic and elastic waves. The ability to control the polarization of light has enabled a broad range of applications, including optical communications, spectroscopy and microscopy^[31,91,92]. Moreover, a broad range of new functionality has been observed in elastic systems with architecture designed to manipulate both the longitudinal and shear polarizations of linear elastic waves^[19,93]. While the field initially focused on linear elastic vibrations, it has been recently shown that highly deformable mechanical metamaterials can support elastic vector solitons with two polarizations - one translational and one rotational^[94], but the potential of such solitary waves in applications is unknown and remains to be explored.

Here, we combine experimental, numerical and analytical tools to demonstrate that elastic vector solitons provide unique opportunities to manipulate the propagation of large amplitude vibrations. Specifically, we show that in mechanical metamaterials based on rotating rigid units, both the amplitude of the propagating waves and the symmetry of the underlying building blocks can be used to significantly alter the coupling between the two polarizational components of the vector solitons. We find that such control of the coupling strength results in the emergence of a new phenomenon: the formation of amplitude gaps for solitons. Notably, this new effect can be exploited to realize devices capable of controlling and manipulating the propagation of large amplitude vibrations in unprecedented ways, as demonstrated by the design of soliton splitters and diodes.

2.3 Metamaterial Design and Characterization

Our system consists of a long chain of 2×50 rigid crosses made of LEGO bricks^[95] with arm length $l_a = 19$ mm connected by thin and flexible hinges made of polyester plastic sheets (Artus

Corporation, NJ) with length $l_h = 4$ mm and thickness $t_h = 0.127$ mm, resulting in a spatial periodicity $a = 2l_a + l_h = 42$ mm (Fig. 2.1(a) - see section A1 and Supplementary Video 1 for details on fabrication). To investigate the propagation of elastic pulses in the system, we place the chain (supported by pins to minimize frictions) on a smooth horizontal surface and use an impactor excited by a pendulum to hit the mid-point at its left end (see Fig. 2.1(b)-top and Supplementary Video 2). We apply different input signals to the chain by varying both the initial height of the striking pendulum and the distance traveled by the impactor and find that all of them initiate simultaneous rotation and displacement of the rigid units, with each pair of crosses in a column sharing the same displacement and rotating by the same amount, but in opposite directions (i.e. if the top unit rotates by a certain amount in clockwise direction, then the bottom one rotates by the same amount in counter-clockwise direction, and vice versa). To monitor the displacement, u_i , and rotation, θ_i , of the i -th pair of crosses along the chain as the pulse propagates, we use a high speed camera (SONY RX100V) and track markers via digital image processing (see section A.2).

In Fig. 2.1(c) we report the evolution of the rotation and longitudinal displacement of the second and fortieth pairs of crosses as a function of time during two different experiments. We find that when the amplitude of the input signal is large ($A_2 = \max(\theta_2(t)) = 13^\circ$ in experiment #1) the pulse that propagates through the system conserves its amplitude and shape in both degrees of freedom. Differently, for inputs with small amplitude ($A_2 = 5^\circ$ in experiment #2), the output signal is severely distorted compared to the input one (see Supplementary Video 3). While in Fig. 2.1(c) we focus on two representative experiments, all our experimental results are summarized as triangular markers in Figs. 2.1(e) and 2.1(f), where we present the measured transmission, A_{40}/A_2 (with $A_{40} = \max(\theta_{40}(t))$), and cross-correlation of $\theta_2(t)$ and $\theta_{40}(t)$ as a function of the amplitude of the input signal, A_2 . We find that if $A_2 \gtrsim 7^\circ$ both the transmission and the cross-correlation approach

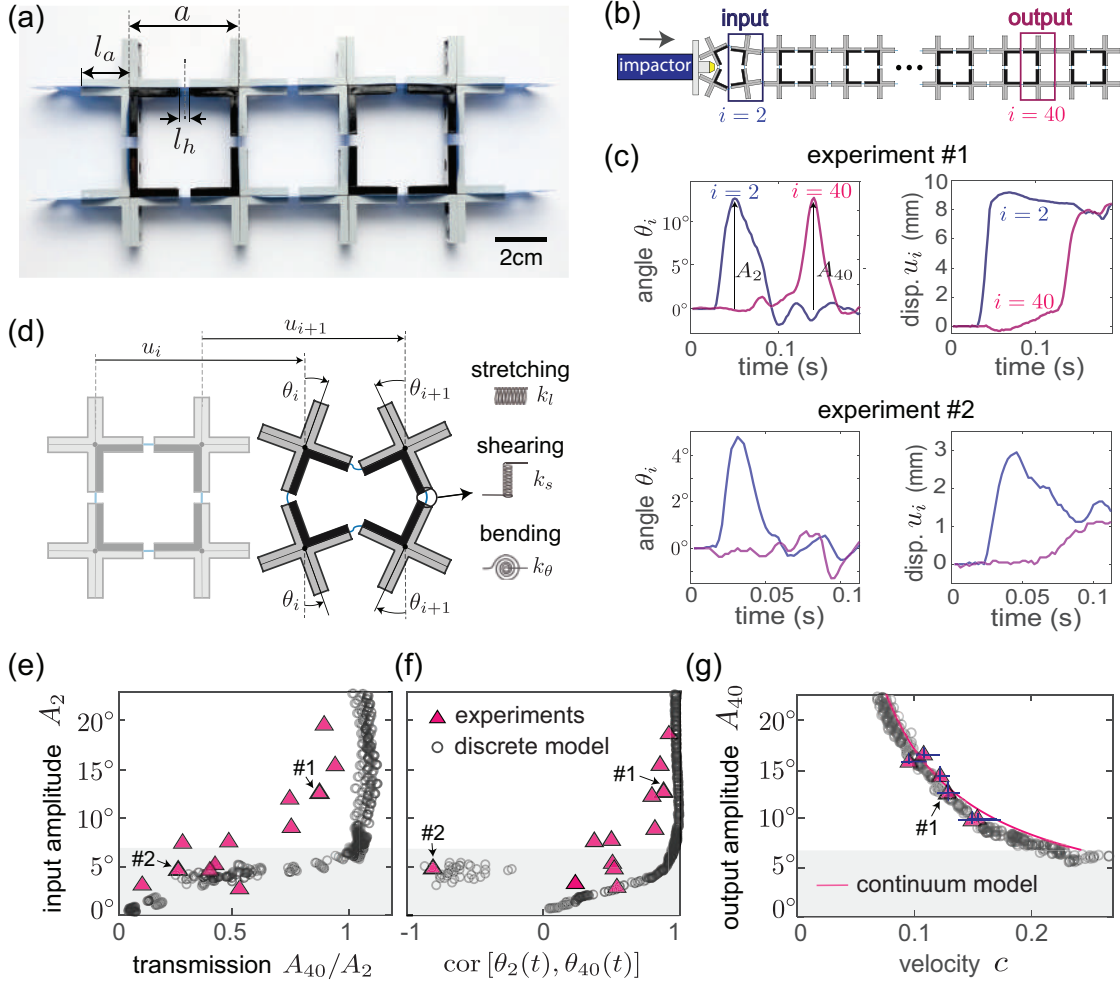


Figure 2.1: Propagation of elastic vector solitons in a chain with all horizontal hinges aligned. (a) Few units of our sample (Scale bar: 2 cm). (b) Schematics of our testing setup. (c) Evolution of the rotation and longitudinal displacement of the second and fortieth units as a function of time during two different experiments. (d) Schematic of the system. (e) Measured transmission, A_{40}/A_2 , as a function of the amplitude of the input signal, A_2 . (f) Measured cross-correlation of $\theta_2(t)$ and $\theta_{40}(t)$ as a function of the amplitude of the input signal, A_2 . (g) Evolution of the pulse velocity c as a function of its amplitude. The grey region in (e)-(g) highlights the amplitude gap as predicted by the continuum model. The error bars in (g) show the 95% confident interval of the measured velocities and amplitudes of solitons in experiments. The corresponding error bars for simulation results are too small to show.

unity, suggesting that for large enough input signals the system supports the propagation of elastic vector solitons. However, for input amplitudes below $\sim 7^\circ$ a transition occurs and both the transmission and the cross-correlation significantly and systematically decrease. This indicates that our system might only support the propagation of solitary waves with amplitude above a certain threshold, manifesting a gap in amplitude for $0^\circ \lesssim A_2 \lesssim 7^\circ$.

2.4 Discrete and Continuum Models

To better understand these experimental results, we establish a discrete model in which the crosses are represented as rigid bodies of mass m and rotational inertia J . Guided by our experiments, we assume that the system has an horizontal line of symmetry and assign two degrees of freedom (u_i and θ_i) to the top unit of the i -th pair of crosses (Fig. 2.1(d)). As for the flexible hinges, they are modeled using a combination of three linear springs: their stretching is captured by a spring with stiffness k_l ; their shearing is described by a spring with stiffness k_s ; their bending is modeled by a torsional spring with stiffness k_θ . Under these assumptions, the dimensionless equations of motion for the i -th top unit are given by (see section A.3)

$$\begin{aligned} \frac{\partial^2 U_i}{\partial T^2} &= U_{i+1} - 2U_i + U_{i-1} - \frac{1}{2}(\cos \theta_{i+1} - \cos \theta_{i-1}), \\ \frac{1}{\alpha^2} \frac{\partial^2 \theta_i}{\partial T^2} &= -K_\theta(\theta_{i+1} + 4\theta_i + \theta_{i-1}) + K_s \cos \theta_i [\sin \theta_{i+1} + \sin \theta_{i-1} - 2 \sin \theta_i] \\ &\quad - \sin \theta_i [2(U_{i+1} - U_{i-1}) + 4 - \cos \theta_{i+1} - 2 \cos \theta_i - \cos \theta_{i-1}], \end{aligned} \quad (2.1)$$

where $U_i = u_i/a$, $T = t\sqrt{k_l/m}$, $K_\theta = 4k_\theta/(k_l a^2)$, $K_s = k_s/k_l$ and $\alpha = a\sqrt{m/(4J)}$ are all non-dimensional parameters, which in our system are measured as $K_s = 0.02$, $K_\theta = 1.5 \times 10^{-4}$ and

$\alpha = 1.8$. Note that, as shown in Fig. 2.1(d), to facilitate the analysis in our model we define the positive direction of rotation alternatively for neighboring crosses (i.e., if for the i -th top unit a clockwise rotation is positive, then for the $(i - 1)$ -th and $(i + 1)$ -th ones counterclockwise rotation is positive).

We start by numerically solving Eqs. (2.1) using the Runge-Kutta method (the code implemented in MATLAB is available online). In our numerical analysis we consider a chain comprising 150 pairs of crosses, apply a longitudinal displacement with the form $U_{\text{input}} = b + b \tanh [(T - T_0)/w]$ to the mid-point at its left end (see section A.3), and implement free-boundary conditions at its right end. In Figs. 2.1(e-f) we report as gray circular markers the results of 480 analyses in which we systematically change the applied displacement U_{input} (with $b \in [0, 0.75]$, $w \in [50, 100]$ and $T_0 = 400$). In good agreement with our experimental data, we find that for $A_2 \lesssim 6^\circ$ the signal does not preserve its amplitude and shape as it propagates through the structure. As such, these numerical results also point to the existence of an amplitude gap for solitons.

2.5 Amplitude Gaps for Solitons

To confirm the existence of such amplitude gap, we further simplify Eqs. (2.1) to obtain an analytical solution. To this end, we assume that the wavelength of the propagating waves is much wider than the cell size and that $\theta \ll 1$, take the continuum limit of Eqs. (2.1) and retain nonlinear terms up to the third order, obtaining (see section A.4)

$$\begin{aligned} \frac{\partial^2 U}{\partial T^2} &= \frac{\partial^2 U}{\partial X^2} + \theta \frac{\partial \theta}{\partial X}, \\ \frac{1}{\alpha^2} \frac{\partial^2 \theta}{\partial T^2} &= (K_s - K_\theta) \frac{\partial^2 \theta}{\partial X^2} - 4 \left[\frac{3K_\theta}{2} + \frac{\partial U}{\partial X} \right] \theta - 2\theta^3, \end{aligned} \tag{2.2}$$

where $X = x/a$ (x denoting the initial position along the chain) and $U(X, T)$ and $\theta(X, T)$ are two continuous functions of X and T . It is easy to show that Eqs. (2.2) admits an analytical solution in the form of an elastic vector soliton with two components^[96]

$$\begin{cases} \theta &= A \operatorname{sech} \left(\frac{X - cT}{W} \right), \\ U &= \frac{A^2 W}{2(1 - c^2)} \left[1 - \tanh \left(\frac{X - cT}{W} \right) \right], \end{cases} \quad (2.3)$$

where c is the pulse velocity, and A and W are the amplitude and width of the solitary wave, which can be expressed in terms of c and the structural parameters as (see section A.4)

$$A = \pm \sqrt{\frac{6K_\theta(1 - c^2)}{c^2}}, \quad \text{and} \quad W = \sqrt{\frac{\alpha^2(K_s - K_\theta) - c^2}{6\alpha^2 K_\theta}}. \quad (2.4)$$

At this point it is important to note that, since the width W needs to be real-valued

$$c^2 < \alpha^2(K_s - K_\theta), \quad (2.5)$$

yielding

$$|A| > A_{\text{upper}} = \sqrt{\frac{6K_\theta}{\alpha^2(K_s - K_\theta)} - 6K_\theta}. \quad (2.6)$$

Condition (3.5) clearly indicates that our system has an amplitude gap for solitons, since only solitary waves with amplitude greater than $A_{\text{upper}} = 6.55^\circ$ are physically admissible solutions. Such amplitude gap is reported as shaded area in Figs. 2.1(e-f) and is in excellent agreement with our numerical and experimental results. Note that this gap (and the associated amplitude threshold A_{upper} below which solitary waves cannot propagate) is fundamentally different from the nonlinear

supratransmission effect (limited to weakly nonlinear periodic waves with certain frequency^[97]), classical amplitude-dependent dissipation^[98] and so-called "sonic vacuum" found in not precompressed granular chains^[99]. The amplitude gaps for solitons reported in our work are robust features of the system, intrinsically determined by its architecture and its ability to support elastic vector solitons.

Looking into the mechanism behind the emergence of this amplitude gap, it is important to note that the propagation of vector solitons requires a strong coupling among different polarizations^[100,101]. However, Eqs. (2.2) show that the coefficients of the coupling terms in our structure are proportional to θ , so that large enough rotations are needed in order to activate them and enable the propagation of vector solitons (see section A.5). Finally, to further verify the validity of our continuum model, in Fig. 2.1(g) we compare the relation between A and c as predicted by our analysis (magenta line) and measured in our experiments (triangular markers) and numerical direct simulations (circular markers) and find good agreement among all three sets of data.

2.6 Enhanced Tunability via Symmetry Breaking

Eq. (3.5) indicates that in our system the width of the amplitude gap can be controlled by changing K_s , K_θ and α (see Fig. A14). More excitingly, the tunability and functionality of the proposed mechanical metamaterial can be further enhanced by breaking the symmetry in each rigid cross to alter the coupling strength between the two polarizational components. In our system this is achieved by shifting neighboring horizontal hinges by $a \tan \varphi_0$ in vertical direction (see Fig. 2.2(a) and Supplementary Video 4). While for the chain with all horizontal hinges aligned (for which $\varphi_0 = 0^\circ$) the energy cost to rotate any unit in clockwise and counter-clockwise directions is identical,

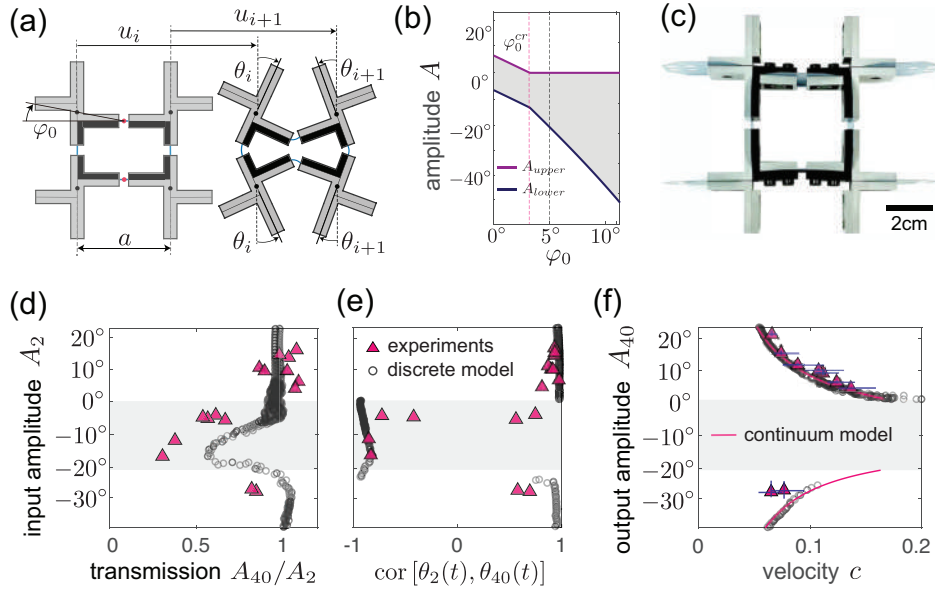


Figure 2.2: Propagation of elastic vector solitons in a chain with vertically shifted neighboring horizontal hinges. (a) Schematic of the system. Neighboring horizontal hinges are shifted by $a \tan \varphi_0$ in vertical direction. (b) Evolution of the amplitude gap as a function of the angle φ_0 . (c) Few units of our sample characterized by $\varphi_0 = 5^\circ$ (Scale bar: 2 cm). (d) Measured transmission, A_{40}/A_2 , as a function of the amplitude of the input signal, A_2 . (e) Measured cross-correlation of $\theta_2(t)$ and $\theta_{40}(t)$ as a function of the amplitude of the input signal, A_2 . (f) Evolution of the pulse velocity c as a function of its amplitude. The grey region in (b) and (d)-(f) highlights the amplitude gap as predicted by the continuum model. The error bars in (f) show the 95% confident interval of the measured velocities and amplitudes of solitons in experiments. The corresponding error bars for simulation results are too small to show.

the hinges shifting (i.e. $\varphi_0 \neq 0^\circ$) introduces a disparity between the two directions of rotation. Under compression in longitudinal direction, for all units of the shifted chain with the left hinge higher than the right one it is energetically more favorable to rotate in clockwise direction, while for the ones with a lower left hinge rotations in counter-clockwise direction are preferred (Figs. 2.2(a) and Fig. A6). By extending our analytical model to units with $\varphi_0 \neq 0^\circ$ and assuming for each unit the positive direction of rotation to be the one that is naturally induced by compression, we find that such disparity introduced by the asymmetry is reflected in the amplitude gap (see section A.5). For the aligned chain (i.e. for $\varphi_0 = 0^\circ$) the upper (A_{upper}) and lower (A_{lower}) limits of the amplitude gap are identical in magnitude (i.e. $A_{\text{lower}} = -A_{\text{upper}}$, so that in Figs. 2.1(c) and d we

only show A_{upper}). By contrast, as a result of the bias introduced by the hinges shifting, when φ_0 increases, $|A_{\text{lower}}|$ and A_{upper} become larger and smaller, respectively (see section A.5). We also find that a critical angle φ_0^{cr} exists at which A_{upper} vanishes. In structures with $\varphi_0 > \varphi_0^{cr}$ all solitons that induce an energetically favorable rotation at the i -th pair of crosses can propagate through the system, regardless of their magnitude. The validity of our analysis is confirmed by numerical simulations and experiments conducted on a chain comprising 2×50 and 2×150 crosses characterized by $\varphi_0 = 5^\circ$, respectively. For such system our continuum model predicts $A_{\text{upper}} = 0^\circ$ and $A_{\text{lower}} = -20.91^\circ$. In agreement with this analytical prediction, the amplitude transmission ratio and signal shape cross-correlation between the input, $\theta_2(t)$, and the output, $\theta_{40}(t)$, measured in both experiments and discrete simulations significantly drop when the input amplitude falls inside the gap (Figs. 2.2(d-e)). Moreover, the numerical and experimental data also closely match the amplitude-velocity relation predicted by our continuum model (Fig. 2.2(f)), confirming that the hinges shifting induces an asymmetric gap.

2.7 Functional Devices Based on Amplitude Gaps

Having discovered the existence of amplitude gaps in our system, we next focus on how such effect can be exploited to design new functional devices to control mechanical signals, and, therefore, to provide new opportunities for phononic computing and mechanical logic. In analogy to beam splitters^[102], which are widely used in photonics to split an incident light beam into two or more beams, we start by taking advantage of amplitude gaps to design a soliton splitter - a device capable of splitting an incoming elastic vector soliton into a transmitted and a reflected ones. Remarkably, this can be achieved by simply introducing a pair of stiffer hinges within an aligned chain with $\varphi_0 = 0^\circ$. To demonstrate the concept we take our 2×50 sample with $\varphi_0 = 0^\circ$ and

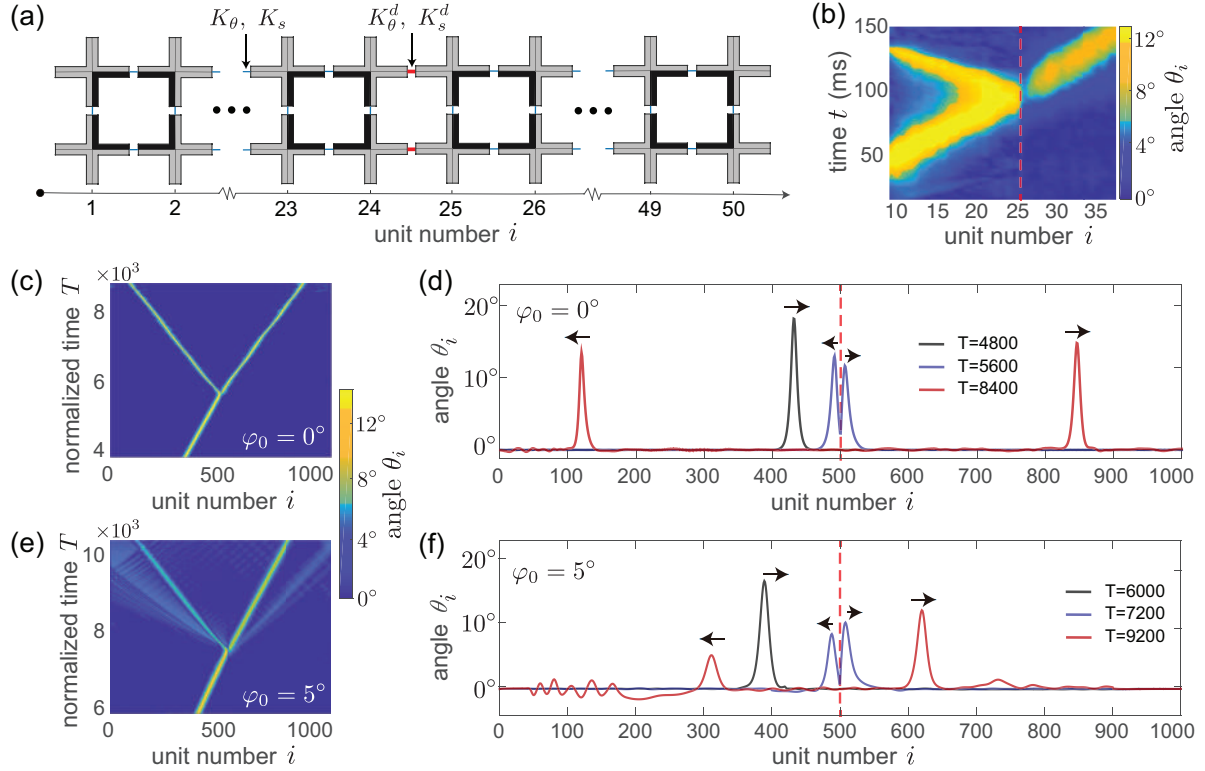


Figure 2.3: Soliton splitter. (a) Schematics of our soliton splitter. A pair of stiffer hinges (with stiffness K_s^d and K_θ^d) is introduced to connect the 24th and the 25th pairs of crosses. (b) Rotation of the pairs of crosses during the propagation of the pulse, as recorded with our high-speed camera. The location of the stiff pair of hinges is indicated by the dashed red line. (c and d) Simulations corresponding to the experiments shown in B. The numerical analysis are conducted on a 2×1000 chain with symmetric crosses characterized by $\varphi_0 = 0^\circ$ and a pair of stiffer hinges placed between the 500th and the 501st units. (e and f) Numerical results for a 2×1000 chain with asymmetric crosses characterized by $\varphi_0 = 5^\circ$ and a pair of stiffer hinges placed between the 500th and the 501st units.

introduce two stiffer hinges (made of polyester sheets with thickness $t_h^d = 0.635\text{mm}$) to connect the 24th and the 25th pairs of units (Fig. 2.3(a)). We find that, if the amplitude of the input signal is large enough to be outside the amplitude gap, the excited solitary wave is split into two pulses by the pair of stiffer hinges (see Fig. 2.3(b)). To better understand the nature of the transmitted and reflected waves, we integrate Eqs. (2.1) to simulate the response of a chain comprising 1000 units with $\varphi_0 = 0$ and a pair of stiffer hinges (with stiffness K_s^d and K_θ^d) connecting the 500th and 501st rigid crosses. The numerical results for a chain with $K_s^d/K_s = K_\theta^d/K_\theta = 30$ are shown in

Figs. 2.3(c-d). We find that the pair of stiffer hinges split the incoming soliton into two pulses that propagate with stable shape and constant velocity and that no trains of solitons are generated. As for the radiation of linear waves, we find that the interaction between the incoming solitary wave and the stiffer pair of hinges generates only translational vibrations, since the frequency content of our solitons overlaps with a low-frequency band gap for rotation. However, we estimate that only 4% of the energy carried by the incoming soliton is finally transferred to translational linear vibrations (see Supplementary Notes 8-10). As such, these results clearly indicate that our simple structure acts as a splitter for solitons. Note that this behavior is remarkably different from that previously observed in unloaded granular chains, where heterogeneities have been found to split the propagating solitary wave into trains of solitons and to generate stress oscillations localized near the impurities^[103]. Such difference is due to the presence of the amplitude gap, which in our mechanical metamaterial prevents fragmentation of the propagating pulse by suppressing the propagation of small amplitude solitons. To demonstrate this important point, we simulate the response of a 2×1000 chain with $\varphi_0 = 5^\circ$ and a pair of stiffer hinges in the middle. Note that this structure enables the propagation of solitary waves of any amplitude if they induce energetically favorable rotations (since $A_{\text{upper}} = 0^\circ$ and there is no amplitude gap for such waves). We find that, when such waves are excited and hit the pair of stiffer hinges, trains of pulses are generated (see Fig. 2.3(e) and f), confirming the important role played by the amplitude gap. Finally, our numerical results also indicate that our soliton splitter is a robust device, since the ratio between the energy carried by the transmitted and reflected solitons only depends on the ratio $K_s^d/K_s = K_\theta^d/K_\theta$ and not on the amplitude of the input signal, with the amount of reflected energy monotonically increasing with the stiffness ratio (see Fig. A23).

Further, we design a mechanical diode^[104] for solitary waves – a system that is transparent to

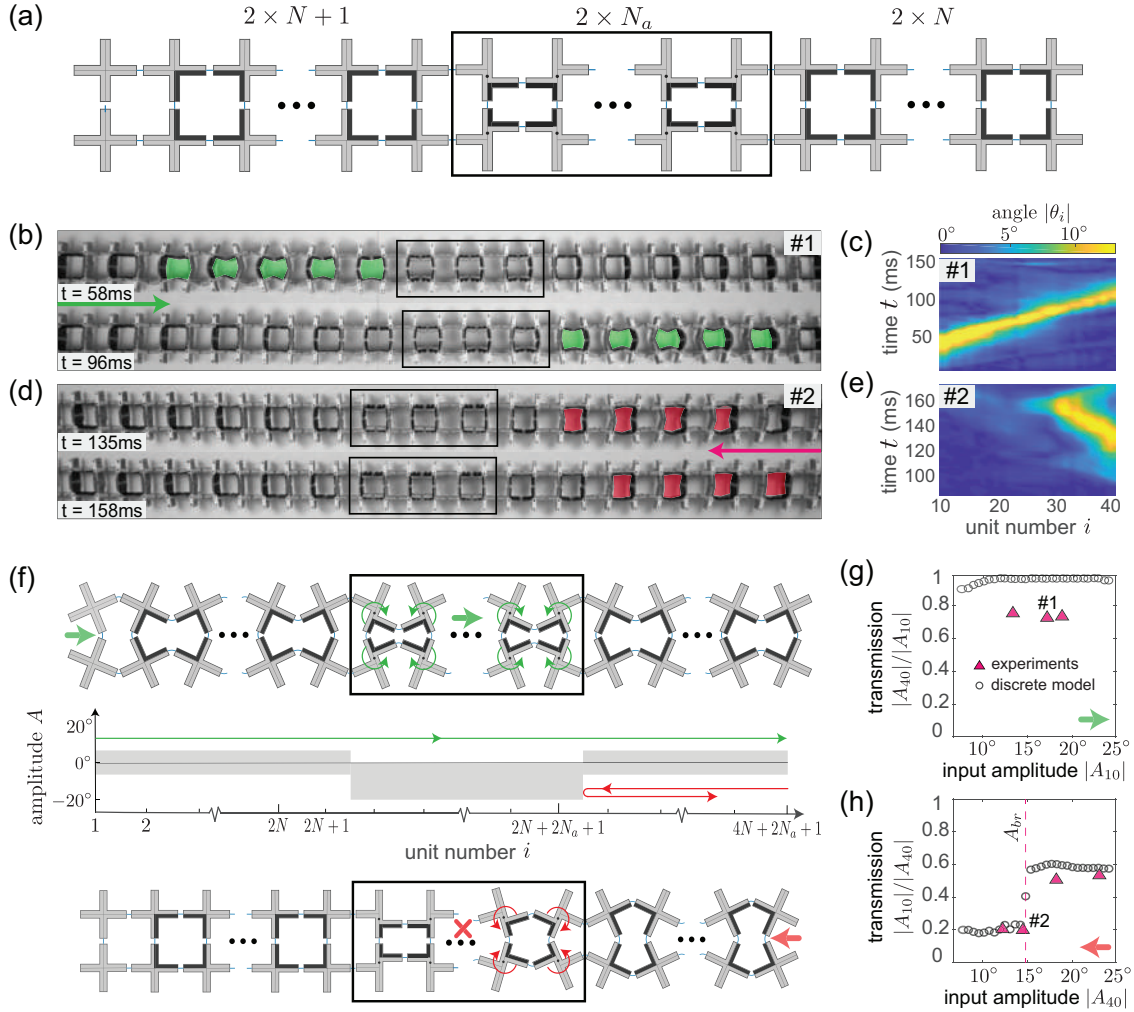


Figure 2.4: Mechanical diode. (a) Schematics of our mechanical diode. (b) Optical images showing the propagation of a solitary wave excited at the left end of the chain. (c) Rotation of the pairs of crosses induced by a pulse excited at the left of the chain. (d) Optical images showing the propagation of a solitary wave excited at the right end of the chain. (e) Rotation of the pairs of crosses induced by a pulse excited at the right of the chain. (f) Schematic highlighting the working principles of our mechanical diode. (g) Measured transmission, $|A_{40}|/|A_{10}|$, as a function of the input amplitude, $|A_{10}|$, for pulses excited at the left end of the chain. (h) Measured transmission, $|A_{10}|/|A_{40}|$, as a function of the input amplitude, $|A_{40}|$, for pulses excited at the right end of the chain.

solitons incoming from one direction but blocks those propagating in the other one. While such nonreciprocal wave transmission has been previously reported for periodic waves^[105–107], irreversible transition waves^[28] and wave packets^[108], here we extend the concept to solitary wave pulses. To achieve this, we introduce a few pairs of crosses with $\varphi_0 \neq 0$ within a chain with $\varphi_0 = 0^\circ$.

More specifically, our diode comprises two external sections with $2N$ and $(2N+1)$ pairs of crosses characterized by $\varphi_0 = 0$ and a central portion consisting of $2N_a$ pairs of crosses with $\varphi_0 = 5^\circ$ (Fig. 2.4(a)). Experiments conducted on a sample with $N = 12$, $N_a = 3$ and the section with $2N+1$ units placed on the left show that a pulse initiated at the left end propagates through the entire structure (Figs. 2.4(b-c)), while a solitary wave excited at the right end is completely reflected by the boundary between the regions with $\varphi_0 = 0^\circ$ and 5° (Figs. 2.4(d-e)). This remarkable behavior is induced by the asymmetric amplitude gap of the region with $\varphi_0 = 5^\circ$. Solitons excited at the left end of the chain induce energetically favorable rotations at the units with $\varphi_0 = 5^\circ$ and, since there is no amplitude gap for such waves (i.e. $A_{\text{upper}}^{\varphi_0=5^\circ} = 0$), they are able to propagate through the entire chain (Fig. 2.4(f)). In contrast, solitons initiated at the right end of the chain result in energetically unfavorable rotations for the crosses with $\varphi_0 = 5^\circ$ and, since $A_{\text{lower}}^{\varphi_0=5^\circ} \ll A_{\text{lower}}^{\varphi_0=0^\circ}$, they are almost completely blocked by the boundary between aligned and shifted crosses (Fig. 2.4(f)). To explore the performance of our mechanical diode, we apply different input signals at the left and right end of the chain in both experiments and discrete simulations. We find that for all pulses with amplitude larger than $A_{\text{upper}}^{\varphi_0=0^\circ} = 6.55^\circ$ initiated at the left end of the system the transmission, $|A_{40}|/|A_{10}|$, approaches unity (Fig. 2.4(g)). Differently, when the excitation is applied at the right end of the chain, the transmission, $|A_{10}|/|A_{40}|$, is close to zero even if the amplitude of the input signal is outside the gap of the region with $\varphi_0 = 0$ (i.e. $|A_{40}| > A_{\text{upper}}^{\varphi_0=0^\circ}$). However, as typically observed in electronic and thermal diodes^[109], if the amplitude of the pulses becomes too large, the diode experiences a condition known as breakdown. As a result, solitary waves with amplitude larger than $A_{br} \approx 15^\circ$ propagate through the diode (i.e. if $|A_{40}| > A_{br} \approx 15^\circ$, then $|A_{10}|/|A_{40}| \sim 0.6$ - see section A.11 for a detailed numerical study on the dependency of A_{br} on φ_0 and N_a).

2.8 Discussion

In this study, we have experimentally observed, numerically simulated and mathematically analyzed the existence of amplitude gaps for elastic vector solitons in highly deformable mechanical metamaterials consisting of rigid units and elastic hinges. First, we have shown that such amplitude gaps can be tuned by altering both the structural parameters and the symmetry of the crosses. Then, we have demonstrated that amplitude gaps can be exploited to design clean splitters and diodes for highly nonlinear solitary waves. In recent years, many strategies have been proposed to manipulate the propagation of elastic waves^[107,110], enabling a wide range of applications such as spatial guiding^[111–113], frequency filtering^[24,114,115], noise/impact mitigation^[116,117] and non-reciprocal transmission^[19,118]. However, the vast majority of devices focus on small-amplitude vibrations and take advantage of spectral gaps in frequency^[107,110?]. As such, our study on amplitude gaps for highly nonlinear solitary waves adds a whole new dimension to our ability to design structures and materials with tailored dynamic behavior and open avenues for potential technological breakthroughs.

Chapter 3

Anomalous Collisions of Elastic Vector Solitons in Mechanical Metamaterials

By: Bolei Deng, Vincent Tournat, Pai Wang Katia Bertoldi. Published in *Physical Review Letters*,
on Feb. 1 2019. [doi:10.1103/PhysRevLett.122.044101](https://doi.org/10.1103/PhysRevLett.122.044101)

3.1 Abstract

We investigate via a combination of experiments and numerical analyses the collision of elastic vector solitons in a chain of rigid units connected by flexible hinges. Due to the vectorial nature of these solitons, very unusual behaviors are observed: while, as expected, the solitons emerge unaltered from the collision if they excite rotations of the same direction, they do not penetrate each other and instead repel one another if they induce rotations of opposite direction. Our analysis reveals that such anomalous collisions are a consequence of the large-amplitude characteristics of the solitons, which locally modify the properties of the underlying media. Specifically, their large rotations create a significant barrier for pulses that excite rotations of opposite direction and this may block their propagation. Our findings provide new insights into the collision dynamics of elastic solitary waves. Furthermore, the observed anomalous collisions pave new ways towards the advanced control of large amplitude mechanical pulses, as they provide opportunities to remotely detect, change or destruct high-amplitude signals and impacts.

3.2 Introduction

Collisions are one of the most fascinating features of solitary waves and have been investigated in many areas of science, including optics^[31,32], electronics^[33], plasmonics^[34,35], quantum mechanics^[36], general relativity^[37] and mechanics^[38–40]. Typically, the solitons are found to emerge from the collision unchanged (except for a phase shift^[33,35,36] or the formation of small secondary waves^[38–40]), as if there had been no interaction at all. This remarkable behavior led Zabusky and Kruskal^[119] to coin the name 'soliton' (after photon, proton, etc.), to emphasize the particle-

like character of these wave pulses^[29]. While passing through one another without change of shape, amplitude, or speed is one of the defining properties of solitons^[36], few exceptions have been found for solitary waves that propagate in systems that are either damped or not fully integrable. Specifically, the collision between a kink and its anti-kink pair has been shown to lead to a trapped breather in the integrable sine-Gordon system with damping^[82], to a localized bound pair in the non-integrable φ^4 model^[120] and to different types of kinks in the non-integrable double sine-Gordon model^[82].

In this study, we focus on a mechanical metamaterial based on rotating rigid units^[94,121–123] and use a combination of experiments and numerical analyses to study the collisions between two supported elastic vector solitons. Surprisingly, despite of the fact that the propagation of a single soliton is accurately captured by the completely integrable modified Korteweg-de Vries (mKdV) equation, not all solitary waves emerge unaltered from the collisions. If the propagating solitons induce rotations of opposite direction at a given unit in the system, they repel each other upon collision. We show that this highly unusual behavior is closely related to the vectorial nature of the supported solitons, which in turn leads to the formation of amplitude gaps - ranges in amplitude where elastic soliton propagation is forbidden. The large rotations induced by a soliton create a barrier for pulses with rotational component of opposite sign that blocks their propagation. Our study provides new insights into the collision dynamics of elastic solitary waves and reveals that in vector solitons the coupling between the different components can lead to completely unexplored and new phenomena.

3.3 Elastic Vector Solitons

Our mechanical metamaterial consists of a chain of N pairs of rigid crosses connected by thin and flexible hinges (see Fig. 3.1(a)). It has been recently shown that the propagation of a single soliton in such system is accurately described by a nonlinear Klein-Gordon equation^[121], which can be rewritten in the form of the completely integrable mKdV equation^[96]. The solution of such equation indicates that the considered metamaterial supports the propagation of elastic vector solitons that induce simultaneous longitudinal displacement u_i and rotation θ_i at the i -th pair of crosses, with all neighboring units rotating in opposite directions (see Fig. 3.1(a)). Specifically, u_i and θ_i are defined by^[121] (see Supplementary Materials)

$$u_i(t) = \frac{aA^2 W}{2(1 - c^2/c_0^2)} \left[1 - \tanh\left(\frac{ia - ct}{W}\right) \right] \quad (3.1)$$

and

$$\theta_i(t) = A \operatorname{sech}\left(\frac{ia - ct}{W}\right), \quad (3.2)$$

where a denotes the center-to-center distance between neighboring units and c_0 is the velocity of the supported linear longitudinal waves in the long wavelength limit. Moreover, A , c and W denote the amplitude, speed and width of the pulses, with speed and width that can be expressed in terms of amplitude as

$$c = \pm c_0 \sqrt{\frac{6K_\theta}{A^2 + 6K_\theta}}, \quad (3.3)$$

and

$$W = \frac{a}{\alpha} \sqrt{\frac{a^2(K_s - K_\theta) - 6K_\theta/(A^2 + 6K_\theta)}{6K_\theta}}. \quad (3.4)$$

where α represents the normalized mass, and K_s and K_θ are the normalized shear and bending stiffnesses of the hinges. At this point it is important to note that the propagation of the vector solitons defined by Eqs. (3.1) and (3.2) requires a strong coupling among their two components u_i and θ_i ^[100]. Since in our system such strong coupling is activated only for large enough rotations, vector solitons with

$$|A| < \sqrt{\frac{6K_s}{\alpha^2(K_s - K_\theta)} - 6K_\theta} \quad (3.5)$$

cannot propagate, resulting in the emergence of amplitude gaps^[121]. While Eq. (3.5) fully defines the amplitude gap for a chain in which all hinges are aligned, pre-rotations of the crosses significantly increase the magnitude of the lower threshold, as they make the propagation of solitons that induce energetically unfavourable rotation more difficult^[121]. Notably, our analysis will reveal that such pre-rotation effect on the amplitude gap plays a central role in defining the collision dynamics.

3.4 Anomalous Collisions Between Vector Solitons

To investigate the collision of solitons in our system, we test a structure comprising $N = 50$ pairs of crosses made with LEGO bricks and connected via polyester plastic sheets. To initiate elastic vector solitons, we use two impactors that induce simultaneous rotation and displacement of the crosses at both ends of the sample (see Figs. 3.1(b) and (c), and Supplementary Materials). We control the amplitude of the pulses by varying the maximum distance traveled by the impactors. As for the direction of rotation imposed to the first and last pairs of crosses, we select it by using two different types of impactors. Specifically, since we define as positive a clockwise (counter-

clockwise) rotation of the top unit in the even (odd) pairs, we use an impactor that hits the mid-point of the end pairs to excite positive θ_i (see Fig. 3.1(b)) and one that hits their external arms to excite negative θ_i (see Fig. 3.1(c) - note that the direction of rotations imposed by the impactors changes if the chain comprises an odd number of pairs, see Supplementary Materials). In addition to the experiments, we also simulate the response of a chain with $N = 500$ pairs of crosses (to eliminate possible boundary effects) by numerically integrating the $2N$ ordinary differential equations with parameters $\alpha = 1.8$, $K_s = 0.02$ and $K_\theta = 1.5 \times 10^{-4}$ [121].

In Figs. 3.1(e-f) and (h-i), we present experimental and numerical results for two sets of input signals applied to the left and right ends of the chain. First, the impactors excite solitons with amplitude $A_{\text{left}} = A_{10} = 0.2$ and $A_{\text{right}} = A_{N-10} = 0.2$ (A_i being the amplitude of θ_i before the collision). Both our experimental and numerical results indicate that the two pulses, which induce rotations with the same direction at any given unit in the chain (see Fig. 3.1(d)), penetrate each other without change of shape, amplitude or speed (see Fig. 3.1(e-f) and Supplementary Video 5). As commonly observed when two solitons collide[33–40], only a slight time delay may be observed, confirming that our metamaterial can respond similarly to a fully integrable system such as a KdV system[82,124]. Second, we apply $A_{\text{left}} = -0.2$ and $A_{\text{right}} = 0.2$ to excite two pulses that induce rotations of opposite sign at any given unit (see Fig. 3.1(g)). Surprisingly, we find that in this case the solitons do not penetrate each other and instead reflect one another (see Figs. 3.1(h-i) and Supplementary Video 5). This phenomenon is especially visible from the absence of rotations of the units in the center of the system. It is also important to note that, while in the experiments there is inevitably some dissipation due to both friction and viscous effects, in our numerical simulation we do not include any damping. As such, our results indicate that the observed anomalous collisions are not due to the presence of damping or boundary effects, and are rather a robust feature of the

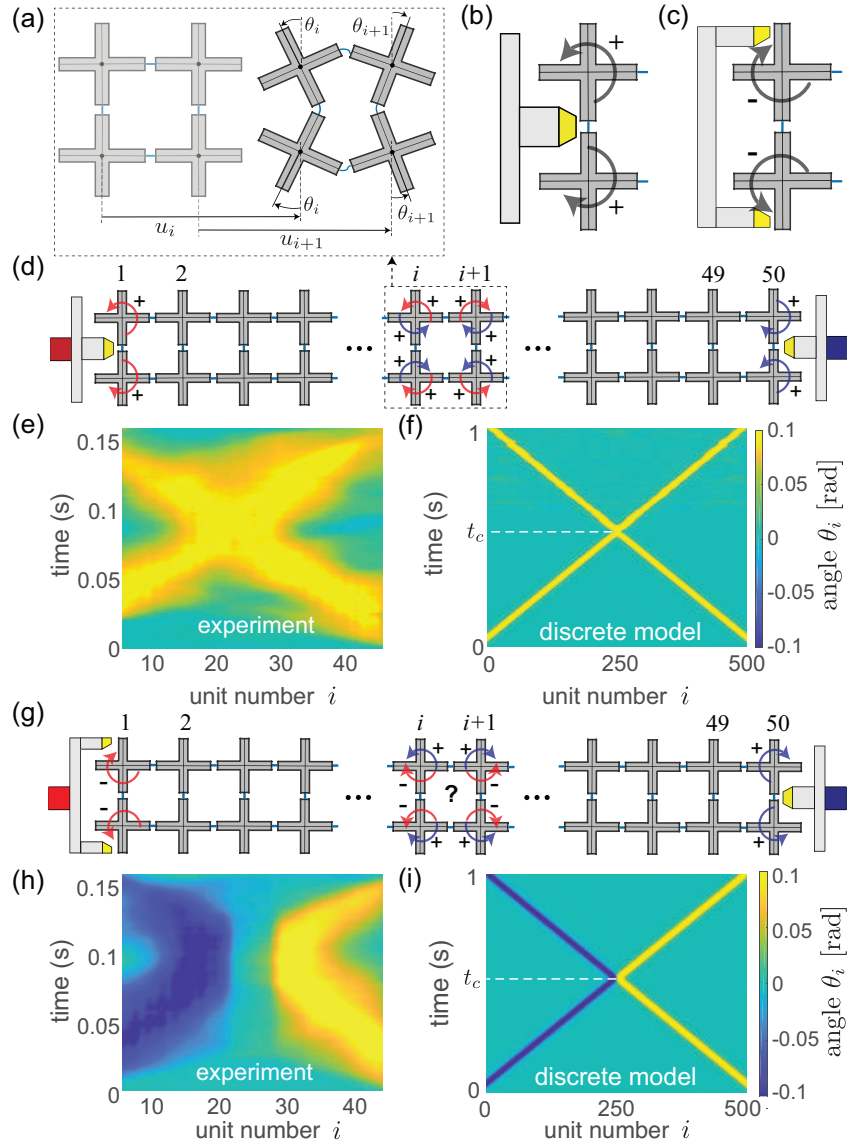


Figure 3.1: Experiments on collisions between elastic vector solitons. (a) Schematic of the system. (b)-(c) Schematics of the impactors used to excite (b) positive and (c) negative rotations. (d) Schematic of our first experiment. (e)-(f) Rotation of the pairs of crosses during the propagation of the pulses, as recorded during our first test in (e) experiments and (f) numerical simulations. (g) Schematic of our second experiment. (h)-(i) Rotation of the pairs of crosses during the propagation of the pulses, as recorded during our second test in (h) experiments and (i) numerical simulations.

system.

To better understand how two colliding solitons interact in our system, we focus on the left-initiated pulse and systematically investigate how it is affected by the collision with the right-

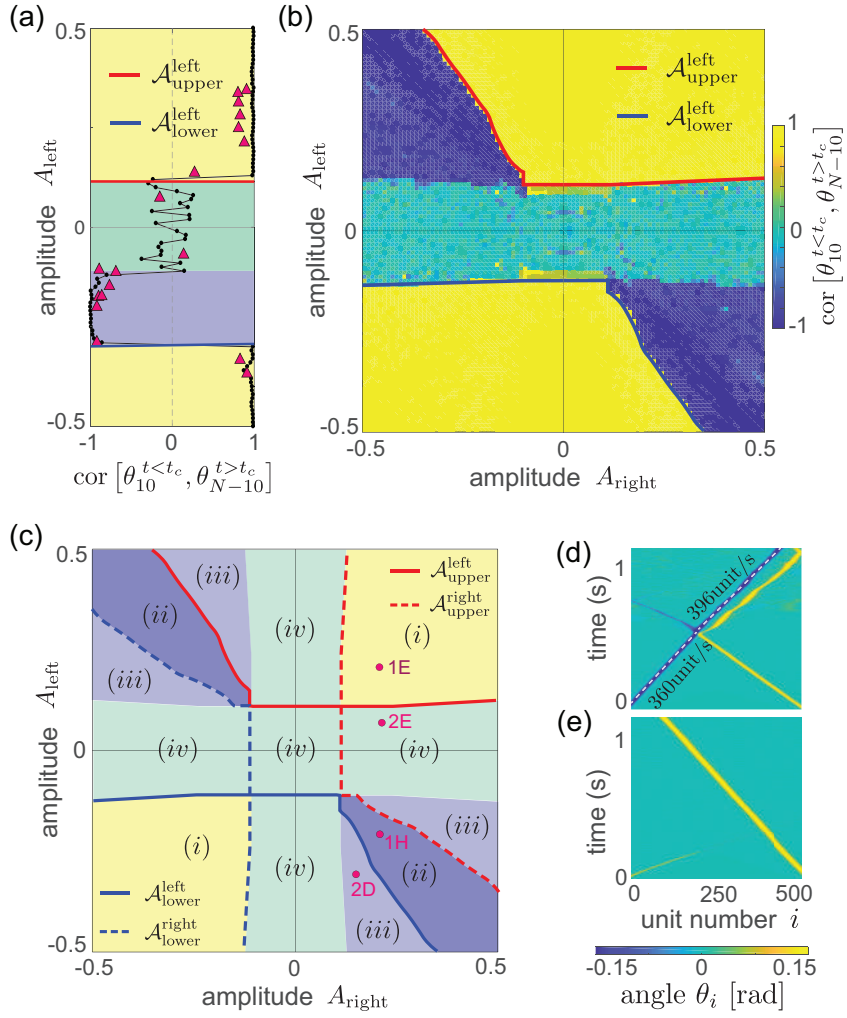


Figure 3.2: Numerical simulations and complete phase diagram of vector soliton collisions. (a) Cross-correlation between $\theta_{10}(t < t_c)$ and $\theta_{N-10}(t > t_c)$ as a function of A_{left} for $A_{\text{right}} = 0.2$. Triangular markers correspond to experimental data, while the black line is generated using numerical simulations. (b) Numerically obtained cross-correlation between $\theta_{10}(t < t_c)$ and $\theta_{N-10}(t > t_c)$ as a function of A_{left} and A_{right} . (c) Complete picture of the collision dynamic between the pulses supported by the system. (d)-(e) Rotations of the pairs of crosses during the propagation of the pulses as found in numerical simulations for (d) $(A_{\text{left}}, A_{\text{right}}) = (-0.3, 0.22)$ and (e) $(0.08, 0.3)$.

initiated one. To quantify such effect, we calculate the cross-correlation between $\theta_{10}(t < t_c)$ and $\theta_{N-10}(t > t_c)$ (t_c denoting the time at which the collision occurs) as a function of A_{left} , while keeping $A_{\text{right}} = 0.2$. As shown in Fig. 3.2(a), we find that the response of the system is characterized by two distinct regions. For $A_{\text{left}} < \mathcal{A}_{\text{lower}}^{\text{left}} = -0.28$ and $A_{\text{left}} > \mathcal{A}_{\text{upper}}^{\text{left}} = 0.12$ the left-initiated elastic vector solitons propagate through the entire structure unaffected by the collision with the right-initiated

pulses and the cross-correlation approaches unity. By contrast, for $\mathcal{A}_{\text{lower}}^{\text{left}} < A_{\text{left}} < \mathcal{A}_{\text{upper}}^{\text{left}}$ the left-initiated pulse does not reach the other end of the chain and the cross-correlation is $\ll 1$. Focusing on this region of low cross-correlation, two recognizably different behaviors are observed. First, for $-0.12 < A_{\text{left}} < \mathcal{A}_{\text{upper}}^{\text{left}}$ the cross-correlation approaches zero, since the propagation of the left-initiated soliton is prevented by the amplitude gap of the chain defined by Eq. (3.5) (note that for this range of amplitudes no collision occurs, since the left-initiated soliton dies before reaching the right-initiated one). Second, for $\mathcal{A}_{\text{lower}}^{\text{left}} < A_{\text{left}} < -0.12$ the cross-correlation approaches -1. For this range of amplitudes a solitary wave that induces rotations with direction opposite from those excited by the left-initiated soliton is detected at the right end after collision - a clear signature of an anomalous collision dynamics that results in the (partial or total) reflection of the right-initiated soliton.

Next, we consider the effect on the collision of both A_{left} and A_{right} . The heat map shown in Fig. 3.2(b) confirms that, while typical collisions that do not alter the left-initiated soliton (resulting in a cross-correlation that approaches 1) occur when the two colliding solitons induce rotation of the same direction (i.e. $A_{\text{left}} A_{\text{right}} > 0$), anomalous collisions that change the left-initiated pulse (leading to a cross-correlation $\ll 1$) may also exist when two colliding solitons induce rotations of opposite direction (i.e. $A_{\text{left}} A_{\text{right}} < 0$). We then construct a plot analogous to that shown in Fig. 3.2(b), but focused on the right-initiated pulses by considering the cross-correlation between $\theta_{N-10}(t < t_c)$ and $\theta_{10}(t > t_c)$ (see Fig. B.7). By combining Fig. 3.2(b) with Fig. B.7, we find that four different scenarios are possible upon collision (see Fig. 3.2(c)): (i) both solitons penetrate, as typical for collisions between solitons (see yellow area in Fig. 3.2(c) and Figs. 3.1(d-e)); (ii) both solitons are reflected - a clear signature of an anomalous collision (see dark blue area in Fig. 3.2(c) and Figs. 3.1(g-h)); (iii) one soliton is blocked and the other penetrates - again signature of an

anomalous collision (see shallow blue area in Fig. 3.2(c) and Fig. 3.2(d)); (iv) one or no soliton travels through the system due to the existence of the amplitude gap, so that no collision occurs (see green area in Fig. 3.2(c) and Fig. 3.2(e)). Therefore, our numerical investigation describes quantitatively all possible two-solitons heads-on collisions and provides a complete picture of the collision dynamic between the pulses supported by the system.

3.5 Amplitude Gap Theory with Frozen Solitons

The results of Figs. 3.1 and 3.2 reveal that our system supports anomalous collisions that alter the characteristics of the solitons. Such surprising phenomenon can be fully explained via the concept of amplitude gaps. The large rotations generated by a soliton effectively enlarge the amplitude gap for pulses that induce rotations of opposite sign, stopping their propagation when they come close enough. To demonstrate this important point, we freeze solitons of different amplitude A_f in the middle of the chain and numerically investigate their effect on the propagation of solitary waves initiated at the left end. Specifically, we consider a chain in which the i -th pair of crosses is rotated according to theoretical solution of soliton (see Fig. 3.3(a) and Supplementary Materials), excite pulses of different amplitude A_{left} at its left end and investigate the interaction between the left-initiated soliton and the frozen perturbation by looking at the cross-correlation between $\theta_{10}(t)$ and $\theta_{N-10}(t)$. The numerical results reported in Fig. 3.3(b) clearly indicate that there is a well-defined region in the $A_{\text{left}}-A_f$ space resulting in left-initiated solitons that do not reach the right end of the chain (note that in this region the cross-correlation is close to zero everywhere, as there is no propagating right-initiated pulse that can be reflected).

Notably, we also find that the lower thresholds of the low cross-correlation region obtained

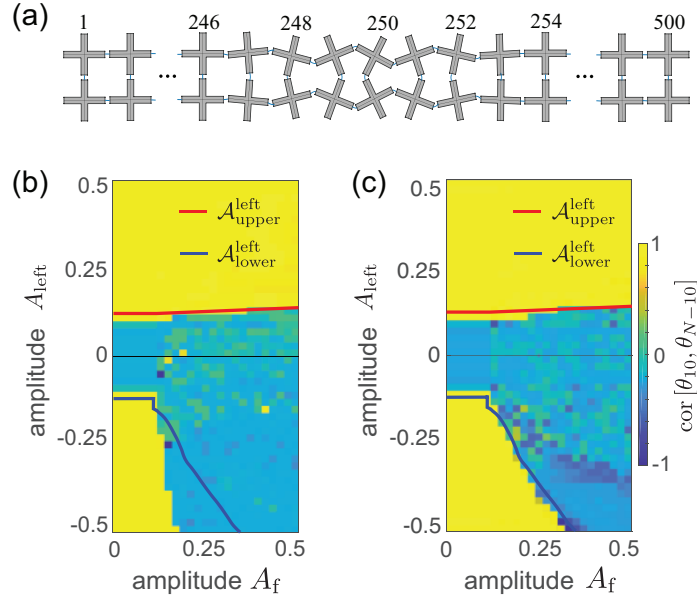


Figure 3.3: Interaction between propagating solitons and a frozen soliton. (a) A $N = 500$ chain with a frozen soliton placed in the middle of it. (b)-(c) Numerically obtained cross-correlation between $\theta_{10}(t)$ and $\theta_{N-10}(t)$ as a function of A_{left} and A_f with frozen solitons of width defined by (b) W_f and (c) W_f^{eff} .

considering a frozen perturbation or a right-initiated pulse follow similar trends (see Fig. 3.3(b)). However, there is a significant quantitative discrepancy between them that arises because the left-initiated soliton interacts for a time $\Delta t \propto (c_{\text{left}} + c_{\text{right}})^{-1}$ with the right-initiated pulse (c_{left} and c_{right} denoting the velocities of the left-initiated and right-initiated solitary waves before collision, respectively) and $\Delta t \propto c_{\text{left}}^{-1}$ with the frozen perturbation. To overcome this difference, we equate the interaction times by shrinking the width of the frozen soliton according to

$$W_f^{\text{eff}} = \frac{c_{\text{left}}}{c_{\text{right}} + c_{\text{left}}} W_f , \quad (3.6)$$

where c_{right} is given by Eq. (3.3) with $A = A_f$. Remarkably, by replacing the width of the frozen solitons W_f with W_f^{eff} , we find that the boundaries of the low cross-correlation region match extremely well the thresholds $\mathcal{A}_{\text{upper}}^{\text{left}}$ and $\mathcal{A}_{\text{lower}}^{\text{left}}$ (see Fig. 3.3(c)). As such, our analysis reveals that

the anomalous collisions observed in our system are a consequence of the soliton large-amplitude characteristics, which modify the properties of the underlying media. Specifically, the large rotations induced in the chain by a pulse enlarge the amplitude gap for solitons that excite rotations of opposite direction and this may block their propagation.

While in Figs. 3.1-3.3 we focus on the interaction between pulses initiated at the two ends of the chain, anomalous collisions can also be triggered when the solitons are sequentially excited at the same end. To demonstrate this, we numerically study the collision between two solitons with amplitude $A_{\text{left},1}$ and $A_{\text{left},2}$ initiated at the left end at time $t_1 = 0$ and $t_2 = 0.3\text{s}$, respectively. We find that if the two solitons excite rotations of the same sign and the second one is faster, the second pulse penetrates and overtakes the first one, and neither of them change their amplitude, shape or velocity (see Fig. 3.4(a)). By contrast, if the two solitons induce rotations of opposite sign, a single pulse emerges from the collision with the same direction as the first one, but with larger amplitude and, therefore, lower velocity (see Fig. 3.4(b)).

3.6 Applications

Having demonstrated that our system can support anomalous collisions that alter the characteristics of the interacting solitons, we now explore how these unusual effects can be exploited to actively manipulate and control the propagation of pulses. First, we note that anomalous collisions provide opportunities to remotely induce changes in the propagation velocity of a soliton, as they can either reverse (see Figs. 3.1(h-i)), increase (see Fig. 3.2(d)) or lower (see Fig. 3.4(b)) the pulses speed (see also Fig. B.A). Second, we find that anomalous collisions can be exploited to probe the direction of the rotations of a pulse by monitoring the "echo" of a probing soliton (see Figs. 3.4(c) and B.8).

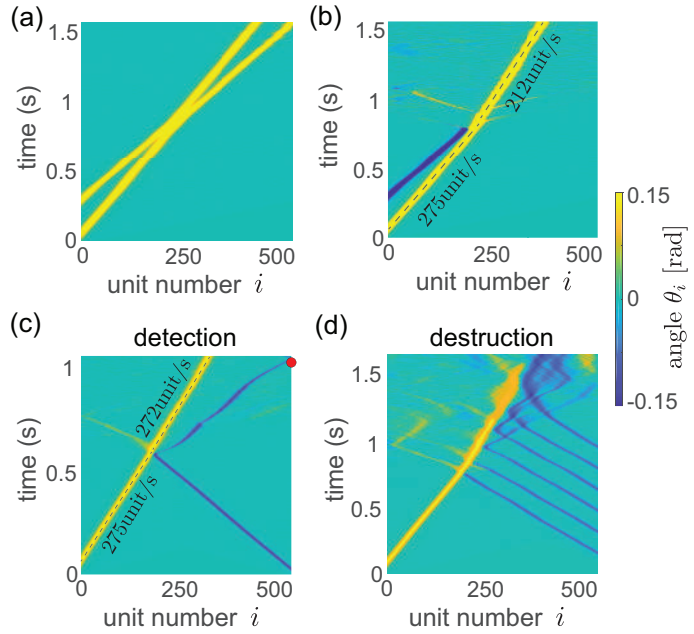


Figure 3.4: Other types of collisions and potential applications. (a)-(b) Rotations of the pairs of crosses as numerically found when considering two solitons of amplitude $A_{\text{left},1}$ and $A_{\text{left},2}$ initiated at the left end at time $t_1 = 0$ and $t_2 = 0.3$ s. $(A_{\text{left},1}, A_{\text{left},2}) = (0.4, 0.3)$ in (a) and $(0.4, -0.3)$ in (b). (c) A soliton with amplitude $A_{\text{right}} = -0.18$ is excited from the right end as a probing soliton to detect the rotation direction of the main soliton of amplitude $A_{\text{left}} = 0.4$. (d) An amplitude $A_{\text{left}} = 0.4$ soliton is destroyed by six small solitons of amplitude $A_{\text{right},k} = -0.2$, (with $k = 1, \dots, 6$).

Third, if the direction of rotations excited by the soliton is known, we can block its propagation by sending a sequence of relatively small pulses with opposite rotation direction (see Figs. 3.4(d) and B.8).

To summarize, our experiments show that anomalous interactions can occur for vector elastic solitons supported by a mechanical metamaterial based on rigid rotating units. While two solitons that induce rotations of the same direction penetrate each other when they meet, two solitons with opposite rotational component may repel each other and change both their amplitudes and velocities upon collision. Remarkably, our numerical analyses can fully explain the experimental findings and provide a complete description of these exotic two-soliton interactions. The geometric changes induced by one soliton significantly enlarge the effective amplitude gaps for other solitons with

opposite rotational component and may block their propagation when they come close enough. We envision that the reported anomalous collisions between solitons could be used for remote control of the propagating nonlinear pulses, as they result in changes of the pulse velocity that can be engineered to remotely detect, change or destruct high-impact signals.

Chapter 4

Characterization, Stability and Application of Domain Walls in Flexible Mechanical Metamaterials

By: Bolei Deng*, Siqin Yu*, Antonio E Forte, Vincent Tournat, Katia Bertoldi. Published in *PNAS*,
on Nov. 20 2020. [doi:10.1073/pnas.2015847117](https://doi.org/10.1073/pnas.2015847117)

4.1 Abstract

Domain walls, commonly occurring at the interface of different phases in solid-state materials, have recently been harnessed at the structural scale to enable new modes of functionality. Here, we combine experimental, numerical and theoretical tools to investigate the domain walls emerging upon uniaxial compression in a mechanical metamaterial based on the rotating-squares mechanism. We first show that these interfaces can be generated and controlled by carefully arranging a few phase-inducing defects. We establish an analytical model to capture the evolution of the domain walls as a function of the applied deformation. We then employ this model as a guideline to realize interfaces of complex shape. Finally, we show that the engineered domain walls modify the global response of the metamaterial and can be effectively exploited to tune its stiffness as well as to guide the propagation of elastic waves.

4.2 Significance Statement

Mechanical metamaterials are an interesting platform to reproduce atomistic-scale phenomena at the macro-scale and to exploit them to achieve new functionalities. An interesting feature of many ordered solid-state materials is the formation of domain walls that separate regions of different phases. While these interfaces have been reproduced in a variety of mechanical materials, understanding of how to control them is still poor owing to their structural complexity. Here, we use a combination of experimental, numerical and theoretical tools to engineer the domain walls emerging upon uniaxial compression in a mechanical metamaterial based on the rotating-squares mechanism. Our study reveals new territories in the mechanical metamaterials design space which

could unlock new tools for information encryption, stiffness tuning and wave guiding.

4.3 Introduction

The coexistence of two or more phases plays a central role in many ordered solid-state materials, including ferroelectrics^[43–45], ferromagnets^[46,47], ferroelastics^[48,49], shape memory alloys^[49,50] and liquid crystals^[51]. Despite being intrinsically different, these materials all share the emergence of domain walls - a type of topological defect that separates regions of different phases^[125]. Such interfaces are crucial for the control of many material properties, including coercivity, resistance and/or fatigue^[126] and have also been exploited to enable logic operations^[52], racetrack memory^[53] and line scanners for reading optical memories^[54]. Inspired by the recent advancements in domain walls control strategies at the atomistic scale, a variety of non-linear mechanical structures have been designed to support these interfaces^[5,27,28,55–62]. Domain walls engineered at the structural scale have facilitated the control of elastic pulses^[28,56,58,62], the encryption of information^[5] and the realization of deployable structures^[59] as well as of phase transforming metamaterials^[55,57]. However, due to the structural complexity of mechanical metamaterials, no analytical solution has been proposed that fully describes the physics of such domain walls. This limits their systematic application in the design of smart structures and devices and hinders the discovery of new functionalities.

Here, we use a combination of experiments and analyses to study the domain walls emerging in a mechanical metamaterial based on the rotating-squares mechanism. We start by introducing defects into the system to locally impose nucleation of one of the two supported buckling-induced rotated phases upon compression. Importantly, when such defects lead to the coexistence of two

phases within the specimen, domain walls form, across which the angle of individual squares switch from one direction of rotation to the other. We establish an analytical model that fully describes the emerging domain walls, including their profile and position as a function of the applied deformation. Guided by our model, we then introduce pinning defects to reshape the energy landscape of the system and, therefore, engineer domain walls along arbitrary complex paths. Based on our findings we foresee the exploitation of domain walls in the realm of mechanical metamaterials to realize novel functionalities, as we hereby demonstrate by achieving stiffness tuning and reconfigurable elastic wave guiding.

4.4 Flexible Mechanical Metamaterial Based on the Rotating-squares Mechanism

We consider an elastomeric structure of thickness $t = 3$ mm comprising an array of 21×21 squares with center-to-center distance $a = 10$ mm, connected at their vertices by ligaments with width and length of 1 mm (Fig. 4.1(a) and (section C.1 for fabrication details)). In all our tests we uniaxially compress the structure by applying a vertical displacement Δ_{stage} to the top edge (which results in a nominal longitudinal strain $\varepsilon_{\text{applied}}^{yy} = \Delta_{\text{stage}}/(21a)$), while using a transparent acrylic plate to prevent its out-of-plane deformation. The deformation of the sample is captured with a camera (SONY, RX100), and the position and rotation of the squares are tracked via image processing conducted in Matlab (section C.2 for testing details). Under the applied compression, one of the beam-like ligaments in the sample buckles first, because of immeasurable small imperfections introduced during fabrication. This provides a unique nucleation site that leads to the formation of a

uniform buckling pattern in which all squares alternately rotate in clockwise and counterclockwise directions (Fig. 4.1(b) and Supplementary Video 6). Note that to facilitate the analysis, we define the positive direction of rotation alternately for neighboring squares. Specifically, we choose the square at the bottom-left corner to be unit [1, 1] and define a counter clockwise rotation of the $[i,j]$ th square (i.e. the square located on the i^{th} row and j^{th} column) positive if $i + j$ is an even number and negative if $i + j$ is odd (Fig. 4.1(a)). Using these definitions, we find that in our sample, buckling induces a negative rotation of all squares. On the other hand, if the ligament that acts as a nucleation site had buckled in the opposite direction, all units would have experienced a positive rotation.

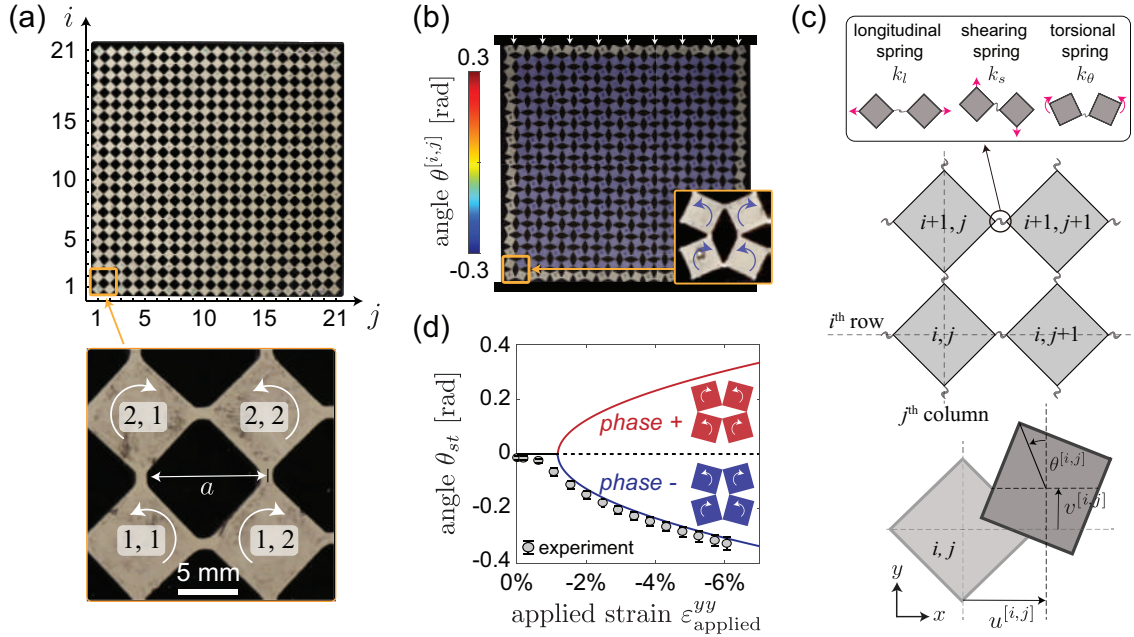


Figure 4.1: The rotating square system. (a) The system consists of a network of 21×21 square domains connected by thin ligaments. The positive direction of rotation alternates for neighboring squares: a counter clockwise rotation of the $[i,j]^{\text{th}}$ square (the square located on the i^{th} row and j^{th} column) is defined positive if $i + j$ is an even number and negative if $i + j$ is odd. (b) Deformation of the sample when subjected to $\varepsilon_{\text{applied}}^{\text{yy}} = -4\%$. The color indicates the rotation of the squares. (c) We model the system as an array of rigid squares connected at their vertices by elastic springs. (d) Evolution of θ_{st} as a function of $\varepsilon_{st}^{\text{yy}}$ as predicted (solid lines) and measured in our experiment (markers).

The non-linear behavior of our system can be captured using a discrete model comprising rigid squares connected at their vertices by a combination of springs (Fig. 4.1(c))^[94,121,127–129]. Three

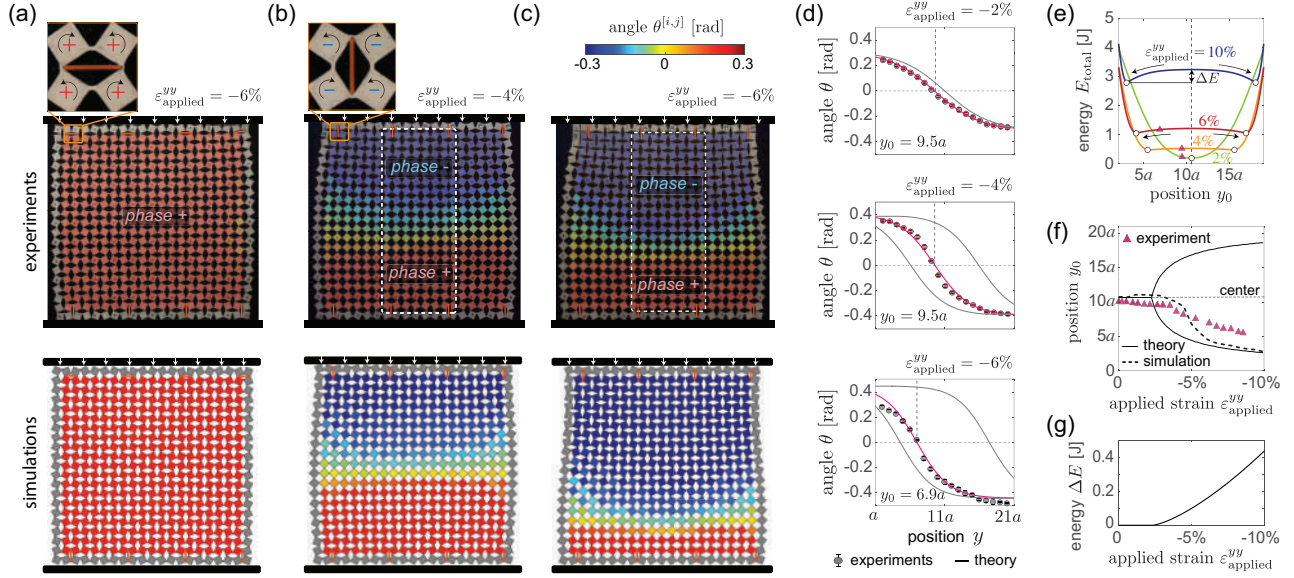


Figure 4.2: Uniaxial compression of the rotating-square structure with phase inducing defects. (a) Deformation at $\varepsilon_{\text{applied}}^{\text{yy}} = -4\%$ of a sample with 8 phase-inducing defects arranged to induce nucleation of *phase+*. (b)-(c) Deformation at (b) $\varepsilon_{\text{applied}}^{\text{yy}} = -4\%$ and (c) $\varepsilon_{\text{applied}}^{\text{yy}} = -6\%$ of a sample with 8 phase-inducing defects arranged to induce nucleation of *phase+* near to the bottom boundary and *phase-* near the top one. Experimental and numerical snapshots are shown on top and bottom, respectively. The color corresponds to the rotation of the squares. Zoom-ins of the defects are also shown. (d) Comparison between analytically predicted (solid lines) and experimentally extracted (circular markers) evolution of the squares' rotation θ across the sample for different values of applied strain. (e) Analytically predicted evolution of the total energy of the structure as a function of domain wall position y_0 for different values of applied strain. (f) Evolution of the domain wall position y_0 as a function of the applied strain $\varepsilon_{\text{applied}}^{\text{yy}}$ as predicted by theory (continuous line), numerical simulations (dashed line) and extracted from experiments (markers). (g) Evolution of the energy barrier ΔE as a function of applied strain $\varepsilon_{\text{applied}}^{\text{yy}}$.

degrees of freedom are assigned to the $[i,j]$ -th rigid square: (i) the displacement in x direction, $u^{[i,j]}$; (ii) the displacement in y direction, $v^{[i,j]}$; and (iii) the rotation around the z -axis, $\theta^{[i,j]}$. As for the ligaments, their longitudinal and shearing response is captured by linear springs with stiffness k_l and k_s respectively, whereas their bending behavior is modeled by using a non-linear hardening rotational spring with linear and cubic terms that exert a torque $M = k_\theta(\Delta\theta + \gamma\Delta\theta^3)$, where $\Delta\theta$ is the relative rotation between the connected squares, k_θ is the bending stiffness and γ is a dimensionless parameter (section C.3.1). Note that for the structure considered in this study $k_l = 1080$ N/m, $k_s = 239$ N/m, $k_\theta = 1.62 \times 10^{-4}$ N·m and $\gamma = 0.5$ (section C.3.5). and that, to facilitate the analysis,

we assume that the longitudinal and shearing springs are always parallel either to x or y axis (an assumption which is valid only for small global rotations of the system). When adopting such discrete model, the response of a structure comprising $N_x \times N_y$ units can be obtained by numerically solving the $3N_xN_y$ coupled non-linear equations derived by imposing force equilibrium at each square. Further, a deeper insight can be achieved by deriving analytical solutions. To this end, we assume small rotation of the squares and take the continuum limit of the discrete equilibrium equations to obtain (section C.4)

$$k_l \partial_{xx} u + k_s \partial_{yy} u + k_l \theta \partial_x \theta = 0, \quad (4.1a)$$

$$k_l \partial_{yy} v + k_s \partial_{xx} v + k_l \theta \partial_y \theta = 0, \quad (4.1b)$$

$$\begin{aligned} & -a^2(k_s a^2 - 4k_\theta) \nabla^2 \theta + 32k_\theta \theta + 4(k_l a^2 + 32\gamma k_\theta) \theta^3 \\ & + 4k_l a^2(\theta - \theta^3/6) (\partial_x u + \partial_y v) = 0, \end{aligned} \quad (4.1c)$$

where $\partial_a f = \partial f / \partial a$, $\nabla^2 = \partial_{xx} + \partial_{yy}$, and u , v and θ are three continuum functions that interpolate the discrete variables $u^{[i,j]}$, $v^{[i,j]}$ and $\theta^{[i,j]}$ as,

$$\begin{aligned} u(x = aj, y = ai) &= u^{[i,j]}, \\ v(x = aj, y = ai) &= v^{[i,j]}, \\ \theta(x = aj, y = ai) &= \theta^{[i,j]}. \end{aligned} \quad (4.2)$$

The uniaxial compression loading considered in our experiments is then modeled by imposing

$$v(y = aN_y) - v(y = a) = a(N_y - 1)\varepsilon_{\text{applied}}^{yy}, \quad (4.3)$$

and

$$\partial_x u + \theta^2/2 = 0, \quad (4.4)$$

where Eq. (4.4) is obtained by requiring the longitudinal forces in all horizontal ligaments to vanish (since the vertical edges of the structure are traction-free).

For the case of an homogeneous deformation (as that shown in Fig. 4.1(b)), both the rotation of the squares and the longitudinal strain in y -direction are spatially constant (i.e. $\theta = \theta_{st}$ and $\partial_y v = \varepsilon_{st}^{yy}$, where θ_{st} and ε_{st}^{yy} are the constant rotation and longitudinal strain). It follows that, when substituting Eq. (4.4) into Eqs. (4.1), Eqs. (4.1a) and (4.1b) vanish, whereas Eq. (4.1c) becomes

$$\left(1 - \frac{(24\gamma + 1)\varepsilon_{cr}^{yy}}{3}\right)\theta_{st}^3 + 2(\varepsilon_{st}^{yy} - \varepsilon_{cr}^{yy})\theta_{st} = 0, \quad (4.5)$$

where $\varepsilon_{cr}^{yy} = -8k_\theta/k_l a^2$. Further, Eq. (4.3) reduces to $\varepsilon_{st}^{yy} = \varepsilon_{\text{applied}}^{yy}$. Eq. (4.5) can be solved to obtain the rotation of the squares, θ_{st} , as a function of the strain ε_{st}^{yy} as

$$\theta_{st} = \begin{cases} 0, & \varepsilon_{st}^{yy} > \varepsilon_{cr}^{yy} \\ \pm \sqrt{\frac{-6(\varepsilon_{st}^{yy} - \varepsilon_{cr}^{yy})}{3 - (24\gamma + 1)\varepsilon_{cr}^{yy}}}, & \varepsilon_{st}^{yy} < \varepsilon_{cr}^{yy} \end{cases} \quad (4.6)$$

Eq. (4.6) defines the pitchfork-shape bifurcation diagram shown in Fig. 4.1(d). At ε_{cr}^{yy} the initially stable solution ($\theta_{st} = 0$) bifurcates into two new stable branches that correspond to positive and negative rotation of the squares and, therefore, to the two buckling-induced phases supported by the system (which we refer to as *phase+* and *phase-*). Note that the evolution of the average rotation of the squares as a function of $\varepsilon_{\text{applied}}^{yy}$ extracted from the experiments (circular markers in Fig. 4.1(d)) nicely follows the *phase-* branch, confirming the validity of our model.

4.5 Phase-inducing Defects and Domain Walls

While in our sample the emerging buckling-induced phase is determined by unavoidable small imperfections introduced during fabrication, one can impose a prescribed phase by placing stiff plastic plates with length $l_d = 1.2a$ into selected holes to act as phase-inducing defects (Figs. 4.5(a) and Fig. C.2). Such plates fully determine the buckling direction of the ligaments to which they are connected and, therefore, depending on their position and orientation, can induce the formation of either *phase+* or *phase-*. To demonstrate our approach, we evenly distribute eight of such defects in the holes next to the horizontal boundaries. We find that when the eight defects are located and oriented as shown in Fig. 4.5(a) (see Fig. C.3 for details), they overcome the imperfections introduced during fabrication and make *phase+* appear upon buckling (Fig. 4.5(a) and Supplementary Video 7). Further, by simply rotating the defects next to the top boundary by 90 degrees (Fig. C.3), we can get *phase-* to propagate from the top boundary and *phase+* from the bottom one (Fig. 4.5(b)). This leads to the coexistence of two phases within the specimen and to the formation of a horizontal domain wall in which the angles of individual squares switch from positive to negative values. For $\varepsilon_{\text{applied}}^{yy} = -4\%$ such a domain wall is located near the center of the specimen. However, when the applied compression is increased to $\varepsilon_{\text{applied}}^{yy} = -6\%$, it shifts towards the bottom (Fig. 4.5(c)) and (Supplementary Video 7).

To ensure that the phenomena observed in the experiments are not artifacts introduced by friction or unavoidable imperfections, we next conduct discrete simulations in which we model the phase-inducing defects as stiff springs with stiffness $k_d \gg k_l$ and length at rest l_d (section C.3.2). We find a very good agreement between the numerical and experimental results (Figs. 4.5(a-c)), with the simulations capturing both the deformation-induced shifting and thinning of the domain

walls (Supplementary Video 7 and Figs. C.12-18 for simulation results conducted on larger 51×51 structures). Having confirmed that our experimental observations emerge because of the bulk properties of the medium (rather than friction or geometrical imperfections), we then seek analytical solutions to describe both the profile and position of the emerging domain walls. To this end, since both our experiments and discrete simulations indicate that gradient of deformation along the domain wall are negligible (Figs. 4.5(b) and (c)), we assume that $\partial_x(\cdot) = 0$ (section C.4.1). It follows that Eqs. (4.1) and (4.4) reduce to

$$d_{yy}v + \theta d_y\theta = 0, \quad (4.7a)$$

$$\begin{aligned} -a^2(k_s a^2 - 4k_\theta)d_{yy}\theta + 32k_\theta\theta + 2(k_l a^2 + 64\gamma k_\theta)\theta^3 \\ + 4k_l a^2(\theta - \theta^3/6)d_y v = 0, \end{aligned} \quad (4.7b)$$

Next, we integrate Eq. (4.7a) to obtain

$$d_y v = -\theta^2/2 + C, \quad (4.8)$$

where C is an integration constant that can be determined by assuming homogeneous deformation inside each phase (i.e. far away from domain wall). Specifically, by imposing

$$\partial_y v \Big|_{phase \pm} = \varepsilon_{st}^{yy}, \quad \theta \Big|_{phase \pm} = \pm \theta_{st}, \quad (4.9)$$

and using Eq. (4.5) to connect ε_{st}^{yy} and θ_{st} , C is determined as

$$C = \varepsilon_{cr}^{yy} \left[1 + \frac{(24\gamma + 1)\theta_{st}^2}{6} \right]. \quad (4.10)$$

Finally, by substituting Eqs. (4.8) and (4.10) into Eq. (4.7b) we obtain

$$d_{yy}\theta = \frac{16k_\theta(1+24\gamma)}{3a^2(k_s a^2 - 4k_\theta)} \theta(\theta - \theta_{st})(\theta + \theta_{st}). \quad (4.11)$$

Eq. (4.11) has the form of the Klein-Gordon Equation with quadratic and cubic nonlinearities and has been shown to admit analytical solutions of the form^[27,96,122],

$$\theta = \theta_{st} \tanh \frac{y - y_0}{w}, \quad (4.12)$$

where y_0 denotes the position of domain wall and

$$w = \frac{a}{\theta_{st}} \sqrt{\frac{3(k_s(a)^2 - 4k_\theta)}{8k_\theta(1+24\gamma)}}, \quad (4.13)$$

indicates its characteristic width. Having determined θ , the solution for the displacement field $u(x, y)$ and $v(x, y)$ is then calculated by integrating Eqs. (4.4) and (4.8) and θ_{st} is determined as a function of $\varepsilon_{\text{applied}}^{yy}$ by imposing Eq. (4.3) (note that because of the existence of the domain wall $\varepsilon_{st}^{yy} \neq \varepsilon_{\text{applied}}^{yy}$ (section C.4.1)). At this point, it is worth noticing that by multiplying both sides of Eq. (4.11) by $d_y\theta$ and integrating with respect to y , its effective Lagrangian (from which Eq. (4.11) can be retrieved by imposing $d_y\mathcal{L} = 0$) is obtained as

$$\mathcal{L} = \frac{1}{2} (d_y\theta)^2 - \frac{1}{w^2} \left[\frac{\theta^4}{2\theta_{st}^2} - \theta^2 \right]. \quad (4.14)$$

Remarkably, Eq. (4.14) is identical to the Lagrangian of the φ^4 mode — a well-known model established to describe second order phase transitions and domain walls in solid state materials^[130].

Next, we verify the validity of our analytical solution by comparing the evolution of the squares' rotation across the sample as recorded in our tests and predicted by Eq. (4.12) (Fig. 4.5(d)). When choosing y_0 to best match the experimentally observed location of the domain wall (magenta lines in Fig. 4.5(d)), we find an excellent agreement between analytical and experimental results, with the analytical solution nicely capturing the deformation-induced thinning of the domain wall. However, it is important to note that y_0 can also be calculated by minimizing the total energy of the system, E_{total} (SI Appendix, sections 3.3 and 4.2). As shown in Figs. 4.5(e), we find that initially (i.e. for $\varepsilon_{\text{applied}}^{yy} > -2.3\%$) E_{total} is a convex function with a minimum located at the center of the specimen (i.e., at $y_0 = 11 a$). However, as the applied compression is increased, it gradually turns into a multi-welled landscape with a local maximum at the center and two minima that progressively move towards the horizontal boundaries. Therefore, since the structure always seeks to minimize its total energy, our model indicates that for $\varepsilon_{\text{applied}}^{yy} < -2.3\%$ the domain wall tends to shift towards one of the horizontal boundaries (see solid line in Fig. 4.5(f)). While such shifting of the domain wall is present in both our experiments and simulations, it is found to start for larger values of applied deformation in simulations (see markers and dashed line in Fig. 4.5(f)). Such discrepancy is attributed to the small energy barrier ΔE for moderate levels of applied strain (Fig. 4.5(g)), which makes the shifting very sensitive to imperfections and friction. However, despite this discrepancy, the results of Fig. 4.5 indicate that our analytical model captures all the experimentally observed salient features of the emerging domain walls.

4.6 Pinning Defects and Stable Domain Walls

As shown in Fig. 4.5, by carefully arranging a few phase-inducing defects in the metamaterial we can induce the formation of a domain wall, whose location varies as a function of the applied deformation. In order to program the position of the domain wall, one can prevent the rotation of selected squares by introducing pinning defects consisting of square shaped rigid plates (with size $0.95a \times 0.95a$) placed into neighboring holes (Fig. C.2). In Figs. 4.3(a) we present results for a sample with four pinning defects equally spaced along a horizontal line (see Fig. C.4 for details), in addition to the previous eight phase-inducing defects arranged as in Figs. 4.5(b) and (c). We find that in this case the location of the domain wall is fully determined by the square defects that act as pinning sites (see Fig. 4.3(a) for $\varepsilon_{\text{applied}}^{yy} = -6\%$ and Supplementary Video 8). This is due to the pinning defects that modify the total energy of the system and make it convex for any value of applied deformation, with a clear minimum at the defects' locations (Fig. 4.3(b) and Fig. C.19-20 for additional results). Moreover, we find that the density of the pinning defects plays an important role. For example, it is possible to create a wavy domain wall by increasing the spatial separation between defects. In Fig. 4.3(c) and Supplementary Video 8, we show a 60×21 sample (larger width to minimize boundary effects) with pinning defects separated by 10 holes instead of 5. The competition between the pinning sites and the tendency of the domain wall to shift towards the boundary to minimize the total energy, both cooperate in the formation of an undulating phase separation (see Figs. S21-S23 for additional results). Finally, while in Fig. 4.3 we considered pinning defects positioned on the central line, the location of the domain wall can be programmed at any location in the sample (see Fig. C.19 for additional results).

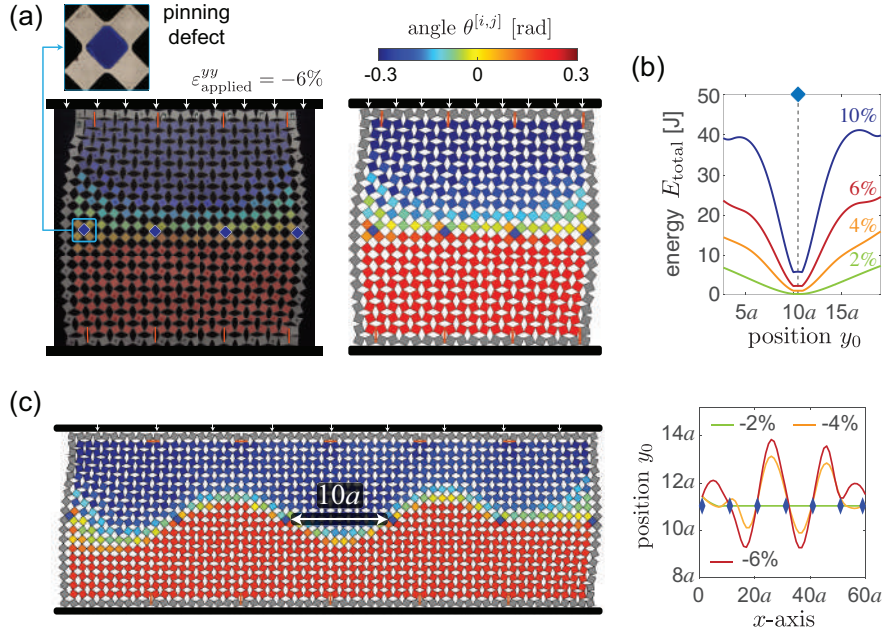


Figure 4.3: The effects of pinning defects. (a) Deformation at $\varepsilon_{\text{applied}}^{\text{yy}} = -6\%$ of a sample with 4 pinning defects and 8 phase-inducing defects. Experimental and numerical snapshots are shown on left and right, respectively. The color corresponds to the rotation of the squares. A zoom-in of a pinning defect is also shown. (b) Analytically predicted evolution of the total energy of the structure as a function of domain wall position y_0 for different values of applied strain. (c) Numerically predicted deformation at $\varepsilon_{\text{applied}}^{\text{yy}} = -6\%$ of structures comprising 21×60 squares with pinning defect separated by 10 holes. The domain wall becomes wavy for large enough values of applied compression.

4.7 Domain Walls with Arbitrary Orientations

The domain wall's orientation can be easily varied by arranging the defects along lines that form an angle φ_d with the horizontal axis. In Fig. 4.4(a) we show samples with 8 phase-inducing defects linearly arranged and angled at $\varphi_d = \arctan(1/2)$ and $\pi/4$ to induce opposite phases across the joining line (see Fig. C.3 for details on the arrangement of the defects). We find that at $\varepsilon_{\text{applied}}^{\text{yy}} = -4\%$ not only are the emerging domain walls shifted from the center of the region defined by the line of defects, but they also have a very different orientation than that prescribed by the defects (i.e. the domain wall forms an angle $\varphi = 21^\circ$ and 19° with the horizontal axis for $\varphi_d = \arctan(1/2)$ and $\pi/4$, respectively - see also Supplementary Video 9). To understand this behavior, we extend

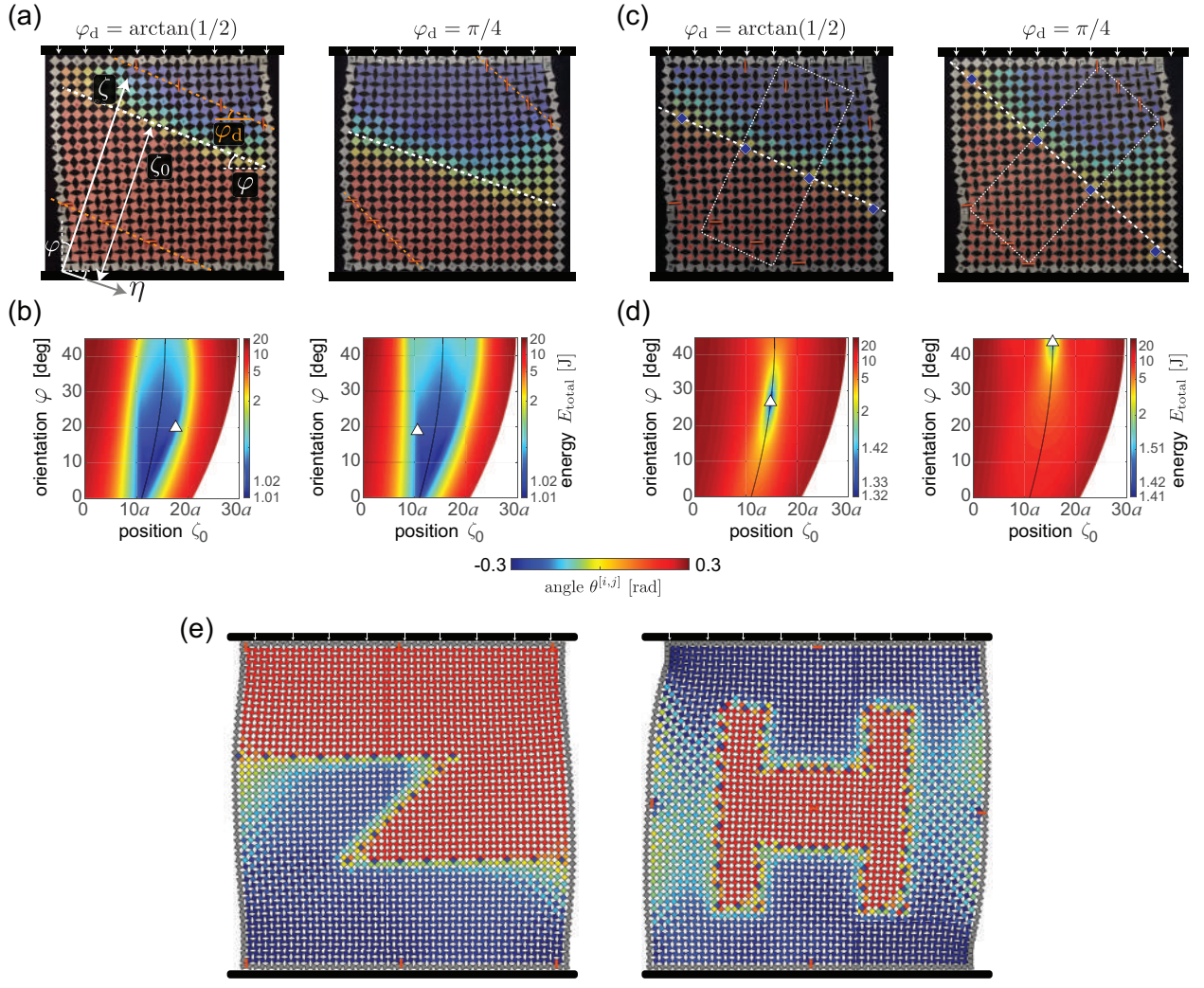


Figure 4.4: Domain walls at different orientations. (a) Deformation at $\varepsilon_{\text{applied}}^{\text{yy}} = -4\%$ of a sample with 8 phase-inducing defects arranged along two lines that form an angle $\varphi_d = \arctan(1/2)$ and $\pi/4$ with the horizontal axis. (b) Analytically predicted evolution of E_{total} at $\varepsilon_{\text{applied}}^{\text{yy}} = -4\%$ as a function of ζ_0 and φ . The triangular marker corresponds to the configuration of the experimentally observed domain wall. (c) Deformation at $\varepsilon_{\text{applied}}^{\text{yy}} = -4\%$ of a sample with 4 pinning defects in addition to 8 phase-inducing defects arranged as in A. (d) Analytically predicted evolution of E_{total} at $\varepsilon_{\text{applied}}^{\text{yy}} = -4\%$ as a function of domain wall position ζ_0 and orientation φ . The triangular marker corresponds to the configuration of the experimentally observed domain wall. (e) Numerically predicted deformation at $\varepsilon_{\text{applied}}^{\text{yy}} = -4\%$ for 51×51 structures with the pinning defects arranged along complex paths (in addition to phase-inducing defects to initiate phase+ and phase- at desired locations). The color in all snapshots corresponds to the rotation of the squares.

our model to domain walls with $\varphi \neq 0$ by introducing the local coordinates (Fig. 4.4(a))

$$\zeta = x \sin \varphi + y \cos \varphi, \quad \eta = x \cos \varphi - y \sin \varphi. \quad (4.15)$$

When we neglect the variation of deformation along the domain wall (i.e. we assume $\partial_\eta(\cdot) = 0$), we find that the profile of the domain wall is described by (section C.4.1),

$$\theta = \theta_{st} \tanh \frac{\zeta - \zeta_0}{w}, \quad (4.16)$$

where ζ_0 denotes the position along the ζ -axis of the domain wall and

$$w = \frac{a}{\theta_{st}} \sqrt{\frac{3(k_s(a)^2 - 4k_\theta)}{8k_\theta(1 + 24\gamma) + \frac{3k_sk_la^2 \sin^2 \varphi}{k_s \sin^2 \varphi + k_l \cos^2 \varphi}}}. \quad (4.17)$$

Using the analytical solution given by Eq. (4.16), we then calculate the total energy of the system as a function of the orientation φ and position ζ_0 of the domain wall. As shown in Fig. 4.4(b), we find that the domain walls observed in our experiments minimize E_{total} (see also Figs. S24-25). However, once again the position and orientation of the domain walls can be controlled by introducing a few square pinning defects to reshape the energy landscape of the structure. For example, by placing four pinning defects along a line which runs parallel to those defined by the phase-inducing defects (Fig. 4.4(c) and Supplementary Video 9), we can manipulate E_{total} to assume a single-welled landscape with a minimum at $\varphi = \varphi_d$ and $\zeta_0 = 21a/\cos \varphi_d$ (Fig. 4.4(d)). Hence, given this energy landscape, the domain walls form exactly along the lines defined by the pinning defects (Fig. 4.4(c)). Further, by arranging the pinning defects along complex paths and carefully placing a few phase-inducing defects to initiate *phase+* and *phase-* at desired locations, information in the form of arbitrary images can be encoded into the system, which can be revealed upon the application of a large enough compressive load (Fig. 4.4(e) and Supplementary Video 9).

4.8 Applications

Having demonstrated that domain walls can be engineered by arranging few defects in selected locations, we then explore how these can be harnessed to enhance the static and dynamic behavior of the system. To begin with, we focus on the effect of the domain walls on the non-linear stress-strain response of the material. If we assume that near the horizontal boundaries of the structures (i.e. far away from the domain wall) the deformation is homogeneous (i.e., $\theta = \theta_{st}$ and $\partial v / \partial y = \varepsilon_{st}^{yy}$), the averaged normal stress in the y -direction can be analytically obtained by taking the continuum limit of the longitudinal forces acting on the vertical hinges as (section C.4.3)

$$\sigma^{yy} = \frac{k_l}{t} \left(\varepsilon_{st}^{yy} + \frac{\theta_{st}^2}{2} \right). \quad (4.18)$$

In the absence of domain walls (i.e. for the case of homogeneous deformation), $\varepsilon_{st}^{yy} = \varepsilon_{\text{applied}}^{yy}$ and θ_{st} can be determined as a function of $\varepsilon_{\text{applied}}^{yy}$ using Eq. (4.5). Differently, in the presence of a domain wall θ_{st} and ε_{st}^{yy} are simultaneously determined as a function of $\varepsilon_{\text{applied}}^{yy}$ by imposing Eqs. (4.3) and (4.5). In Fig. 4.5(a) we report the stress-strain curves predicted by Eq. (4.18) for systems with and without domain walls. We find that the structures become stiffer when a domain wall arises and the two opposite phases interact.

Moreover, in Fig. 4.5(a) we compare the stress-strain curves predicted by our analytical model with those numerically calculated and the ones measured experimentally in 21×21 structures with (i) no defects (green line) and (ii) eight phase-inducing defects arranged as in Figs. 4.5(b) and (c) (magenta line). The good agreement between all set of data shows that our analytical model has potential to complement numerical tools for the design of systems with a targeted mechanical response. In its current form the model can only capture the response of systems with a single

domain wall. However, we show in Fig. 4.5(b) that this stiffening effect can be amplified by the interactions of multiple domain walls. Therefore our future work will aim at improving the current analytical model to predict more complex scenarios with multiple domain walls.

Next, we study the effect of the domain walls on the propagation of small amplitude elastic waves. To this end, we consider a metamaterial with alternating light (with mass m) and heavy (with mass $3m/2$) squares and numerically calculate its dispersion relations as a function of θ_{st} , assuming a state of homogeneous deformation (Fig. 4.5(d) and section C.3.6). We find that for $\theta = 0$ (i.e. for unrotated squares) a complete band gap exists at frequency $f = 3293 - 3674$ Hz (highlighted as the grey-shaded area in Fig. 4.5(c)), so that waves within this frequency range are not expected to propagate in the system. However, as the rotation of the squares is increased, this band gap shifts to a lower frequency range ($f = 2652 - 2941$ Hz - see Figs. 4.5(c) and (d)). Importantly, since $|\theta| \sim 0$ within the domain wall and $|\theta| > 0$ in the surrounding compressed medium, such shifting can be harnessed to guide elastic waves along the paths defined by the domain walls. Our analytical model can be used to predict the width of the propagating channels, w_{channel} , at a given frequency f . To demonstrate this, we focus on $f = 2800$ Hz - a frequency for which waves can propagate only if $-0.25 < \theta < 0.25$ (Fig. 4.5(d)). In Fig. 4.5(e) we report the evolution of θ predicted by Eq. (4.12) along the y -direction for a 21×21 sample at three different deformation levels $\varepsilon_{\text{applied}}^{yy} = 0\%$, -4% and -8% . The width of the propagating channels can be easily determined by identifying the region in which $-0.25 < \theta < 0.25$. For this specific case we find that $w_{\text{channel}} = 21a$ (entire structure), $8.0a$ and $5.5a$ at $\varepsilon_{\text{applied}}^{yy} = 0$, -4% and -8% , respectively. Next, to verify these predictions, we report the eigenmodes associated to the frequency of $f \sim 2800$ kHz at $\varepsilon_{\text{applied}}^{yy} = 0$, -4% and -8% for a system with defects arranged to form a horizontal domain

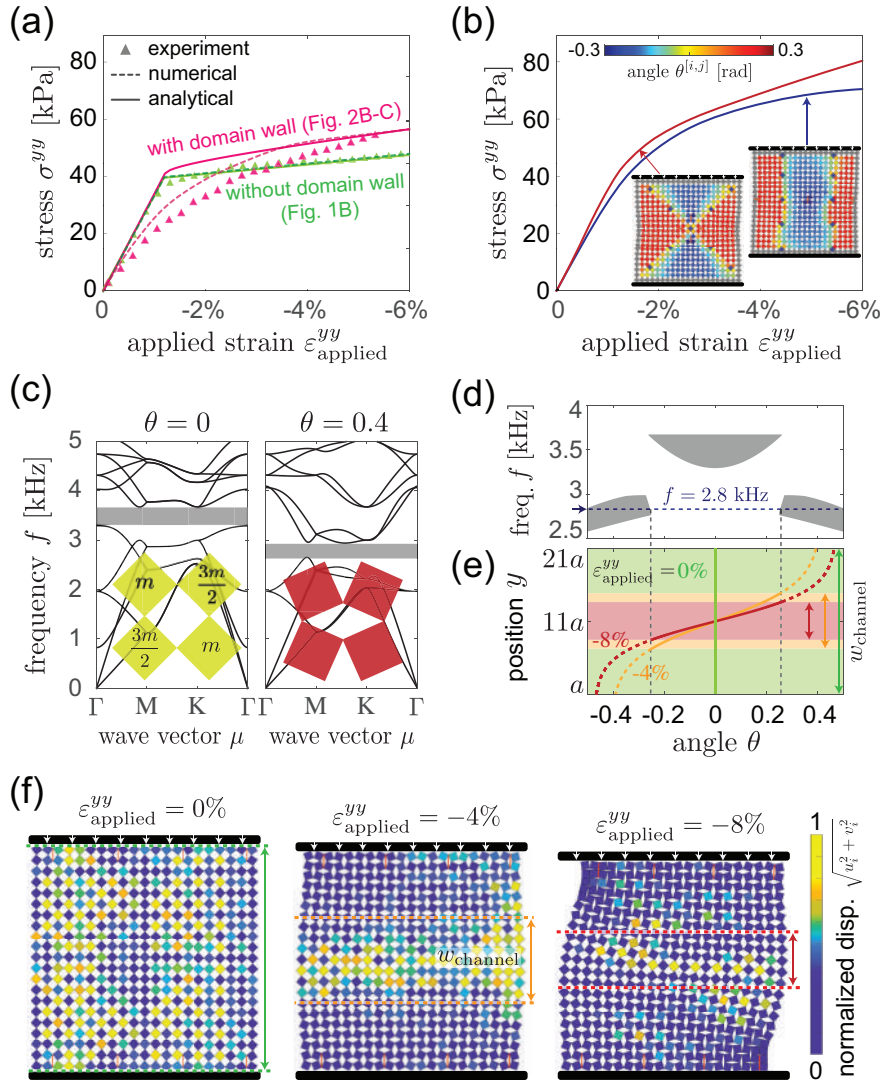


Figure 4.5: Potential applications of domain walls in mechanical metamaterials. (a) Experimentally measured (markers), numerically calculated (dashed lines) and theoretically predicted (solid lines) stress-strain curves for 21×21 structures without domain wall and with a horizontal domain wall. Note that the numerical and analytical predictions for the structure without domain wall match perfectly, so that the green solid and dashed lines overlap. (b) Numerically calculated stress-strain curve for 21×21 structures with two vertical domain walls (blue line) and two perpendicular domain walls at $\varphi = \pi/4$ (red line). The corresponding deformations are shown as insets. (c) Dispersion relations for planar elastic waves in the undeformed ($\theta = 0$) and compressed ($\theta = 0.4$) configurations. (d) Evolution of the band gap frequency, f , as a function of the squares rotation θ . (e) Evolution of θ along the y -direction for a 21×21 sample with an horizontal domain wall at $\varepsilon_{\text{applied}}^{yy} = 0\%$, -4% and -8% . (f) Modal displacement fields at $\varepsilon_{\text{applied}}^{yy} = 0\%$ ($f = 2811$ Hz), -4% ($f = 2812$ Hz) and -8% ($f = 2779$ Hz).

wall (Fig. 4.5(f) and (section C.3.6)). As predicted by our continuum model, we find that, when the system is undeformed (i.e. for $\varepsilon_{\text{applied}}^{yy} = 0\%$), the vibrations are spread through the entire structure.

Differently, at $\varepsilon_{\text{applied}}^{yy} = -4\%$ and -8% they are confined near the domain wall, in a prescribed region. Importantly, the width of this region is very close to the one predicted by our analytical model w_{channel} . As such, our results indicate that domain walls generated by localized defects can be exploited to tune global properties of the system such as stiffness and wave guiding and that our analytical model can be leveraged to guide the design of functional systems.

4.9 Conclusions

To summarize, we have shown that in a rotating-squares based mechanical metamaterial domain walls across which the rotation of the squares varies from positive to negative values can be formed by carefully arranging a few phase-inducing defects that control the nucleation of the two rotated buckling-induced phases. We have established an analytical model that explicitly describes the spatial profile of the domain walls for different orientations and predicts their evolution as a function of the applied deformation. Further, guided by this model, we have shown that domain walls of arbitrary shapes can be engineered by introducing a few pinning defects to modify the energy landscape of the structure. Importantly, since the considered defects can be easily placed and removed (the deformation is purely elastic), our platform can be used to efficiently explore how the shape and orientation of the emerging domain walls affect the mechanical properties of the material. Moreover, our study indicates that the metamaterial creates long range interactions between the local defects, which may generate domain walls and ultimately affect the material's global mechanical properties. We envision the exploitation of domain walls in order to encode new modes of functionality in mechanical systems, including information encryption, stiffness tuning and wave guiding.

Chapter 5

Liquid-induced Topological Transformations of Cellular Microstructures

By: Shucong Li*, Bolei Deng*, Alison Grinthal, Alyssha Schneider-Yamamura, Jinliang Kang, Reese S. Martens, Cathy T. Zhang, Jian Li, Siqin Yu, Katia Bertoldi, Joanna Aizenberg. Published in *Nature*, on Apr. 14 2021. **doi:10.1038/s41586-021-03404-7**

5.1 Abstract

The fundamental topology of cellular structures—the location, number, and connectivity of nodes and compartments—can profoundly impact their acoustic^[68–71], electrical^[72], chemical^[73,74], mechanical^[75,76], and optical^[77] properties, as well as heat^[68,78], fluid^[79,80] and particle transport^[81]. Approaches harnessing swelling^[4,64], electromagnetic^[5,65] actuation as well as mechanical instabilities in cellular materials^[26,66,67] have enabled a variety of interesting wall deformations and compartment shape alterations, but the resulting structures generally preserve the defining connectivity features of the initial topology. Achieving topological transformation presents a distinct challenge for existing strategies: it requires complex reorganization, repacking, and coordinated bending, stretching, and folding, particularly around each node where elastic resistance is highest due to connectivity. Here we introduce a two-tiered dynamic strategy to achieve systematic reversible transformations of the fundamental topology of cellular microstructures that can be applied to a wide range of material compositions and geometries. Our approach only requires exposing the structure to a liquid whose composition is selected to have the ability to first infiltrate and soften the material at the molecular scale, and then, upon evaporation, to form a network of localized capillary forces at the architectural scale that zip the edges of the softened lattice into a new topological structure, which subsequently re-stiffens and remains kinetically trapped. Reversibility is induced by applying a mixture of liquids separately acting at the molecular and architectural scales—thus offering modular temporal control over the sequence of the softening-evaporation-stiffening actions—restoring the original topology or providing access to intermediate modes. Guided by a generalized theoretical model connecting cellular geometries, material stiffness and capillary forces, we demonstrate programmed reversible topological transformations of various lattice geometries

and responsive materials, undergoing fast global or localized deformations. We then harness dynamic topologies for developing active surfaces with information encryption, selective particle trapping and bubble release, and tunable mechanical, chemical and acoustic properties.

5.2 Introduction

Liquid during evaporation has been shown to deform and assemble simple, isolated microscale structures, such as arrays of base-attached pillars and plates, via the capillary forces of the formed liquid/vapor menisci^[131–134]. We anticipated that when a liquid is applied to a cellular structure, the formation of a complex network of menisci on the interconnected geometry generates an intricate localized force field centered at each node, providing a finer level of control than can be achieved with global force fields^[5,65]. However, as a base-attached interconnected structure, a cellular lattice generally requires much higher energy to deform compared to simple bending in the isolated structures, usually making capillary forces too weak for such transitions. Though the capillarity-induced reconfiguration could potentially be enabled by using a floppy material with low elastic restoring energy^[135] and high surface adhesion^[133,136,137] to maintain the assembly, such systems are impractical for most applications. This apparent paradox can be potentially solved by a transient softening of polymeric materials. It has been shown that certain liquids are able to infiltrate and soften polymeric materials at the molecular scale, thus altering their bulk mechanical properties^[138–143].

5.3 A Two-tiered Dynamic Strategy

Based on the latter considerations, we introduce a novel strategy to achieve fast, reversible, and tunable topological transformation of cellular microstructures through capillary assembly that is broadly applicable to a wide range of geometries and materials. The key concept is for the applied liquid to not only form menisci at the architectural (micro)scale, as generally occurs in evaporation-induced assembly^{23–26} (Fig. 5.1(a)), but first to transiently infiltrate, swell and soften the material (Fig. 5.1(b)). Critically, as the liquid begins to evaporate from inside the compartments, capillary forces are exerted on the softened structure, acting locally at each individual node and zipping the edges together in a coordinated manner. This leads to a change in the connectivity of the original nodes or to their disappearance and creation of new nodes, while also changing the number and coordination of compartments, resulting in transformation to a new lattice topology. Finally, as the liquid rapidly evaporates from inside the material at the molecular scale, the dried structure regains its stiffness and the new geometry remains trapped (Fig. 5.1(b)).

$$E_{cr} = \frac{6\gamma l \sec \frac{\alpha}{2}}{3lb \left(\sec \frac{\alpha}{2} - 1 - \delta \right)^2 + ab^2(1 + \delta)^2} \quad (5.1)$$

where δ is the swelling ratio of the material by the liquid and γ is the surface tension of the liquid. E_{cr} provides an upper limit for the material stiffness above which the transformation will not occur. In Fig. 5.1d, we present the evolution of E_{cr} as a function of the angle α and wall thickness b (varying from 5 μm to 500 μm) for structures with a constant slenderness ratio $l/b = 15$ and $\gamma = 25 \times 10^{-3} \text{ N/m}$ (for typical volatile liquids, such as acetone). According to the contour plot, E_{cr} decreases drastically down to a few kPa with increasing (b) indicating that the smallest dimensions (i.e., wall thickness b) of the considered structure must stay within the micron scale for reasonable

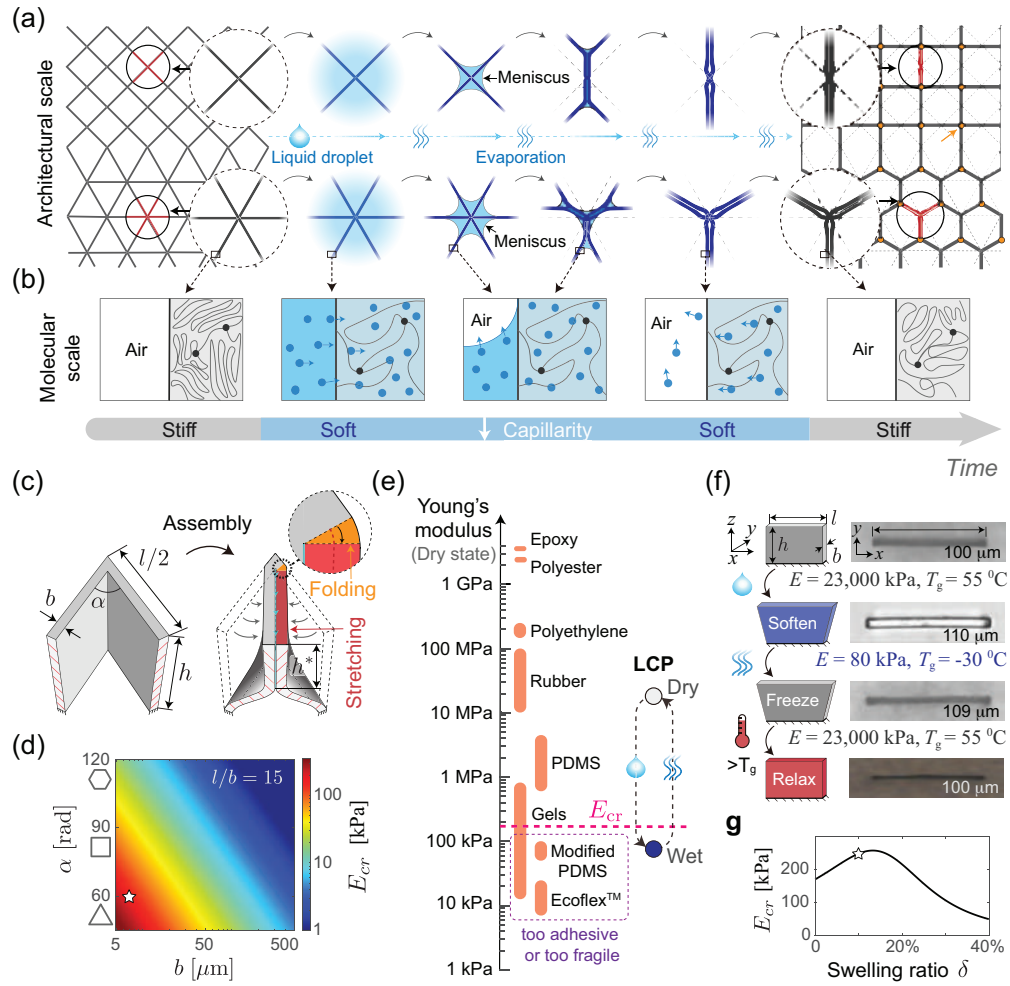


Figure 5.1: Strategy for topological transformation of cellular structures. (a-b), Schematic illustration of topological transformation occurring at the architectural scale during liquid immersion and evaporation (a), and corresponding changes in the polymer network at the molecular scale (b). Since the liquid in the compartments evaporates prior to that inside the polymer network, the capillary forces introduced at the air-liquid interface always act on the softened structure, enabling the structure to deform, and the edges to be zipped together. This results in the formation of new nodes (shown in orange and indicated by orange arrow on the right), and in the disappearance or change in connectivity of the original nodes (shown in red). (c) Schematics of the assembly of two adjacent walls from a cellular structure characterized by angle α , edge length l , thickness b and height h . The walls are stretched and folded by the capillary forces.(d) Contour plot of critical Young's modulus E_{cr} with respect to structural parameters α and b while the slenderness ratio is fixed as $l/b = 15$. The star marker denotes the corresponding parameters of the considered structure.(e) A list of commonly used polymeric materials and their Young's moduli in a dry state. In particular, the Young's modulus of a liquid crystalline polymer (LCP) changes reversibly from 23,000 kPa in the dry state to 80kPa in the wet state.(f) Micrographs of an LCP microplate with dimensions $l = 100 \mu\text{m}$, $b = 7 \mu\text{m}$ and $h = 70 \mu\text{m}$ after exposure to acetone.(g) Critical modulus E_{cr} as a function of swelling ratio δ . The star marker represents the swelling ratio of the selected material.

material stiffness. Moreover, E_{cr} also decreases with increasing angle α showing that structures with larger angles, such as square and hexagonal lattices, are much more difficult to transform than those with smaller angles.

While our model can predict the assembly behavior of a wide range of cellular architectures (Fig. D.2), we selected a triangular ($\alpha = 60^\circ$) micro-cellular structure with dimensions $l = 100 \mu\text{m}$, $b = 7 \mu\text{m}$ and $h = 70 \mu\text{m}$ as an initial experimental test case. For such a structure, Eq. (1) provides a critical modulus $E_{cr} \approx 175 \text{ kPa}$, which is much lower than that of most commonly used polymers, such as PDMS, rubber, polyethylene, or epoxy (Fig. 5.1(e)). Though there exist soft materials with Young's modulus below the E_{cr} , such as Ecoflex or PDMS with low crosslinking density²⁸, bottle-brush PDMS²⁷, or hydrogels³⁸, they are normally either too sticky or too fragile to be compatible with the molding fabrication procedure of high-aspect-ratio microstructures, and commonly undergo permanent distortion after demolding or irreversible collapse (Fig. D.3). In contrast, the transient solvent-induced softening allows topological transformation to be extended to high-Young's-modulus polymers that can be easily molded, temporarily softened during assembly, and re-stiffened after evaporation. Key features in selecting a polymer-solvent pair suitable for topological transformation are the solubility, volatility and Flory-Huggins parameters^[138–140,142], which describe the ability of the solvent to swell and soften the elastic network below E_{cr} , while high volatility allows for fast transformation. In addition, the properties of the polymer matrix, including the chemical nature, crosslinking density, crystallization (molecular packing/physical crosslinking), porosity, and chain topology^[141,143] can be leveraged to modify the solvent-polymer interaction.

As a representative material, a polydomain liquid crystalline polymer (LCP) with an initial modulus of $\approx 23,000 \text{ kPa}$ in the dry state (far above E_{cr}) was selected as a model system (Fig. 5.1(e))

and Fig. D.4a). To focus on the material properties of the LCP during the liquid treatment while eliminating complex assembly behavior, an isolated base-attached LCP microplate was fabricated with the same dimensions as an edge of the considered lattice structure ($l = 100 \mu\text{m}$, $h = 70 \mu\text{m}$ and $b = 7 \mu\text{m}$) to assure comparable dynamics and kinetics of evaporation (see Fig. 5.1(f)). When the plate is swelled by the wetting liquid acetone—a good solvent of the LCP, with a vapor pressure of 57.3 kPa at 25 °C—the solvent molecules penetrate into the polymer matrix, break the packing of the polymer chains, and plasticize the material^[142,144], reducing T_g from 58 °C to –30 °C and softening the material drastically down to ≈ 80 kPa (Fig. D.5), while also swelling the plate to a 10% strain along the length of the top edge. Upon fast evaporation (within seconds when 50 μL is applied to a 1cm² sample under ambient conditions), T_g returns to 58 °C as the material returns to its original stiffness of $\approx 23,000\text{kPa}$ and the dried plate is kinetically trapped with a 9% strain in the dry glassy state at room temperature—the extended conformation of polymer chains in the swollen state is locked due to the fast evaporation of liquid in the microscopic system^[145,146]. The plate is also capable of relaxing back to the initial length when heated above T_g as the polymer chains return to the original conformation (Fig. 5.1(f), Supplementary Video 10). According to our theoretical model, such swelling of the material facilitates assembly as it compensates for the required stretching of the walls, and trapping plays a critical role in maintaining the assembly after the capillary force ceases (Fig. 5.1(g)). Trapping is expected to occur for materials that have a dry-state T_g that is higher than the ambient temperature. Without this effect, an approximate adhesion energy of 3.3 J/m² would be required to hold the re-stiffened structure together (section D.2.3), which is much higher than the adhesion energy of commonly used materials^[147,148].

5.4 Liquid-induced Topological Transformations

To test our strategy, the triangular cellular microstructure was molded from LCP by soft lithography (Fig. 5.2(a)). Droplets of acetone ($\sim 50 \mu\text{L}$ for a $\sim 1 \text{ cm}^2$ sample) were placed on horizontal substrates to immerse the cellular structure and allowed to evaporate under ambient conditions (for a systematic study of other liquids see Fig. D.6). After evaporation, the upper portion of the triangular lattice was transformed to hexagonal, with triangular geometry retained at the base (Fig. 5.2(b)). The transformation results in the change of the fundamental topology of the microstructure: the node connectivity changes from six to three, the number of compartments is halved and the number of nodes and size of compartments are doubled. Additionally, according to optical 3D surface profilometry (Fig. 5.2(c), Fig. D.7), the initial 2D lattice becomes a true 3D structure with a non-planar top surface after the assembly, due to the formation of enclosures and a more complex height profile, as the new nodes formed by the inward bending plates are $10 \mu\text{m}$ shorter than the original nodes.

The dynamics of the assembly process was monitored by fluorescent confocal microscopy (Fig. 5.2(d), Supplementary Video 11): The liquid first swells the material leading to a buckled configuration of the lattice ($t = 3 \text{ s}$) and forms menisci upon evaporation where the localized capillary forces break the symmetry of each node ($t = 8 \text{ s}$); the menisci, compatible with complex and evolving geometries, further zip up the buckled walls and ultimately transform node connectivity from six to three ($t = 9 \text{ s}$); due to the integrity of the cellular structure and the continuous evaporation line, neighboring nodes transform coordinately, forming ordered domains (Fig. D.8); Finally, as the material deswells, the structure is locked in the hexagonal topology with straightened double-walls ($t = 12 \text{ s}$). Both trapping of the material and adhesion between the assembled

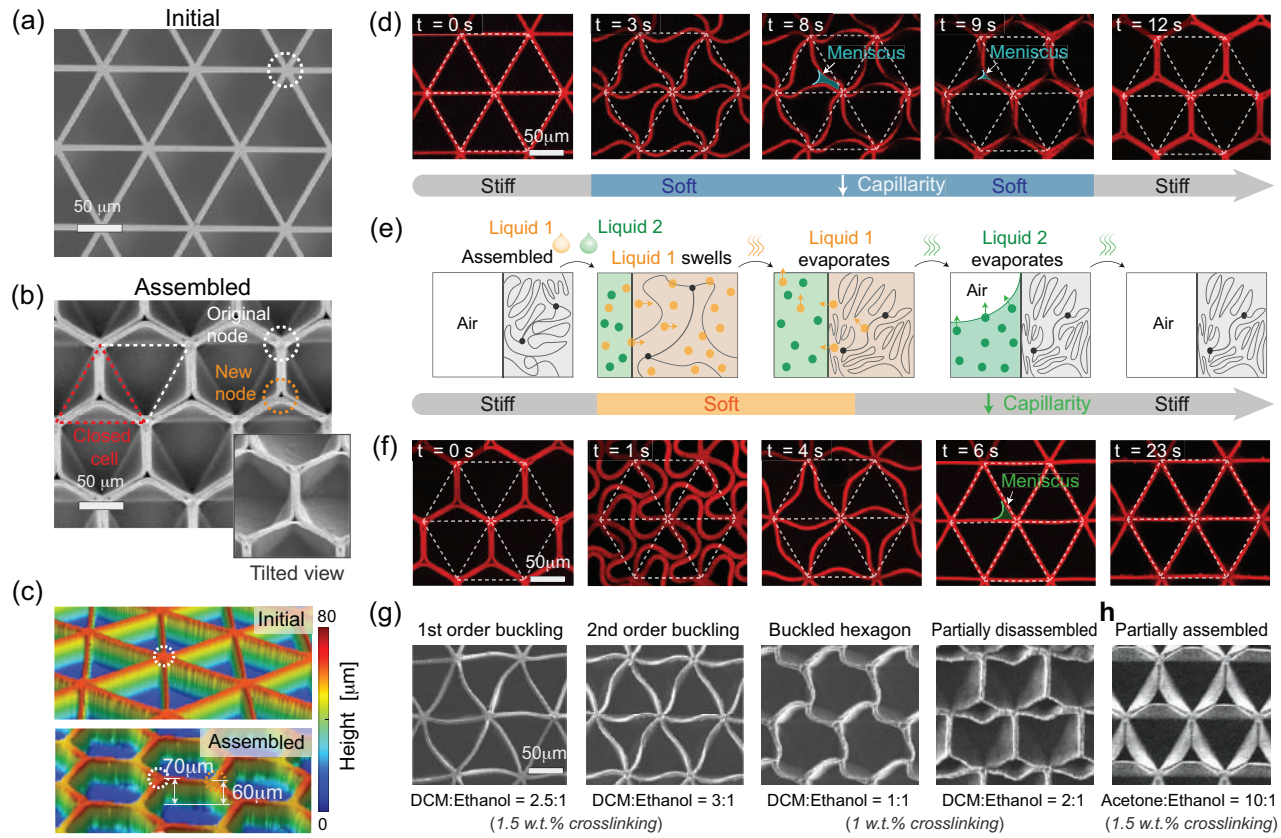


Figure 5.2: Experimental characterization of the assembly and disassembly of a triangular lattice. (a) Top view of the initial triangular micro-cellular structure imaged by scanning electron microscope (SEM). (b) Top and tilted views of the assembled micro-cellular structure. The initial triangular lattice is transformed to a hexagonal lattice upon application of an acetone droplet. One of the new nodes is marked with an orange circle, and one of the original nodes with a white circle. (c) Profilometer 3D surface topography of the initial (top) and assembled microstructure (bottom). While the top surface of the original structure is planar, the assembled structure contains nodes of two different heights due to the deformation of the walls. (d) Fluorescence confocal (FC) images of the microstructures at different stages of the assembly. Rhodamine B was co-polymerized into the polymer for characterization by FC microscopy. (e) Schematic representation of the generalized mechanism of the disassembly process showing how the mixture of two different liquids decouples the two scales, with one, highly volatile liquid, acting at the molecular scale and another, chemically inert, less volatile liquid, returning the structure to its original state at the micron scale. (f) Fluorescence confocal images of the LCP microstructures at different stages during the disassembly induced by the DCM:ethanol mixture at 2:1 ratio, with DCM swelling the assembled structure significantly to disassociate the assembled walls, and ethanol exerting capillary forces on a stiffened structure after evaporation of DCM. (g) Selective trapping of intermediate stages by tuning the evaporation kinetics (imaged by SEM) using different solvent concentrations and polymer compositions. All the presented structures are transformed from the assembled hexagonal lattice. (h) Partial topological transformation of the initial triangular lattice into a hierarchical triangular lattice with two compartment sizes using a mixture of acetone and ethanol.

walls contribute to retaining the new topology, which remains robust under harsh conditions, including heating above T_g or immersing in various non-swelling liquids for several days (Fig. D.9,

Supplementary Video 12).

5.5 Reverse Transformations and Modular Control

Disassembling the structure and restoring the original topology requires overcoming both the kinetic trapping of the polymer conformation and the interfacial adhesion between the walls. Although heat or plasticizers can untrap the material, they also tend to decrease the elastic restoring force. However, both requirements can be fulfilled simultaneously by applying a liquid that softens and swells the underlying material with a much greater swelling ratio than that of the liquid used for the assembly, to trigger drastic bending of the assembled walls. Since the bending energy of a double-wall is much higher than that of two single walls, such swelling-induced bending would rapidly disassociate the walls, overcoming the adhesion and initiating disassembly. However, as the liquid evaporates, the formed menisci would re-assemble the structure, counteracting the disassembly process. To reduce capillary forces, a second liquid—less volatile but non-swelling—is mixed with the first to delay any capillary forces until after the material has finished disassembling and become stiff again (Fig. 5.2(e)). To demonstrate this unique disassembly mechanism experimentally, we used a mixture of dichloromethane (DCM)—a good solvent of the LCP that swells the LCP substantially (with > 30% strain)—as the first volatile liquid (vapor pressure of 57.3 kPa, 25 °C), and ethanol—a poor solvent of the LCP—as the second, less volatile liquid (vapor pressure of 5.59 kPa, 20 °C) (Fig. 5.2(f) and Supplementary Video 13). Compared to the assembly process, where a single liquid both softens the material at the molecular scale and generates capillary forces at the architectural scale, the mixture enables modular control over the timescales of the two actions, with DCM controlling the molecular scale and ethanol governing the architectural

scale separately and consecutively to yield desired outcomes.

In addition to restoring the original triangular structure, such modular control enables trapping of a series of intermediate states during disassembly by varying the ratios of the DCM-ethanol mixture (Fig. 5.2(g)). The ratio of DCM to ethanol affects both the swelling extent of the LCP and the volatility of DCM when dispersed in ethanol, and thus the trapping strain and modes of disassembly. Similar concepts can also be used to tailor the original assembly process. For example, Figure 2h shows that partial assembly of the triangular lattice can be achieved by adding to acetone a trace amount of ethanol, which diminishes the softening effect and increases the elastic restoring energy during assembly. Notably, assembly and disassembly processes take only seconds and are highly reversible and fatigue-free (Fig. D.10), enabling a durable and fast switching between different topologies.

5.6 Generalization of the strategy

The methodology can be generalized to different geometries with more complex symmetries, anisotropies, and combinations of compartment shapes and sizes. An arbitrary lattice can be considered a combination of nodes connected to edges that form different angles, with the capillary forces preferentially assembling edge pairs with smaller angles (Fig. 5.3(a)). Based on this principle, we designed and experimentally tested a variety of cellular structures undergoing programmed, robust topological transitions (Fig. 5.3(a) and Fig. D.11). The approach is also readily applicable to structures with different dimensions and to other polymeric materials (Fig. D.12-13). It can also be integrated with orthogonal response mechanisms to enable multimodal transformations of a given structure upon application of different triggers. For example, LCPs can be imprinted with anisotropic ther-

mal responses by aligning the LC molecules inside the cellular structures into a nematic liquid crystalline phase (Fig. D.13b)^[149,150]. Figure 3b presents an exemplary diamond lattice with the LC director aligned perpendicular to the base⁴⁶ that is transformed to a hexagonal lattice via capillary assembly, and then to a brick pattern through its thermal nematic-to-isotropic ($> T_{NI}$) phase transition (Supplementary Video 14). We further note that the presented strategy is applicable to any 2D or 3D geometries including base-attached or free-standing (see Fig. D.14). Here we intentionally choose a rigid base-attached configuration for its better structural stability, applicability to any lattice geometry, and the ability to form closed cavities upon topological transformation—a unique compartmentalization feature explored in applications below. Moreover, benefiting from the localized capillary force fields and the compartmentalized nature of the cellular structure, we demonstrate interesting region-specific assembly-disassembly transformations through the application of small droplets locally—another property unachievable with global fields (Fig. 5.3(c-d), Fig. D.15).

5.7 Applications

By carefully programming the spatial distribution of angular perturbations at each node, we can eliminate or engineer the location of domain boundaries in assembled structures at will (section D.3.8, Fig. D.16-17 and Supplementary Video 15). Considering the large triangular lattice shown in Fig. 5.4(a), the nodes inside the magenta region are designed to transition to Y-shaped (phase I) and the nodes inside the orange region are programmed to transition to inverted Y-shaped (phase II). The written-in phase information is not optically visible before assembly and becomes evident only after solvent treatment (Fig. 5.4(a), and Fig. D.17). The information encryption and read-out

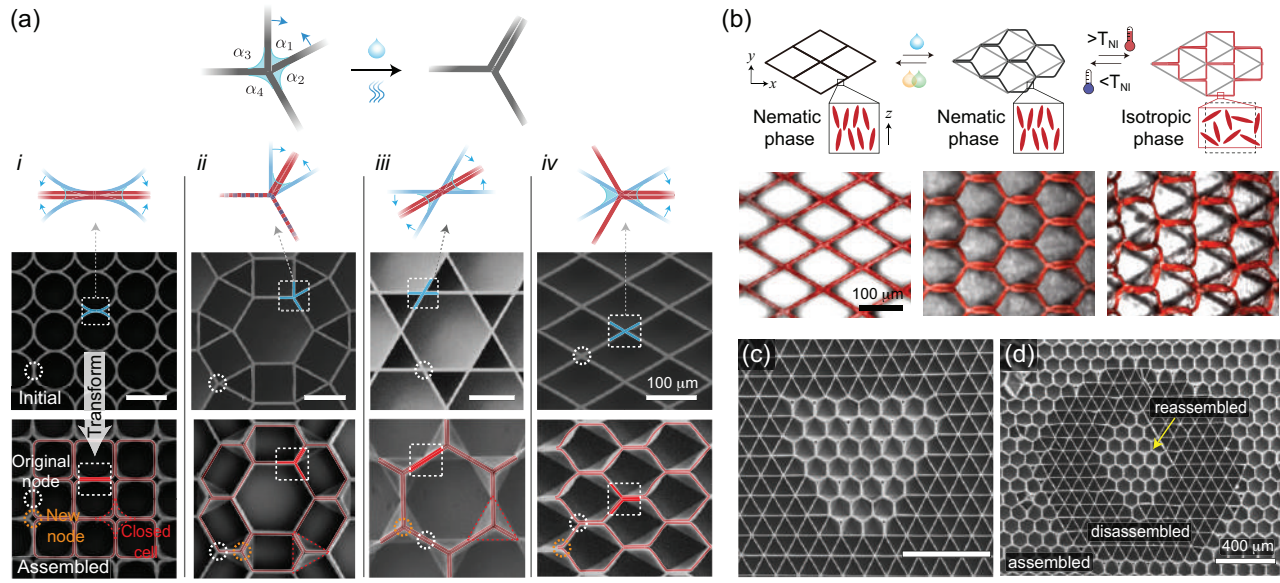


Figure 5.3: Generalization of topological transformation principle. (a) Generalized lattice consists of nodes with different angles. The edges forming the smallest angle will undergo zipping for angle-guided capillary-driven transformations from: i, Circular to square, ii, Rhombitrihexagonal to hybrid hexagonal, iii, Kagome to hexagonal and iv, Rhombus to hexagonal. Note that compared to the triangular-transformed and kagome-transformed hexagonal lattices, which are comprised of nodes connecting three equal double-walls, nodes in the hexagonal lattice assembled from the diamond structure comprise two single walls and one double wall – resulting in additional anisotropy along the horizontal direction. (b) Multi-stimuli deformation of molecularly aligned LCP diamond-shaped cellular structures with director oriented along the z-axis. (c-d), Regional triangular-hexagonal transformations through localized multi-step assembly-disassembly.

can be reversed by treating the LCP microstructure with different solvent systems as discussed previously. Note that the location information of the designed phase boundaries is not merely stored on the phase boundaries but encoded in every node of the structure via their preferred phase, which makes such information encryption extremely robust.

Topological changes of the cellular surfaces—such as the closure of subsets of compartments and ability to induce global or localized transformations—provide opportunities for a number of unprecedented applications. As shown in Fig. 5.4(b), the cellular surface can selectively trap and sort microparticles with diameters $<50 \mu\text{m}$ that are able to enter the initially triangular compartment. Furthermore, the closed chambers also create ordered cavities that each capture and release uniform microscale bubbles upon assembly-disassembly (Fig. 5.4(c), Supplementary Video 16)

that can be used as miniaturized chemical reaction chambers. The resilience of the cellular surface also changes significantly after the topological transformation, as demonstrated by ball-bouncing test results (Fig. 5.4(d), Supplementary Video 16). Compared to the uniform or buckled triangular structure displaying broken walls upon impact, the transformed hexagonal surface exhibits larger craters with no detectable structural damage. We believe that the formed closed chambers constitute a cushion layer and offer extra structural flexibility, which increases the efficiency in absorbing the impact energy.

The change of geometry combined with the formation of double-walls also serves as a platform for tunable phononic crystals, where the bandgaps and propagation velocity of elastic waves can be altered reversibly (Fig. 5.4(e)). As noted above, the 3D height profile of the structure is also changed through edge assembly and node formation (Fig. 5.2(c)), giving rise to modified surface planarity and anisotropy that affect surface properties such as wetting and friction (Fig. 5.4(f)), and both surface properties can be further changed by localized, areal topological transformations. For example, the surface becomes much more adhesive to water droplets when transformed from a triangular to a non-planar hexagonal lattice (Supplementary Video 16), which can most likely be attributed to the pinning points that are created when new nodes form, and the overall elongation of walls that causes the water-polymer contact area to increase slightly. Moreover, anisotropic, directional wetting properties can be achieved through a diamond-to-hexagon transformation in which the initial diamond lattice shows an isotropic wetting along the x-axis, but after assembly the sliding angle toward the left is much higher ($> 90^\circ$, pinned) than toward the right ($\approx 34^\circ$). This can be explained by the asymmetric tetrahedral containers formed by the slanted walls that pin the left-traveling droplet to the surface. Similarly, the friction coefficient of the cellular surface is also tunable via topological transformations (Fig. 5.4(g)).

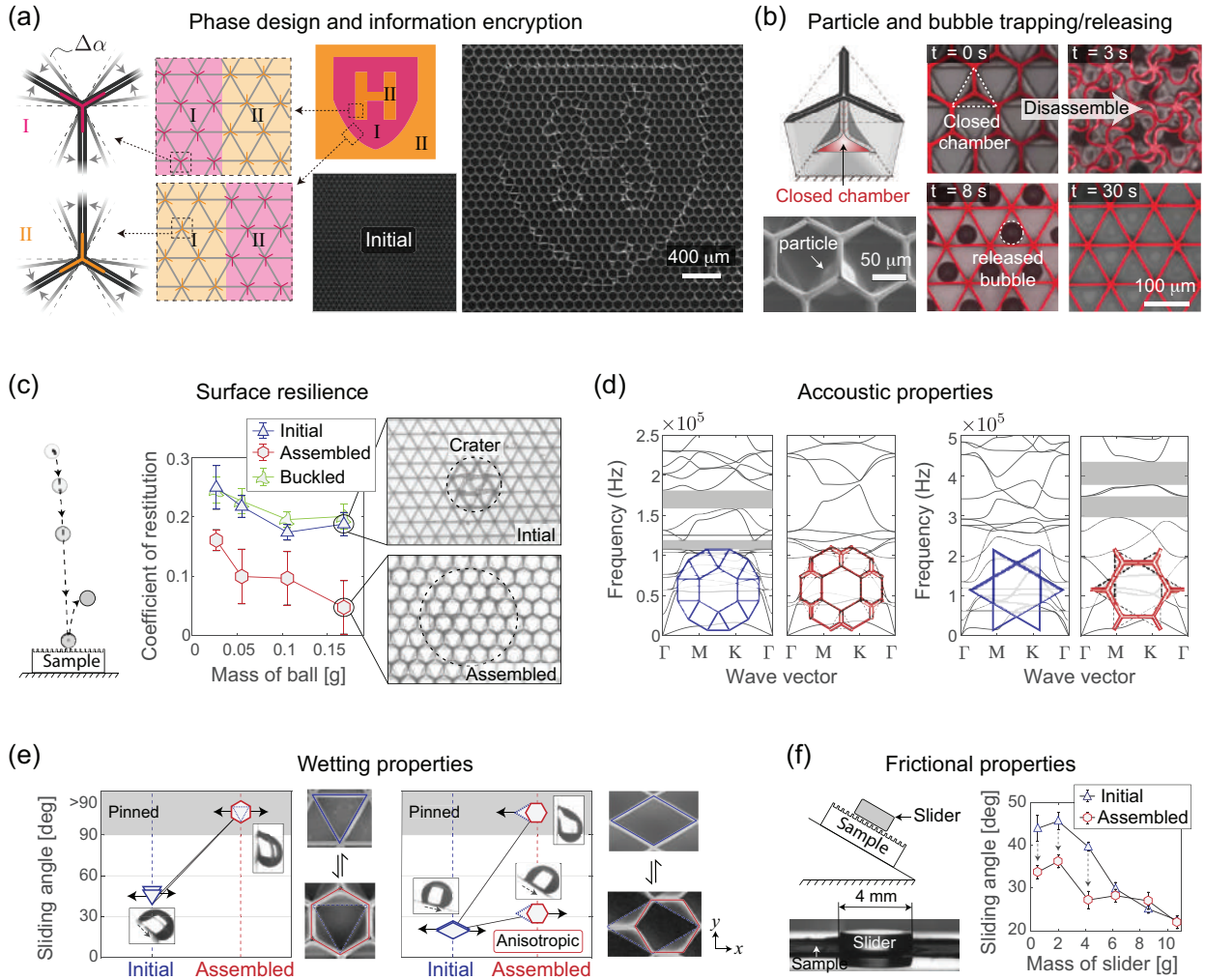


Figure 5.4: Exemplary applications of lattice structures undergoing topological transformations. (a) Information encryption. Heart shape and Harvard shield outlined by the phase boundaries appear upon topological transformation of the triangular lattice. The shape and location of phase boundaries are designed by manipulating the distribution of the initial angular perturbations, with the nodes in the pink regions encrypted to transform to a "Y" shape and nodes in the orange regions to transform to an inverted "Y" (shown schematically on the left). (b) Particle and bubble trapping/releasing through the closed chambers formed by topological transformation. (c) Ball bouncing test to measure the resilience of the surface before and after transformation. Note that the topological transformation is necessary to change the coefficient of restitution, as simply-buckled and undeformed structures show the same resilience. (d) Bandgaps at a particular frequency can be tuned by capillarity-driven assembly for some lattices. Examples for bandgaps in rhombitrihexagonal and Kagome lattices are shown. (e-f), Controlling surface properties upon topological transformations: (e) Wetting; (f) Friction.

5.8 Conclusions

In conclusion, we have presented a simple, widely applicable strategy that gives rise to complex topological transformations of cellular structures. The defining feature of our approach is that the applied liquid plays dual roles by acting at two scales: it transiently softens and swells the material at the molecular level and creates an intricate network of localized capillary forces at the architectural scale; and these actions at two scales take place in a sequentially controlled manner. Modular control over the timing and extent of the softening/re-stiffening/evaporation events through customized polymer-liquid pairs enables the reversibility and switching between various intermediate topologies. Our theoretical model provides a quantitative foundation for rationally guiding the materials selection and the structural design. Compared to existing reconfiguration methods—that produce buckling or shearing deformations without controllable topological changes^[5,26,64–66], are often either irreversible or unable to hold the reconfigured shape without external stimuli^[64,65], or require complex material compositions, sophisticated and costly fabrication procedures not applicable at the microscale^[4,5,65], and long response times^[5,64], our strategy enables extremely fast, robust and reversible topological transformations and is compatible with a simple molding fabrication procedure. The demonstrated applications can be integrated with localized transformations, phase boundary design, and active materials responding to orthogonal stimuli, to control functional properties across different scales and application fields. In principle, our strategy can be applied to nanoscale structures and will open avenues for designing tunable photonic meta-surfaces where the topology plays a key role. The opportunities offered by this strategy to systematically manipulate the topological transformation provide a platform for fundamental study of the topology-dimension-material relation and the underlying multiscale physico-chemical mechanisms.

Chapter 6

Conclusions

This dissertation investigates two exciting aspects of flexMMs: the propagation of solitary waves and phase transitions. Motivated by experimental observations, we used a combination of numerical simulations and theoretical analyses to understand the physics of these two phenomena and exploit them to achieve new functionalities.

I close this dissertation by identifying several challenges for future work.

New flexMM designs. So far, the nonlinear dynamic response of a limited number of flexMM designs has been investigated. FlexMM based on origami, kirigami, tensegrity structures, and rotating-units other than squares (e.g. triangles or hexagons) may provide additional opportunities to manipulate the propagation of nonlinear waves. Also, the nonlinear dynamic responses of three-dimensional architectures remain largely unexplored, and may open new avenues for wave management.

Going beyond periodic systems. While most previous studies have focused on the propagation of nonlinear pulses in periodic and homogeneous structures, new opportunities may arise when investigating the interactions of large-amplitude waves with free surfaces, inhomogeneous structures, and sharp interfaces. How do the nonlinear pulses propagate along free surfaces? What is the effect of internal interfaces on soliton propagation? How do other spatial variations such as gradients in initial angle, gradients in mass, or gradients in the stiffness of the hinges affect the propagation of waves through the material? Can these be used to steer a beam or otherwise affect an incident plane wave? All these questions remain unanswered.

Targeted nonlinear dynamical responses. While the focus so far has been on the development of tools to predict and characterize the propagating nonlinear waves in flexMM, an important question that is still unanswered is: How should one design the structure, including unit cell geometry, inhomogeneities such as gradients and interfaces, etc., to enable a target dynamic response? Tar-

get dynamic responses may include highly efficient damping for impact mitigation; optimal wave guiding (i.e., optimal energy confinement and propagation along a determined path); and lensing of solitons for optimal energy concentration. To allow the automated design of flexMM architectures that are optimal for achieving a specified set of target dynamic properties, one could couple discrete models with machine learning algorithms, such as neural networks and deep learning.

Control of nonlinear waves on the fly. Since the characteristics (i.e., shape, velocity, and amplitude) of nonlinear waves propagating through FlexMM can be tuned by varying the nonlinear response of the underlying medium, which can be effectively altered by (locally) deforming the metamaterial, we envision that the applied deformation could be a powerful tool to manipulate the pulses. Local deformations applied to the FlexMM could provide a mechanism to change the characteristics as well as the path of the propagating pulses on the fly. This could provide opportunities for time-space modulation of the propagating pulses^[151], real-time control of waves, and tunable non-reciprocal transmission^[152]. Further, since collisions of solitons in flexMM may result in anomalous interactions that provide opportunities to remotely detect, change, or eliminate high-amplitude signals and impacts^[128], we envision the use of collisions to pave new ways toward the advanced control of large amplitude mechanical pulses.

Appendix A

Supplementary Information:

Metamaterials with Amplitude Gaps for Elastic Solitons

By: Bolei Deng, Pai Wang, Qi He, Vincent Tournat, Katia Bertoldi. Published in *Nature Communications*, on Aug. 24 2018. [doi:10.1038/s41467-018-05908-9](https://doi.org/10.1038/s41467-018-05908-9)

A.1 Fabrication

Our system consists of a long chain of 2×50 crosses made of LEGO bricks and connected by thin and flexible hinges made of plastic shims. Two different samples are built: one in which the horizontal hinges are all aligned (see Fig. A.1 and Supplementary Video 1) and another one in which neighboring horizontal hinges are shifted in vertical direction (see Fig. A.2 and Supplementary Video 4). In the following we will refer to the former as the aligned chain and to the latter as the shifted chain.

In the aligned chain each cross-shaped unit is realized using four brackets $2 \times 2-2 \times 2$ (LEGO part 3956), as shown in Fig. A.1. Differently, the cross-shaped units in the shifted sample are realized using three brackets $2 \times 2-2 \times 2$ (LEGO part 3956) and two plates 2×2 (LEGO part 3022), as shown in Fig. A.2. Note that in both samples identical bricks of different colors (black and gray) are used to facilitate visualization of the propagating pulses.

In both samples the hinges are realized by laser cutting the octagonal shape shown in Fig. A.1(a) and Fig. A.2(a) out of polyester plastic sheets (Artus Corporation, NJ - 0.005", Blue) with thickness $t_h = 0.127$ mm, Young's modulus $E = 4.33$ GPa and Poisson's ratio $\nu = 0.4$. The size of the octagonal shape is chosen to leave hinges of length $l_h = 4$ mm between the cross-shaped rigid units. Note that eight circular holes are incorporated into each hinge. They fit into the LEGO knobs and enable us to fix the hinges between the interlocking LEGO bricks (see Fig. A.1(b) and Fig. A.2(b)).

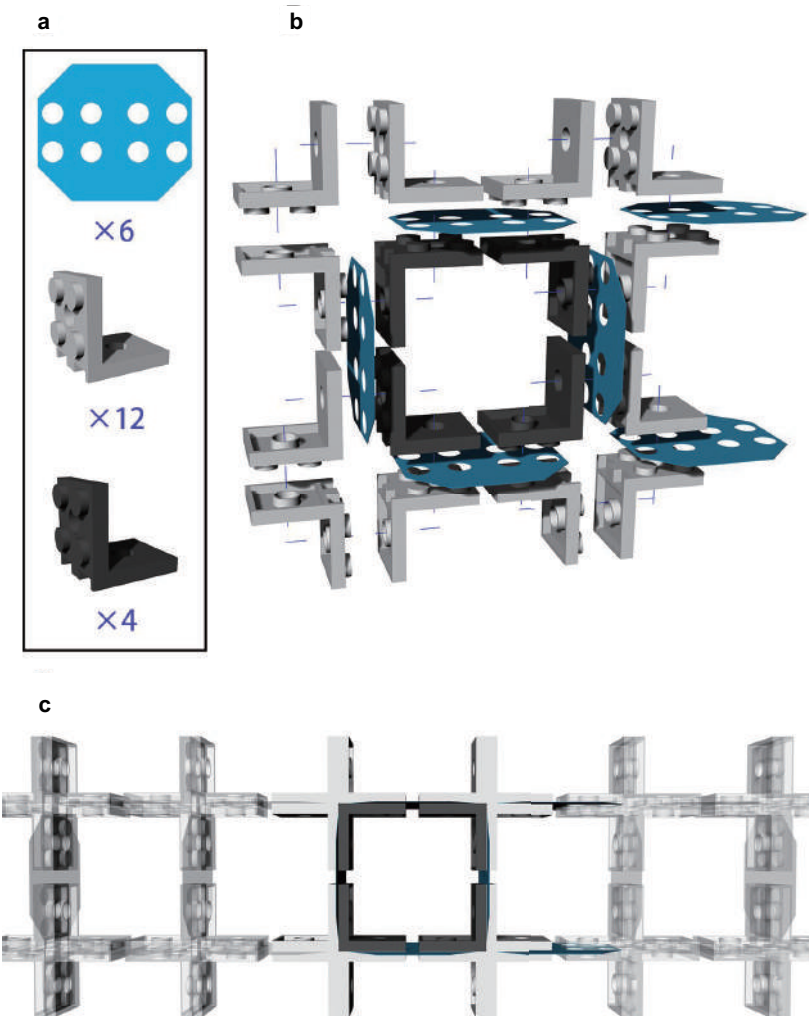


Figure A.1: Fabrication of the aligned chain. (a) Parts used to fabricate the unit cell. (b) Exploded view of the two pairs of crosses. (c) The chain is realized by putting together a number of unit cells.

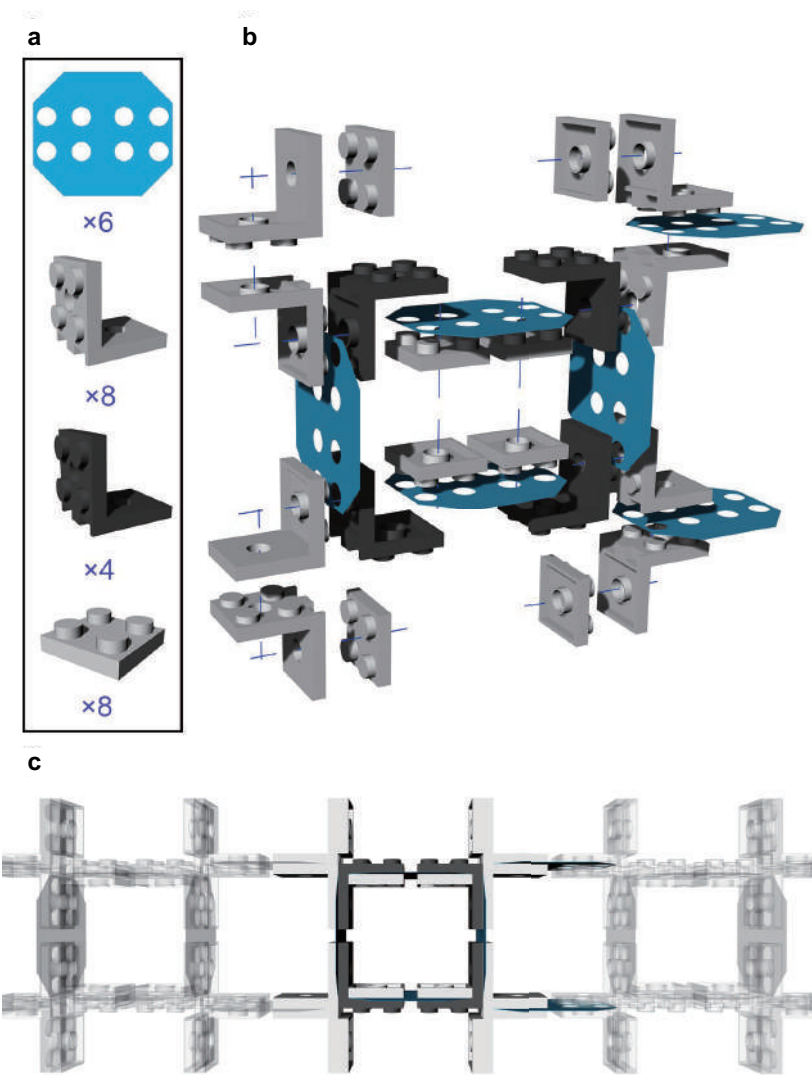


Figure A.2: Fabrication of the shifted chain. (a) Parts used to fabricate the unit cell. (b) Exploded view of two pairs of crosses. (c) The chain is realized by putting together a number of unit cells.

A.2 Testing

To investigate the propagation of pulses in our samples, we place the chain on a smooth horizontal surface (see Figs. A.3(a-b)), while supporting each rigid unit with pins to minimize the effect of friction (see Fig. A.3(g)). We use an impactor excited by a pendulum to hit the mid point at the left end of the chain (see Figs. A.3(c-f) and Supplementary Video 2). Different input signals are applied to the chain by varying both the strength of the pulse (controlled by the initial height of the striking pendulum, h_{input} - see Fig. A.3(d)) and the amplitude of the pulse (controlled by the distance traveled by the impactor, u_{input} - see Fig. A.3(c)). We find that all of them initiate simultaneous rotation and displacement of the rigid units, with each pair of crosses sharing the same displacement and rotating by the same amount, but in opposite directions (i.e. if the top unit rotates by a certain amount in clockwise direction, then the bottom one rotates by the same amount in counter-clockwise direction, and vice versa). To monitor the displacement, u_i , and rotation, θ_i , of i -th pair of crosses along the chain as the pulses propagate, we use a high speed camera (SONY RX100V) recording at 480 fps and track four markers placed on the external arms of each pair of crosses (see Fig. A.4) via digital image correlation analysis^[153]. More specifically, the longitudinal displacement u_i and rotation θ_i of the i -th pair of rigid units is obtained as

$$u_i(t) = \frac{1}{2} \sum_{\gamma=1,2} \left[x_i^{(\gamma)}(t) - x_i^{(\gamma)}(0) \right]$$

$$\theta_i(t) = \frac{1}{2} \sum_{\gamma=1,2} (-1)^{i+\gamma} \arcsin \left[\frac{\left(x_i^{(\gamma+2)}(t) - x_i^{(\gamma+2)}(0) \right) - \left(x_i^{(\gamma)}(t) - x_i^{(\gamma)}(0) \right)}{\sqrt{\left(x_i^{(\gamma+2)}(0) - x_i^{(\gamma)}(0) \right)^2 + \left(y_i^{(\gamma+2)}(0) - y_i^{(\gamma)}(0) \right)^2}} \right] \quad (\text{A.1})$$

where $(x_i^{(\gamma)}(t), y_i^{(\gamma)}(t))$ and $(x_i^{(\gamma)}(0), y_i^{(\gamma)}(0))$ are the coordinates of the γ -th marker placed on the i -th pair of rigid units at time t and that time $t = 0$ (i.e. before the impact), respectively.

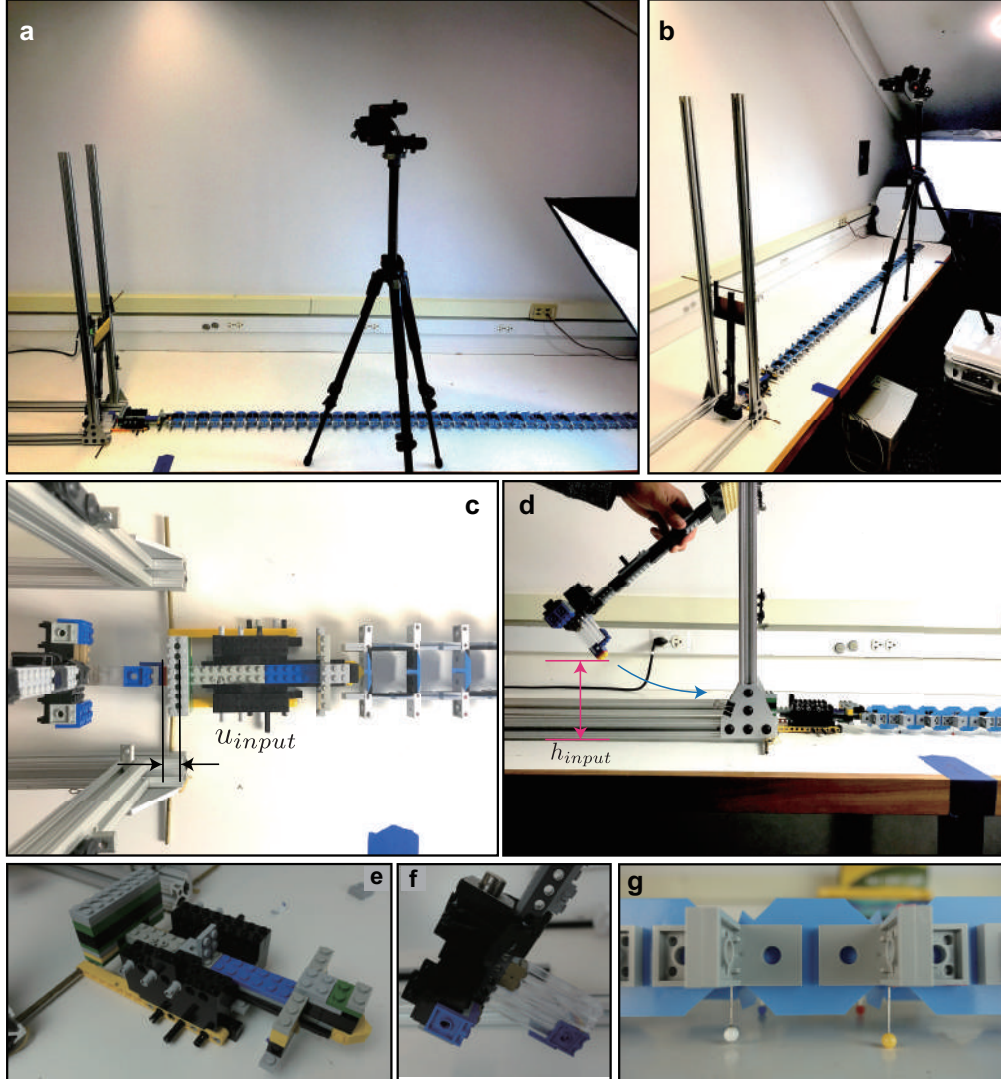


Figure A.3: Experimental setup. (a)-(b) Pictures of our experimental setup showing the sample, the lamp used to illuminate it, the pendulum and the impactor used to excite the pulses and the camera used to monitor the propagation of the pulses. (c) Top-view of the pendulum and the impactor. (d) Side-view of the pendulum and the impactor. (e) Close-up view of the impactor. (f) Close-up view of the end of the pendulum. (g) Friction is minimized by supporting each rigid unit with pins.

Finally, we note that, while for the aligned chain the energy cost to rotate any unit in clockwise and counter-clockwise directions is identical, for the shifted chain there is a disparity between the

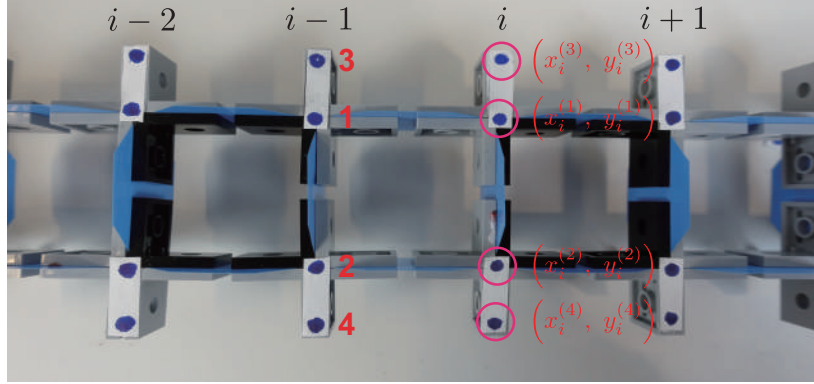


Figure A.4: Digital image correlation analysis. For each pair of rigid crosses four markers (blue dots) are tracked.

two directions of rotation. Under compression in the longitudinal direction, for all units of the shifted chain with the left hinge higher than the right one, it is energetically more favorable to rotate in the clockwise direction, while for the ones with a lower left hinge, rotations in counter-clockwise direction are preferred. In our experiments, we can excite any cross of the shifted chain in either direction of rotation by changing the type of unit placed at the left end of the structure. To excite energetically favorable rotations (i.e. to rotate all crosses with the left hinge higher than the right one in clockwise direction and all crosses with the right hinge higher than the left one in counter-clockwise direction), we place a pair of crosses with $\varphi_0 = 0$ at the left end of the chain (see Fig. A.5(a)). Energetically unfavorable rotations are excited by placing a pair of units with $\varphi_0 \neq 0$ at the left end of the chain (see Fig. A.5(b)).

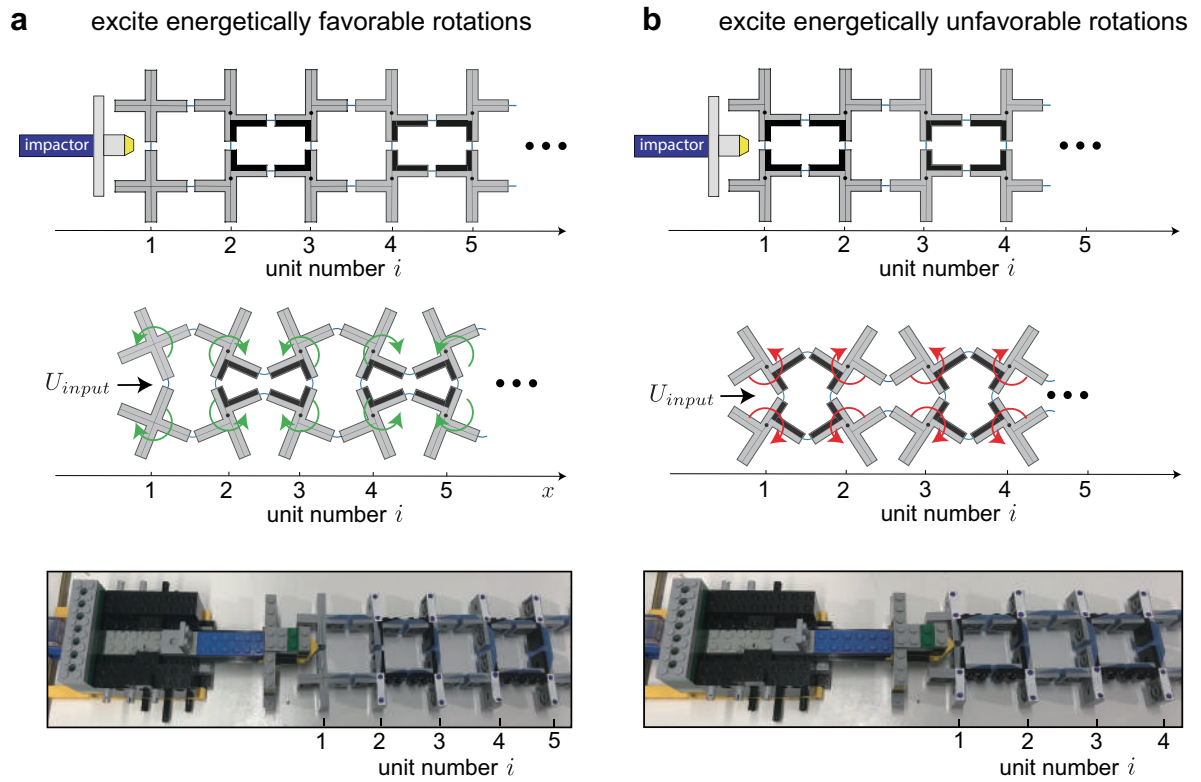


Figure A.5: Exciting different rotations in the shifted chain. (a) Energetically favorable rotations are excited by placing a pair of crosses with $\varphi_0 = 0$ at the left end of the chain. (b) Energetically unfavorable rotations are excited by placing a pair of crosses with $\varphi_0 \neq 0$ at the left end of the chain.

A.3 Discrete Model

Our system consists of a long chain of $2 \times N$ crosses with center-to-center distance a connected by thin and flexible hinges (see Fig. A.6). In our model we focus on the most general case in which neighboring horizontal hinges are shifted in vertical direction by $a \tan \varphi_0$ (see Fig. A.6(a)). Note that the response of the configuration with all horizontal hinges aligned (see Fig. A.6(b)) can be then simply obtained by setting $\varphi_0 = 0$.

Since in this work we focus on the propagation of longitudinal nonlinear waves along the chain, we assign two degrees of freedom to each rigid cross: the longitudinal displacement u and the rotation in the $x - y$ plane θ . Moreover, guided by our experiments, we assume that each pair of crosses shares the same displacement and rotates by the same amount, but in opposite directions (i.e. if the top cross rotates by a certain amount in clockwise direction, then the bottom one rotates by the same amount in counter-clockwise direction, and vice versa). As such, two degrees of freedom are assigned to the i -th pair of crosses: the longitudinal displacement u_i and the rotation θ_i (see Figs. A.6(a-b)). Moreover, to facilitate the analysis, we define the positive direction of rotation alternatively for neighboring units along the x -axis. Specifically, for each cross we assume the energetically favorable direction of rotation to be the positive one. As such, for the i -th top unit (for which the left horizontal hinge is higher than the right one - see Fig. A.6(a)) a clockwise rotation is positive, while for the $i - 1$ -th and $i + 1$ -th top ones (for which the left horizontal hinges are lower than the right ones - see Fig. A.6(a)), counterclockwise rotations are considered positive.

As for the hinges, we model them using a combination of three linear springs: (i) their stretching is captured by a spring with stiffness k_l ; (ii) their shearing is governed by a spring with stiffness k_s ; (iii) their bending is captured by a torsional spring with stiffness k_θ (see Fig. A.6(a)).

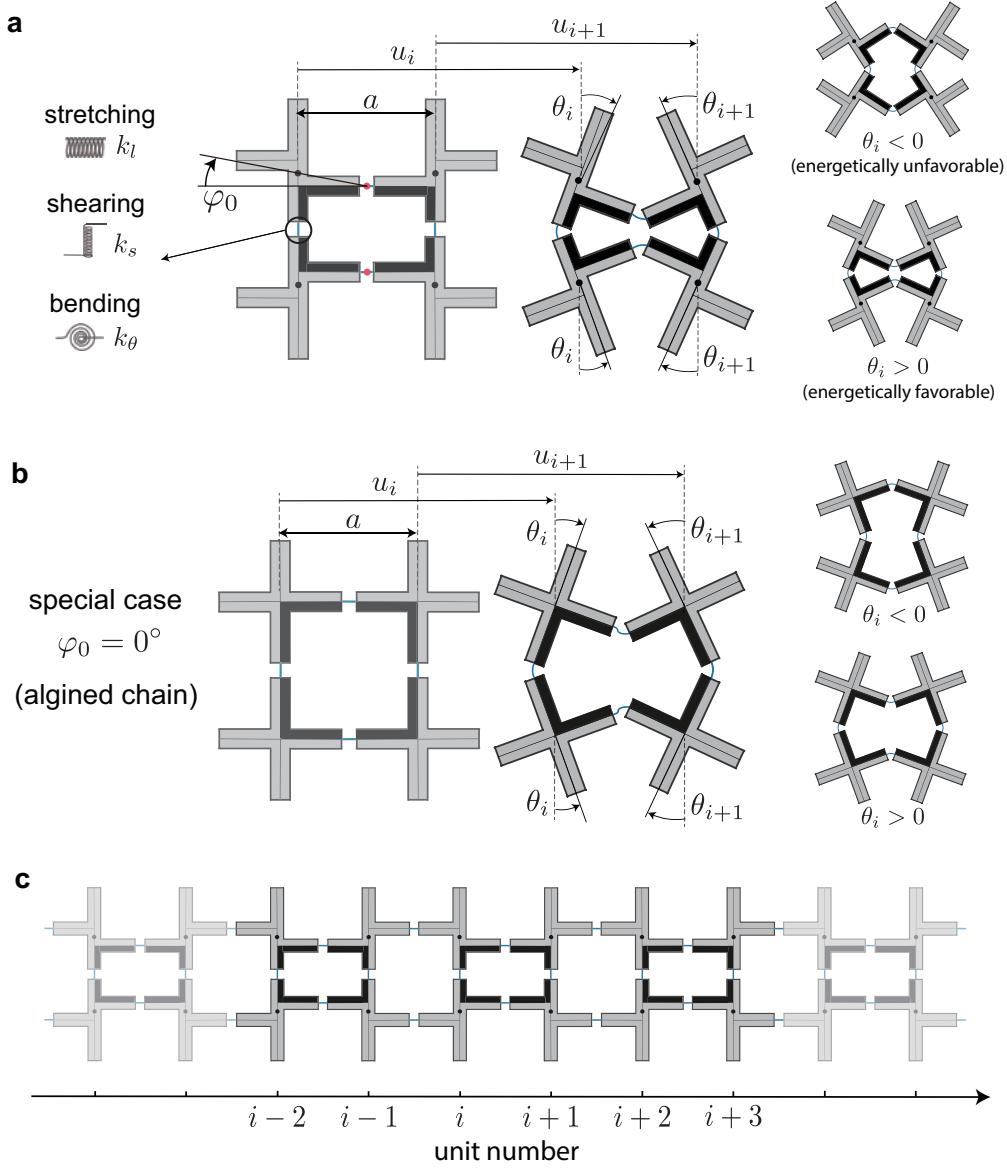


Figure A.6: Schematics of the system. (a) Configuration in which neighboring horizontal hinges are shifted in vertical direction by $a \sin \varphi_0$. (b) Configuration in the horizontal hinges are all aligned. (c) Chain comprising 2×10 cross-shaped rigid units.

Under these assumptions, the equations of motion for the i -th pair of crosses are given by

$$\begin{aligned}
 m\ddot{u}_i = & k_l \left[u_{i+1} - 2u_i + u_{i-1} - \frac{a}{2 \cos \varphi_0} (\cos(\theta_{i+1} + \varphi_0) - \cos(\theta_{i-1} + \varphi_0)) \right], \\
 J\ddot{\theta}_i = & -k_\theta(\theta_{i+1} + 4\theta_i + \theta_{i-1}) + \frac{k_s a^2}{4 \cos^2 \varphi_0} \cos(\theta_i + \varphi_0) [\sin(\theta_{i+1} + \varphi_0) - 2 \sin(\theta_i + \varphi_0) \\
 & + \sin(\theta_{i-1} + \varphi_0)] - \frac{k_l a}{2 \cos \varphi_0} \sin(\theta_i + \varphi_0) [(u_{i+1} - u_{i-1}) \\
 & + \frac{a}{2 \cos \varphi_0} (4 \cos(\varphi_0) - \cos(\theta_{i+1} + \varphi_0) - 2 \cos(\theta_i + \varphi_0) - \cos(\theta_{i-1} + \varphi_0))],
 \end{aligned} \tag{A.2}$$

where m and J are the mass and moment of inertia of the rigid crosses, respectively.

Next, we introduce the normalized displacement $U_i = u_i/a$, time $T = t\sqrt{k_l/m}$, inertia $\alpha = a/(2 \cos \varphi_0) \sqrt{m/J}$ and stiffness ratios $K_\theta = 4k_\theta \cos^2 \varphi_0 / (k_l a^2)$ and $K_s = k_s/k_l$. Eqs. (A.2) can then be written in dimensionless form as

$$\begin{aligned} \frac{\partial^2 U_i}{\partial T^2} &= U_{i+1} - 2U_i + U_{i-1} - \frac{\cos(\theta_{i+1} + \varphi_0) - \cos(\theta_{i-1} + \varphi_0)}{2 \cos \varphi_0}, \\ \frac{1}{\alpha^2} \frac{\partial^2 \theta_i}{\partial T^2} &= -K_\theta(\theta_{i+1} + 4\theta_i + \theta_{i-1}) + K_s \cos(\theta_i + \varphi_0) \\ &\quad \times \left[\sin(\theta_{i+1} + \varphi_0) + \sin(\theta_{i-1} + \varphi_0) - 2 \sin(\theta_i + \varphi_0) \right] \\ &\quad - \sin(\theta_i + \varphi_0) \left[2 \cos(\varphi_0) (U_{i+1} - U_{i-1}) + 4 \cos(\varphi_0) - \right. \\ &\quad \left. \cos(\theta_{i+1} + \varphi_0) - 2 \cos(\theta_i + \varphi_0) - \cos(\theta_{i-1} + \varphi_0) \right]. \end{aligned} \quad (\text{A.3})$$

For a chain comprising N pairs of units Eqs. (A.3) result in a system of $2N$ coupled differential equations, which can be numerically solved for a given set of initial and boundary conditions. In this study, we use the 4th order Runge-Kutta method (via the Matlab function *ode45*) to numerically solve Eqs. (A.3) (the code implemented in MATLAB is available online). Moreover, as initial conditions we set $U = 0$ and $\theta = 0$ for all pairs of crosses. Finally, we enforce two different sets of boundary conditions:

- First, to compare the numerical predictions to our experimental results and verify the relevance of our discrete model, we apply the experimentally extracted displacement, $u_2(t)$, and rotation, $\theta_2(t)$, signals to the first pair of crosses at the left end of the chain, while implementing free-boundary conditions at the right end;
- Second, to generate the numerical results reported in the main text, as in our experiments, we apply a displacement

$$U_{input}(T) = b + b \tanh \frac{T - T_0}{w} \quad (\text{A.4})$$

in the longitudinal direction to the mid-point at the left end of the chain (see Fig. A.7). In our simulations we use $b \in [0, 0.75]$, $w \in [50, 100]$ and choose $T_0 = 400$ to ensure that $U_{input} \rightarrow 0$

at $T = 0$. Such applied displacement induces simultaneous translation and rotation of the first pair of crosses, which in turn results in a normalized translation of the excited mid-point equal to $U_1 + 1/2 \sin \theta_1$. Finally, it is important to note that, to avoid numerical instabilities, we do not apply $U_{input}(t)$ directly to the mid-point at the left end of the chain, but to a linear spring with stiffness $K_{input} = 1$ connected to it (note that the numerical results are not influenced by the particular value chosen for K_{input}). Therefore, $U_{input}(t)$ results in a longitudinal force

$$F_{input} = K_{input} \left[U_{input} - U_1 - \frac{1}{2} \sin \theta_1 \right], \quad (\text{A.5})$$

and in a moment

$$M_{input} = \frac{1}{2} F_{input} \cos \theta_1, \quad (\text{A.6})$$

applied to the first pair of crosses. As such, the governing discrete equations for the first pair of crosses become

$$\begin{aligned} \frac{\partial^2 U_1}{\partial T^2} &= U_2 - U_1 + \frac{2 \cos \varphi_0 - \cos(\theta_1 + \varphi_0) - \cos(\theta_2 + \varphi_0)}{2 \cos \varphi_0} + F_{input}, \\ \frac{1}{\alpha^2} \frac{\partial^2 \theta_1}{\partial T^2} &= -K_\theta(\theta_2 + 3\theta_1) + K_s \cos(\theta_1 + \varphi_0) \left[\sin(\theta_2 + \varphi_0) - \sin(\theta_1 + \varphi_0) \right] \\ &\quad - \sin(\theta_1 + \varphi_0) \left[2 \cos(\varphi_0) (U_2 - U_1) + 2 \cos(\varphi_0) - \cos(\theta_1 + \varphi_0) - \cos(\theta_2 + \varphi_0) \right] \\ &\quad + M_{input}, \end{aligned} \quad (\text{A.7})$$

while the response of all other crosses is governed by Eqs. (A.3).

Estimation of K_θ , K_s and α

To connect the discrete model to our experimental sample, we need to estimate the mass of the cross-shaped units (m), their rotational inertia (J) and the spring stiffnesses (k_l , k_s and k_θ). *Mass*

m : Since the mass of a single LEGO bracket (LEGO part 3956) is 1.13 g and the mass of a single LEGO plate (LEGO part 3022) is 0.60 g, the mass of a rigid cross in our aligned sample is

$$m = 1.13 \times 4 = 4.52 \text{ g}, \quad (\text{A.8})$$

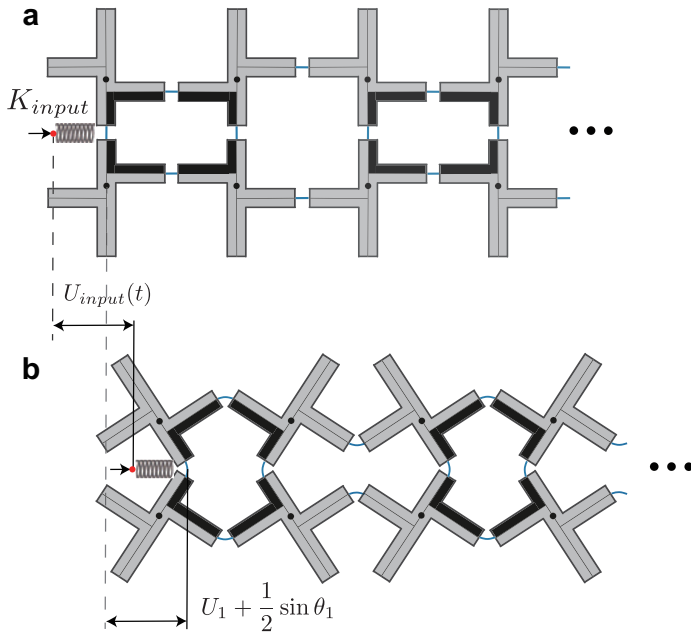


Figure A.7: Schematics showing how U_{input} is applied in our discrete simulations. (a) A linear spring with stiffness $K_{input} = 1$ is connected to the mid-point at the left end of the chain. (b) U_{input} is applied to this spring.

and the mass of a rigid cross in our shifted sample is

$$m = 1.13 \times 3 + 0.60 \times 2 = 4.59 \text{ g.} \quad (\text{A.9})$$

Rotational inertia J: The rotational inertia J can be calculated from the geometry of the rigid crosses (see Eqs. (A.8a-b)) as

$$J = \int_{area} r^2 \, dm \quad (\text{A.10})$$

where r denotes the distance from the center of mass. We find that for the rigid crosses in the aligned structure $J = 605 \text{ g}\cdot\text{mm}^2$, while for the crosses in the shifted structure $J = 615 \text{ g}\cdot\text{mm}^2$.

Spring stiffness k_s and k_l : To determine the stiffnesses k_s and k_l we build a small structure consisting of four parallel hinges connected at both ends to interlocked LEGO plates (see Figs. A.8(c-e)). We

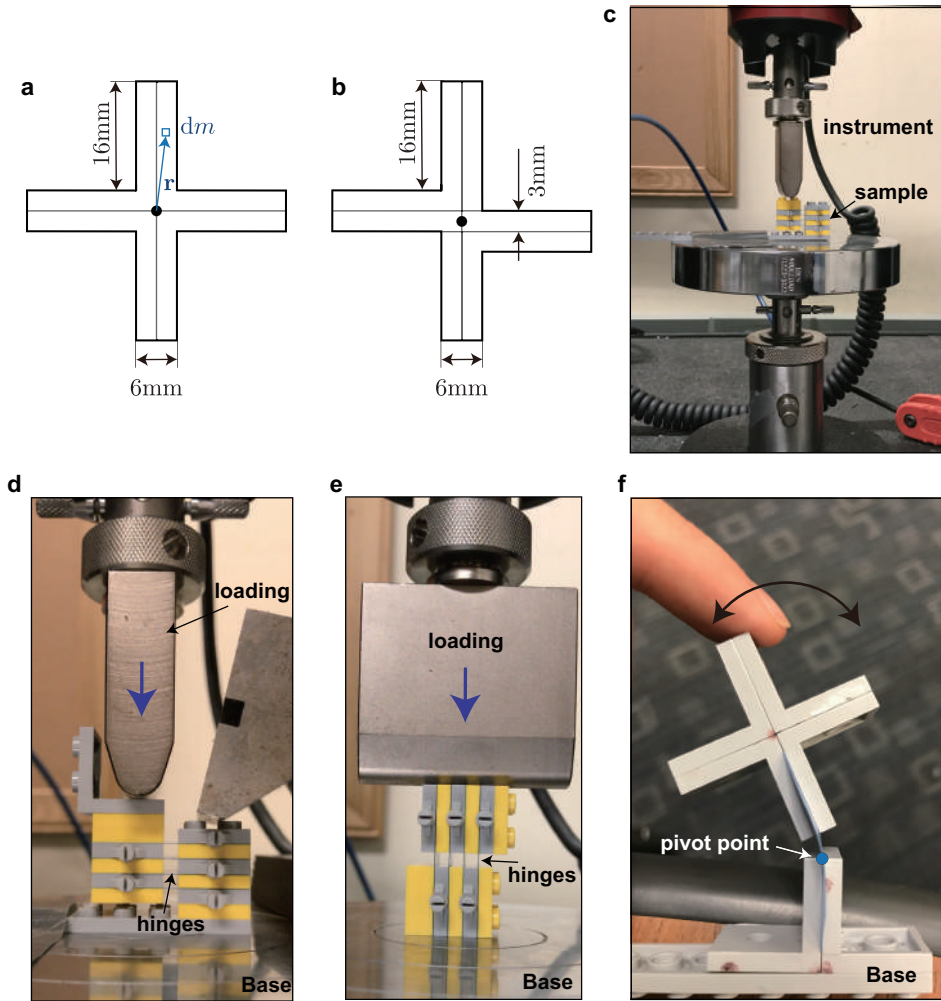


Figure A.8: (a) Geometry of the rigid unit in our aligned chain. (b) Geometry of the rigid unit in our shifted chain. The back dot represent the center of mass. (c) View of the experimental setup used to estimate k_s and k_l . (d) Picture showing the test conducted to estimate k_s . (e) Picture showing the test conducted to estimate k_l . (f) Picture showing the test conducted to estimate k_θ .

start by fixing one column of LEGO plates and applying a displacement u_1 to the other one in direction perpendicular to the hinges (see Fig. A.8(d)), so that the hinges are only subjected to shearing deformations. The stiffness k_s is then obtained from the measured force F_1 as

$$k_s = \frac{F_1}{4u_1} = 1.325 \frac{\text{N}}{\text{mm}}. \quad (\text{A.11})$$

Next, we apply a displacement u_2 to one column of LEGO plates in direction parallel to the hinges (see Fig. A.8(e)), with u_2 small enough so that the hinges are only compressed axially and do not buckle. The stiffness k_l is then obtained from the measured force F_2 as

$$k_l = \frac{F_2}{4u_2} = 71.69 \frac{\text{N}}{\text{mm}}. \quad (\text{A.12})$$

Spring stiffness k_θ : To determine the stiffness k_θ of the torsional spring we connect an hinge to a fixed base and to a cross made of four LEGO brackets (see Fig. A.8(f)). We then apply an initial rotation to the systems and let it free to vibrate. k_θ can be obtained from the experimentally measured frequency of vibration f using

$$f = \frac{1}{2\pi} \sqrt{\frac{k_\theta}{J'}} \quad (\text{A.13})$$

where $J' = 3000 \text{ g}\cdot\text{mm}^2$ is the rotational inertia of the cross with respect to the pivot point. Since we measure $f = 6.4 \text{ Hz}$, we find that

$$k_\theta = 4\pi^2 f^2 J' = 4.85 \text{ N}\cdot\text{mm}. \quad (\text{A.14})$$

Dimensionless parameters K_θ , K_s and α : From the parameters above, we obtain that

- for the aligned structure

$$\alpha = \frac{a}{2} \sqrt{\frac{m}{J}} = 1.815, \quad K_s = \frac{k_s}{k_l} = 0.0185, \quad K_\theta = \frac{4k_\theta}{k_l a^2} = 1.534 \times 10^{-4}, \quad (\text{A.15})$$

- for the shifted structure

$$\alpha = \frac{a}{2 \cos \varphi_0} \sqrt{\frac{m}{J}} = 1.821, \quad K_s = \frac{k_s}{k_l} = 0.0185, \quad K_\theta = \frac{4k_\theta \cos^2 \varphi_0}{k_l a^2} = 1.522 \times 10^{-4}. \quad (\text{A.16})$$

Since the nondimensional parameters for the two different structures are reasonably close, in this study we use

$$\alpha = 1.8, \quad K_s = 0.0185, \quad K_\theta = 1.5 \times 10^{-4}, \quad (\text{A.17})$$

for both structures.

Numerical results

To verify the relevance of our discrete model, we apply the experimentally extracted input displacement and rotation to the first pair of crosses and then compare the signal recorded at the 40th unit in both experiment and simulations. In Fig. A.9 we present such comparison for the two experiments shown in Fig. 2.1(c) of the main text. We find that the pulse profiles and amplitudes are well captured by the discrete model. When the amplitude of the input signal is large as in experiment #1 (for which $A_2 = \max(\theta_2(t)) = 13^\circ$), our numerical simulations reveal the propagation of a pulse that conserves its amplitude and shape in both degrees of freedom (see Fig. A.9(a)). Differently, for inputs with small amplitude as in experiment #2 (for which $A_2 = 5^\circ$), the numerical analyses predict an output signal that is severely distorted compared to the input one, in full agreement with our experimental results (see Fig. A.9(b)).

All of the numerical results reported in the main text are obtained by a displacement $U_{\text{input}} = b + b \tanh(T/w)$ in the longitudinal direction to the mid-point at the left end of the chain, as described in Supplementary Note 3: Discrete Model. In Fig. A.10 we show the response of a 2×150 chain with $\varphi_0 = 0^\circ$ excited by an applied displacement characterized by $b = 0.25$ and $w = 50$. The numerical results indicate that the applied input signal excites a pulse with two polarizational components (one rotational and one translational), which propagates with constant amplitude and velocity.

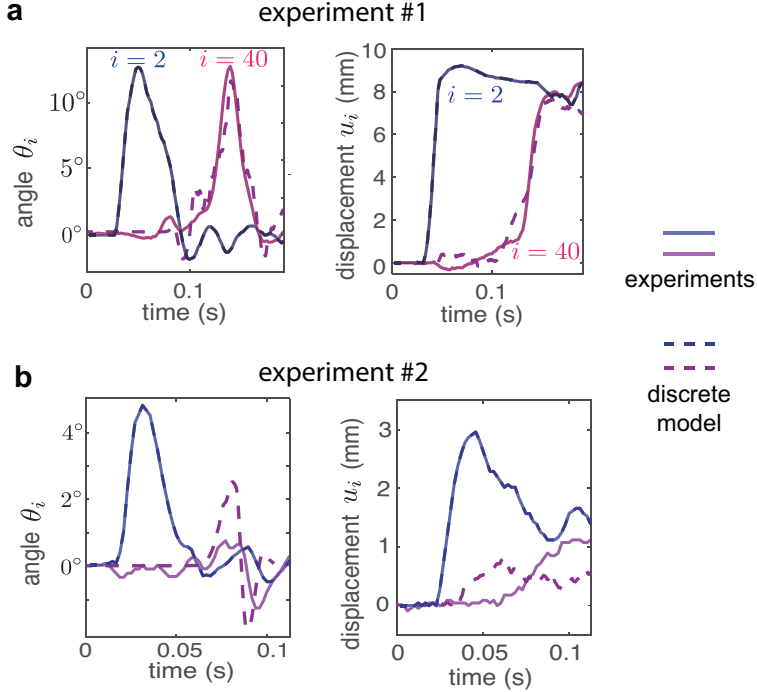


Figure A.9: Comparison between experimental and numerical results for (a) experiment #1 and (b) experiment #2 shown in Fig. 2.1(c) of the main text. Experimental (solid lines) and numerical (dashed lines) signals recorded at the 2nd (blue lines) and 40th (magenta lines) pairs of crosses are reported as a function of time. In our numerical simulations, we apply the experimental signal recorded at 2nd pair of crosses as boundary conditions.

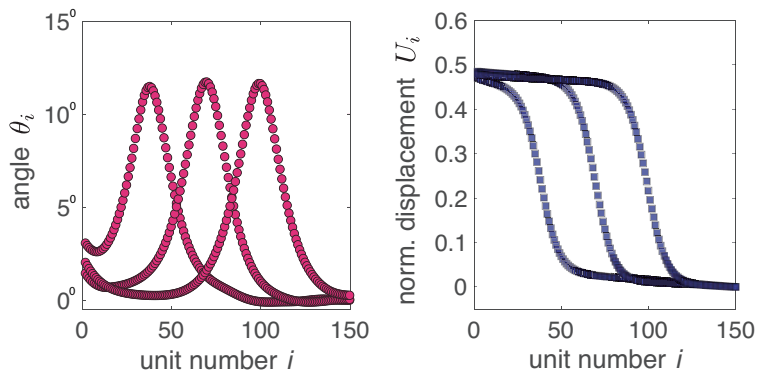


Figure A.10: Numerical results for a chain comprising 2×150 crosses with $\varphi_0 = 0^\circ$. Rotation (left) and normalized displacement (right) profiles are shown at $T = 1050, 1550$, and 2050 .

A.4 Continuum Model

Although Eqs. (A.3) can be numerically solved to obtain the response of the system, a deeper insight into the dynamics of the system can be achieved by simplifying the equations to derive analytical solutions. To this end, we introduce two continuous functions $U(X, T)$ and $\theta(X, T)$ that interpolate the displacement and rotation of the i -th pair of crosses located at $x_i = i a$ as

$$U(X_i, T) = U_i(T), \quad \theta(X_i, T) = \theta_i(T) \quad (\text{A.18})$$

where $X_i = x_i/a = i$. Assuming that the width of the propagating waves is much larger than the unit cell size, the displacement U and rotation θ in correspondence of the $i+1$ and $i-1$ -th pairs of crosses can then be expressed using Taylor expansion as

$$\begin{aligned} U_{i\pm 1}(T) &= U(X_{i\pm 1}, T) \approx U\Big|_{X_i, T} \pm \frac{\partial U}{\partial X}\Big|_{X_i, T} + \frac{1}{2} \frac{\partial^2 U}{\partial X^2}\Big|_{X_i, T} \\ \theta_{i\pm 1}(T) &= \theta(X_{i\pm 1}, T) \approx \theta\Big|_{X_i, T} \pm \frac{\partial \theta}{\partial X}\Big|_{X_i, T} + \frac{1}{2} \frac{\partial^2 \theta}{\partial X^2}\Big|_{X_i, T} \\ \cos \theta_{i\pm 1}(T) &= \cos [\theta(X_{i\pm 1}, T)] \approx \cos \theta\Big|_{X_i, T} \pm \frac{\partial \cos \theta}{\partial X}\Big|_{X_i, T} + \frac{1}{2} \frac{\partial^2 \cos \theta}{\partial X^2}\Big|_{X_i, T} \\ \sin \theta_{i\pm 1}(T) &= \sin [\theta(X_{i\pm 1}, T)] \approx \sin \theta\Big|_{X_i, T} \pm \frac{\partial \sin \theta}{\partial X}\Big|_{X_i, T} + \frac{1}{2} \frac{\partial^2 \sin \theta}{\partial X^2}\Big|_{X_i, T} \end{aligned} \quad (\text{A.19})$$

Substitution of Eqs. (A.19) into Eqs. (A.3) yields

$$\begin{aligned} \frac{\partial^2 U}{\partial T^2} &= \frac{\partial^2 U}{\partial X^2} - \frac{1}{\cos \varphi_0} \frac{\partial \cos(\theta + \varphi_0)}{\partial X}, \\ \frac{1}{a^2} \frac{\partial^2 \theta}{\partial T^2} &= -K_\theta \frac{\partial^2 \theta}{\partial X^2} + K_s \cos(\theta + \varphi_0) \frac{\partial^2 \sin(\theta + \varphi_0)}{\partial X^2} + \sin(\theta + \varphi_0) \frac{\partial^2 \cos(\theta + \varphi_0)}{\partial X^2} \\ &\quad - 6K_\theta \theta - 4 \sin(\theta + \varphi_0) \left[\cos \varphi_0 \frac{\partial U}{\partial X} + \cos \varphi_0 - \cos(\theta + \varphi_0) \right], \end{aligned} \quad (\text{A.20})$$

which represent the continuum governing equations of the system. Since these two coupled partial differential equations cannot be solved analytically, guided by our experiments, we further assume that $\theta \sim \varphi_0 \ll 1$, so that

$$\begin{aligned}\sin(\theta + \varphi_0) &\approx \sin \varphi_0 + \theta \cos \varphi_0 - \frac{\sin \varphi_0}{2} \theta^2 - \frac{\cos \varphi_0}{6} \theta^3, \\ \cos(\theta + \varphi_0) &\approx \cos \varphi_0 - \theta \sin \varphi_0 - \frac{\cos \varphi_0}{2} \theta^2 + \frac{\sin \varphi_0}{6} \theta^3.\end{aligned}\quad (\text{A.21})$$

By substituting Eqs. (A.21) into Eqs. (A.20) and retaining the nonlinear terms up to third order, we obtain

$$\begin{aligned}\frac{\partial^2 U}{\partial T^2} &= \frac{\partial^2 U}{\partial X^2} + \left[\tan(\varphi_0) + \theta - \frac{\tan(\varphi_0)}{2} \theta^2 \right] \frac{\partial \theta}{\partial X}, \\ \frac{1}{\alpha^2} \frac{\partial^2 \theta}{\partial T^2} &= (K_s - K_\theta) \frac{\partial^2 \theta}{\partial X^2} - 2 (2 \sin^2(\varphi_0) + 3K_\theta) \theta - 3 \sin(2\varphi_0) \theta^2 - \frac{7 \cos(2\varphi_0) - 1}{3} \theta^3 \\ &\quad - [2 \sin(2\varphi_0) + 4 \cos^2(\varphi_0) \theta - \sin(2\varphi_0) \theta^2] \frac{\partial U}{\partial X}.\end{aligned}\quad (\text{A.22})$$

Finally, we introduce the traveling wave coordinate $\zeta = X - cT$, c being the normalized pulse velocity (the dimensional pulse velocity is $ca\sqrt{k/m}$), so that Eqs. (A.22) become

$$\begin{aligned}\frac{\partial^2 U}{\partial \zeta^2} &= -\frac{1}{1 - c^2} \left[\tan \varphi_0 \frac{\partial \theta}{\partial \zeta} + \theta \frac{\partial \theta}{\partial \zeta} - \frac{\tan \varphi_0}{2} \theta^2 \frac{\partial \theta}{\partial \zeta} \right], \\ \frac{1}{\beta} \frac{\partial^2 \theta}{\partial \zeta^2} &= 2 (2 \sin^2 \varphi_0 + 3K_\theta) \theta + 3 \sin(2\varphi_0) \theta^2 + \frac{7 \cos(2\varphi_0) - 1}{3} \theta^3 \\ &\quad + [2 \sin(2\varphi_0) + 4 \cos^2(\varphi_0) \theta - \sin(2\varphi_0) \theta^2] \frac{\partial U}{\partial \zeta},\end{aligned}\quad (\text{A.23})$$

where

$$\beta = \frac{\alpha^2}{\alpha^2(K_s - K_\theta) - c^2}. \quad (\text{A.24})$$

By integrating Eq. (A.23)₁ with respect to ζ we obtain,

$$\frac{\partial U}{\partial \zeta} = -\frac{1}{1-c^2} \left[\theta \tan \varphi_0 + \frac{\theta^2}{2} - \frac{\tan(\varphi_0)}{6} \theta^3 \right] + C \quad (\text{A.25})$$

where C is the integration constant. Since in this study we focus on the propagation of waves with a finite temporal support and do not consider periodic waves, we require that

$$\frac{\partial U}{\partial \zeta} \Big|_{\zeta \rightarrow \infty} = 0, \quad (\text{A.26})$$

from which we obtain $C = 0$. Substitution of Eq. (A.25) into Eq. (A.23)₂ yields

$$\frac{\partial^2 \theta}{\partial \zeta^2} = C_1 \theta + C_2 \theta^2 + C_3 \theta^3 \quad (\text{A.27})$$

with

$$\begin{aligned} C_1 &= 2\beta \left[3K_\theta - \frac{2c^2 \sin^2 \varphi_0}{1-c^2} \right], \\ C_2 &= -\frac{3\beta c^2}{(1-c^2)} \sin(2\varphi_0), \\ C_3 &= -\frac{\beta c^2}{3(1-c^2)} (7 \cos(2\varphi_0) - 1), \end{aligned} \quad (\text{A.28})$$

which is the Klein-Gordon equation with quadratic and cubic nonlinearities^[96]. Note that Eq. (A.27) differs from the equation recently derived to study the propagation of solitary waves in structures comprising a network of squares connected by thin hinges^[94]. While in the previous work only terms up to the second order were considered in the continuum model (see Eq. (8) in^[94]), here also the third order terms are included. This enable us to investigate waves with amplitude equal

or larger than φ_0 .

The analytical solution of Eq. (A.27) exists in the form of

$$\theta = \frac{1}{D_1 \pm D_2 \cosh(\zeta/W)} \quad (\text{A.29})$$

where D_1 , D_2 and W are solution parameters. Eq. (A.29) defines a solitary wave with characteristic width W and amplitude

$$A = \theta(\zeta = 0) = \frac{1}{D_1 \pm D_2}. \quad (\text{A.30})$$

Next, we determine D_1 , D_2 and W as a function of the geometry of the system and the pulse velocity c . To this end, we substitute the solution (A.29) into Eq. (A.27) and find that the latter is identically satisfied only if

$$D_1 = -\frac{C_2}{3C_1}, \quad D_2 = \sqrt{\frac{C_2^2}{9C_1^2} - \frac{C_3}{2C_1}}, \quad \text{and} \quad W = \frac{1}{\sqrt{C_1}}, \quad (\text{A.31})$$

where C_1 , C_2 and C_3 are defined in Eqs. (A.28). Finally, the solution for the displacement U is found by integrating Eq. (A.25) with θ given by Eq. (A.29),

$$\begin{aligned} U &= \int_{\zeta}^{\infty} \frac{1}{1-c^2} \left[\tan \varphi_0 \theta(\zeta') + \frac{\theta(\zeta')^2}{2} - \frac{\tan \varphi_0}{6} \theta(\zeta')^3 \right] d\zeta' \\ &= \frac{W}{12(1-c^2)} \left[2 \left(\arctan \frac{D_1 \pm D_2}{\sqrt{D_2^2 - D_1^2}} - \arctan \frac{(D_1 \pm D_2) \tanh(\zeta/W)}{\sqrt{D_2^2 - D_1^2}} \right) \right. \\ &\quad \left(6D_1(D_2^2 - D_1^2)^{-3/2} + \tan \varphi_0 \frac{D_2^2 - 12D_1^4 - 12D_2^4 + D_1^2(2 + 24D_2^2)}{(D_2^2 - D_1^2)^{5/2}} \right) \\ &\quad + \frac{6(D_2^2 - D_1^2) + 3D_1 \tan \varphi_0}{(D_1^2 - D_2^2)^2} - D_2 \sinh \frac{\zeta}{W} \left(\frac{\pm 6}{(D_1^2 - D_2^2)(D_1 \mp D_2 \cosh(\zeta/W))} \right. \\ &\quad \left. \left. + \tan \varphi_0 \frac{\mp 4D_1^2 \pm D_2^2 + 3D_1 D_2 \cosh(\zeta/W)}{(D_1^2 - D_2^2)^2 (D_1 \mp D_2 \cosh(\zeta/W))^2} \right) \right] \end{aligned} \quad (\text{A.32})$$

As recently found for structures comprising a network of squares connected by thin and highly deformable ligaments^[94], Eqs. (A.29) and (A.32) reveal that our system supports the propagation of elastic vector solitons (i.e. solitary waves with two components - one translational and one rotational - that are coupled together and co-propagate without dispersion).

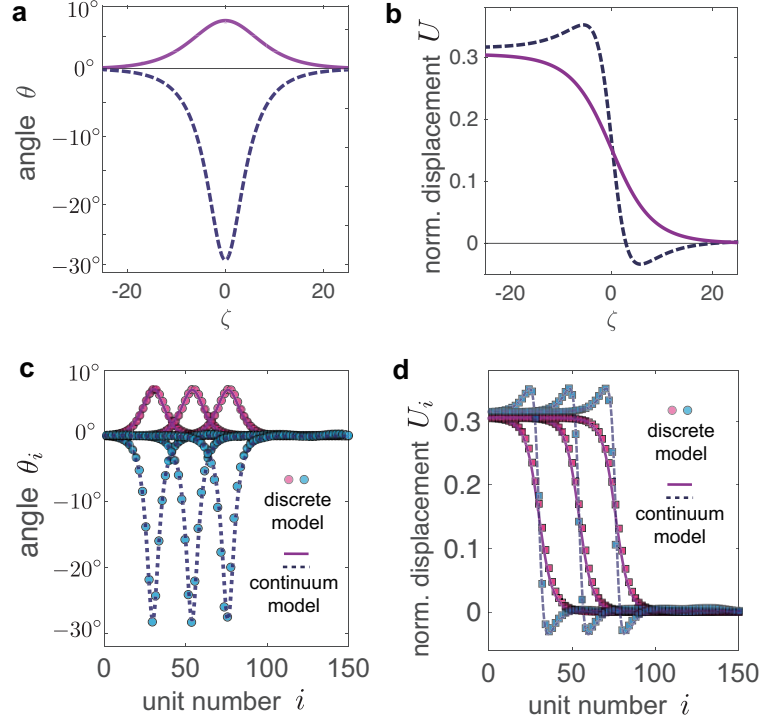


Figure A.11: (a)-(b) Analytical solution for a structure characterized by $K_s = 0.0185$, $K_\theta = 1.5 \times 10^{-4}$, $\alpha = 1.8$, $c = 0.1$ and $\varphi_0 = 5^\circ$. (c)-(d) Comparison between analytically (lines) and numerically (markers) predicted rotation and normalized displacement profiles at $T = 840$, 1080 , and 1320 . Also in this case we assume that $K_s = 0.0185$, $K_\theta = 1.5 \times 10^{-4}$, $\alpha = 1.8$, $c = 0.1$ and $\varphi_0 = 5^\circ$.

In Figs. A.11(a-b) we report the solution given by Eqs. (A.29) and (A.32), assuming that $K_s = 0.02$, $K_\theta = 1.5 \times 10^{-4}$, $\alpha = 1.8$, $c = 0.1$ and $\varphi_0 = 5^\circ$. We find that the two vector solitons supported by the system are both characterized by positive values of longitudinal displacement U (i.e. both waves are accompanied by a translation from left to right - see Fig. A.11(b)). As for the rotational component, one solution is characterized by positive θ and the other one by negative θ (see Fig. A.11(a)). This means that in one case the top unit of the i -th pair of crosses rotates

clockwise, while in the other it rotates counter-clockwise (in both cases neighboring units rotate in opposite directions). It is also important to note that, while the two solutions for U have comparable magnitude, the negative solution for θ (i.e. the one that involves counter-clockwise rotation for the top unit of the i -th pair of crosses) has much larger amplitude than the positive one. Such disparity is due to the asymmetry of the structure with $\varphi_0 \neq 0$, which makes rotation in clockwise direction for the i -th unit (for which the left horizontal hinge is higher than the right one) energetically more favorable. Finally, to verify the validity of our analytical solution, in Fig. A.11(c-d) we compare the analytical solutions to numerical results obtained by direct integration of the full discrete model (Eqs. (A.3)). Note that in this set of simulations we consider a chain with 2×150 crosses and input our theoretical solutions (i.e. Eqs. (A.29) and (A.32)) as boundary conditions for the first pair of crosses at the left end of the chain, while implementing free-boundary conditions at its right end. We find an excellent agreement between our analytical (lines) and numerical (markers) results, indicating that the assumptions we made, i.e., wave length \ll unit length and $\theta \sim \varphi_0 \ll 1$, are appropriate.

A.5 Amplitude Gaps for Solitons

Eq. (A.29) defines the solitary waves with stable profile that propagate in our system. However, inspection of Eqs. (A.29) and (A.31) reveals that such waves exist only if:

- (i) W is real, yielding

$$C_1 > 0 \quad (\text{A.33})$$

since an imaginary W results in a periodic solution, which violates Eq. (A.26);

- (ii) D_2 is a real number, yielding

$$\frac{C_2^2}{9C_1^2} - \frac{C_3}{2C_1} > 0 \quad (\text{A.34})$$

since we want the solution θ to be real;

(iii) the denominator in Eq. (A.29) is different from zero, yielding

$$D_1 \pm D_2 \cosh(W\zeta) \neq 0 \quad \forall \zeta \quad (\text{A.35})$$

since we require the solution θ to be of finite amplitude. Note that, since $D_2 > 0$ (see Eq. (A.34)) and $\cosh(W\zeta) \in [1, \infty)$, if we require both solutions of Eq. (A.29) to exist, Eq. (A.35) can be rewritten as

$$-D_2 < D_1 < D_2. \quad (\text{A.36})$$

Differently, if $D_1 > D_2$ or $D_1 < -D_2$, only one of the two solitary waves supported by the system exists. While in this Section we focus on the case where condition (A.36) is satisfied (so that both solutions exist), in Supplementary Note 6: Solitons excited by pulling, we investigate the case in which only one solution exists.

By substituting Eqs. (A.24) and (A.28) into conditions (A.33), (A.34) and (A.36) and assuming that $c < 1$ (note that in all our experiments and simulations $c \in [0.05, 0.5]$) and that $\varphi_0 < 0.7137 = 41^\circ$ (so that $7 \cos(2\varphi_0) > 1$), we find that solitary waves exist in our system only if

$$c^2 < \alpha^2 (K_s - K_\theta) \quad \text{and} \quad c^2 < \frac{3K_\theta}{2 \sin^2 \varphi_0 + 3K_\theta}. \quad (\text{A.37})$$

Conditions (A.37) clearly show that there is an upper limit for the velocity of the propagating solitary waves, i.e.,

$$c < c_{max} \quad (\text{A.38})$$

where

$$c_{max} = \min \left\{ \alpha \sqrt{K_s - K_\theta}, \sqrt{\frac{3K_\theta}{2 \sin^2 \varphi_0 + 3K_\theta}} \right\}. \quad (\text{A.39})$$

Substitution of condition (A.38) into Eq. (A.30) yields

$$A > A_{upper} = \frac{1}{D_1 + D_2} \Bigg|_{c=c_{max}} \quad \text{and} \quad A < A_{lower} = \frac{1}{D_1 - D_2} \Bigg|_{c=c_{max}} \quad (\text{A.40})$$

indicating that solitary waves can propagate in our system only if their amplitude is larger than A_{upper} and lower than A_{lower} . Therefore, conditions (A.40) define an amplitude gap for solitons. By substituting Eqs. (A.31) and (A.28) into (A.40), A_{upper} and A_{lower} can be expressed in terms of structural parameters as,

$$\begin{aligned} A_{upper} &= \frac{2\sqrt{3/\gamma}\sqrt{2\gamma\cos(4\varphi_0) + \cos(2\varphi_0)[21K_\theta - (21K_\theta + 8)\gamma] + 6\gamma + 3K_\theta(\gamma - 1)} - 6\alpha\sin(2\varphi_0)}{7\cos(2\varphi_0) - 1}, \\ A_{lower} &= \frac{-2\sqrt{3/\gamma}\sqrt{2\gamma\cos(4\varphi_0) + \cos(2\varphi_0)[21K_\theta - (21K_\theta + 8)\gamma] + 6\gamma + 3K_\theta(\gamma - 1)} - 6\alpha\sin(2\varphi_0)}{7\cos(2\varphi_0) - 1} \end{aligned} \quad (\text{A.41})$$

if $\sin\varphi_0 < \sqrt{3K_\theta(1 - \gamma)/(2\gamma)}$, or as

$$A_{upper} = 0 \quad \text{and} \quad A_{lower} = \frac{-12\sin(2\varphi_0)}{7\cos(2\varphi_0) - 1} \quad (\text{A.42})$$

if $\sin\varphi_0 > \sqrt{3K_\theta(1 - \gamma)/(2\gamma)}$, with $\gamma = \alpha^2(K_s - K_\theta)$.

In Figs. A.12(a-c) we report the evolution of A_{upper} (solid purple line) and A_{lower} (solid blue line) as a function of φ_0 for chains characterized by $\alpha = 1.8$ and $(K_\theta, K_s) = (1.5 \times 10^{-4}, 0.02)$ (Fig. A.12(a)), $(1.0 \times 10^{-4}, 0.02)$ (Fig. A.12(b)) and $(1.5 \times 10^{-4}, 0.1)$ (Fig. A.12(c)). We find that, while for $\varphi_0 = 0^\circ$ (i.e. when all horizontal hinges are aligned) $A_{lower} = -A_{upper}$, $|A_{lower}|$ and A_{upper} become larger and smaller, respectively, as φ_0 increases. This is because the hinges shifting (i.e. $\varphi_0 \neq 0^\circ$) introduces a disparity between the two directions of rotation. Under compression in the longitudinal direction,

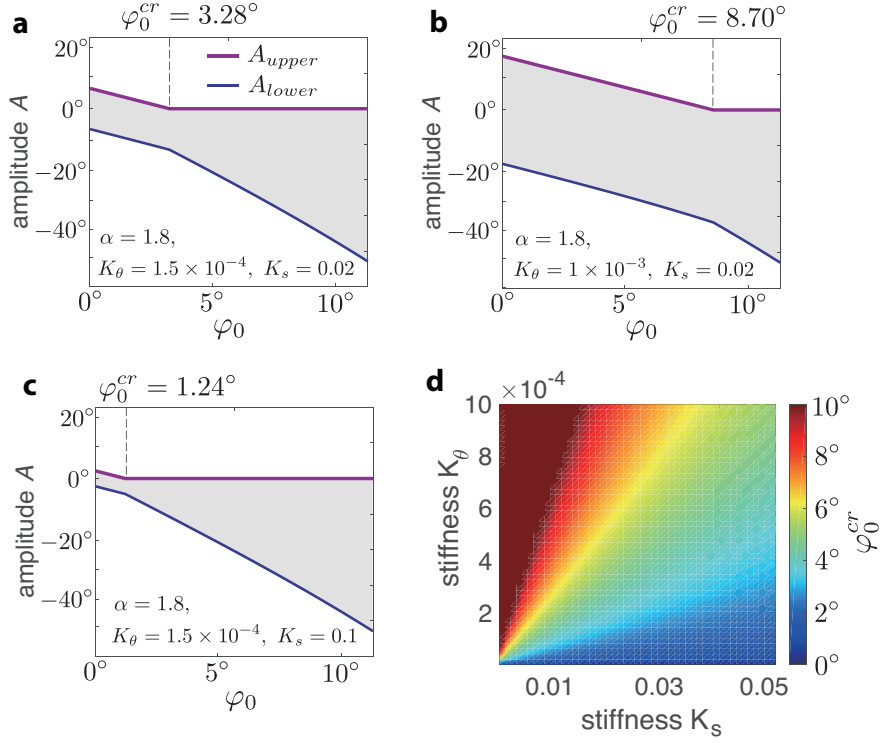


Figure A.12: (a)-(c) Evolution of the amplitude gap as a function of the angle φ_0 chains characterized by (a) $\alpha=1.8$, $K_\theta=1.5 \times 10^{-4}$ and $K_s=0.02$; (b) $\alpha=1.8$, $K_\theta=1.0 \times 10^{-3}$ and $K_s=0.02$; (c) $\alpha=1.8$, $K_\theta=1.5 \times 10^{-4}$ and $K_s=0.1$. (d) Evolution of φ_0^{cr} as a function of K_s and K_θ , assuming $\alpha = 1.8$.

for all units of the shifted chain with the left hinge higher than the right one, it is energetically more favorable to rotate in the clockwise direction, while for the ones with a lower left hinge, rotations in the counter-clockwise direction are preferred. As such, pulses that excite energetically favorable rotations can propagate more easily than those inducing energetically unfavorable rotations. We also note that a critical angle

$$\varphi_0^{cr} = \arcsin \sqrt{\frac{3K_\theta(1-\gamma)}{2\gamma}} \quad (\text{A.43})$$

exists at which A_{upper} eventually vanishes. In structures with $\varphi_0 > \varphi_0^{cr}$ all solitons that induce energetically favorable rotations can propagate through the system, irrespectively of their magnitude. In Fig. A.12(d) we report the evolution of the angle φ_0^{cr} as a function of K_s and K_θ (assuming

$\alpha = 1.8$). We find that φ_0^{cr} increases for larger values of K_θ , while it decreases as K_s becomes larger.

Focusing on the mechanism behind the emergence of the observed amplitude gap for solitons, it is important to note that the propagations of vector solitons require a strong coupling among different polarizations^[100,101]. As such, we expect such amplitude gaps to emerge when there is weak coupling between the two polarizational components. According to Eqs. (A.22), the coupling terms in our system are

$$\left[\tan \varphi_0 + \theta - \frac{\tan \varphi_0}{2} \theta^2 \right] \frac{\partial \theta}{\partial X} \sim (\varphi_0 + \theta) \frac{\partial \theta}{\partial X} \quad (\text{A.44})$$

and

$$[2 \sin(2\varphi_0) + 4\theta \cos^2 \varphi_0 - \theta^2 \sin(2\varphi_0)] \frac{\partial U}{\partial X} \sim 4(\varphi_0 + \theta) \frac{\partial U}{\partial X}. \quad (\text{A.45})$$

Eqs. (A.44) and (A.45) clearly show that if $\varphi_0 = 0$ (i.e. for the aligned structure), the coefficients of both coupling terms are proportional to θ , so that large enough rotations are needed in order to activate them and enable the propagation of vector solitons. Differently, if $\varphi_0 \neq 0$ (i.e. for the shifted structure), the coefficients are proportional to $\varphi_0 + \theta$ and the strength of the coupling depends on the direction of rotation. The coupling among U and θ is strong when the wave induces an energetically favorable rotation (since φ_0 and θ have the same sign and their effect sums up), resulting in lower values for A_{upper} as φ_0 increases. By contrast, if the wave induces an energetically unfavorable rotation (i.e. $\theta < 0$), large rotations are required to make the coupling strong enough (i.e. $\theta < 0$ has to go more negative to compensate for the bias induced by the positive φ_0), resulting in large $|A_{lower}|$.

A.6 Solution for the Aligned Chain

While in Supplementary Note 4: Continuum model and Supplementary Note 5: Amplitude gaps for solitons we derived the analytical solution for the most general case of a system in which neighboring horizontal hinges are shifted vertically by $a \sin \varphi_0$, here we specialized it to a structure in which all horizontal hinges are aligned (i.e. $\varphi_0 = 0$). If $\varphi_0 = 0$, the solution given by Eqs. (A.29)-(A.32) reduces to,

$$\theta = A \operatorname{sech} \left(\frac{\zeta}{W} \right), \quad U = \frac{A^2 W}{2(1 - c^2)} \left[1 - \tanh \left(\frac{\zeta}{W} \right) \right] \quad (\text{A.46})$$

with

$$A = \pm \sqrt{\frac{6K_\theta(1 - c^2)}{c^2}} \quad \text{and} \quad W = \sqrt{\frac{\alpha^2(K_s - K_\theta) - c^2}{6\alpha^2 K_\theta}}. \quad (\text{A.47})$$

In Figs. A.13(a-b) we plot the analytical solution given by Eqs. (A.46), assuming $K_s = 0.0185$, $K_\theta = 1.5 \times 10^{-4}$, $\alpha = 1.8$ and $c = 0.1$. We find that the two solutions supported by the system are characterized by identical translational components. The rotational components are also identical, but have opposite direction. Note that the two solutions have the same magnitude because in the aligned chain the units do not have a preferential direction of rotation. Finally, in Figs. A.13(c-d), we compare the analytical solution to numerical results obtained by direct integration of the full discrete model (Eqs. (A.3)). Note that in this set of simulations we consider a chain with 2×150 crosses and assign the displacement and rotation signals given by Eqs. (A.46) to the first pair of units on the left, while keeping free boundary conditions at the right end. Again, we find an excellent agreement between our analytical (lines) and numerical (markers) results.

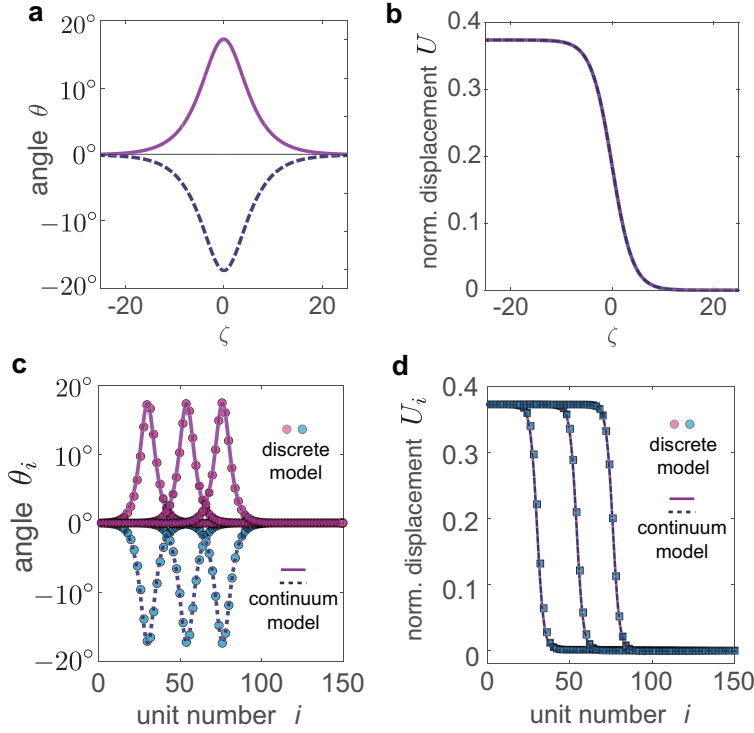


Figure A.13: (a)-(b) Analytical solution for a structure characterized by $K_s = 0.0185$, $K_\theta = 1.5 \times 10^{-4}$, $\alpha = 1.8$, $c = 0.1$ and $\varphi_0 = 0.0$. (c)-(d) Comparison between analytically (lines) and numerically (markers) predicted rotation and normalized displacement profiles at $T = 840, 1080$, and 1320 . Also, in this case we assume that $K_s = 0.0185$, $K_\theta = 1.5 \times 10^{-4}$, $\alpha = 1.8$, $c = 0.1$ and $\varphi_0 = 0^\circ$.

As for the amplitude gap, if $\varphi_0 = 0$, Eqs. (A.41) and (A.42) reduce to

$$A_{upper} = -A_{lower} = \sqrt{\frac{6K_\theta}{\alpha^2(K_s - K_\theta)} - 6K_\theta}. \quad (\text{A.48})$$

In Fig. A.14 we report the evolution $A_{upper} = -A_{lower}$ as a function of K_s , K_θ and α . The contour plots indicate that A_{upper} can be tuned by varying either K_s or K_θ , while α has a more moderate effect.

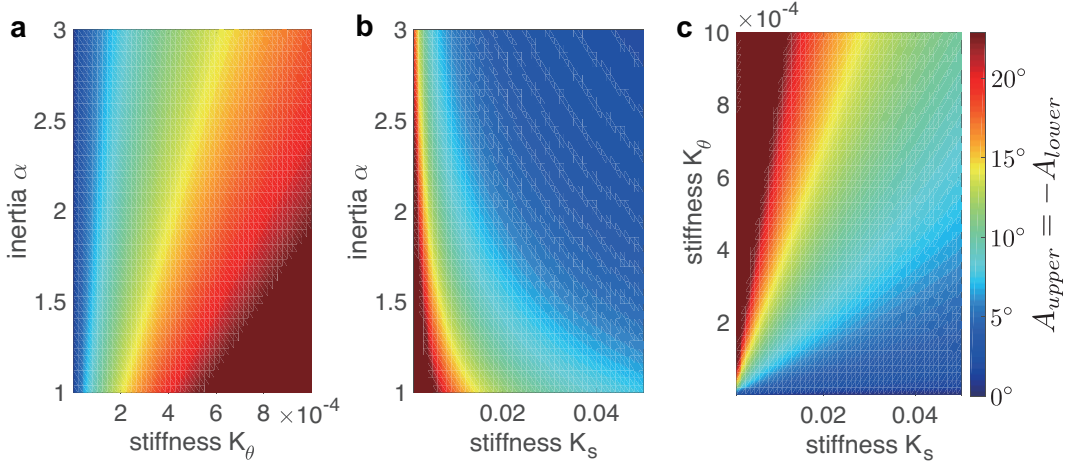


Figure A.14: (a) Evolution of $A_{upper} = -A_{lower}$ as a function of α and K_θ (assuming $K_s = 0.02$). (b) Evolution of $A_{upper} = -A_{lower}$ as a function of α and K_s (assuming $K_\theta = 1.5 \times 10^{-4}$). (c) Evolution of $A_{upper} = -A_{lower}$ as a function of K_θ and K_s (assuming $\alpha = 1.8$).

A.7 Solitons Excited by Pulling

While in Supplementary Note 5, we consider the case in which condition (A.36) is satisfied and the system supports two elastic vector solitons, here we investigate the response of the system when only one elastic vector soliton exists (i.e. when $D_1 > D_2$ or $D_1 < -D_2$). Let us consider the case $D_1 < -D_2$. Existence of such solitary wave requires that

$$C_1 > 0, \quad \frac{C_2^2}{9C_1^2} - \frac{C_3}{2C_1} > 0 \quad \text{and} \quad D_1 < -D_2. \quad (\text{A.49})$$

Substitution of Eqs. (A.24) and (A.28) into conditions (A.49) yields,

$$\begin{aligned} c^2 &> \alpha^2 (K_s - K_\theta), \quad c^2 > \frac{3K_\theta}{2 \sin^2 \varphi_0 + 3K_\theta}, \\ \text{and } c^2 &> \frac{3K_\theta (7 \cos(2\varphi_0) - 1)}{\cos(2\varphi_0)(21K_\theta + 8) - 2 \cos(4\varphi_0) - 6 - 3K_\theta}. \end{aligned} \quad (\text{A.50})$$

Assuming that $\varphi_0 < 0.7137 = 41^\circ$ (so that $7 \cos(2\varphi_0) > 1$), condition (A.50)₃ is only satisfied if

$$\cos(2\varphi_0)(21K_\theta + 8) - 2 \cos(4\varphi_0) - 6 - 3K_\theta < 0 \quad (\text{A.51})$$

since positive values of the denominator always lead to $c > 1$. In Fig. A.15(a), we report the region of the φ_0 - K_θ domain in which condition Eq. (A.51) is satisfied as the shaded area. We find that this type of solitary waves is supported by the system only for large enough φ_0 .

Conditions Eqs. (A.50)_{1,2} clearly show that there is a lower limit for the velocity of the propagating solitary waves, i.e.

$$c > c_{min} \quad (\text{A.52})$$

where

$$c_{min} = \max \left\{ \alpha \sqrt{K_s - K_\theta}, \sqrt{\frac{3K_\theta}{2 \sin^2 \varphi_0 + 3K_\theta}} \right\}. \quad (\text{A.53})$$

When constraint Eq. (A.52) is satisfied, the system supports only one solution in the form

$$\theta = \frac{1}{D_1 - D_2 \cosh(\zeta/W)} \quad (\text{A.54})$$

where D_1 and D_2 are defined in Eqs. (A.28) and (A.31). This solution is plotted in Fig. A.15(b), assuming $K_s = 0.0185$, $K_\theta = 1.5 \times 10^{-4}$, $\alpha = 1.8$, $c = 0.5$ and $\varphi_0 = 8^\circ$. Moreover, in Fig. A.15(c) we report the displacement component, obtained via Eq. (A.32). We notice that, in contrast to the cases considered in the previous sections, the displacement is negative and has a positive gradient, indicating that the soliton stretches the structure in the longitudinal direction during propagation (note that all solitons considered in previous sections induce compressive stresses within the chain).

As such, these solitary waves can be excited by pulling one end of the chain.

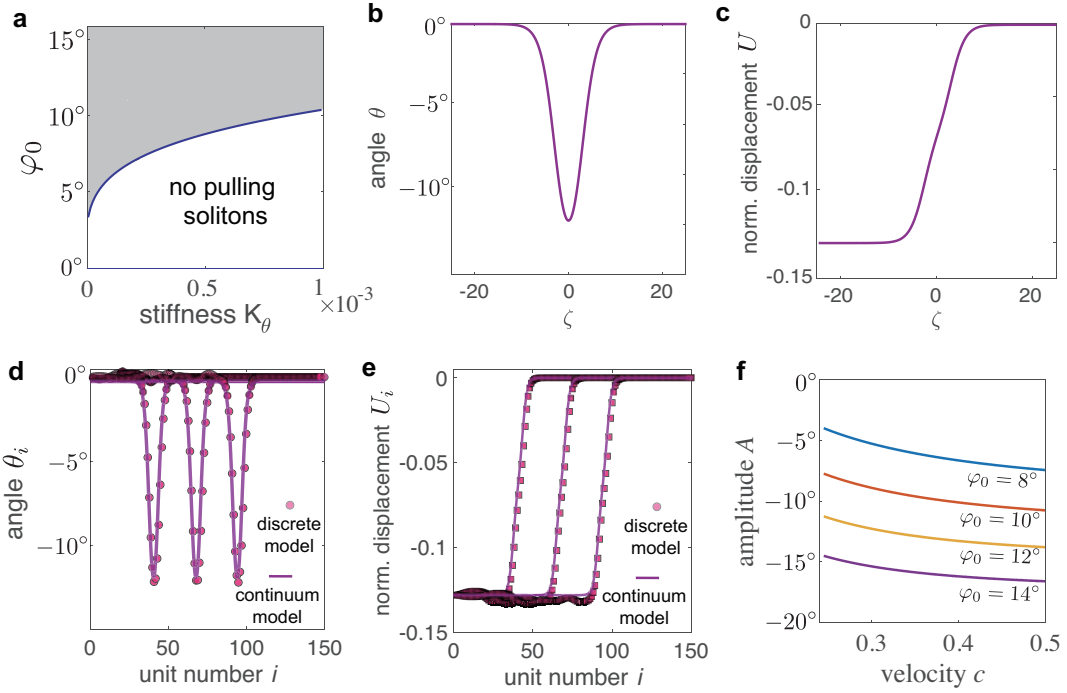


Figure A.15: (a) Region (shaded area) of the φ_0 - K_θ domain in which pulling solitons exist. (b)-(c) Analytical solution for a structure characterized by $K_s = 0.0185$, $K_\theta = 1.5 \times 10^{-4}$, $\alpha = 1.8$, $c = 0.5$ and $\varphi_0 = 8^\circ$. (d)-(e) Comparison between analytically (lines) and numerically (markers) predicted rotation and normalized displacement on the same structure at $T = 226, 294$, and 360 . (f) Relation between pulse velocity and amplitude for pulling solitons propagating in structures characterized by different angles φ_0 .

To verify the validity of our analytical solution, in Figs. A.15(d-e) we compare the analytical solutions to numerical results obtained by direct integration of the full discrete model (Eqs. (A.3)). Note that in this set of simulations we consider a chain with 2×150 crosses and input our theoretical solutions (i.e. Eqs. (A.54)) as boundary conditions for the first pair of crosses at the left end of the chain, while implementing free-boundary conditions at its right end. We find an excellent agreement between our analytical (lines) and numerical (markers) results, confirming the validity of our continuum model. Finally in Fig. A.15(f), we present the c - A relation for solitary waves excited by pulling. Unlike the case of compressive solitons, which propagate faster for smaller amplitudes, we find that the ones with larger amplitude travel faster (i.e. c always increases when

the amplitude A increases). This difference is due to the fact that under compression our system exhibits nonlinear strain softening, while under tension it exhibits strain hardening. Finally, we note that we expect pulling solitons to be difficult experimentally observe, since they require an excitation applied at a very high speed.

A.8 Energy Carried by Solitons

In this section we determine the energy carried by the elastic vector solitons supported by our system. To begin with, we focus on the i -th pair of crosses, whose total energy is given by the sum of the elastic energy stored in the hinges and the kinetic energy of two rigid crosses. As shown in Fig. A.16, there are two types of hinges associated to the i -th pair of crosses: two horizontal hinges (whose deformation is characterized by $\delta_{l_H}^i$, $\delta_{s_H}^i$ and $\delta_{\theta_H}^i$) and one vertical hinge (whose deformation is characterized by $\delta_{l_V}^i$, $\delta_{s_V}^i$ and $\delta_{\theta_V}^i$).

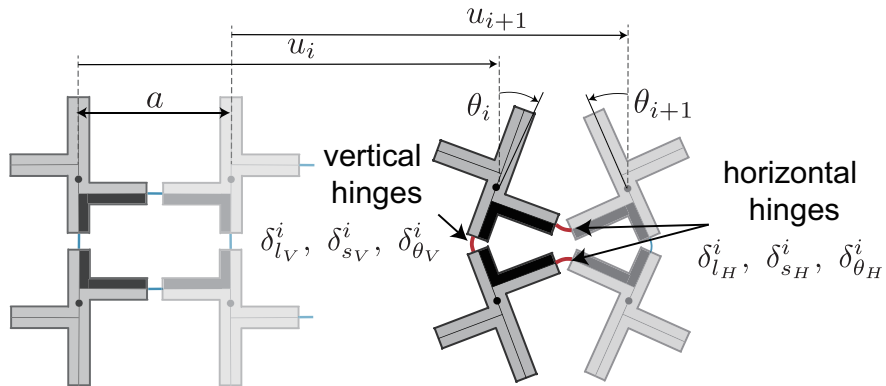


Figure A.16: A schematic diagram for the analysis of unit cell energy.

It follows that the total energy for the i -th pair of crosses can be expressed as,

$$e_i = \frac{1}{2}k_l(2\delta_{l_H}^i)^2 + \frac{1}{2}k_s(2\delta_{s_H}^i)^2 + \frac{1}{2}k_\theta(2\delta_{\theta_H}^i)^2 + m\left(\frac{\partial u_i}{\partial t}\right)^2 + J\left(\frac{\partial \theta_i}{\partial t}\right)^2, \quad (\text{A.55})$$

where

$$\begin{aligned} \delta_{l_H}^i &= u_{i+1} - u_i + \frac{a}{2 \cos \varphi_0} [2 \cos \varphi_0 - \cos(\varphi_0 + \theta_i) - \cos(\varphi_0 + \theta_{i+1})], \\ \delta_{s_H}^i &= \frac{a}{2 \cos \varphi_0} [\sin(\varphi_0 + \theta_{i+1}) - \sin(\varphi_0 + \theta_i)], \\ \delta_{\theta_H}^i &= \theta_{i+1} + \theta_i, \\ \delta_{l_V}^i &= \delta_{s_V}^i = 0, \\ \delta_{\theta_V}^i &= 2\theta_i. \end{aligned} \quad (\text{A.56})$$

Eq. (A.55) can be written in dimensionless form as

$$E_i = \frac{e_i}{ka} = \Delta_{l_H}^{i,2} + K_s \Delta_{s_H}^{i,2} + \frac{K_\theta}{8 \cos^2 \varphi_0} (2\delta_{\theta_H}^i)^2 + \left(\frac{\partial U_i}{\partial T}\right)^2 + \frac{1}{4a^2 \cos^2 \varphi_0} \left(\frac{\partial \theta_i}{\partial T}\right)^2 \quad (\text{A.57})$$

where $\Delta_*^i = \delta_*^i/a$ are the normalized deflections

$$\begin{aligned} \Delta_{l_H}^i &= U_{i+1} - U_i + \frac{1}{2 \cos \varphi_0} [2 \cos \varphi_0 - \cos(\varphi_0 + \theta_i) - \cos(\varphi_0 + \theta_{i+1})], \\ \Delta_{s_H}^i &= \frac{1}{2 \cos \varphi_0} [\sin(\varphi_0 + \theta_{i+1}) - \sin(\varphi_0 + \theta_i)]. \end{aligned} \quad (\text{A.58})$$

Next, we introduce the continuum functions $\theta(X, T)$ and $U(X, T)$ and assume that the width of the propagating waves is much larger than the unit cell size and that $\theta \sim \varphi_0 \ll 1$. The total energy of

the i -th pair of crosses (Eq. (A.57)) can then be approximated as

$$E(X, T) = \left(\frac{\partial U}{\partial X} + \frac{\cos \varphi_0 - \cos(\varphi_0 + \theta)}{\cos \varphi_0} \right)^2 + \frac{K_s}{4} \left(\frac{\partial \theta}{\partial X} \right)^2 + \frac{3K_\theta \theta^2}{2 \cos^2 \varphi_0} + \left(\frac{\partial U}{\partial T} \right)^2 + \frac{1}{4\alpha^2 \cos^2 \varphi_0} \left(\frac{\partial \theta}{\partial T} \right)^2, \quad (\text{A.59})$$

which can be rewritten in terms of the traveling coordinate $\zeta = X - cT$ as

$$E(\zeta) = \left(\frac{\partial U}{\partial \zeta} + \frac{\cos \varphi_0 - \cos(\varphi_0 + \theta)}{\cos \varphi_0} \right)^2 + \frac{K_s}{4} \left(\frac{\partial \theta}{\partial \zeta} \right)^2 + \frac{3K_\theta \theta^2}{2 \cos^2 \varphi_0} + c^2 \left(\frac{\partial U}{\partial \zeta} \right)^2 + \frac{c^2}{4\alpha^2 \cos^2 \varphi_0} \left(\frac{\partial \theta}{\partial \zeta} \right)^2 \quad (\text{A.60})$$

Finally, the energy carried by the elastic vector solitons is given by

$$E_S = \int_{-\infty}^{+\infty} E(\zeta) d\zeta, \quad (\text{A.61})$$

where U and θ entering in Eq. (A.60) are defined by Eqs. (A.29) and (A.32).

In Fig. A.17 we report the evolution of E_S as a function of the amplitude A as predicted by Eq. (A.61) for the aligned (i.e. $\varphi_0 = 0$) and shifted (i.e. $\varphi_0 = 5^\circ$) chains.

A.9 Dispersion Relation

In this section we linearize the discrete governing equations of the system (Eqs. (A.3)) to derive its dispersion relation. We start by assuming that θ_{i+p} (with $p = 0, \pm 1$) is small, so that

$$\begin{aligned} \sin(\theta_{i+p} + \varphi_0) &\approx \sin(\varphi_0) + \cos(\varphi_0)\theta_{i+p}, \\ \cos(\theta_{i+p} + \varphi_0) &\approx \cos(\varphi_0) - \sin(\varphi_0)\theta_{i+p}. \end{aligned} \quad (\text{A.62})$$

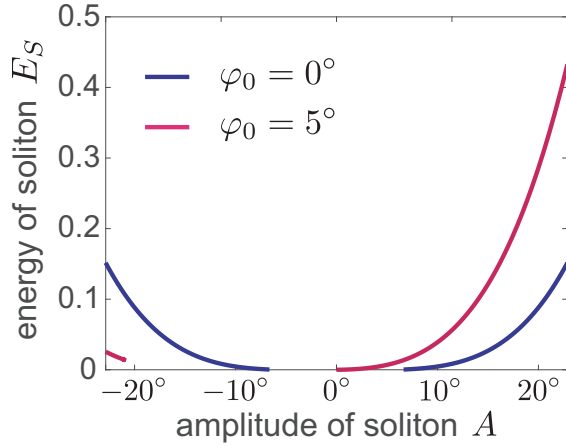


Figure A.17: Evolution of E_S as a function of the amplitude A for the aligned (blue line) and shifted (purple line) chains.

Substitution of Eqs. (A.62) into Eqs. (A.3) yields the linearized equations,

$$\begin{aligned} \frac{\partial^2 U_i}{\partial T^2} &= U_{i+1} - 2U_i + U_{i-1} + \frac{1}{2} \tan(\varphi_0) (\theta_{i+1} - \theta_{i-1}), \\ \frac{1}{\alpha^2} \frac{\partial^2 \theta_i}{\partial T^2} &= (K_s \cos^2(\varphi_0) - \sin^2(\varphi_0) - K_\theta) (\theta_{i+1} + \theta_{i-1}) \\ &\quad - 2 (K_s \cos^2(\varphi_0) + \sin^2(\varphi_0) + 2K_\theta) \theta_i - \sin(2\varphi_0) (U_{i+1} - U_{i-1}), \end{aligned} \quad (\text{A.63})$$

which can be written in matrix form as

$$\mathbf{M} \ddot{\Phi}_i + \sum_{p=-1,0,1} \mathbf{K}^{(p)} \Phi_{i+p} = 0, \quad (\text{A.64})$$

where

$$\mathbf{M} = \begin{bmatrix} 1 & 0 \\ 0 & \alpha^{-2} \end{bmatrix}, \quad \Phi_{i+p} = \begin{bmatrix} U_{i+p} \\ \theta_{i+p} \end{bmatrix},$$

$$\mathbf{K}^{(0)} = \begin{bmatrix} 2 & 0 \\ 0 & 2(K_s \cos^2(\varphi_0) + \sin^2(\varphi_0) + 2K_\theta) \end{bmatrix}, \quad (\text{A.65})$$

$$\mathbf{K}^{(\pm 1)} = \begin{bmatrix} -1 & \mp \tan(\varphi_0) \\ \pm \sin(2\varphi_0) & -(K_s \cos^2(\varphi_0) - \sin^2(\varphi_0) - K_\theta) \end{bmatrix}.$$

Next, we seek a solution of Eqs. (A.64) in the form of a harmonic wave

$$\Phi_i(T) = \tilde{\Phi}_i(\mu) \exp i(\mu X_i - \omega T), \quad (\text{A.66})$$

where ω is the normalized cyclic frequency of harmonic motion (the dimensional cyclic frequency is $\omega\sqrt{k_l/m}$), μ is the wavenumber, $i = \sqrt{-1}$ and $\tilde{\Phi}_i = [\tilde{U}_i, \tilde{\theta}_i]$ is a vector that defines the amplitude of wave motion. Substitution of Eq. (A.66) into Eq. (A.64) yields

$$-\omega^2 \mathbf{M} \tilde{\Phi}_i + \sum_{p=-1,0,1} \mathbf{K}^{(p)} \tilde{\Phi}_{i+p} e^{i\mu X_{i+p}} = 0, \quad (\text{A.67})$$

with $X_{i+p} = i + p$. Eq. (A.67) is an eigenvalue problem that yields two dispersion branches, $\omega^{(1)}(\mu)$ and $\omega^{(2)}(\mu)$, each corresponding to a linear wave mode. While for the general case $\varphi_0 \neq 0$ Eq. (A.67) can only be solved numerically to find $\omega^{(1)}$ and $\omega^{(2)}$, for the special case $\varphi_0 = 0$ an analytical

solution exists

$$\begin{aligned}\omega^{(1)} &= \sqrt{2 - 2 \cos \mu}, \\ \omega^{(2)} &= \alpha \sqrt{2(K_s + 2K_\theta) - 2(K_s - K_\theta) \cos \mu}.\end{aligned}\tag{A.68}$$

with the corresponding eigenvectors given by

$$\tilde{\Phi}^{(1)} = [1, 0]^T \text{ and } \tilde{\Phi}^{(2)} = [0, 1]^T\tag{A.69}$$

In Figs. A.18(a-b) we report the dispersion relation for a chain with $\varphi_0 = 0^\circ$ and 5° , respectively. Note that each point on the dispersion curves is color-coded to show the corresponding modal polarization, which for the k -th branch is defined as

$$\eta_\theta^{(k)} = \frac{\tilde{\theta}_i^{(k)}}{\sqrt{\left(\tilde{\theta}^{(k)}\right)^2 + \left(\tilde{U}_i^{(k)}\right)^2}}, \text{ with } k = 1, 2.\tag{A.70}$$

We find that the linear modes of the structure with $\varphi_0 = 5^\circ$ contain both rotational and translational component (i.e., the two degrees of freedom are coupled). Differently, for the special case $\varphi_0 = 0^\circ$ the two propagation modes are fully decoupled, each associated with a single degree of freedom (i.e. since $\eta_\theta = 0$ on the first branch and $\eta_\theta = 1$ on the second one, the corresponding modes are purely translational and rotational, respectively). We also find that for the case $\varphi_0 = 0^\circ$ the purely rotational mode branch starts at a finite frequency (i.e. linear waves with rotational component are not supported for $\omega < \alpha\sqrt{6K_\theta}$), indicating that the system possesses a linear low-frequency band gap for rotation (highlighted in green in Fig. A.18(a)). To demonstrate the effect of such linear frequency gap, we numerically solve the ODEs given by Eqs. (A.3) for a chain with 150 pairs of

crosses excited by a longitudinal displacement $U_{input} = 10^{-4} \sin \omega T$ applied to the mid-point at its left end. In Figs. A.18 (c-d) we report the numerically recorded transmittance for both rotational and translational component, $\max(\theta_{100}(T)) / \max(\theta_2(T))$ and $\max(U_{100}(T)) / \max(U_2(T))$. We find that for the case $\varphi_0 = 0$ the transmission of rotational modes significantly drops at low frequencies, confirming the existence of the low-frequency band gap for rotations. By contrast, no such drop in transmission is observed for the system with $\varphi_0 = 5^\circ$, a consequence of the absence of any type of gap.

Lastly, it is important to note that the frequency content of the solitary waves supported by our system overlaps with this low-frequency band gap for rotation (see Fig. A.18(e) for a typical soliton characterized by $A = 0.30$). As discussed in the main text and in Supplementary Note 9, the behavior of our soliton splitters is affected by such overlap, which prevents radiation of rotational vibrations.

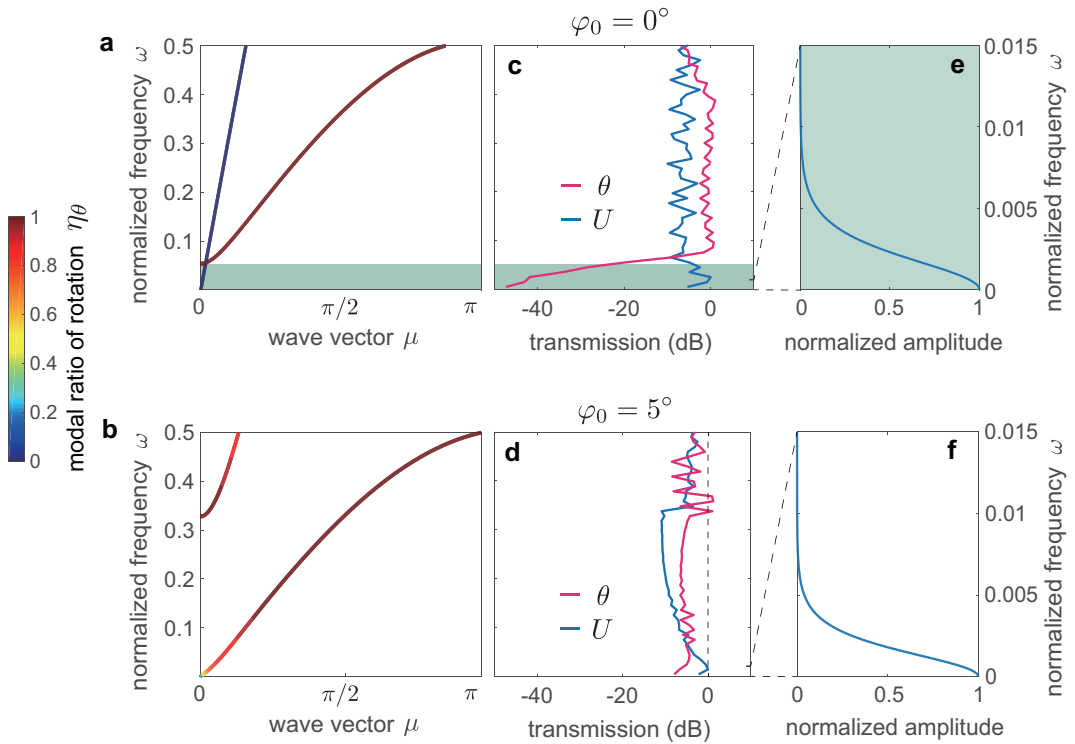


Figure A.18: (a)-(b) Linear dispersion relations for a chain with $\varphi_0 = 0$ and $\varphi_0 = 5^\circ$, respectively. The dispersion curves are color-coded to show the modal ratio of rotation η_θ . (c)-(d) Amplitude transmission coefficients of the two linear modes for a chain with $\varphi_0 = 0$ and $\varphi_0 = 5^\circ$, respectively; (e)-(f) Frequency content of a typical soliton supported by a chain with $\varphi_0 = 0$ and $\varphi_0 = 5^\circ$, respectively. Note that the frequency range is changed in order to show the low frequency dominance in the soliton.

A.10 Additional Results for Splitter

In this Section, we report the results of additional numerical analysis and experiments conducted on our soliton splitter.

A.10.1 Experimental results

While in the main text we show experimental results for a soliton splitter with a pair of stiffer hinges made of polyester sheets with thickness $t_h^d = 0.635$ mm (so that $K_s^d/K_s = K_\theta^d/K_\theta = 30$), in Fig. A.19 we present experimental results for our 2×50 sample with $\varphi_0 = 0$ and two stiffer hinges made of polyester sheets with thickness $t_h^d = 0.508$ mm (Fig. A.19(a)) and $t_h^d = 0.635$ mm (Fig. A.19(b)) and paper clips (Fig. A.19(c)), which connect the 24th and the 25th pairs of crosses. Note that these three pairs of stiffer hinges result in $K_s^d/K_s = K_\theta^d/K_\theta = 18, 30$ and 175 , respectively. The results clearly indicate that the amount of reflected and transmitted energy can be controlled by varying the stiffness ratio. For the splitter characterized by $K_s^d/K_s = K_\theta^d/K_\theta = 18$, most of the energy of the incident pulse is carried by the transmitted soliton and only a small portion by the reflected one; for the splitter characterized by $K_s^d/K_s = K_\theta^d/K_\theta = 30$, as described in main text, the energy carried by the incident pulse is roughly equally split between the transmitted and reflected solitons; for the splitter characterized by $K_s^d/K_s = K_\theta^d/K_\theta = 175$, most of the energy of the incident pulse is carried by the reflected soliton.

Finally, in Fig. A.20 we compare the experimentally measured rotation during the propagation of the pulse in a chain characterized by $\varphi_0 = 0^\circ$ (Fig. A.20(a)) and $\varphi_0 = 5^\circ$ (Fig. A.20(b)). Note that in both cases the sample comprises 2×50 units and a stiffer pair of hinges made of polyester sheets with thickness $t_h^d = 0.635$ mm is introduced to connect the 24th and the 25th pairs of crosses. While

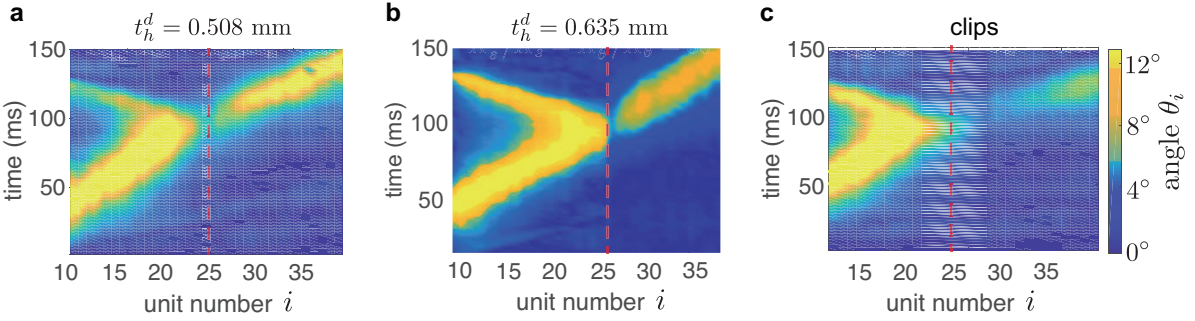


Figure A.19: Experimentally measured rotation of the pairs of crosses during the propagation of the pulse for soliton splitters with two stiffer hinges made of (a) polyester sheets with thickness $t_h^d = 0.508$ mm, (b) polyester sheets with thickness $t_h^d = 0.635$ mm and (c) paper clips. The location of the stiff pair of hinges is indicated by the dashed red line

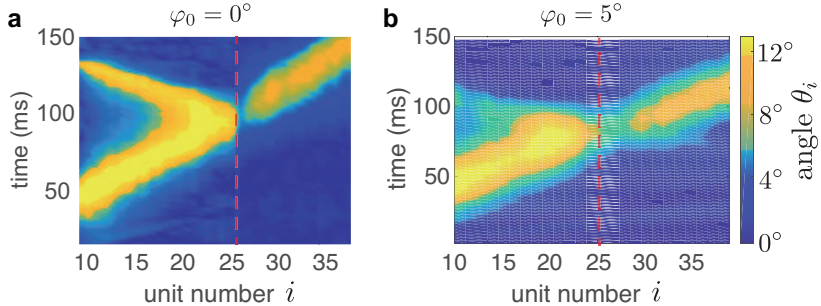


Figure A.20: Experimentally measured rotation during the propagation of the pulse for soliton splitters characterized by (a) $\varphi_0 = 0^\circ$ and (b) $\varphi_0 = 5^\circ$. The location of the stiff pair of hinges (made of polyester sheets with thickness $t_h^d = 0.635$ mm) is indicated by the dashed red line

in the aligned chain, the pulse excited at the left end of the chain is split into two clean solitons by the pair of stiffer hinges, in the shifted chain the signal both transmitted and reflected by the stiffer pair of hinges is much more noisy.

A.10.2 Numerical results

While in Fig. 2.3 of the main text we present results only for the rotational component θ , in Fig. A.21 we show also the evolution of U as the solitary wave propagates in a 2×1000 chain characterized by $\varphi_0 = 0$ with a pair of stiffer hinges (with $K_s^d/K_s = K_\theta^d/K_\theta = 30$) connecting the 500th and 501st rigid crosses. The spatio-temporal plots for both θ (Fig. A.21(a)) and U (Fig. A.21(c)) clearly

indicate that the pair of stiffer hinges splits the incoming soliton into two pulses that propagate with stable shape and constant velocity and that no trains of solitons are generated. As for the radiation of linear waves, we find that the interaction between the soliton and the stiffer hinges generate only translational vibrations (see small fluctuations in Fig. A.21c), since the overlap between the frequency content of the solitary waves supported by our system and the low-frequency band gap for rotation (see Fig. A.18) prevents radiation of small amplitude rotational waves. We also note that the energy transferred to the translational vibrations can be estimated by comparing the energy carried by the incident soliton to that carried by the reflected and transmitted ones. Since in the aligned chain (i.e. for $\varphi_0 = 0$) the amplitudes of the incident, reflected and transmitted solitons are measured to be $A_i = 17.2^\circ$, $A_r = 13.75^\circ$ and $A_t = 14.89^\circ$ (see Figs. A.21 (a-b)), using Eq. (A.61) and the results of Fig. A.17 we find that the normalized energy carried by them is $E_{S,i} = 0.0465$, $E_{S,r} = 0.0184$ and $E_{S,t} = 0.0262$, respectively. Hence, since in our splitter $(E_{S,r} + E_{S,t})/E_{S,i} = 0.96$, only 4% of the energy carried by the incoming soliton is transferred to translational linear vibrations. By contrast, for the shifted structure (for which $\varphi_0 = 5^\circ$) we measure $A_i = 16.45^\circ$, $A_r = 5.45^\circ$ and $A_t = 12.08^\circ$ (see Figs. A.21(e-f)), so that $E_{S,i} = 0.1575$, $E_{S,r} = 0.008$ and $E_{S,t} = 0.064$. As such, in the shifted structure, which lacks both an amplitude gap for solitons and a low-frequency band gap for linear rotational vibrations, $\sim 54\%$ of the energy carried by the incoming solitary wave is transferred to small amplitude solitons and linear vibrations. Finally, it is important to point out that the group velocity of the longitudinal vibrations supported by the chain characterized by $\varphi_0 = 0$ is one magnitude larger than the typical velocity of solitons (i.e. the solitons propagating in the chain have velocity $c \sim 0.1$, whereas the velocity of the longitudinal vibration in the long wavelength limit is found from the dispersion relation of Fig. A.18(a) to be ~ 1). As such, the linear waves propagating in our splitter are very fast and do not interfere with the transmitted and

reflected solitary waves, leading to a clean splitter for solitons.

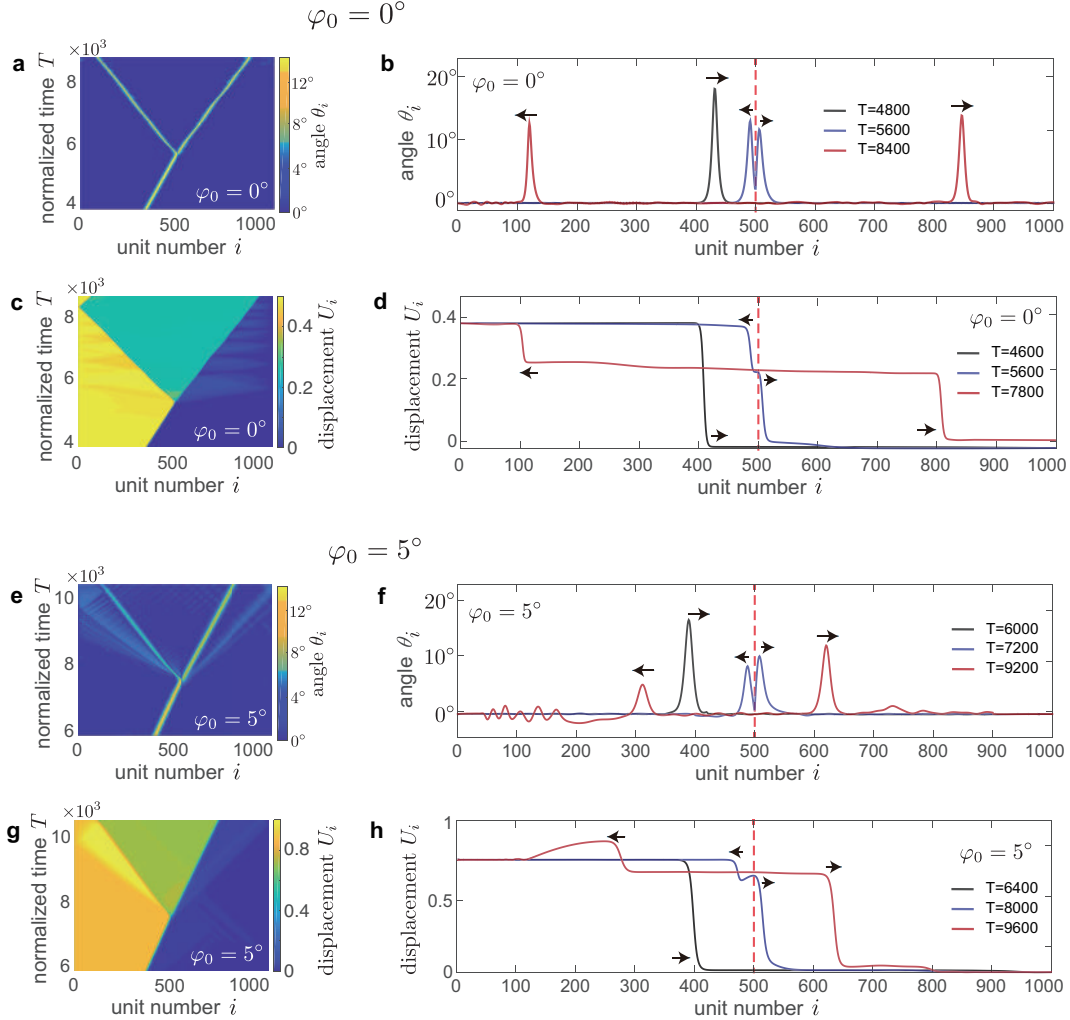


Figure A.21: Soliton splitter with a stiff defect ($K_s^d/K_s = K_\theta^d/K_\theta = 30$) between the 500th and 501st rigid crosses. (a)-(d) Numerical results for a 2×1000 chain with symmetric crosses characterized by $\varphi = 0^\circ$. (e)-(h) Numerical results for a 2×1000 chain with asymmetric crosses characterized by $\varphi = 5^\circ$.

While the results reported in Fig. A.21 are for a chain with a stiffer hinge, we also conducted an additional numerical simulation on a chain that embeds a softer hinge. More specifically, we considered a chain comprising 1000 units and a pair of softer hinges (with $K_s^d/K_s = K_\theta^d/K_\theta = 1/30$) connecting the 500th and 501st rigid crosses. The results shown in Figs. A.22(a-d) indicate that in the system with $\varphi_0 = 0$ the fragmented oscillations are wiped out due to the amplitude gap and that

only a small amount of purely translational vibrations are generated by the interaction between the soliton and the softer pair of hinges. Differently, for the shifted chain ($\varphi_0 = 5^\circ$) due to the absence of both the amplitude gap for solitary waves (i.e. $A_{upper} = 0^\circ$ for the system) and the low-frequency linear gap for rotational vibrations, trains of pulses and linear vibrations are generated when the propagating soliton hits the pair of softer hinges.

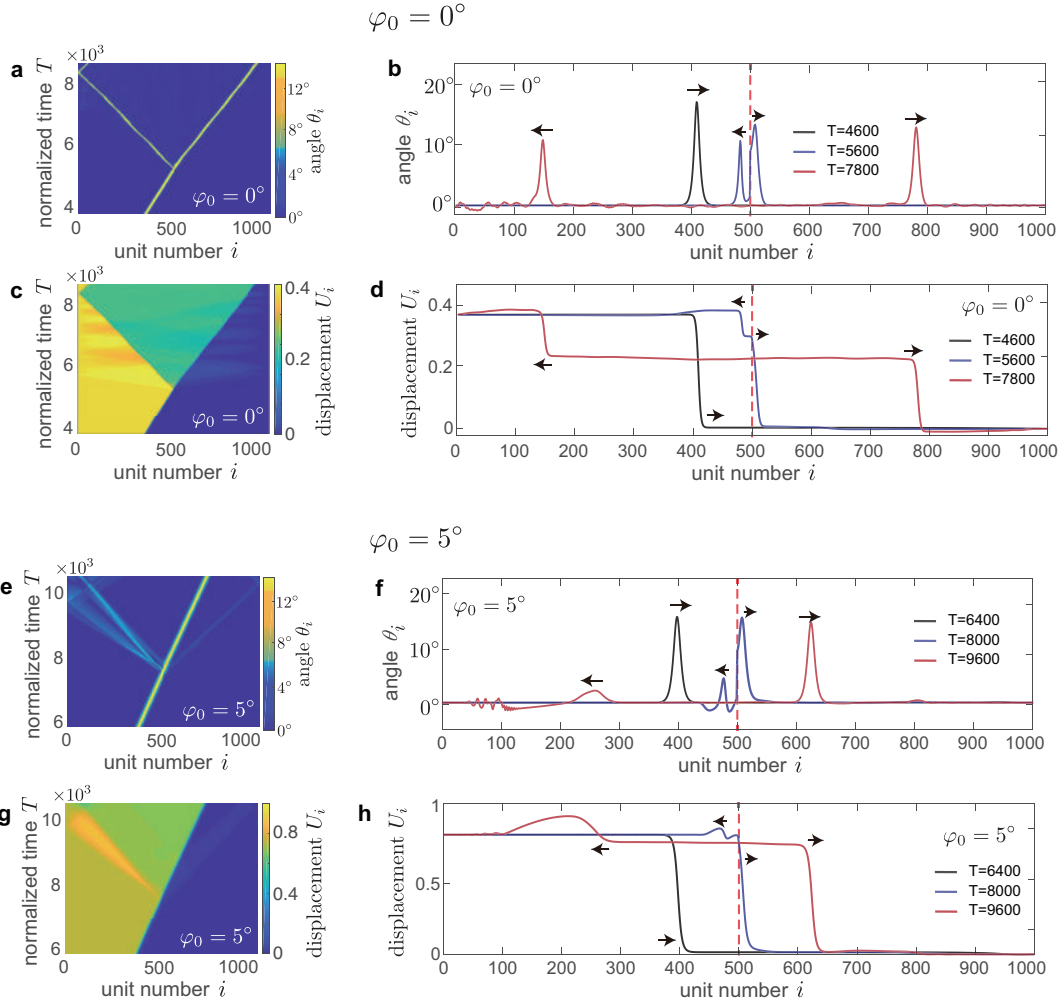


Figure A.22: Soliton splitter with a softer defect ($K_s^d/K_s = K_\theta^d/K_\theta = 1/30$) between the 500th and 501st rigid crosses. (a)-(d) Numerical results for a 2×1000 chain with symmetric crosses characterized by $\varphi = 0^\circ$. (e)-(h) Numerical results for a 2×1000 chain with asymmetric crosses characterized by $\varphi = 5^\circ$.

Finally, we conduct a set of discrete numerical simulations on an aligned chains to further

explore the effect of the stiffness ratio $K_s^d/K_s = K_\theta^d/K_\theta$ on the response of the system. In all our simulations we consider an aligned chains (i.e. $\varphi_0 = 0^\circ$) comprising 2×1000 crosses and a pair of stiffer hinges (with stiffness K_s^d and K_θ^d) connecting the 500th and 501st units. In our simulations we

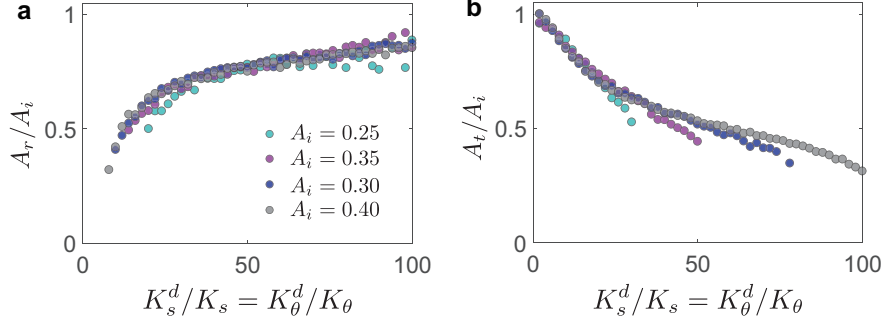


Figure A.23: Numerical results showing the effect of $K_s^d/K_s = K_\theta^d/K_\theta$ on the amplitude of the transmitted and reflected solitons. Amplitude ratios (a) A_r/A_i and (b) A_t/A_i as a function of $K_s^d/K_s = K_\theta^d/K_\theta$ for different values of A_i . The splitter considered in our simulations comprises a chain of 2×1000 crosses with $\varphi_0 = 0^\circ$, $K_s = 0.02$, $K_\theta = 1.5 \times 10^{-4}$, $\alpha = 1.8$ and $\varphi = 0^\circ$. A pair of stiffer hinges are inserted at the center of the chain with stiffness ratio $K_s^d/K_s = K_\theta^d/K_\theta \in [1, 100]$.

consider $K_s^d/K_s = K_\theta^d/K_\theta \in [1, 100]$ and input our theoretical solutions (i.e. Eqs. (A.29) and (A.32)) as boundary conditions for the first pair of crosses at the left end of the chain, while implementing free-boundary conditions at its right end. We consider input signal of different magnitude (A_i), identify the normalized time T_c at which the pulse is split by the stiffer pair of hinges and then monitor the amplitude of the reflected (A_r) and transmitted (A_t) solitons at T_c+1000 . In Figs. A.23(a-b) we show the amplitude ratios A_r/A_i and A_t/A_i for $A_i = 0.25, 0.30, 0.35$ and 0.40 . We find that: (i) the amplitude of the reflected soliton A_r increases monotonically with $K_\theta^d/K_\theta = K_s^d/K_s$; (ii) the amplitude of the transmitted soliton A_t decreases monotonically for increasing $K_\theta^d/K_\theta = K_s^d/K_s$; (iii) Both A_r/A_i and A_t/A_i do not depend on the amplitude of the input signal, suggesting that our soliton splitter is a robust device.

A.11 Additional Results for Diode

In this Section, we provide additional experimental and numerical results for our mechanical diode.

A.11.1 Experimental results

In Fig. 2.4 of the main text we report the spatio-temporal rotation diagrams for two of the experiments we conducted on our mechanical diode. In Fig. A.24 we show the experimental results for the remaining five experiments.

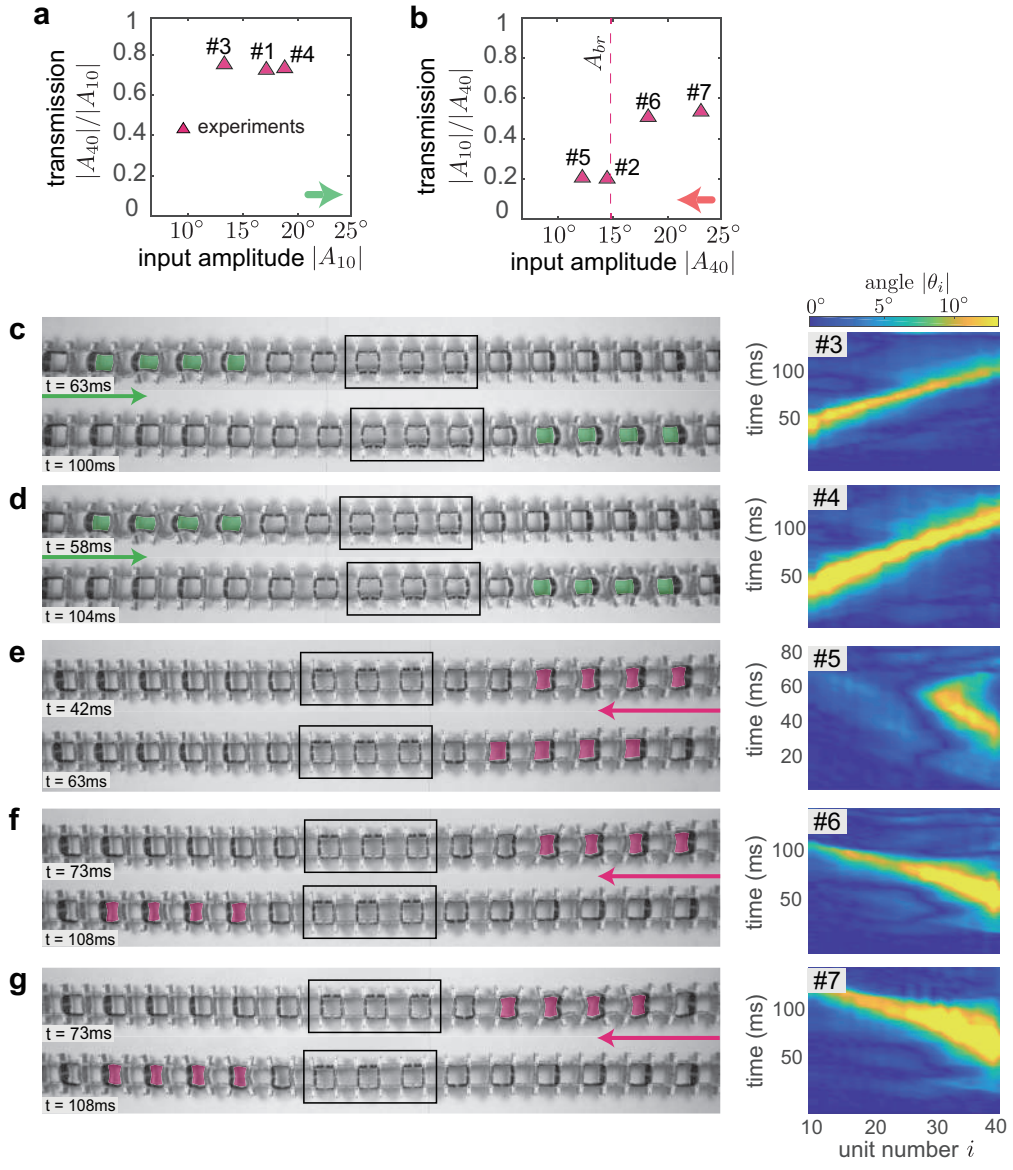


Figure A.24: (a) Experimentally measured transmission, $|A_{40}|/|A_{10}|$, as a function of the input amplitude, $|A_{10}|$, for pulses excited at the left end of the chain. (b) Experimentally measured transmission, $|A_{10}|/|A_{40}|$, as a function of the input amplitude, $|A_{40}|$, for pulses excited at the right end of the chain. (c)-(g) Optical images and corresponding rotation of the pairs of crosses as measured in five different experiments.

A.11.2 Numerical results

In the main text, we have investigated the response of a mechanical diode with $2N$ and $(2N + 1)$ pairs of crosses characterized by $\varphi_0 = 0$ and a central portion consisting of $2N_a$ pairs of crosses with

$\varphi_0 = 5^\circ$, assuming $N = 12$ and $N_a = 3$ (see Fig. 2.4 of the main text). We found that for all pulses with amplitude larger than $A_{upper}^{\varphi_0=0} = 6.55^\circ$ initiated at the left end of the system the transmission, $|A_{40}|/|A_{10}|$ approaches unity. Differently, when the excitation is applied at the right end of the chain, the transmission $|A_{10}|/|A_{40}|$ is close to zero, even if the amplitude of the input signal is outside the gap of the region with $\varphi_0 = 0$ (i.e. $|A_{40}| > A_{upper}^{\varphi_0=0}$). However, as typically observed in electronic^[154] and thermal^[109] diodes, if the amplitude of the pulses becomes too large, the diode experiences a condition known as breakdown. As a result, solitary waves with amplitude larger than $A_{br} \approx 15^\circ$ propagate through the diode (i.e. if $|A_{40}| > A_{br} \approx 15^\circ$, then $|A_{10}|/|A_{40}| \sim 0.6$). It is important to note that the breakdown amplitude A_{br} is analogous to the breakdown voltage of electronic diodes and determines the reliability of the device, since it defines the largest amplitude of a soliton that the diode can block.

To study the effect of φ_0 and N_a on A_{br} , we conduct a set of discrete simulations in which we excite pulses of different amplitude at the right end of the chain and measure the transmission $|A_{10}|/|A_{40}|$. In Fig. A.25(a) we report the measured transmission as a function of the amplitude of the input signal for diodes characterized by different values of N_a and $\varphi_0 = 5^\circ$ (while keeping $N=12$). We find that as N_a increases, A_{br} becomes larger, indicating a longer shifted section enhances the performance of our diode. We also note that for $N_a = 1$, the transmission is always close to unity and our structure no longer functions as a diode. In fact, every incident soliton large enough to propagate through the aligned chain tunnels through such a diode.

In Fig. A.25(b) we report the measured transmission as a function of the amplitude of the input signal for diodes characterized by $N_a = 3$, $\varphi_0 = 3^\circ$ and 7° , and $N=12$. We find that lower values of φ_0 make the diode less reliable, since A_{br} decreases ($A_{br} \approx 15^\circ$ for $\varphi_0 = 5^\circ$ and $A_{br} \approx 10^\circ$ for $\varphi_0 = 3^\circ$). Differently, for $\varphi_0 = 7^\circ$, all pulses considered in the simulations are blocked by the diode

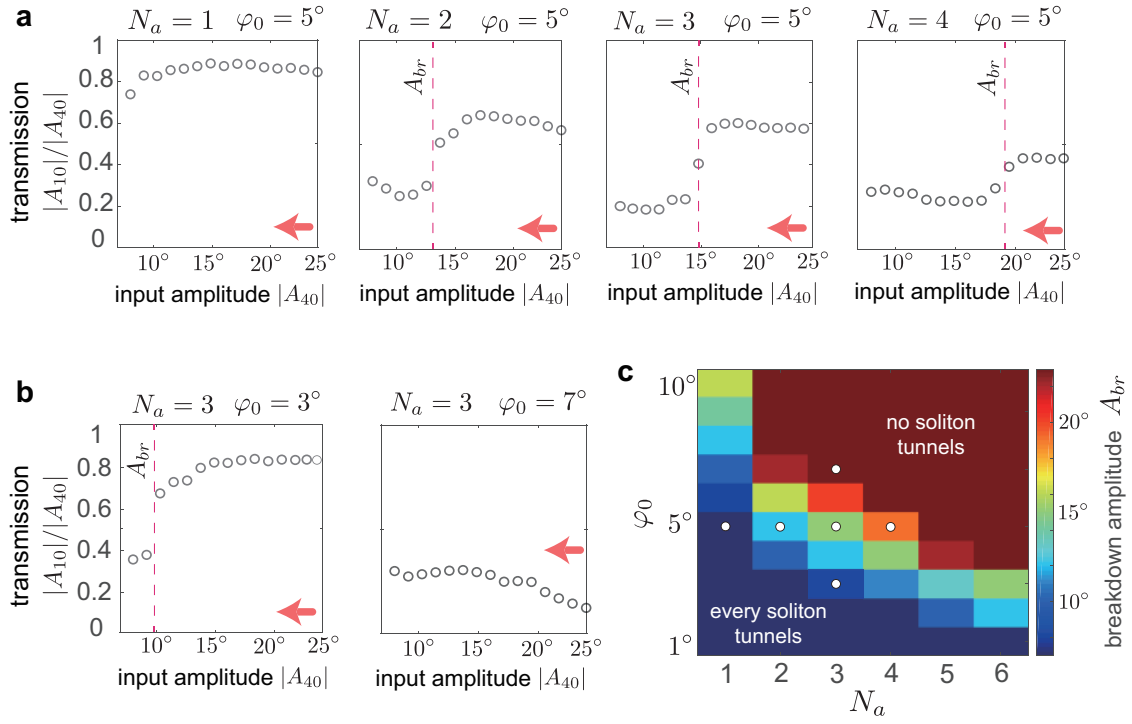


Figure A.25: Numerical results showing the effect of N_a and φ_0 on the breakdown amplitude A_{br} . (a) Transmission as a function of the amplitude of the input signal for diodes characterized by different numbers N_a of pairs of crosses with $\varphi_0 = 5^\circ$ (while keeping $N=12$). (b) Transmission as a function of the amplitude of the input signal for diodes characterized by $N_a = 3$ and $\varphi_0 = 3^\circ$ and 7° (while keeping $N=12$). (c) Evolution of the breakdown amplitude A_{br} as a function of N_a and φ_0 .

and no solitons tunnel through.

Finally, in Fig. A.25(c) we summarize all of our numerical results and report the evolution of A_{br} as a function of N_a and φ_0 .

Appendix B

Supplementary Information:

Anomalous Collisions of Elastic Vector Solitons in Mechanical Metamaterials

By: Bolei Deng, Vincent Tournat, Pai Wang Katia Bertoldi. Published in *Physical Review Letters*,
on Feb. 1 2019. [doi:10.1103/PhysRevLett.122.044101](https://doi.org/10.1103/PhysRevLett.122.044101)

B.1 Fabrication

Our system is identical to that recently considered in^[12] and consists of a long chain of 2×50 crosses made of LEGO bricks that are connected by thin and flexible hinges made of plastic shims. Each cross-shaped unit is realized using four brackets $2 \times 2-2 \times 2$ (LEGO part 3956), as shown in Fig. B.1. The hinges are realized by laser cutting the octagonal shape shown in Fig. B.1(a) out of polyester plastic sheets (Artus Corporation, NJ - 0.005", Blue) with thickness $t_h = 0.127$ mm, Young's modulus $E = 4.33$ GPa and Poisson's ratio $\nu = 0.4$. The size of the octagonal shape is chosen to leave hinges of length $l_h = 4$ mm between the cross-shaped rigid units. Note that eight circular holes are incorporated into each hinge. They fit into the LEGO knobs and enable us to fix the hinges between the interlocking LEGO bricks (see Fig. B.1(b)). Note that in both samples identical bricks of different colors (black and gray) are used to facilitate visualization of the propagating pulses.

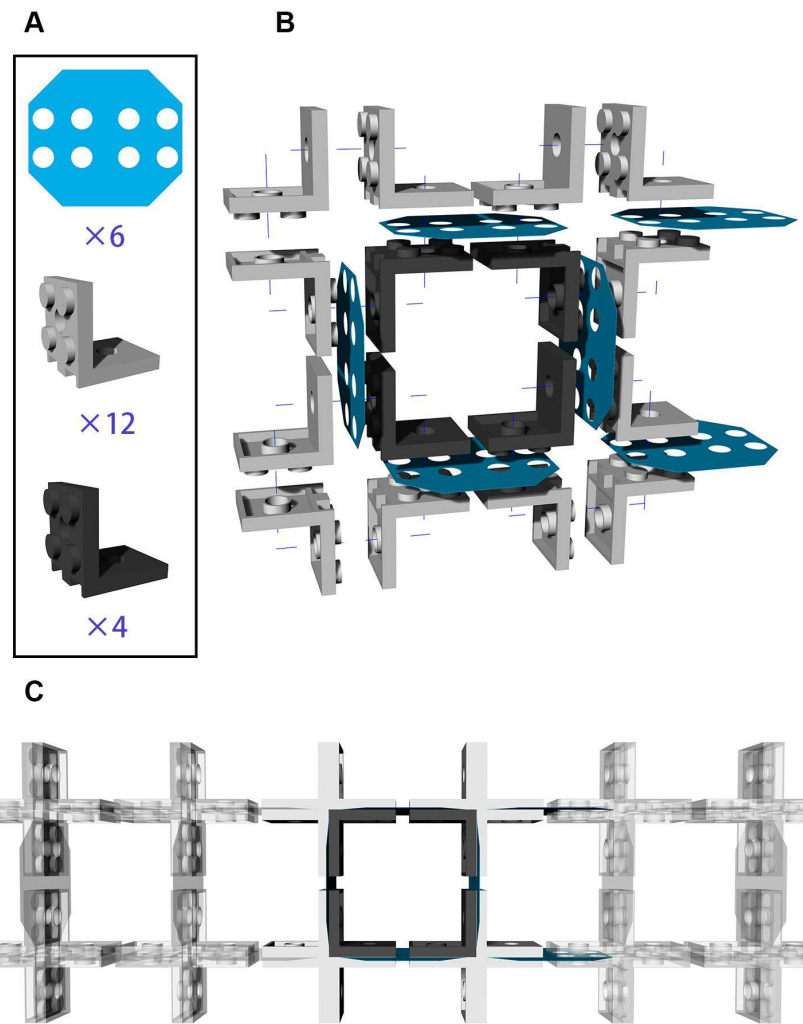


Figure B.1: Fabrication of our structure. (A) Parts used to fabricate a 2×2 unit. (B) Exploded view of two pairs of crosses. (C) The chain is realized by putting together a number of 2×2 units.

B.2 Testing

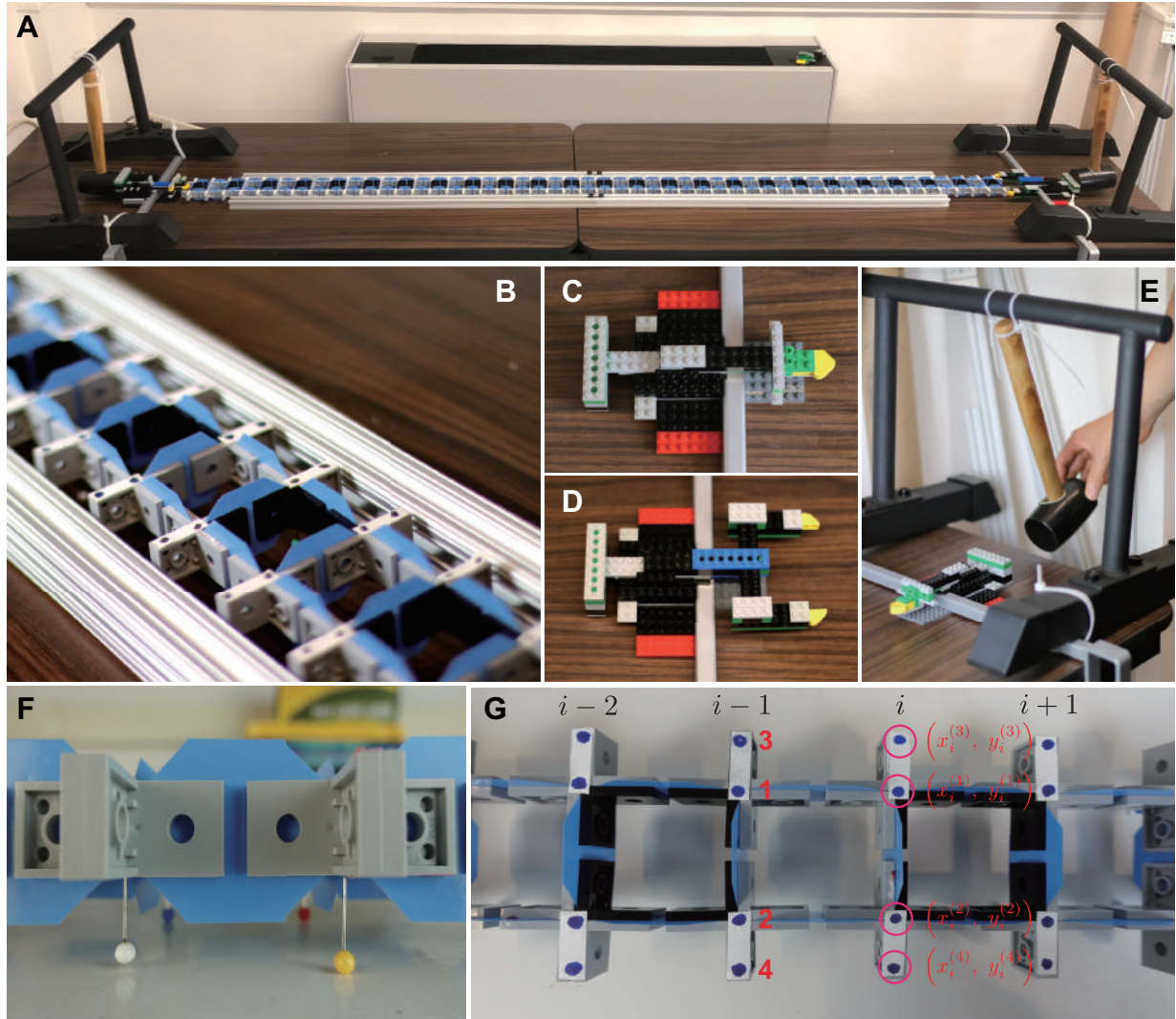


Figure B.2: Experimental setup. (A) Pictures of our experimental setup showing the LEGO chain, the metal bars used to constrain the transverse movement of the chain and the pendulums and impactors used to excite the pulses at both ends. (B) A few units of our sample. (C) The impactor used to initiate solitons that excite positive rotations. (D) The impactor used to initiate solitons that excite negative rotations. (E) Close view of the pendulum consisting of a metal frame and a hammer. (F) Friction is minimized by supporting each rigid unit with pins. (G) Digital image correlation analysis. For each pair of rigid crosses four markers (blue dots) are tracked.

To investigate the propagation of pulses in our sample, we place the chain on a smooth horizontal surface (supported by pins to minimize the effect of friction - see Fig. B.2(f)) and use two

impactors excited by two pendulums (see Figs. B.2(a-b) to initiate the waves. Two metal bars are placed on both sides of the chain to keep it straight. Note that the metal bars are not interacting with the chain during the propagation of nonlinear waves since the structure shrinks transversely due to the rotation of crosses. Different input signals are applied to the chain by varying both the strength of the pulse (controlled by the initial height of the striking pendulum) and the amplitude of the pulse (controlled by the distance traveled by the impactor). Furthermore, the direction of rotation imposed to the first and last pairs of crosses is controlled by using two different types of impactors. Specifically, since we define as positive a clockwise (counter-clockwise) rotation of the top unit in the even (odd) pairs, we use an impactor that hits the mid-point of the end pairs to excite positive rotation (see Fig. B.2(c)) and one that hit their external arms to excite negative θ_i (see Fig. B.2(d)). At this point we also want to point out that the direction of rotations imposed by the impactors changes if the chain comprises an odd number of pairs. If the chain has a odd number of pairs, the impactor that hits the mid-point of the last pair excite negative rotations (see Fig. B.2(c)) and the one that hit the external arms of the last pair excite negative rotations (see Fig. B.2(d)).

To monitor the displacement, u_i , and rotation, θ_i , of i -th pair of crosses along the chain as the pulses propagate, we use a high speed camera (SONY RX100V) recording at 480 fps and track four markers placed on the external arms of each pair of crosses (see Fig. B.2(g)) via digital image correlation analysis^[153]. More specifically, the longitudinal displacement u_i and rotation θ_i of the

i -th pair of rigid units is obtained as

$$u_i(t) = \frac{1}{2} \sum_{\gamma=1,2} \left[x_i^{(\gamma)}(t) - x_i^{(\gamma)}(0) \right]$$

$$\theta_i(t) = \frac{1}{2} \sum_{\gamma=1,2} (-1)^{i+\gamma} \arcsin \left[\frac{\left(x_i^{(\gamma+2)}(t) - x_i^{(\gamma+2)}(0) \right) - \left(x_i^{(\gamma)}(t) - x_i^{(\gamma)}(0) \right)}{\sqrt{\left(x_i^{(\gamma+2)}(0) - x_i^{(\gamma)}(0) \right)^2 + \left(y_i^{(\gamma+2)}(0) - y_i^{(\gamma)}(0) \right)^2}} \right] \quad (\text{B.1})$$

where $(x_i^{(\gamma)}(t), y_i^{(\gamma)}(t))$ and $(x_i^{(\gamma)}(0), y_i^{(\gamma)}(0))$ are the coordinates of the γ -th marker placed on the i -th pair of rigid units at time t and that time $t = 0$ (i.e. before the impact), respectively.

B.3 Mathematical Models

B.3.1 Discrete model

Our system consists of a long chain of $2 \times N$ crosses with center-to-center distance a that are connected by thin and flexible hinges (see Fig. B.3). Since in this work we focus on the propagation of longitudinal nonlinear waves along the chain, we assign two degrees of freedom to each rigid cross: the longitudinal displacement u and the rotation in the $x - y$ plane θ . Moreover, guided by our experiments, we assume that each pair of crosses shares the same displacement and rotates by the same amount, but in opposite directions (i.e. if the top cross rotates by a certain amount in clockwise direction, then the bottom one rotates by the same amount in counter-clockwise direction, and vice versa). As such, two degrees of freedom are assigned to the i -th pair of crosses: the longitudinal displacement u_i and the rotation θ_i (see Fig. B.3). Moreover, to facilitate the analysis, we define a clockwise (counter-clockwise) rotation of the top unit in the even (odd) columns to be positive, and similarly a clockwise (counter-clockwise) rotation of the bottom unit in the odd (even)

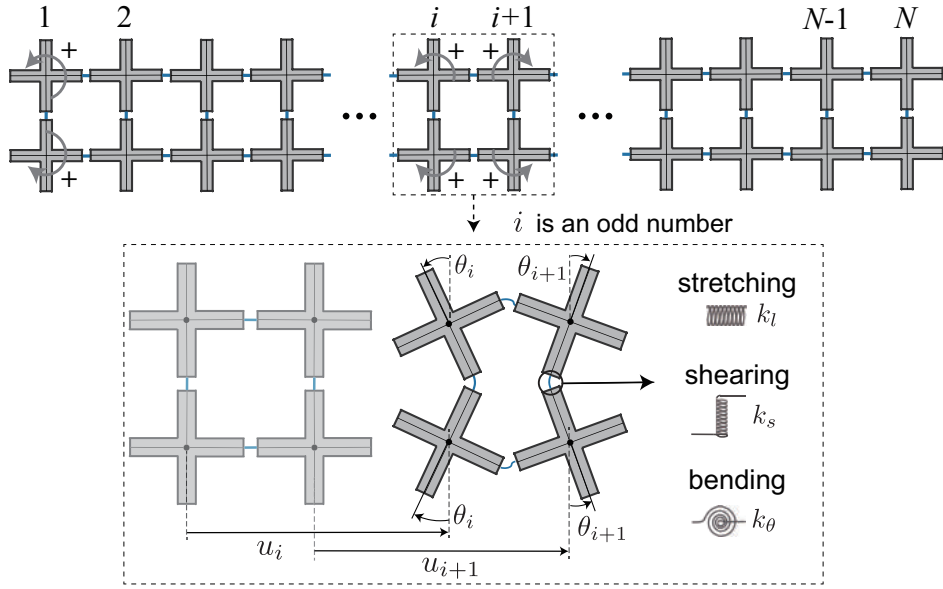


Figure B.3: Schematics of the structure considered in this study.

columns to be negative (positive rotation directions are denoted by yellow arrows in Fig. B.3).

As for the hinges, we model them using a combination of three linear springs: (i) their stretching is captured by a spring with stiffness k_l ; (ii) their shearing is governed by a spring with stiffness k_s ; (iii) their bending is captured by a torsional spring with stiffness k_θ (see Fig. B.3).

Under these assumptions, the equations of motion for the i -th pair of crosses are given by^[121]

$$\begin{aligned} m\ddot{u}_i &= k_l \left[u_{i+1} - 2u_i + u_{i-1} - \frac{a}{2} (\cos \theta_{i+1} - \cos \theta_{i-1}) \right], \\ J\ddot{\theta}_i &= -k_\theta(\theta_{i+1} + 4\theta_i + \theta_{i-1}) + \frac{k_s a^2}{4} \cos \theta_i [\sin \theta_{i+1} - 2 \sin \theta_i + \sin \theta_{i-1}] \\ &\quad - \frac{k_l a}{2} \sin \theta_i [(u_{i+1} - u_{i-1}) + \frac{a}{2} (4 - \cos \theta_{i+1} - 2 \cos \theta_i - \cos \theta_{i-1})], \end{aligned} \quad (\text{B.2})$$

where m and J are the mass and moment of inertia of the rigid crosses, respectively.

Next, we introduce the normalized inertia $\alpha = a\sqrt{m/(4J)}$ and stiffness ratios $K_\theta = 4k_\theta/(k_l a^2)$

and $K_s = k_s/k_l$. Eqs. (B.2) can then be written in dimensionless form as

$$\begin{aligned} \frac{a^2}{c_0^2} \frac{\partial^2 u_i}{\partial t^2} &= u_{i+1} - 2u_i + u_{i-1} - \frac{a}{2} [\cos \theta_{i+1} + \cos \theta_{i-1}], \\ \frac{a^2}{c_0^2 a^2} \frac{\partial^2 \theta_i}{\partial t^2} &= -K_\theta (\theta_{i+1} + 4\theta_i + \theta_{i-1}) + K_s \cos \theta_i \left[\sin \theta_{i+1} + \sin \theta_{i-1} - 2 \sin \theta_i \right] \\ &\quad - \sin \theta_i \left[2(u_{i+1} - u_{i-1}) / a + 4 - \cos \theta_{i+1} - 2 \cos \theta_i - \cos \theta_{i-1} \right], \end{aligned} \quad (\text{B.3})$$

where $c_0 = a\sqrt{k_l/m}$ is the velocity of the longitudinal linear waves supported by the chain in the long wavelength limit. As described in section B.4, since it is extremely challenging to derive an analytical solution that captures the interaction between the solitons propagating in our system, we study collisions by numerically integrating the $2N$ coupled ordinary differential equations given by Eqs. (B.3). Finally, we note that for the system considered in this study $K_s = 0.02$, $K_\theta = 1.5 \times 10^{-4}$ and $\alpha = 1.8$ ^[121].

B.3.2 Analytical solution for a single pulse

Although it is extremely challenging to analytically describe the interactions between the pulses supported by our system, here we derive an analytical model to better characterize the propagation of a single wave. To this end, as recently shown in^[121], we introduce two continuous functions $u(x, t)$ and $\theta(x, t)$ that interpolate the displacement and rotation of the i -th pair of crosses located at $x_i = ia$ as

$$u(x_i, t) = u_i(t), \quad \theta(x_i, t) = \theta_i(t). \quad (\text{B.4})$$

Assuming that the width of the propagating waves is much larger than the unit cell size, the displacement u and rotation θ in correspondence of the $i+1$ and $i-1$ -th pairs of crosses can then be

expressed using Taylor expansion as

$$\begin{aligned}
u_{i\pm 1}(t) &= u(x_{i\pm 1}, t) \approx u\Big|_{x_i, t} \pm a \frac{\partial u}{\partial x}\Big|_{x_i, t} + \frac{a^2}{2} \frac{\partial^2 u}{\partial x^2}\Big|_{x_i, t} \\
\theta_{i\pm 1}(t) &= \theta(x_{i\pm 1}, t) \approx \theta\Big|_{x_i, t} \pm a \frac{\partial \theta}{\partial x}\Big|_{x_i, t} + \frac{a^2}{2} \frac{\partial^2 \theta}{\partial x^2}\Big|_{x_i, t} \\
\cos \theta_{i\pm 1}(t) &= \cos [\theta(x_{i\pm 1}, t)] \approx \cos \theta\Big|_{x_i, t} \pm a \frac{\partial \cos \theta}{\partial x}\Big|_{x_i, t} + \frac{a^2}{2} \frac{\partial^2 \cos \theta}{\partial x^2}\Big|_{x_i, t} \\
\sin \theta_{i\pm 1}(t) &= \sin [\theta(x_{i\pm 1}, t)] \approx \sin \theta\Big|_{x_i, t} \pm a \frac{\partial \sin \theta}{\partial x}\Big|_{x_i, t} + \frac{a^2}{2} \frac{\partial^2 \sin \theta}{\partial x^2}\Big|_{x_i, t}
\end{aligned} \tag{B.5}$$

Substitution of Eqs. (B.5) into Eqs. (B.3) yields

$$\begin{aligned}
\frac{1}{c_0^2} \frac{\partial^2 u}{\partial t^2} &= \frac{\partial^2 u}{\partial x^2} - \frac{\partial \cos \theta}{\partial x}, \\
\frac{a^2}{c_0^2 a^2} \frac{\partial^2 \theta}{\partial t^2} &= -a^2 K_\theta \frac{\partial^2 \theta}{\partial x^2} + a^2 K_s \cos \theta \frac{\partial^2 \sin \theta}{\partial x^2} + a^2 \sin \theta \frac{\partial^2 \cos \theta}{\partial x^2} \\
&\quad - 6K_\theta \theta - 4 \sin(\theta) \left[\frac{\partial u}{\partial x} + 1 - \cos \theta \right],
\end{aligned} \tag{B.6}$$

which represent the continuum governing equations of the system. Since these two coupled partial differential equations cannot be solved analytically, guided by our experiments, we further assume that $\theta \ll 1$, so that

$$\sin \theta \approx \theta - \frac{\theta^3}{6}, \text{ and } \cos \theta \approx 1 - \frac{\theta^2}{2}. \tag{B.7}$$

By substituting Eqs. (B.7) into Eqs. (B.6) and retaining the nonlinear terms up to third order, we obtain

$$\begin{aligned}
\frac{1}{c_0^2} \frac{\partial^2 u}{\partial t^2} &= \frac{\partial^2 u}{\partial x^2} + \theta \frac{\partial \theta}{\partial x}, \\
\frac{a^2}{c_0^2 a^2} \frac{\partial^2 \theta}{\partial t^2} &= a^2 (K_s - K_\theta) \frac{\partial^2 \theta}{\partial x^2} - 4 \left[\frac{3K_\theta}{2} + \frac{\partial u}{\partial x} \right] \theta - 2\theta^3,
\end{aligned} \tag{B.8}$$

Finally, we introduce the traveling wave coordinate $\zeta = x - ct$, c being the pulse velocity, so that Eqs. (B.8) become

$$\begin{aligned}\frac{\partial^2 u}{\partial \zeta^2} &= -\frac{1}{1 - c^2/c_0^2} \theta \frac{\partial \theta}{\partial \zeta} \\ \beta^{-1} \frac{\partial^2 \theta}{\partial \zeta^2} &= 4 \left[\frac{3K_\theta}{2} + \frac{\partial u}{\partial x} \right] \theta + 2\theta^3,\end{aligned}\tag{B.9}$$

where

$$\beta = a^{-2} \left[K_s - K_\theta - \frac{c^2}{a^2 c_0^2} \right]^{-1}\tag{B.10}$$

By integrating Eq. (B.9)₁ with respect to ζ we obtain,

$$\frac{\partial u}{\partial \zeta} = -\frac{1}{1 - c^2/c_0^2} \frac{\theta^2}{2} + C\tag{B.11}$$

where C is the integration constant. Since in this study we focus on the propagation of waves with a finite temporal support and do not consider periodic waves, we require that

$$\left. \frac{\partial u}{\partial \zeta} \right|_{\zeta \rightarrow \infty} = 0,\tag{B.12}$$

from which we obtain $C = 0$. Substitution of Eq. (B.11) into Eq. (B.9)₂ yields

$$\frac{\partial^2 \theta}{\partial \zeta^2} = C_1 \theta + C_3 \theta^3\tag{B.13}$$

with

$$C_1 = 6\beta K_\theta, \text{ and } C_3 = -\frac{2\beta c^2}{c_0^2 - c^2}.\tag{B.14}$$

Eq. (B.13) is the Klein-Gordon equation with cubic nonlinearities, which admits analytical solution in the form of

$$\theta(x, t) = A \operatorname{sech} \left(\frac{x - ct}{W} \right), \quad (\text{B.15})$$

where A , c and W denote the amplitude, speed and width of the pulses. Moreover, by substituting Eq. (B.15) into Eq. (B.13), the solution for the displacement is found as

$$u(x, t) = \begin{cases} \frac{aA^2 W}{2(1 - c^2/c_0^2)} \left[1 - \tanh \left(\frac{x - ct}{W} \right) \right], & \text{for } c > 0 \\ \frac{aA^2 W}{2(1 - c^2/c_0^2)} \left[-1 - \tanh \left(\frac{x - ct}{W} \right) \right], & \text{for } c < 0 \end{cases} \quad (\text{B.16})$$

since for $c > 0$ (i.e. for solitons propagating from left to right) $u(\zeta \rightarrow \infty) = 0$, whereas for $c < 0$ (i.e. for solitons propagating from right to left) $u(\zeta \rightarrow -\infty) = 0$. Eqs (B.15)-(B.16) reveal an important feature of our system: its ability to support an elastic vector soliton. In fact, in our nonlinear system two components — one translational and one rotational — are coupled together and co-propagate without distortion nor splitting.

Next, we determine the relation between A , c , W and the geometry of the system. To this end, we substitute the solution (B.15) into Eq. (B.13) and find that the latter is identically satisfied only if

$$c = \pm c_0 \sqrt{\frac{6K_\theta}{A^2 + 6K_\theta}}, \quad (\text{B.17})$$

and

$$W = a \sqrt{\frac{\alpha^2(K_s - K_\theta) - 6K_\theta/(A^2 + 6K_\theta)}{6\alpha^2 K_\theta}}. \quad (\text{B.18})$$

Eqs. (B.15)-(B.16) define the elastic vector solitons that propagate in our system. However,

the existence of such waves require that W and c are real numbers. Inspection of Eqs. (B.17) and (B.18) reveals that this condition is satisfied only if

$$\mathcal{A}_{\text{upper}} > A > \mathcal{A}_{\text{lower}}, \quad \text{with } \mathcal{A}_{\text{upper}} = -\mathcal{A}_{\text{lower}} = \sqrt{\frac{6K_\theta}{a^2(K_s - K_\theta)} - 6K_\theta}. \quad (\text{B.19})$$

Notably, Eq. (B.19) defines an amplitude gap for solitons, since it indicates that solitary waves with $A \in [\mathcal{A}_{\text{lower}}, \mathcal{A}_{\text{upper}}]$ cannot propagate in our system. Note that for the specific structure used in this study, $\mathcal{A}_{\text{upper}} = 0.12$ and $\mathcal{A}_{\text{lower}} = -0.12$.

Finally, the displacement and rotation induced by the propagating elastic vector solitons at the i -th pair of crosses can be determined from Eqs. (B.15)-(B.16) as

$$\theta_i(t) = \theta(x = ia, t) = A \operatorname{sech} \left(\frac{ia - ct}{W} \right), \quad (\text{B.20})$$

and

$$u_i(t) = \begin{cases} \frac{aA^2 W}{2(1 - c^2/c_0^2)} \left[1 - \tanh \left(\frac{ia - ct}{W} \right) \right], & \text{for } c > 0, \\ \frac{aA^2 W}{2(1 - c^2/c_0^2)} \left[-1 - \tanh \left(\frac{ia - ct}{W} \right) \right], & \text{for } c < 0. \end{cases} \quad (\text{B.21})$$

Equivalence between Eq. (B.13) and the modified Korteweg-de Vries equation At this point we want to emphasize that the modified Korteweg-de Vries (modified KdV) equation can be written into the continuous governing equation of our system (the Klein-Gordon equation with cubic non-linearity given in Eq. (B.13)). Here is the general form of the modified KdV equation^[96]:

$$\frac{\partial \theta}{\partial t} + F_1 \frac{\partial^3 \theta}{\partial x^3} - F_2 \theta^2 \frac{\partial \theta}{\partial x} = 0, \quad (\text{B.22})$$

F_1 and F_2 being constants. To demonstrate such equivalence, we first rewrite Eq. (B.22) in terms of travelling wave coordinate $\zeta = x - ct$, obtaining

$$-c\frac{\partial\theta}{\partial\zeta} + F_1\frac{\partial^3\theta}{\partial\zeta^3} - F_2\theta^2\frac{\partial\theta}{\partial\zeta} = 0, \quad (\text{B.23})$$

and then integrate Eq. (B.23) with respect to ζ yields

$$-c\theta + F_1\frac{\partial^2\theta}{\partial\zeta^2} - F_2\theta^3 = 0, \quad (\text{B.24})$$

considering that the integration constant is zero. This last equation can be rewritten in the same form of Eq. (B.13) with

$$C_1 = \frac{c}{F_1}, \quad \text{and} \quad C_2 = \frac{F_2}{F_1} \quad (\text{B.25})$$

B.4 Numerical Simulations

Since it is extremely challenging to derive an analytical solution that captures the interaction between the solitons propagating in our system, to study the collisions between the pulses supported by our system we numerically integrate the $2N$ coupled ordinary differential equations given by Eqs. (B.3) for a given set of initial and boundary conditions. Specifically, in our simulations we consider 500 pairs of crosses and use $K_s = 0.02$, $K_\theta = 1.5 \times 10^{-4}$ and $\alpha = 1.8$. We use the 4th order Runge-Kutta method (via the Matlab function `ode45`) to numerically solve Eqs. (B.3) (the code implemented in MATLAB is available online). As initial conditions we set $u_i = 0$, $\theta_i = 0$, $\dot{u}_i = 0$, $\dot{\theta}_i = 0$ for all pairs of crosses. Moreover, to excite solitons, we simply apply the analytical solution given by Eqs. (B.20) and (B.21) to the first and last unit of the chain. More specifically, at the left

end we impose

$$\begin{aligned}\theta_1(t) &= A_{\text{left}} \operatorname{sech} \left(\frac{-c_{\text{left}}(t - t_0)}{W_{\text{left}}} \right), \\ u_1(t) &= \frac{aA_{\text{left}}^2 W_{\text{left}}}{2(1 - c_{\text{left}}^2/c_0^2)} \left[1 - \tanh \left(\frac{-c_{\text{left}}(t - t_0)}{W_{\text{left}}} \right) \right]\end{aligned}\quad (\text{B.26})$$

where W_{left} is given by Eq. (B.18) and c_{left} is the positive solution of Eq. (B.17). Moreover, t_0 is a parameter introduced to ensure that $\theta_1 \rightarrow 0$ and $u_1 \rightarrow 0$ at $t = 0$ (in all our simulations we use $t_0 = 0.1$ sec). Differently, at the right end (i.e. for $i = N$) we impose

$$\begin{aligned}\theta_N(t) &= A_{\text{right}} \operatorname{sech} \left(\frac{-c_{\text{right}}(t - t_0)}{W_{\text{right}}} \right), \\ u_N(t) &= \frac{aA_{\text{right}}^2 W_{\text{right}}}{2(1 - c_{\text{right}}^2/c_0^2)} \left[-1 - \tanh \left(\frac{-c_{\text{right}}(t - t_0)}{W_{\text{right}}} \right) \right]\end{aligned}\quad (\text{B.27})$$

where W_{right} is also determined by Eq. (B.18) and c_{right} is the negative solution of Eq. (B.17).

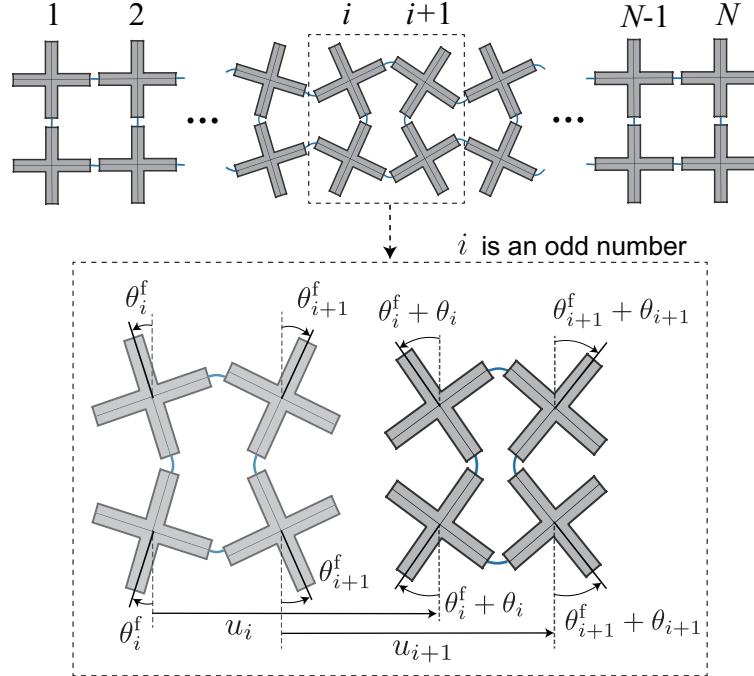


Figure B.4: Schematics of the structure considered in this study with a frozen soliton located at its center.

As a part of this study we also consider frozen solitons of different amplitude A_f in the middle of the chain and numerically investigate their effect on the propagation of solitary waves initiated at the left end. In this case the discrete governing equations of the system (Eqs. (B.3)) modify to

$$\begin{aligned} \frac{a^2}{c_0^2} \frac{\partial^2 u_i}{\partial t^2} &= u_{i+1} - 2u_i + u_{i-1} - \frac{a}{2 \cos \theta_i^f} \left[\cos(\theta_{i+1} + \theta_{i+1}^f) - \cos(\theta_{i-1} + \theta_{i-1}^f) \right], \\ \frac{a^2}{c_0^2 \alpha^2} \frac{\partial^2 \theta_i}{\partial t^2} &= -K_\theta(\theta_{i+1} + 4\theta_i + \theta_{i-1}) + K_s \cos(\theta_i + \theta_i^f) \left[\sin(\theta_{i+1} + \theta_{i+1}^f) \right. \\ &\quad \left. + \sin(\theta_{i-1} + \theta_{i-1}^f) - 2 \sin(\theta_i + \theta_i^f) \right] - \sin(\theta_i + \theta_i^f) \left[2 \cos(\theta_i^f) (u_{i+1} - u_{i-1}) / a \right. \\ &\quad \left. + 4 \cos(\theta_i^f) - \cos(\theta_{i+1} + \theta_{i+1}^f) - 2 \cos(\theta_i + \theta_i^f) - \cos(\theta_{i-1} + \theta_{i-1}^f) \right]. \end{aligned} \quad (\text{B.28})$$

where θ_i^f is the initial rotation of the i -th pair of crosses due introduced because of the frozen pulse.

For the specific case of a frozen soliton placed in middle of the chain,

$$\theta_i^f = A_f \operatorname{sech} \left[\frac{a(i - N/2)}{W_f} \right], \quad (\text{B.29})$$

where A_f denotes the amplitude of frozen soliton and W_f is the width of the frozen soliton, which is determined by Eq. (B.18) setting $A = A_f$. As for boundary conditions, we apply input the theoretical solution at the left end as Eqs. (B.26) and fixed boundary on the right end, i.e.,

$$\theta_N(t) = 0, \quad u_N(t) = 0 \quad (\text{B.30})$$

Finally, we note that the numerical results for pulses characterized by $|A_{\text{left}}| < 0.12$ ($|A_{\text{right}}| < 0.12$) are obtained using Eqs. (B.26) (Eqs. (B.27)) with $W_{\text{left}} = 1$ ($W_{\text{right}} = 1$). This is because for $|A_{\text{left}}| < 0.12$ ($|A_{\text{right}}| < 0.12$) the width of the pulse given by Eq. (B.18) is imaginary. Although this choice of width is arbitrary, quantitatively identical results are obtained for any real width^[121].

B.5 Additional Results

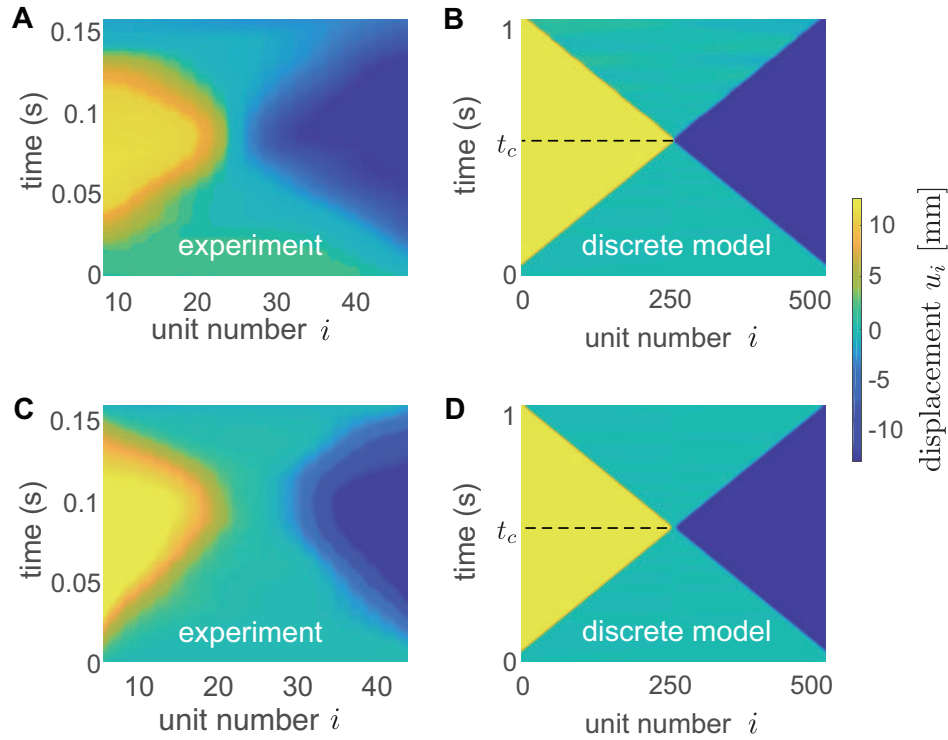


Figure B.5: Displacement signal. (A)-(B) Longitudinal displacement of the pairs of crosses during the propagation of the pulses, as recorded in (A) experiments and (B) numerical simulations. The pulses excited at the left and right end are characterized by $A_{\text{left}} = 0.2$ and $A_{\text{right}} = 0.2$, respectively. (C)-(D) Longitudinal displacement of the pairs of crosses during the propagation of the pulses, as recorded in (C) experiments and (D) numerical simulations. The pulses excited at the left and right end are characterized by $A_{\text{left}} = -0.2$ and $A_{\text{right}} = 0.2$, respectively. In (C) and (D) we find that the units near collision point do not move - an indication of anomalous collisional dynamics.

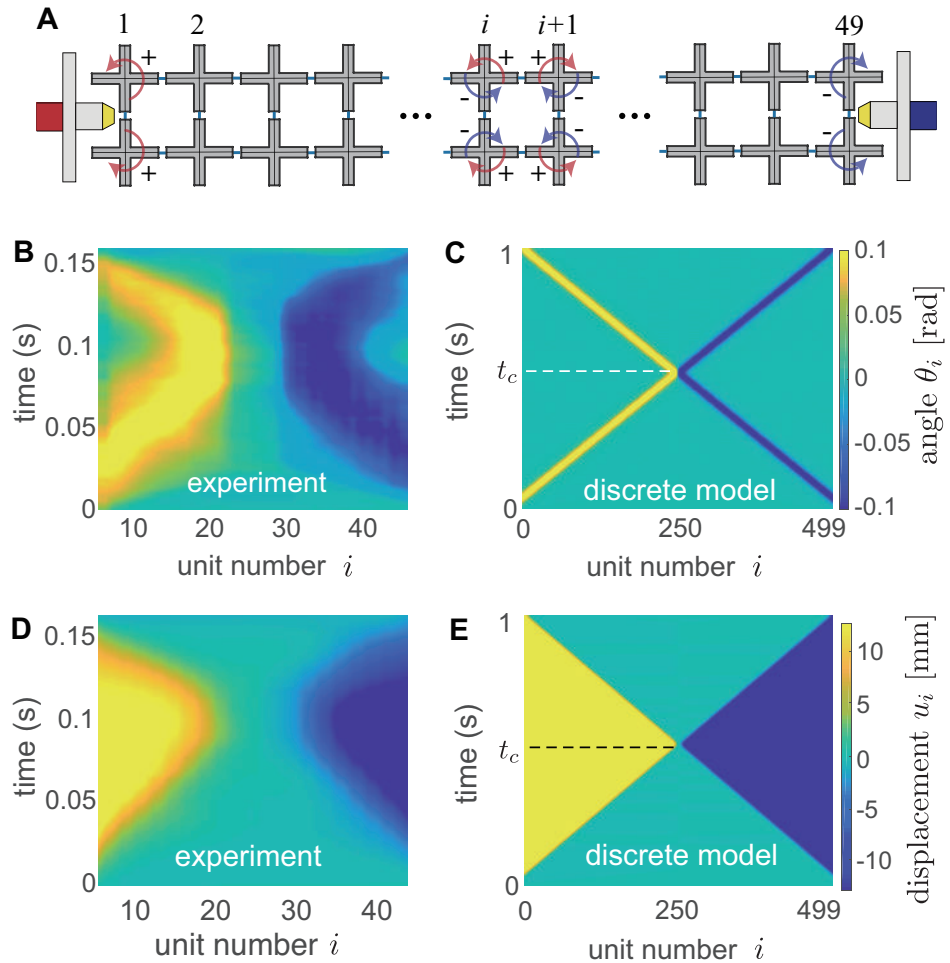


Figure B.6: A chain with odd pairs of crosses. (A) We consider a chain with $N = 49$ pair of crosses. To initiate a soliton at the right end that induces negative rotations, we use an impactor that hits the mid-point of the last pair. (B)-(C) Rotation of the pairs of crosses during the propagation of the pulses, as recorded in (B) experiments and (C) numerical simulations. (D)-(E) Longitudinal displacement of the pairs of crosses during the propagation of the pulses, as recorded in (D) experiments and (E) numerical simulations. The pulses excited at the left and right end are characterized by $A_{\text{left}} = 0.2$ and $A_{\text{right}} = -0.2$, respectively. The experiments are conducted on a chain with 49 pairs of crosses, whereas in the numerical simulations we consider 499 units.

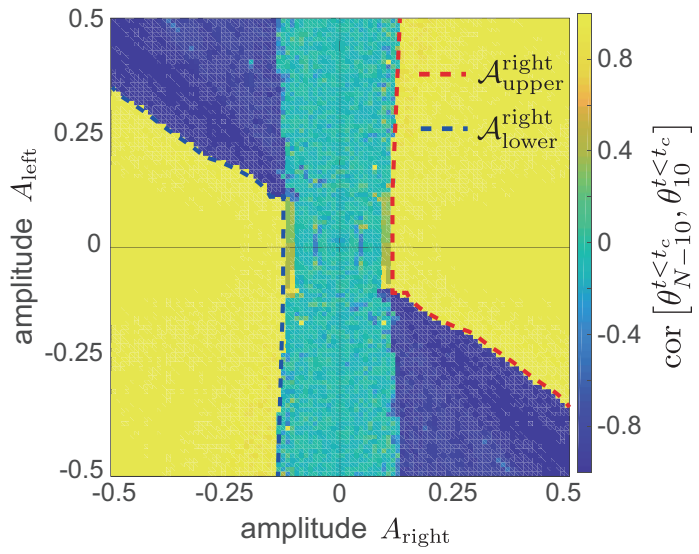


Figure B.7: Numerically obtained cross-correlation between $\theta_{10}(t < t_c)$ and $\theta_{N-10}(t > t_c)$ as a function of A_{left} and A_{right} .

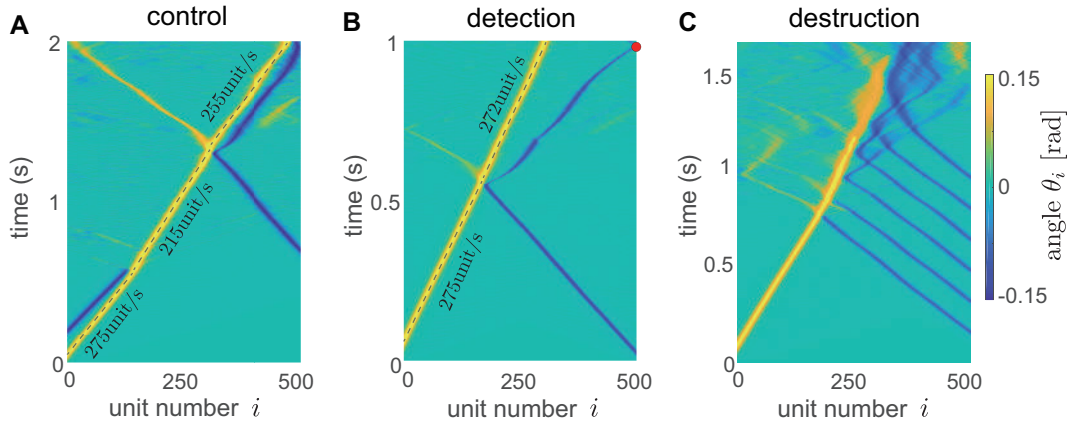


Figure B.8: Anomalous collisions can be exploited to actively manipulate and control the propagation of pulses. (A) Anomalous collisions provide opportunities to remotely induce changes in the propagation velocity of a soliton. To demonstrate this, we consider a left-initiated pulse with $A_{left,1} = 0.4$ and $c = 275$ unit/s and use the interactions with a soliton subsequently excited at the left end to reduce its velocity to $c = 215$ unit/s and with a right-initiated solitary wave to then accelerate it to $c = 255$ unit/s. (B) Anomalous collision can be exploited to block the propagation of a soliton. Specifically, a large propagating soliton can be blocked by sending a sequence of relatively small pulses with opposite rotation direction. As an example, we consider a left-initiated soliton with $A_{left} = 0.4$ and six right-initiated solitons with $A_{right,k} = -0.2$ (with $k = 1, \dots, 6$). Each of the six collisions results in energy radiation to linear waves or to other small amplitude solitons and reduces the amplitude of the left-initiated pulse, which eventually vanishes as its amplitude falls within the amplitude gap of the structure. Therefore, six small pulses efficiently mitigate and destroy the main left-initiated soliton at $t = 2$ s. (C)-(D) Anomalous collisions can also be exploited to probe the direction of the rotational component of a pulse. To demonstrate this, we consider a main left-initiated soliton with $A_{left} = \pm 0.4$ and a probing, small right-initiated pulse with $A_{right} = -0.18$. If $A_{left} = 0.4$ (C), the "echo" of the probing soliton reaches the right end before the main soliton, indicating that it has been reflected by the main soliton. From this information, we therefore deduce that the main soliton is of positive amplitude. If $A_{left} = -0.4$ (D), no "echo" is observed, as the probe penetrates the main soliton. From this information, we therefore deduce that the main soliton is of negative amplitude. Finally, it is important to point out that, since the probing soliton carries much less energy than the main one, the latter is almost unaltered by the collision (i.e. its velocity changes from 275unit/s to 272unit/s).

Appendix C

Supplementary Information: Characterization, Stability and Application of Domain Walls in Flexible Mechanical Metamaterials

By: Bolei Deng*, Siqin Yu*, Antonio E Forte, Vincent Tournat, Katia Bertoldi. Published in *PNAS*,
on Nov. 20 2020. [doi:10.1073/pnas.2015847117](https://doi.org/10.1073/pnas.2015847117)

C.1 Fabrication

Our sample is fabricated by laser cutting a natural sheet with a thickness of 3.2 mm (McMaster-Carr part number: 87145K73). The pattern is designed to comprise 21 square cells in both the horizontal and vertical directions (Fig. C.1(a)). The squares have diagonals of 10mm-length and are connected by hinges with width and length of 1 mm (Fig. C.1(b) and (c)).

Since rubber is notoriously difficult to laser cut, we set up a custom procedure in order to obtain a clean cut. Firstly the geometry is created with a custom code in MATLAB (The MathWorks, Inc.), exported as pdf file and passed on to the laser cut rig (PLS6.150D, Universal Laser Systems). Secondly the distance between the laser head and the rubber sheet is calibrated as instructed in the machine's operating manual, in order to assure a sharp focus. The design is then cut into the rubber sheet, producing a groove of about 1 mm in depth. The parameters used for the cut are 70% of the laser power and 10% of the maximum translation speed of the rig. Next, the laser head is lowered of 1mm in order to move the focus on the base of the groove. The same procedure is repeated for a second and a third time, cutting about 1 mm each time and finally achieving the cut through of the material.

As part of this study we introduce two types of defects to guide the deformation of our samples:

- **Phase-inducing defects:** to determine the direction of rotation of certain squares we insert a stiff orange plate (12 mm × 5 mm × 0.76 mm, laser cut from plastic shim, McMaster-Carr part number: 9513K75) into the adjacent hole (see Fig. C.2(a)). By varying the orientation of this orange plate from horizontal to vertical we can change the direction of rotation of the neighboring squares. Similarly, the direction of rotation can be switched by translating the plate to one of the neighboring holes (while keeping its orientation). In Fig. C.3 we show how we arrange 8 of such defects within the sample to generate the deformation fields shown in Figs. 4.2 and 4 of the main text.
- **Pinning defects:** to prevent certain units to rotate we insert a blue stiff square (9.5 mm × 9.5 mm × 3.18 mm, laser cut from a blue acrylic plate, McMaster-Carr part number: 8505K741,

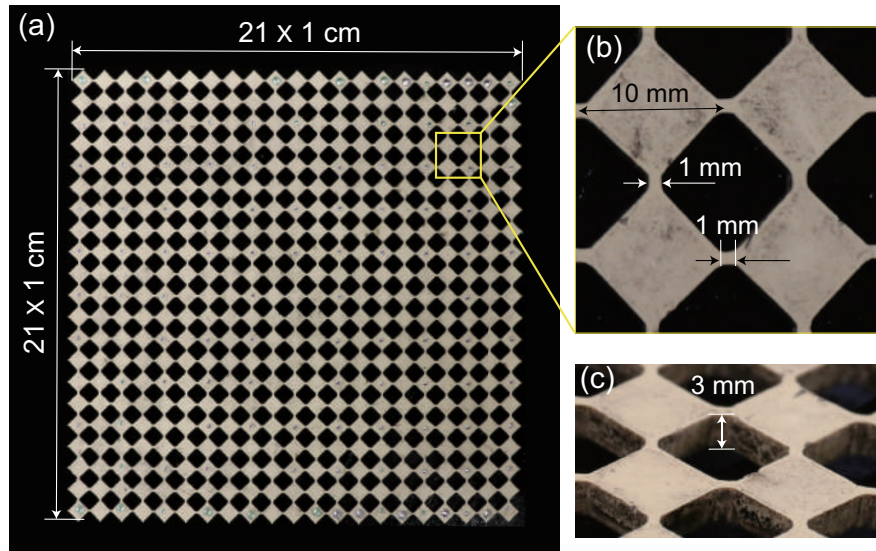


Figure C.1: Snapshots of our sample comprising an array of 21×21 squares connected at their vertices by thin hinges.

see Fig. C.2(b)) into the neighboring hole. In Fig. C.4 we show how we arrange 4 of such defects within the sample to generate the deformation fields shown in Figs. 4.3 and 4 of the main text.

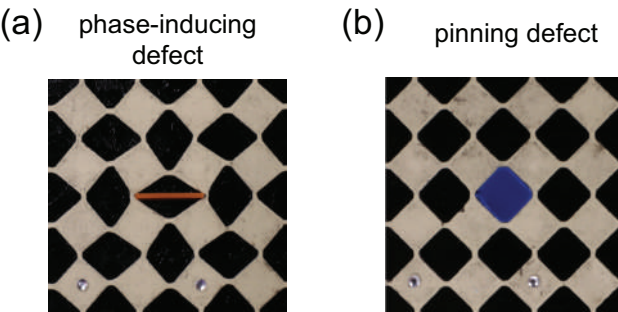


Figure C.2: (a) Magnified view of a phase-inducing defect. (b) Magnified view of a pinning defect.

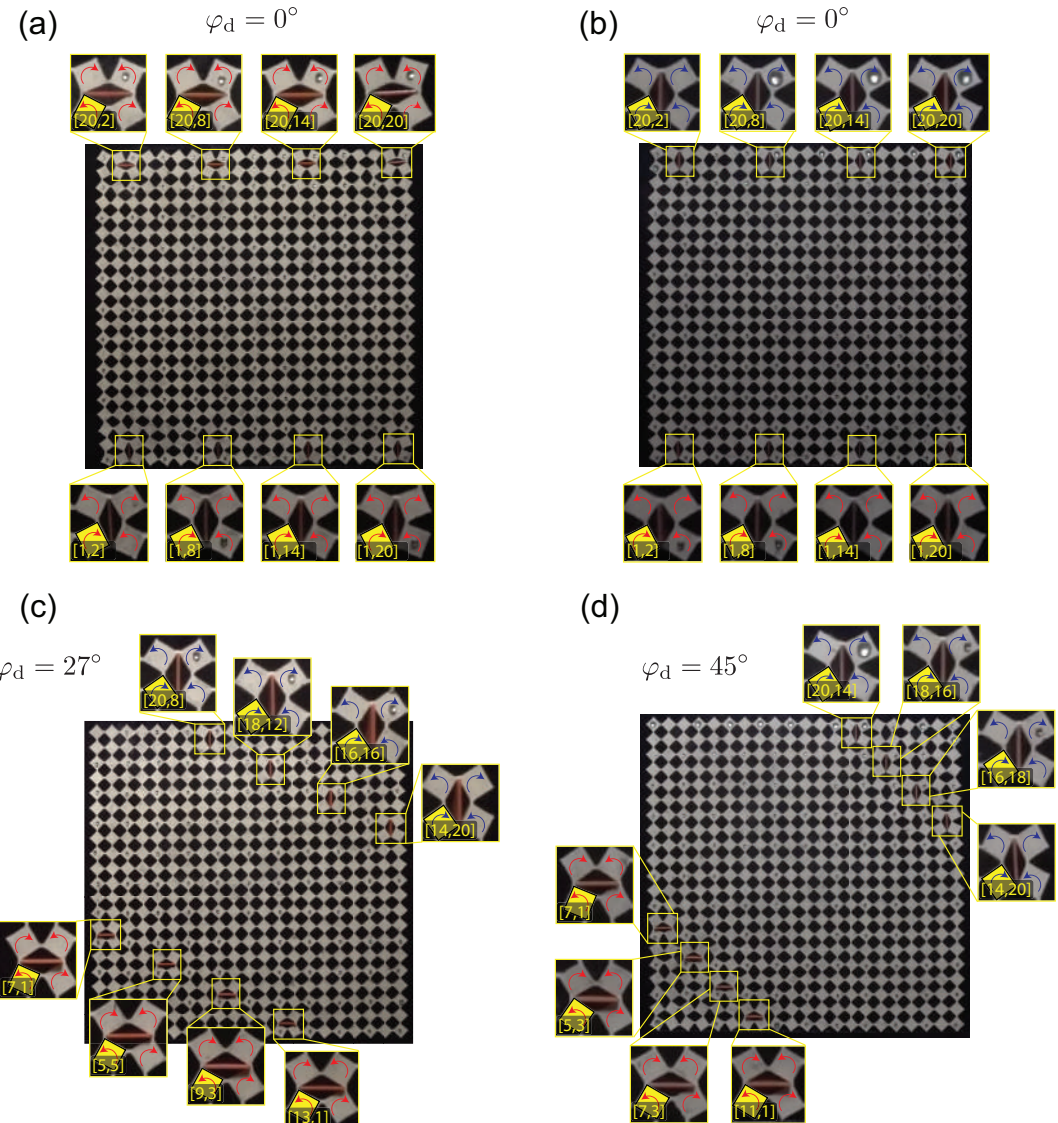


Figure C.3: Distribution of phase-inducing defects within the sample to generate the deformation fields shown in (a) Fig. 4.2A of the main text; (b) Fig. 2B-C of the main text; (c) Fig. 4.4A of the main text ($\varphi_d = \arctan(1/2)$); (d) Fig. 4.4A of the main text ($\varphi_d = \pi/4$).

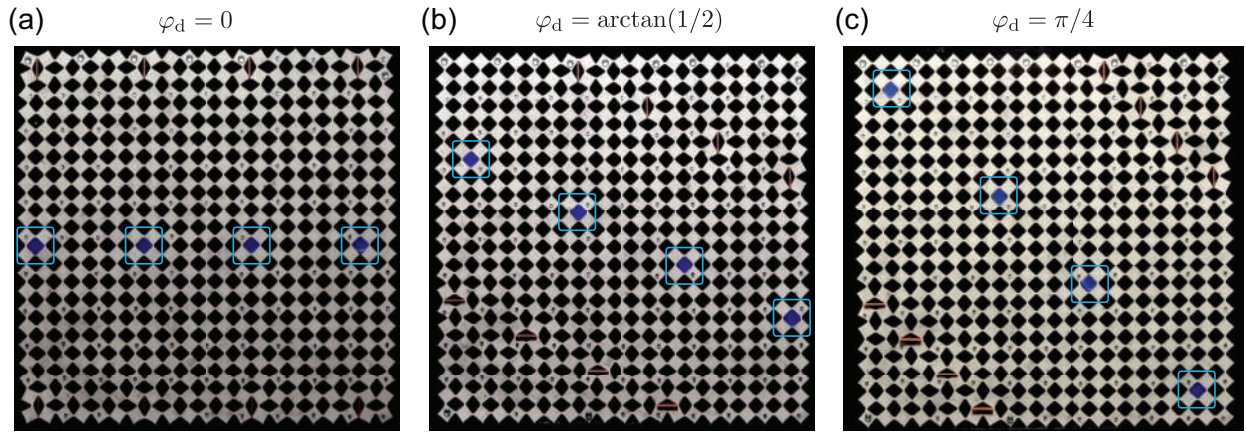


Figure C.4: Distribution of pinning defects within the sample to generate the deformation fields shown in (a) Fig. 4.3A of the main text; (b) Fig. 4.4C of the main text ($\varphi_d = \arctan(1/2)$); (c) Fig. 4.4C of the main text ($\varphi_d = \pi/4$).

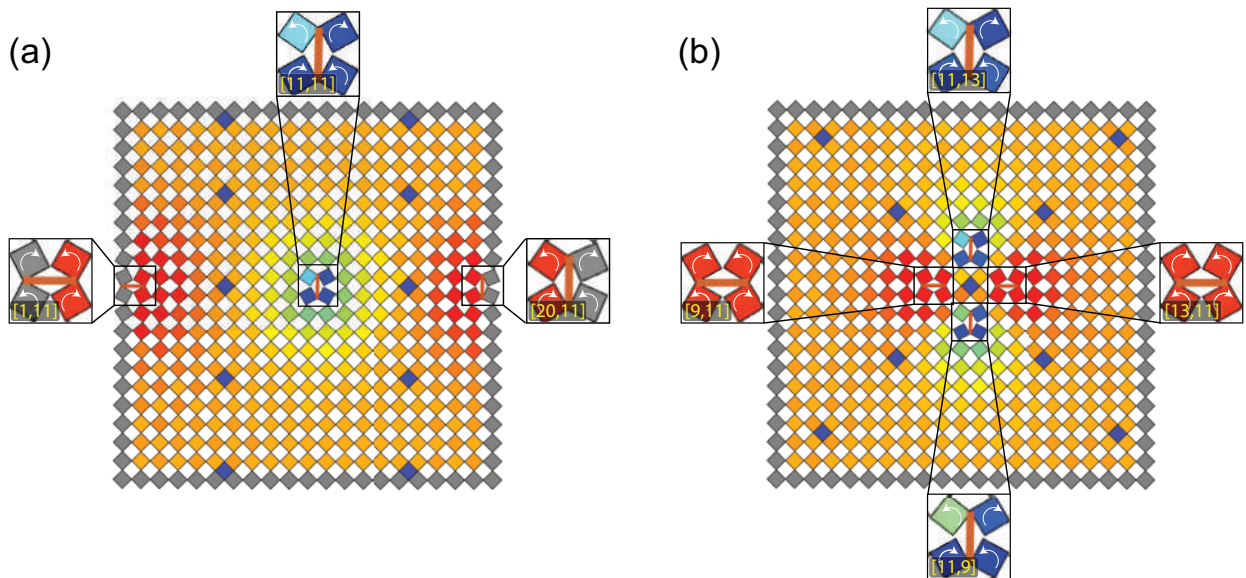


Figure C.5: Distribution of phase-inducing and pinning defects within the sample to generate the deformation fields shown in (a) Fig. 4.5B of the main text; (b) Fig. 4.5C of the main text.

C.2 Testing

To test the mechanical response of our sample, we place it on a base plate (black acrylic plate, 3.18 mm thickness, McMaster-Carr part number: 8505K741) and cover them with a transparent plate (clear acrylic plate, 3.18 mm thickness, McMaster-Carr part number: 8560K239) to prevent out-of-plane buckling while being able to observe its deformation (see Fig.C.6(a) for top view and (b) for side view). Note that to minimize friction between the sample and the plates, plastic stickers (Amazon Standard Identification Number (ASIN): B07M6NDG4X) are glued on the sample (see Fig.C.6(c)).

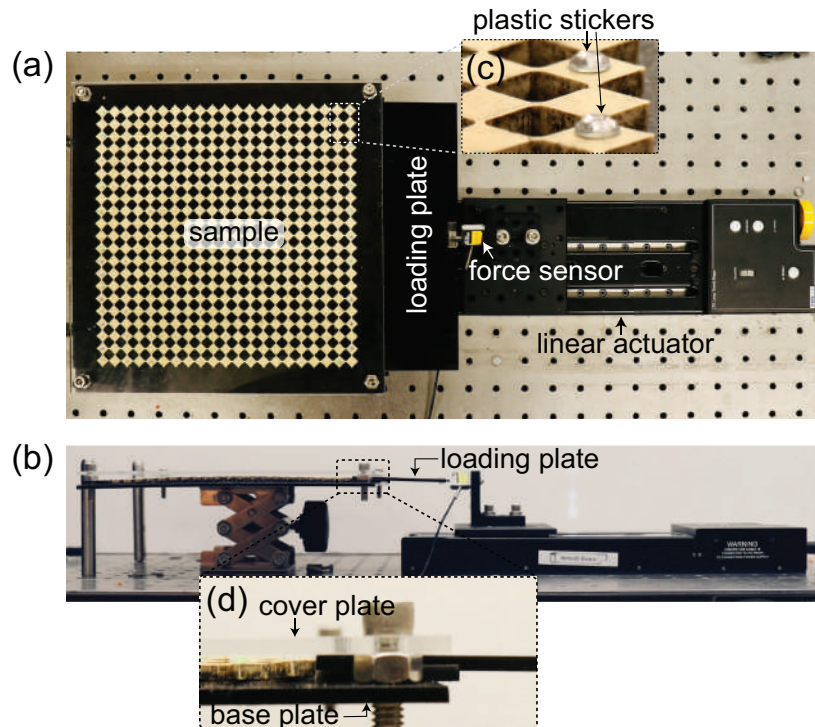


Figure C.6: (a) Top view of the testing setup. (b) Front view of the testing setup. (c) Magnified view of the sample, with plastic stickers on the center of square cells. (d) Magnified view of the setup highlighting the cover and base plates used to prevent out-of-plane deformation.

The samples are uniaxially compressed using two acrylic plates (made using McMaster-Carr part number: 8505K741): an end plate to prevent their motion and a loading plate to apply the

deformation. During the test, the loading plate is inserted in between the cover plate and base plate to compress the sample (see Fig.C.6(d) for a zoomed-in view). The loading plate is connected to a translation stage (LTS300 - Thorlabs) and a force sensor (1 lb Load Cell, LSB200 Miniature S-Beam Load Cell, FUTEK Advanced Sensor Technology, Inc.) is assembled between them to monitor the reaction force from the sample during the test. Note that lubricant is applied to both the end and loading plates so that the squares on the boundaries of the samples can slide along the plates.

The uniaxial compression tests are captured with a camera (SONY, RX100) recording at 30 fps and with a resolution of 1920×1080 pixels and the deformation is tracked via image digital processing conducted in MATLAB. Specifically, the deformation is tracked using the following 3 steps

- **Step 1** Each frame is converted to black-and-white and the holes between the squares are extracted by setting a threshold on gray scale of the image. Since the sample comprises 21×21 squares, 400 holes are extracted (see Step 1 in Fig. C.7).
- **Step 2** The boundaries of each hole are fitted with four segments (see Step 2 of Fig. C.7 - in the zoom-in we highlight the boundaries of one hole with magenta dashed line and the four segments with red, purple, yellow and green continuous lines. Note that the blue dots corresponds to the pixels).
- **Step 3** The position and rotation of each square element is calculated from the position and rotation of the four surrounding segments obtained in Step 2 (see Step 3 of Fig. C.7). Specifically, the position of the square's center is calculated by the averaged coordinates of the center points of the four segments and its rotation by averaging the rotation of the segments. The squares are colored to show their rotation.

Note that the whole process is automatized in Matlab and it typically takes 2 minutes to process a recorded video.

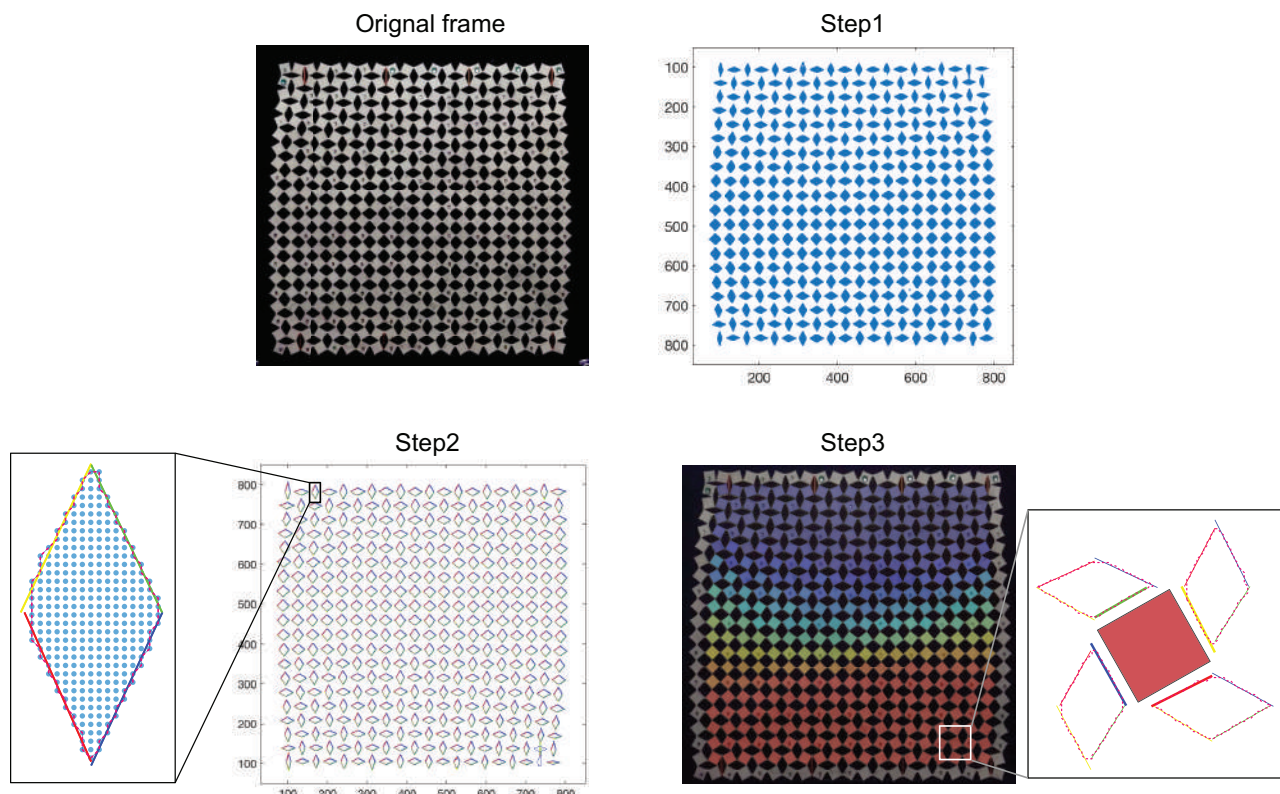


Figure C.7: Procedure for tracking the deformation of our samples.

C.3 Discrete Model

C.3.1 Governing equations

Our system consists of square crosses that are connected by thin and flexible hinges (see Fig. C.1). As recently shown in several studies^[94,121,122,128,129], the response of such system can be accurately captured by modeling it as an array of rigid bodies connected at the vertices via a combination of longitudinal and rotational springs (see Fig. C.8(a) for the schematics). Specifically, in our discrete model we consider the squares to be rigid and to have three degrees of freedom: the displacement in the x -direction, u , the displacement in the y -direction, v , and the rotation around the z -axis, θ (see Fig. C.8(b)). Note that to facilitate the analysis, we define the positive direction of rotation alternatively for neighboring squares. Focusing on the $[i, j]^{th}$ square, we define a counter clockwise rotation positive if $i + j$ is an even number and negative if $i + j$ is odd. As for the hinges, we model them using a combination of three springs. Their longitudinal response is captured by a linear spring with stiffness k_l ; their shearing is captured by a linear spring with stiffness k_s and their bending is captured by a non-linear torsional spring, which obeys

$$M = k_\theta(\theta + \gamma\theta^3), \quad (\text{C.1})$$

where M is the torque exerted by the spring, k_θ is the rotational stiffness and γ is a dimensionless material parameter. Note that, to facilitate the analysis, we assume that the longitudinal and shearing springs are always parallel either to the x or y axis (an assumption which is valid only for small global rotations of the system).

Under the assumptions listed above, the equations of motion for the $[i, j]^{th}$ square are given

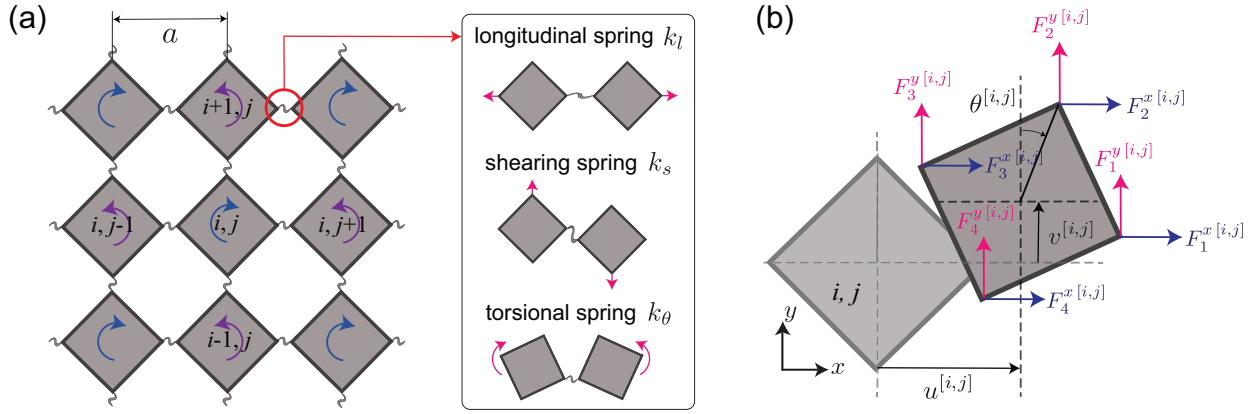


Figure C.8: Discrete model based on rigid units connected at their vertices by springs. (b) Schematic view of the $[i, j]^{\text{th}}$ rigid square unit.

by^[129]

$$\begin{aligned}
 m \frac{\partial^2 u^{[i,j]}}{\partial t^2} &= \sum_{p=1}^4 F_p^{x [i,j]}, \\
 m \frac{\partial^2 v^{[i,j]}}{\partial t^2} &= \sum_{p=1}^4 F_p^{y [i,j]}, \\
 J \frac{\partial^2 \theta^{[i,j]}}{\partial t^2} &= \sum_{p=1}^4 M_p^{[i,j]},
 \end{aligned} \tag{C.2}$$

where m and J are the mass and rotational inertia of the squares, $F_p^{x [i,j]}$ and $F_p^{y [i,j]}$ are the normalized forces in the x -direction and the y -direction generated at the p -th vertex of the $[i, j]^{\text{th}}$ unit by the springs and $M_p^{[i,j]}$ represents the corresponding moment. For the set of springs considered in this

study Eqs. (C.2) specializes to

$$\begin{aligned}
m \frac{\partial^2 u^{[i,j]}}{\partial t^2} &= k_l \left(u^{[i,j+1]} + u^{[i,j-1]} - 2u^{[i,j]} \right) + k_s \left(u^{[i+1,j]} + u^{[i-1,j]} - 2u^{[i,j]} \right) \\
&\quad - \frac{k_l a}{2} \left[\cos(\theta^{[i,j+1]}) - \cos(\theta^{[i,j-1]}) \right] + (-1)^{i+j} \frac{k_s a}{2} \left[\sin(\theta^{[i+1,j]}) - \sin(\theta^{[i-1,j]}) \right], \\
m \frac{\partial^2 v^{[i,j]}}{\partial t^2} &= k_l \left(v^{[i+1,j]} + v^{[i-1,j]} - 2v^{[i,j]} \right) + k_s \left(v^{[i,j+1]} + v^{[i,j-1]} - 2v^{[i,j]} \right) \\
&\quad - \frac{k_l a}{2} \left[\cos(\theta^{[i+1,j]}) - \cos(\theta^{[i-1,j]}) \right] - (-1)^{i+j} \frac{k_s a}{2} \left[\sin(\theta^{[i,j+1]}) - \sin(\theta^{[i,j-1]}) \right], \\
J \frac{\partial^2 \theta^{[i,j]}}{\partial t^2} &= -k_\theta \left(\theta^{[i+1,j]} + \theta^{[i-1,j]} + \theta^{[i,j+1]} + \theta^{[i,j-1]} + 4\theta^{[i,j]} \right) \\
&\quad - \gamma k_\theta \left((\theta^{[i+1,j]} + \theta^{[i,j]})^3 + (\theta^{[i-1,j]} + \theta^{[i,j]})^3 + (\theta^{[i,j+1]} + \theta^{[i,j]})^3 + (\theta^{[i,j-1]} + \theta^{[i,j]})^3 \right) \\
&\quad - \frac{k_l a^2}{4} \sin \theta^{[i,j]} (8 - \cos \theta^{[i+1,j]} - \cos \theta^{[i-1,j]} - \cos \theta^{[i,j+1]} - \cos \theta^{[i,j-1]} - 4 \cos \theta^{[i,j]}) \\
&\quad - \frac{k_l a^2}{2} \sin \theta^{[i,j]} (u^{[i,j+1]} - u^{[i,j-1]} + v^{[i+1,j]} - v^{[i-1,j]}) \\
&\quad + \frac{k_s a^2}{4} \cos \theta^{[i,j]} (\sin \theta^{[i,j+1]} + \sin \theta^{[i,j-1]} + \sin \theta^{[i+1,j]} + \sin \theta^{[i-1,j]} - 4 \sin \theta^{[i,j]}) \\
&\quad + (-1)^{i+j} 2k_l a^2 (-u^{[i+1,j]} + u^{[i-1,j]} + v^{[i,j+1]} - v^{[i,j-1]}).
\end{aligned} \tag{C.3}$$

For a structure comprising N_x rows and N_y columns of squares Eqs. (C.3) result in a system of $3N_x \times N_y$ coupled differential equations, which we numerically solve using the 4th order Runge-Kutta method (via the Matlab function `ode45`). In all our simulations we bind the vertical displacement of the bottom row of squares to zero (i.e. we set $v^{[1,j]} = 0$) and apply a homogeneous displacement Δ_{stage} in the vertical direction onto the top row (i.e. we set $v^{[N_y,j]} = \Delta_{\text{stage}}$). Further, to eliminate rigid body motion, we also set the horizontal displacement of the center unit in the bottom row to be zero (i.e., $u^{[1,\text{floor}(N_x/2)]} = 0$). Note that to minimize dynamic effects the displacement is applied very slowly (i.e. at a velocity three order of magnitude smaller than that of linear waves travelling through the system).

C.3.2 Defects

To model the defects introduced in our samples, we use very stiff linear springs with stiffness $k_d = 10k_l$. Each phase-inducing defect is modelled using one spring with initial length $l_d = 1.2a$ (since the orange plates used in our experiments have a length of $1.2a$) that connects the opposite vertices of the hole (see Fig. C.9(a)). Each pinning defect is modelled using two springs with initial length $l_d = a$ that connect two sets of opposite vertices of the hole (see Fig. C.9(b)). Since the defects are not glued to the sample, we assume that the springs only support compression loads

$$F_{\text{defect}} = \begin{cases} k_d(l_d - l_{\text{ver}}), & \text{if } l_d > l_{\text{ver}} \\ 0, & \text{if } l_d < l_{\text{ver}} \end{cases} \quad (\text{C.4})$$

where l_{ver} denotes the distance in the deformed configurations between the two vertices to which the spring is attached.

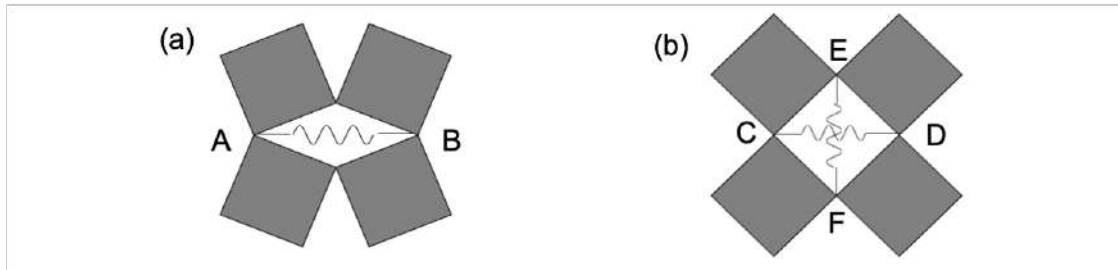


Figure C.9: (a) A phase-inducing defect is modelled using one spring. (b) A pinning defect is modelled using two springs.

C.3.3 Total energy of the structure

Given a deformed configuration defined by $u^{[i,j]}$, $v^{[i,j]}$ and $\theta^{[i,j]}$, the total energy of the structure, E_{total} , can be calculated as

$$\begin{aligned}
 E_{\text{total}} \left(u^{[i,j]}, v^{[i,j]}, \theta^{[i,j]} \right) = & \sum_{i=1}^{N_y} \sum_{j=1}^{N_x-1} \left\{ \frac{1}{2} k_\theta \left[(\theta^{[i,j]} + \theta^{[i,j+1]})^2 + \frac{\gamma}{2} (\theta^{[i,j]} + \theta^{[i,j+1]})^4 \right] \right. \\
 & + \frac{1}{2} k_s \left[v^{[i,j+1]} - v^{[i,j]} - \frac{a}{2} (\sin \theta^{[i,j+1]} + \sin \theta^{[i,j]}) \right]^2 \\
 & + \frac{1}{2} k_l \left[u^{[i,j+1]} - u^{[i,j]} + \frac{a}{2} (2 - \cos \theta^{[i,j+1]} - \cos \theta^{[i,j]}) \right]^2 \Big\} \\
 & + \sum_{i=1}^{N_y-1} \sum_{j=1}^{N_x} \left\{ \frac{1}{2} k_\theta \left[(\theta^{[i,j]} + \theta^{[i+1,j]})^2 + \frac{\gamma}{2} (\theta^{[i+1,j]} + \theta^{[i,j]})^4 \right]^2 \right. \\
 & + \frac{1}{2} k_s \left[u^{[i+1,j]} - u^{[i,j]} - \frac{a}{2} (\sin \theta^{[i+1,j]} + \sin \theta^{[i,j]}) \right]^2 \\
 & \left. + \frac{1}{2} k_l \left[v^{[i+1,j]} - v^{[i,j]} + \frac{a}{2} (2 - \cos \theta^{[i+1,j]} - \cos \theta^{[i,j]}) \right]^2 \right\} \\
 & + E_{\text{defects}},
 \end{aligned} \tag{C.5}$$

where E_{defects} denotes the energy associated to all defects placed into the sample. Specifically, for a structure with n_s stiff springs introduced to mimic the experimental defects, E_{defects} can be written as

$$E_{\text{defects}} = \sum_{p=1}^{n_s} \frac{1}{2} k_d (l_d - l_{\text{ver}}^s)^2, \tag{C.6}$$

where l_{ver}^s denotes the distance in the deformed configuration of the two vertices to which the spring is attached and depends of the location of the defect.

C.3.4 Uniaxial compression of a structure without defects

While in the presence of defects Eqs. (C.3) have to be solved numerically, an analytical solution can be obtained when a sample without defects is subjected to uniaxial compression in the vertical direction. For this case

- (i) the inertia terms can be neglected,

$$\frac{\partial^2 u^{[i,j]}}{\partial t^2} = \frac{\partial^2 v^{[i,j]}}{\partial t^2} = \frac{\partial^2 \theta^{[i,j]}}{\partial t^2} = 0, \quad \forall i, j \quad (\text{C.7})$$

- (ii) the deformation is homogeneous,

$$\begin{aligned} v^{[i+1,j]} - v^{[i,j]} &= a\varepsilon_{st}^{yy}, \\ \theta^{[i,j]} &= \theta_{st}, \quad \forall i, j \end{aligned} \quad (\text{C.8})$$

where ε_{st}^{yy} is the homogeneous strain and θ_{st} is the constant angle by which all squares rotate (with neighboring units rotating in opposite direction) due to the applied static deformation.

- (iii) the longitudinal forces in all horizontal ligaments vanish (since we have traction free boundary conditions on the left and right edges)

$$F_1^{[i,j]} = F_3^{[i,j]} = k_l \left[u^{[i+1,j]} - u^{[i,j]} + \frac{a}{2} \left(2 - \cos \theta^{[i,j]} - \cos \theta^{[i+1,j]} \right) \right] = 0, \quad \forall i, j, \quad (\text{C.9})$$

When substituting Eqs. (C.7) - (C.9) into Eqs. (C.3), we find that the first two equations vanish and the third one simplifies to

$$8k_\theta \theta_{st} (1 + 4\gamma \theta_{st}^2) + k_l a^2 \sin \theta_{st} (1 - \cos \theta_{st}) + k_l a^2 \sin \theta_{st} \varepsilon_{st}^{yy} = 0. \quad (\text{C.10})$$

While Eq. (C.10) can only be solved numerically to find the relation between the strain ε_{st}^{yy} and the resulting rotation of the squares θ_{st} , analytical solution can be obtained by assuming $\theta_{st} \ll 1$, so

that $\sin \theta_{st} \approx \theta_{st} - \theta_{st}^3/6$ and $\cos \theta_{st} \approx 1 - \theta_{st}^2/2$. Under this assumption Eq. (C.10) reduces to

$$\left(1 - \frac{(24\gamma + 1)\varepsilon_{cr}^{yy}}{3}\right)\theta_{st}^3 + 2(\varepsilon_{st}^{yy} - \varepsilon_{cr}^{yy})\theta_{st} = 0, \quad (\text{C.11})$$

with

$$\varepsilon_{cr}^{yy} = -\frac{8k_\theta}{k_l a^2}. \quad (\text{C.12})$$

Eq. (C.11) can be solved analytically to obtain the rotation of the squares, θ_{st} , as a function of the strain ε_{st}^{yy} as

$$\theta_{st} = \begin{cases} 0, & \varepsilon_{st}^{yy} > \varepsilon_{cr}^{yy} \\ \pm \sqrt{\frac{-6(\varepsilon_{st}^{yy} - \varepsilon_{cr}^{yy})}{3 - (24\gamma + 1)\varepsilon_{st}^{yy}}}, & \varepsilon_{st}^{yy} < \varepsilon_{cr}^{yy} \end{cases} \quad (\text{C.13})$$

Eq. (C.13) indicate that, when loaded starting from the undeformed configuration (i.e. from $\varepsilon_{st}^{yy} = 0$ and $\theta_{st} = 0$), the squares initially only translate and do not rotate (i.e. $\theta_{st} = 0$). However, at the critical strain ε_{cr}^{yy} the solution bifurcates; the initial branch $\theta_{st} = 0$ becomes unstable and the squares move to the second branch and start to rotate. Note that a given unit has equal probability to rotate in clockwise or counter-clockwise direction, but its direction of rotation determines that of all the other squares (since neighboring units tend to rotate in opposite directions).

Finally, in an attempt to determine the stress-strain response of the structure, we focus on the longitudinal forces acting on all vertical ligaments,

$$F_2^{[i,j]} = F_4^{[i,j]} = k_l \left[v^{[i+1,j]} - v^{[i,j]} + \frac{a}{2} (2 - \cos \theta^{[i,j]} - \cos \theta^{[i+1,j]}) \right], \quad \forall i, j, \quad (\text{C.14})$$

which in the case of homogeneous deformation (Eq. (C.8)) and $\theta_{st} \ll 1$ (so that $\cos \theta_{st} \sim 1 - \theta_{st}^2/2$)

simplify to

$$F_2^{y [i,j]} = F_4^{y [i,j]} = ak_l \left(\varepsilon_{st}^{yy} + \frac{\theta_{st}^2}{2} \right), \quad \forall i, j, \quad (\text{C.15})$$

It follows that the normal stress in y -direction can be obtained as

$$\sigma^{yy} = \frac{F_2^{y [i,j]}}{at} = \frac{k_l}{t} \left(\varepsilon_{st}^{yy} + \frac{\theta_{st}^2}{2} \right), \quad (\text{C.16})$$

where $t = 3.2$ mm is the thickness of the sample and θ_{st} is defined in Eq. (C.13).

C.3.5 Parameter identification

To make the discrete model parameters relevant to our experimental sample, we need to estimate the mass of the square units (m), their rotational inertia (J), the spring stiffness (k_l , K_s and K_θ) and the non-linear parameter γ .

Mass m . The mass of each square is $m = 0.18$ g (it is calculated by multiplying the volume of the square by the density of the rubber).

Rotational inertia J . It is calculated as $J = ma^2/12 = 0.0152$ g·cm².

Spring stiffness k_l , k_θ and non-linear parameter γ . We focus on the uniaxial compression of a sample without defects (see Fig. C.10(a) - also shown in manuscript Fig. 1B) and fit the theoretically predicted force-strain curve (through Eqs. (C.10) and (??)) to the experimental measurements. In Fig. C.10(b), we show that the experimentally measured stress-strain curve (triangular markers)

can be best fitted by the model (solid line) using

$$k_l = 1080 \text{ N/m}, k_\theta = 1.62 \times 10^{-4} \text{ N} \cdot \text{m}, \text{ and } \gamma = 0.5. \quad (\text{C.17})$$

The initial stiffness is governed by k_l , the critical strain $\varepsilon_{cr}^{yy} = 0.012$ is given by Eq. (C.12), and γ controls the slope of the stress-strain curve in the post-buckling regime.

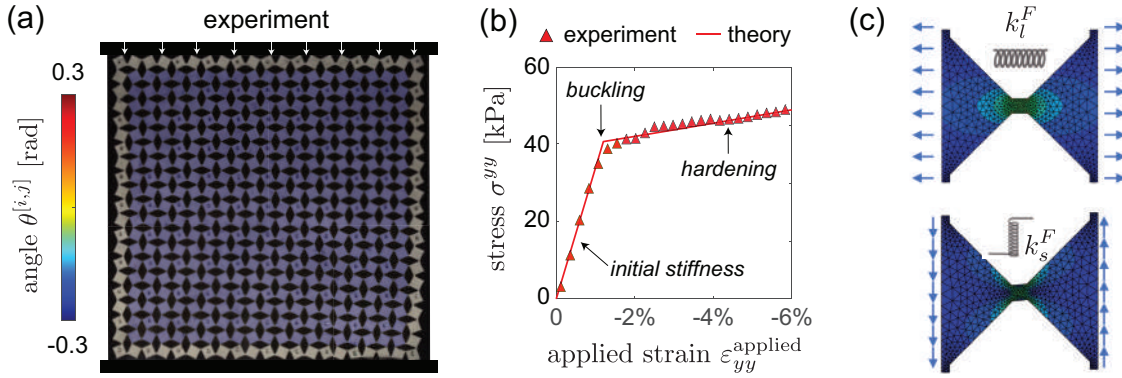


Figure C.10: (a) A snapshot of the experiments where uniaxial compression leads to homogeneous deformation. (b) Matching of the model predicted force-strain relation with the experimental measurements. (c) FEM simulations for the estimation of k_s .

Spring stiffness k_s . To determine the normalized stiffness of the shearing spring, k_s , we conduct Finite Element simulations using the commercial package Abaqus/Standard. In our analysis, (i) we consider two half squares with dimensions identical to those of our samples (see Fig. C.10(c)); (ii) we assume plane stress conditions; (iii) we mesh the models using quadratic triangular elements (Abaqus element type: CPS6) and ascertain the accuracy of the mesh through a mesh refinement study; (iv) we use an incompressible neo-Hookean model with initial shear modulus $\mu_0 = 0.3$ MPa to capture the material response; (v) we account for geometric non-linearities. We run two simulations in which we apply an horizontal displacement δ_l and a vertical displacement δ_s to the two vertical boundaries of our model, respectively (see Fig. C.10(c)). The stiffness k_l and k_s is then

obtained from the measured reaction force F_l and F_s (given by the sum of all reaction forces at the nodes located on one of the two boundaries) as

$$k_l^{\text{FE}} = \frac{F_l}{2\delta_l} = 620 \frac{N}{m}, \quad k_s^{\text{FE}} = \frac{F_s}{2\delta_s} = 137 \frac{N}{m}. \quad (\text{C.18})$$

Note that this longitudinal stiffness calculated via Finite Element k_l^{FE} is different from the experimental measured one k_l . This can be attributed to the fabrication error of the laser cut specimen. Nevertheless, we can assume that the ratio between shear and longitudinal spring stiffness should conserve, and calculate the shear stiffness our specimen as

$$k_s = \frac{k_s^{\text{FE}}}{k_l^{\text{FE}}} k_l = 239 \text{ N/m.} \quad (\text{C.19})$$

C.3.6 Propagation of linear waves

To characterize the propagation of linear waves in the considered metamaterial, we start by linearizing the discrete equations of motion around a deformed equilibrium configuration described by $u_{st}^{[i,j]}$, $v_{st}^{[i,j]}$, and $\theta_{st}^{[i,j]}$ (with $i = 1, \dots, N_y$ and $j = 1, \dots, N_x$). We then consider perturbations $u_w^{[i,j]}$, $v_w^{[i,j]}$ and $\theta_w^{[i,j]}$ of the displacement and rotation of the $[i,j]$ -th square,

$$\begin{aligned} u_w^{[i,j]} &= u^{[i,j]} - u_{st}^{[i,j]} \\ v_w^{[i,j]} &= v^{[i,j]} - v_{st}^{[i,j]} \\ \theta_w^{[i,j]} &= \theta^{[i,j]} - \theta_{st}^{[i,j]} \end{aligned} \quad (\text{C.20})$$

which take the metamaterial to a new equilibrium configuration where Eqs. (C.3) are still satisfied.

By substituting Eqs.(C.20) into Eqs.(C.3) and linearizing them with respect to $u_w^{[i,j]}$, $v_w^{[i,j]}$ and $\theta_w^{[i,j]}$, we find that the incremental equations of motion can be written in matrix form as

$$\mathbf{M} \frac{d^2}{dt^2} (\Phi_w) = \mathbf{K} \Phi_w \quad (\text{C.21})$$

where

$$\Phi_w = [u_w^{[1,1]}, v_w^{[1,1]}, \theta_w^{[1,1]}, u_w^{[1,2]}, v_w^{[1,2]}, \theta_w^{[1,2]}, \dots, u_w^{[N_y, N_x]}, v_w^{[N_y, N_x]}, \theta_w^{[N_y, N_x]}]^T, \quad (\text{C.22})$$

\mathbf{M} is the mass matrix

$$\mathbf{M} = \text{diag}[m, m, J, m, m, J, \dots, m, m, J] \quad (\text{C.23})$$

and \mathbf{K} is the stiffness matrix of the system that can be determined by numerically differentiating the total energy of the structure (Eq.(C.5)) as

$$\mathbf{K} = \frac{\partial^2 E_{\text{total}}(\Phi_{\text{st}})}{\partial \Phi_w \partial \Phi_w'} \quad (\text{C.24})$$

with

$$\Phi_{\text{st}} = [u_{\text{st}}^{[1,1]}, v_{\text{st}}^{[1,1]}, \theta_{\text{st}}^{[1,1]}, u_{\text{st}}^{[1,2]}, v_{\text{st}}^{[1,2]}, \theta_{\text{st}}^{[1,2]}, \dots, u_{\text{st}}^{[N_y, N_x]}, v_{\text{st}}^{[N_y, N_x]}, \theta_{\text{st}}^{[N_y, N_x]}]^T, \quad (\text{C.25})$$

Note that Φ_w and Φ_{st} are vectors with $3N_xN_y$ entries and \mathbf{K} and \mathbf{M} are a $(3N_xN_y) \times (3N_xN_y)$ matrices.

Natural frequencies and eigenmodes. To determine the natural frequencies of the system we seek a solution of Eqs. (C.21) in the form of

$$\Phi_w = \tilde{\Phi}_w e^{i\omega t}, \quad (\text{C.26})$$

where $i = \sqrt{-1}$, ω is the cyclic frequency of harmonic motion and $\tilde{\Phi}_w$ is a vector that defines the amplitude of the eigenmodes. Substitution of Eq. (C.26) into Eq. (C.21) yields

$$(\mathbf{K} + \omega^2 \mathbf{M}) \Phi_w = 0. \quad (\text{C.27})$$

Eq. (C.27) defines an eigenvalue problem that we solve to numerically determine the $3N_x N_y$ natural frequencies of the predeformed metamaterial and associated eigenmodes.

Dispersion relation. To calculate the band structure of the predeformed metamaterial with alternating light (with mass m) and heavy (with mass $3m/2$) squares (reported in Fig. 4.5C of the main text) we focus on a unit cell that comprises four squares and is defined by the two lattice vectors \mathbf{a}_1 and \mathbf{a}_2 (see Fig. C.11). We then consider a supercell comprising 5 unit cells (see Fig. C.11) and seek a solution of Eqs. (C.21) in the form of a harmonic wave,

$$\Phi_w^{[p,q]}(t) = \tilde{\Phi}_w e^{i(\vec{\mu} \cdot \mathbf{r}^{[p,q]} - \omega t)} \quad (\text{C.28})$$

where $\vec{\mu}$ is the two-dimensional wave vector, $\Phi_w^{[p,q]}(t)$ is a vector containing the 12 degree of freedom of the $[p, q]$ -th unit cell and

$$\mathbf{r}^{[p,q]} = p\mathbf{a}_1 + q\mathbf{a}_2 \quad (\text{C.29})$$

with $p, q = -1, 0$ and 1 . Substitution of Eqs. (C.28) into Eq. (C.21) yields

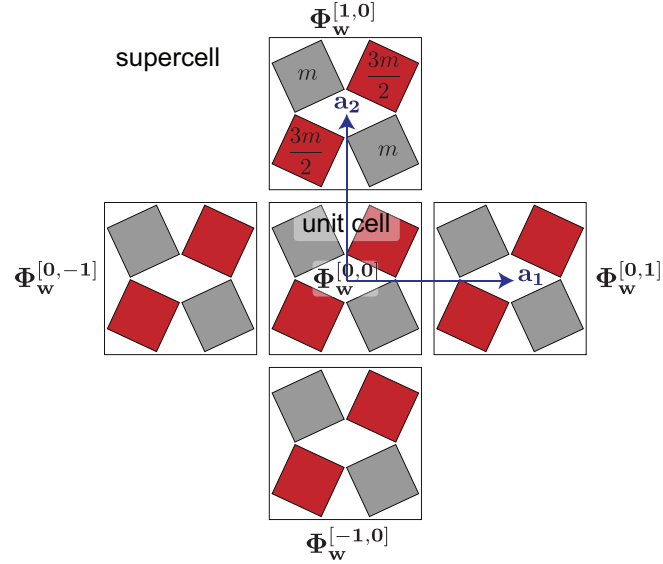


Figure C.11: Supercell used to calculate the dispersion relation.

$$-\omega^2 \mathbf{M} \tilde{\Phi}_w + \sum_{p,q=-1,0,1} \mathbf{K}^{[p,q]} \tilde{\Phi}_w e^{i\vec{\mu} \cdot \mathbf{r}^{[p,q]}} = 0, \quad (\text{C.30})$$

where \mathbf{M} and $\mathbf{K}^{[p,q]}$ are the mass matrix and stiffness matrix of the $[p, q]$ -th unit cell. Eq. (C.30) can be further rewritten as

$$[-\omega^2 \mathbf{M} + \hat{\mathbf{K}}(\vec{\mu})] \Phi_w = 0, \quad (\text{C.31})$$

where

$$\hat{\mathbf{K}}(\vec{\mu}) = \sum_{p,q=-1,0,1} \mathbf{K}^{[p,q]} e^{i\vec{\mu} \cdot \mathbf{r}^{[p,q]}} \quad (\text{C.32})$$

depends on wave vector $\vec{\mu}$. Eq. (C.31) defines an eigenvalue problem that can be solved to obtain frequency ω as a function of wave vector $\vec{\mu}$. Eq. (C.31) yields 12 dispersion branches each corresponding to a linear wave mode that are shown in manuscript Fig. 5C.

C.3.7 Additional numerical results

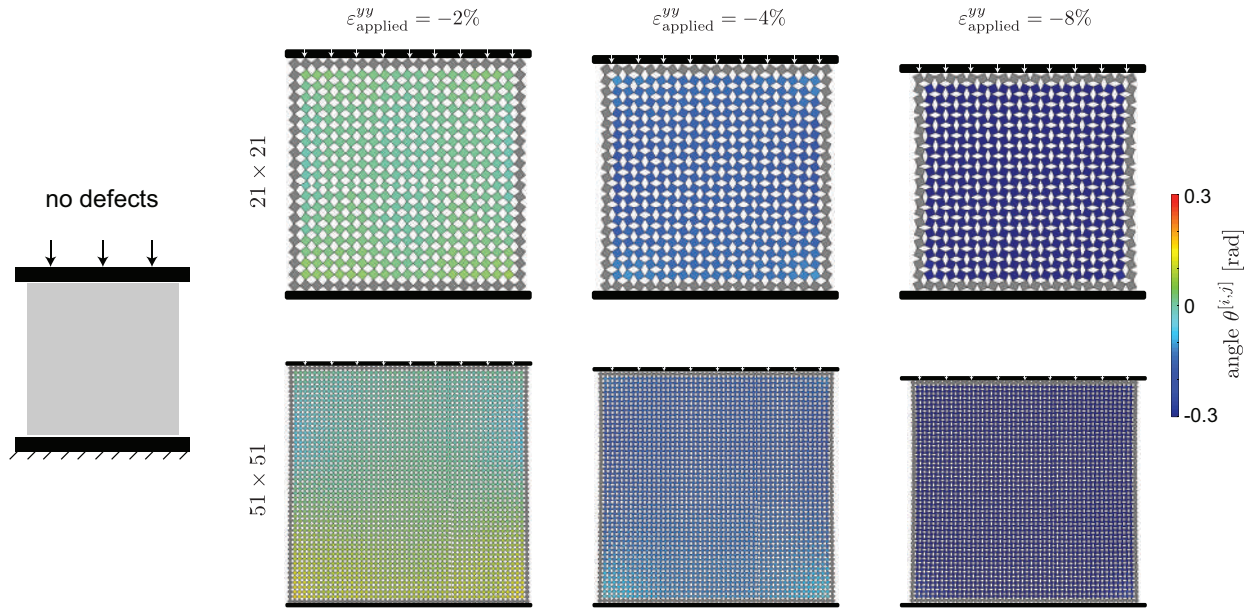


Figure C.12: Numerically predicted deformation at applied strain $\varepsilon_{\text{applied}}^{yy} = -2\%, -4\%$ and -8% of structures comprising 21×21 squares (top) and 51×51 squares (bottom) in the absence of intentional defects.

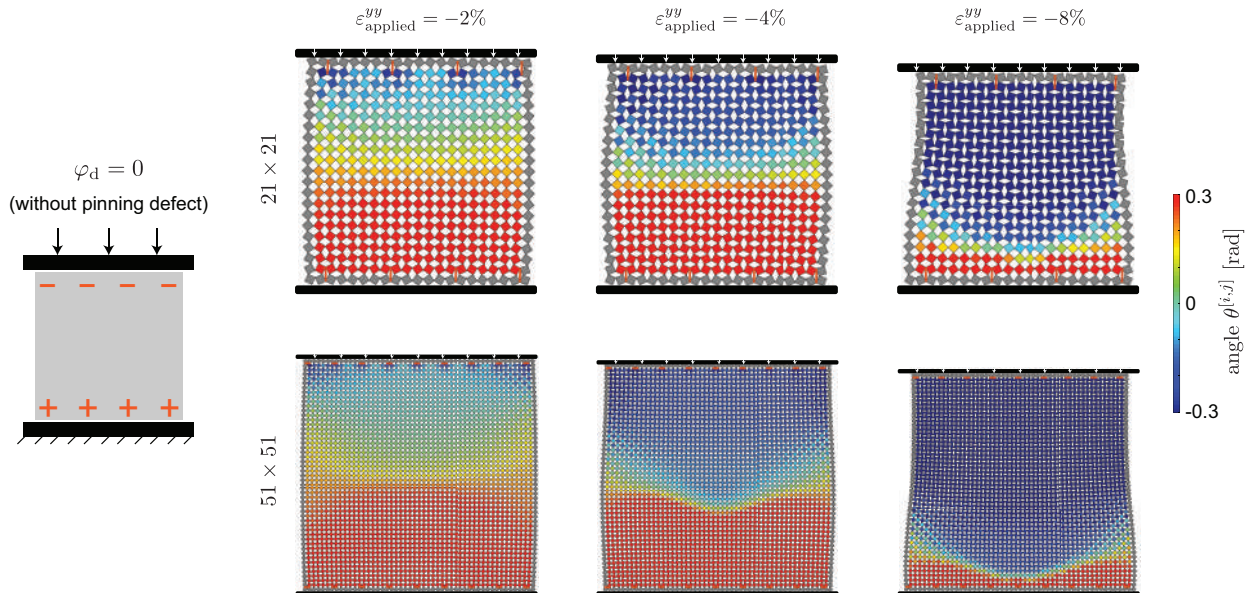


Figure C.13: Numerically predicted deformation at applied strain $\varepsilon_{\text{applied}}^{yy} = -2\%, -4\%$ and -8% of structures comprising 21×21 squares (top) and 51×51 squares (bottom) with phase-inducing defects linearly arranged and angled at $\varphi_d = 0$ to get phase- to propagate from the top boundary and phase+ from the bottom one.

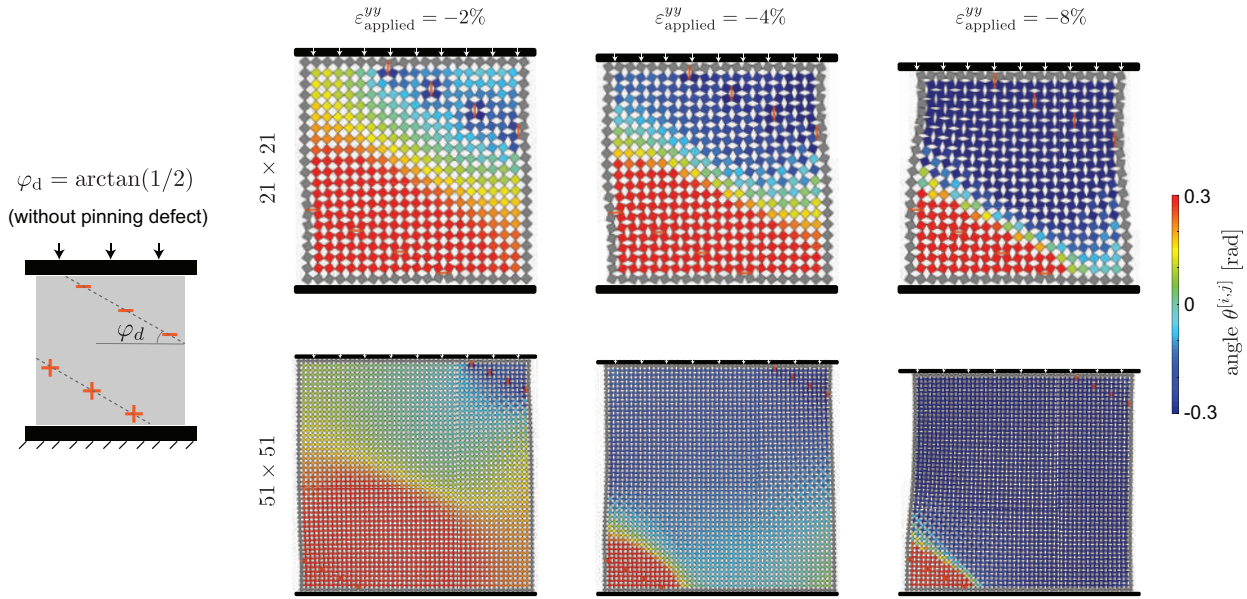


Figure C.14: Numerically predicted deformation at applied strain $\varepsilon_{\text{applied}}^{yy} = -2\%$, -4% and -8% of structures comprising 21×21 squares (top) and 51×51 squares (bottom) with phase-inducing defects linearly arranged and angled at $\varphi_d = \arctan(1/2)$ to get *phase-* to propagate from the top-right corner and *phase+* from the bottom-left one.

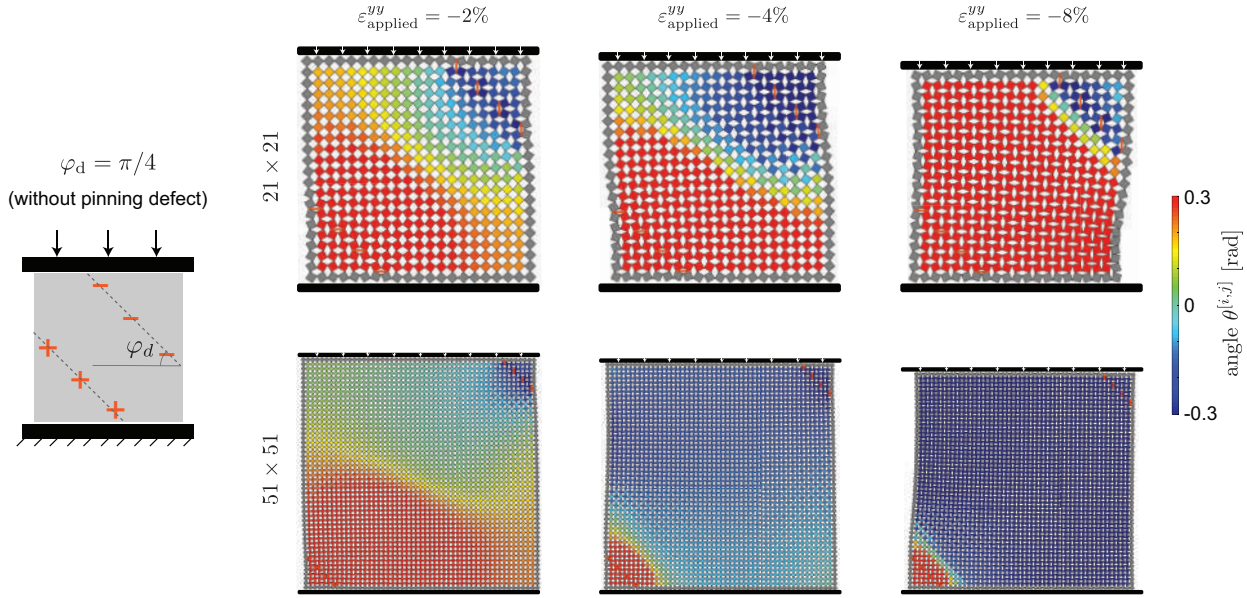


Figure C.15: Numerically predicted deformation at applied strain $\varepsilon_{\text{applied}}^{yy} = -2\%$, -4% and -8% of structures comprising 21×21 squares (top) and 51×51 squares (bottom) with phase-inducing defects linearly arranged and angled at $\varphi_d = \pi/4$ to get *phase-* to propagate from the top-right corner and *phase+* from the bottom-left one.

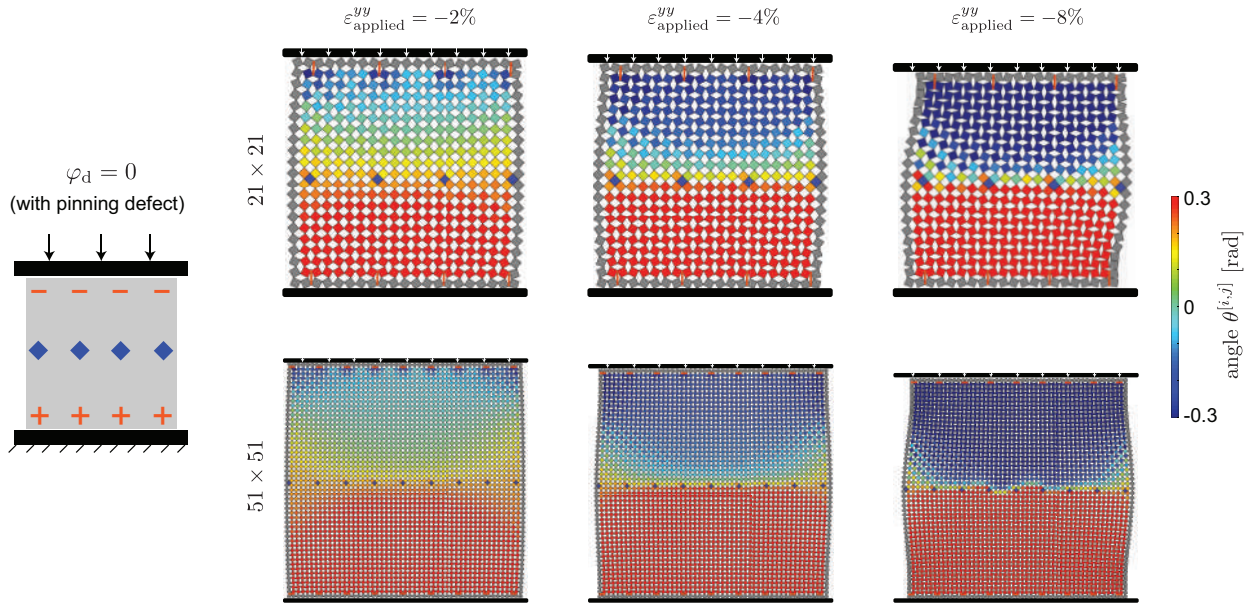


Figure C.16: Numerically predicted deformation at applied strain $\varepsilon_{\text{applied}}^{yy} = -2\%, -4\%$ and -8% of structures comprising 21×21 squares (top) and 51×51 squares (bottom) with pinning defects equally spaced along a horizontal line spanning their center, in addition to the previous phase-inducing defects arranged as in Fig. C.13.

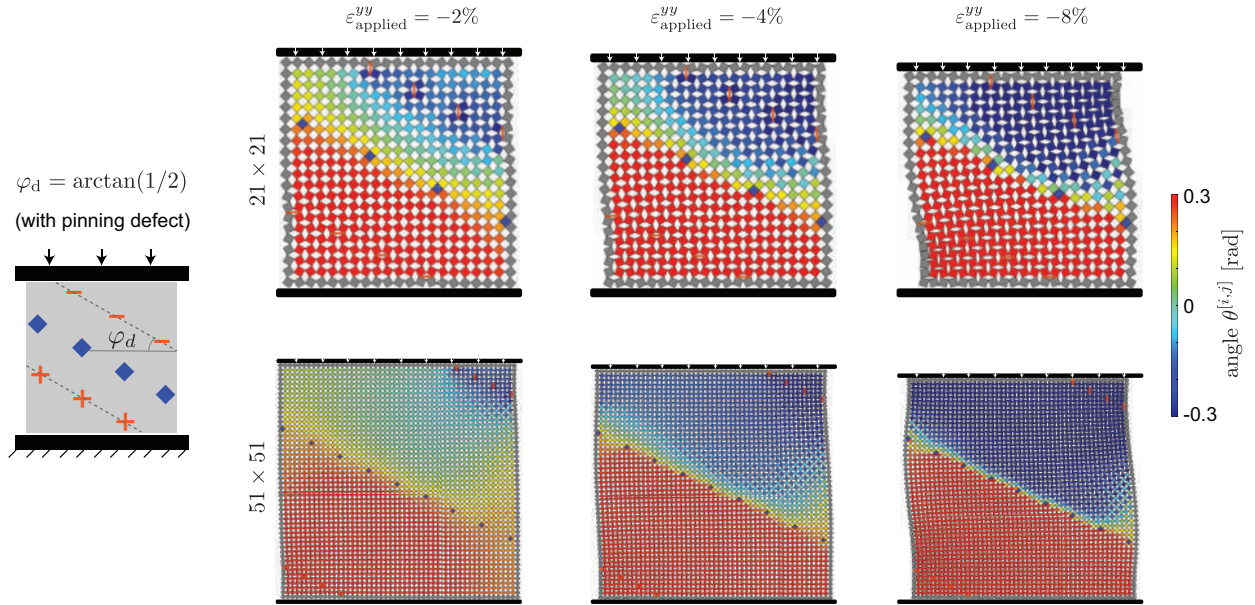


Figure C.17: Numerically predicted deformation at applied strain $\varepsilon_{\text{applied}}^{yy} = -2\%, -4\%$ and -8% of structures comprising 21×21 squares (top) and 51×51 squares (bottom) with pinning defects equally spaced along a line at $\varphi_d = \arctan(1/2)$, in addition to the previous phase-inducing defects arranged as in Fig. C.14.

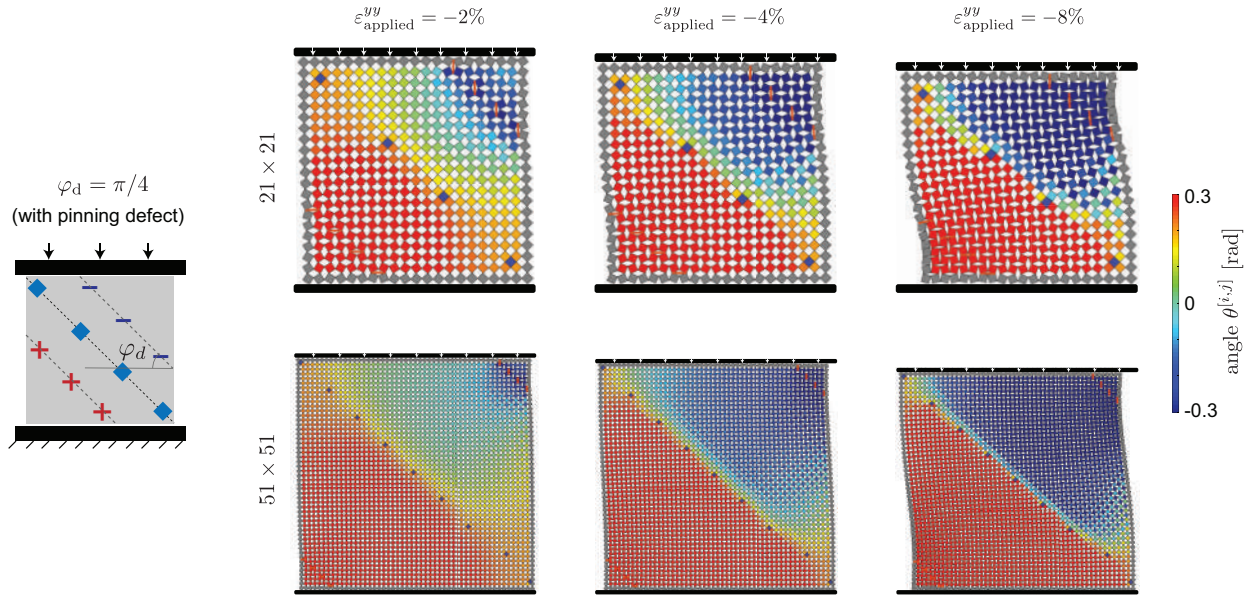


Figure C.18: Numerically predicted deformation at applied strain $\varepsilon_{\text{applied}}^{yy} = -2\%$, -4% and -8% of structures comprising 21×21 squares (top) and 51×51 squares (bottom) with pinning defects equally spaced along a line at $\varphi_d = \pi/4$, in addition to the previous phase-inducing defects arranged as in Fig. C.15.

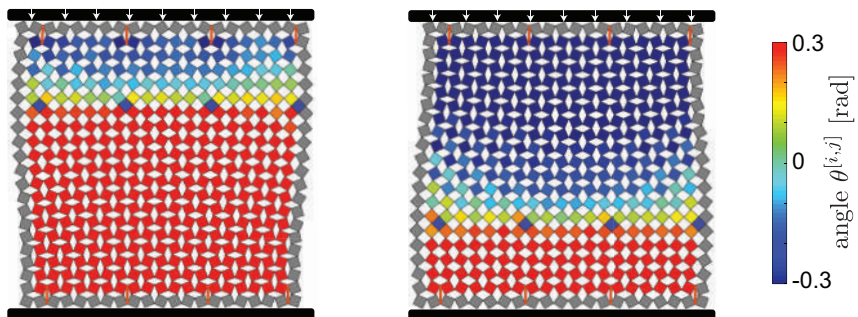


Figure C.19: Numerically predicted deformation at applied strain $\varepsilon_{\text{applied}}^{yy} = -6\%$ of structures comprising 21×21 squares and pinning defects equally spaced along horizontal lines located near the top (left) and bottom (right), in addition to the previous phase-inducing defects arranged as in Fig. 4.2B of the main text.

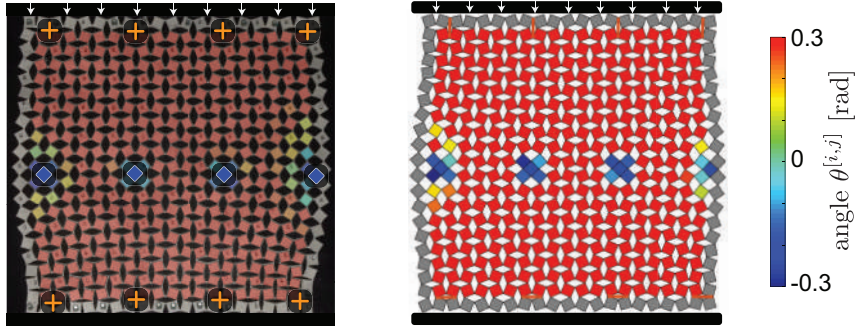


Figure C.20: Deformation at $\varepsilon_{\text{applied}}^{\text{yy}} = -6\%$ of a sample with 4 pinning defects and 8 phase-inducing defects arranged as in Fig. 4.2A of the main text. Since the phase-inducing defects induce the formation of a single phase, no domain wall is generated (i.e. pinning defects along can not lead to the formation of domain walls).

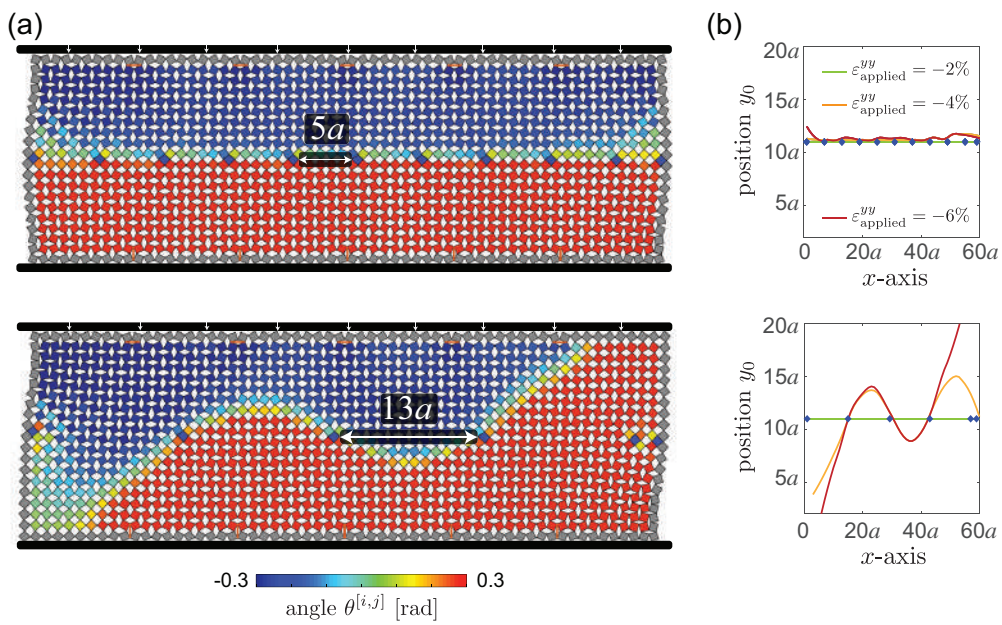


Figure C.21: (a) Numerically predicted deformation at $\varepsilon_{\text{applied}}^{\text{yy}} = -6\%$ of structures comprising 21×60 squares with pinning defect separated by 5 (top) and 13 (bottom) holes (in addition to phase-inducing defects arranged to generate an horizontal domain wall). (b) Corresponding domain wall profiles extracted at $\varepsilon_{\text{applied}}^{\text{yy}} = -2\%$, -4% and -6% .

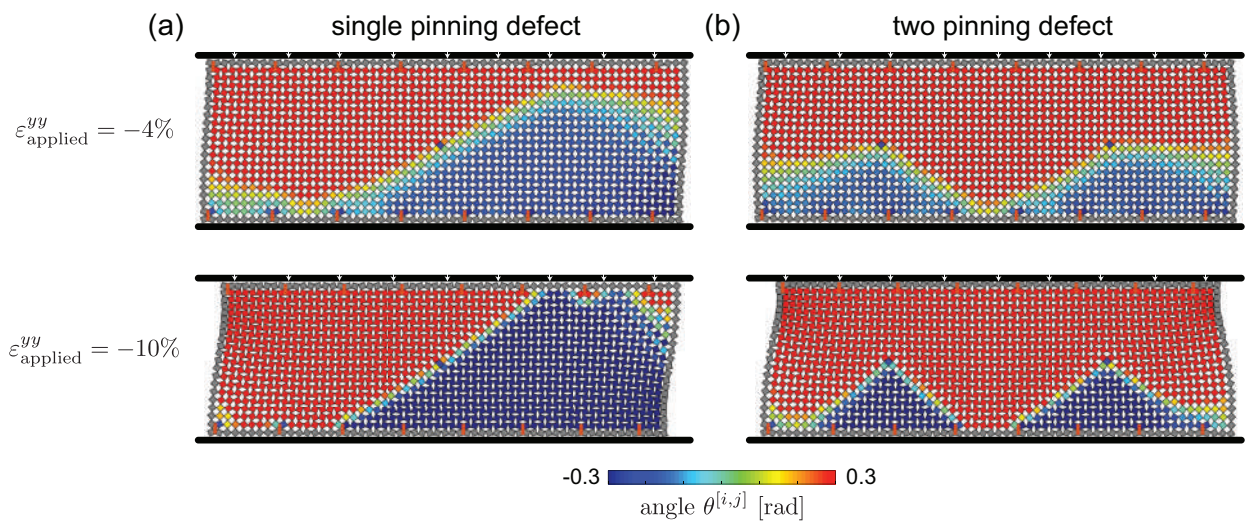


Figure C.22: Numerically predicted deformation at $\varepsilon_{\text{applied}}^{yy} = -4\%$ (top) and -10% (bottom) of structures comprising 21×60 squares with (a) only one pinning defect and (b) two pinning defects at the center (in addition to phase-inducing defects arranged to generate an horizontal domain wall).

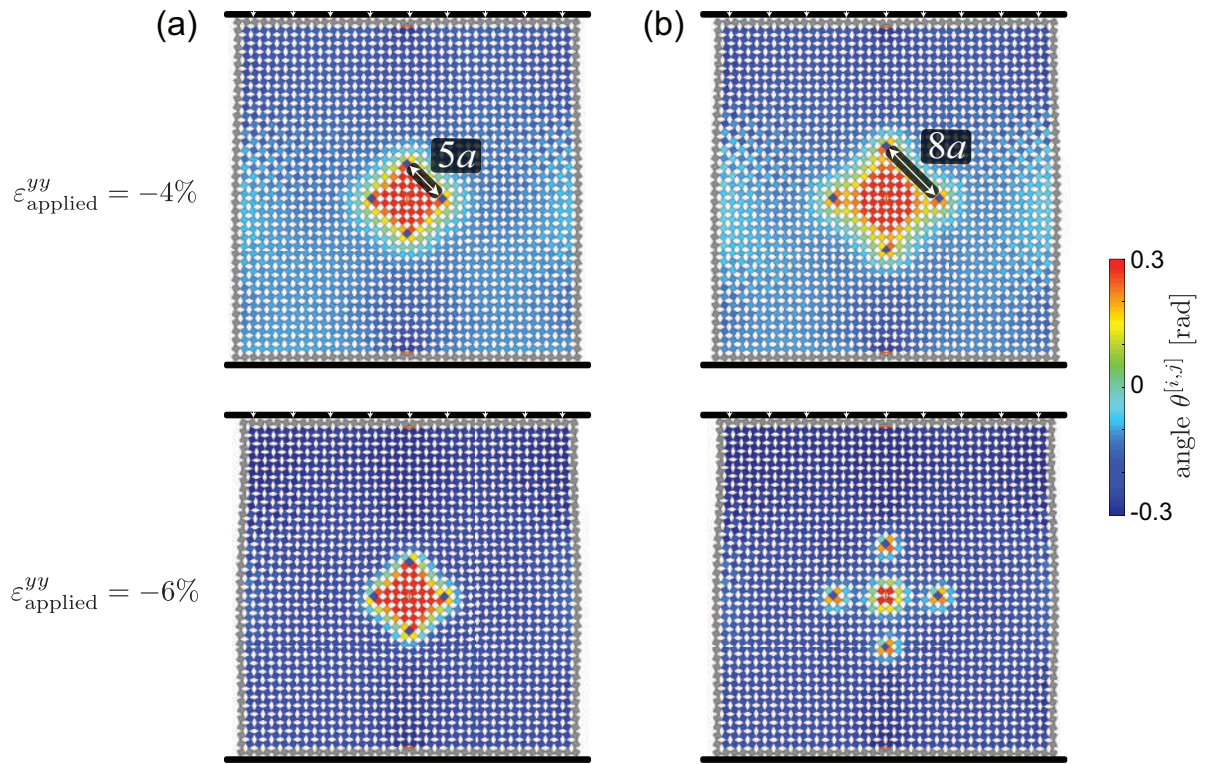


Figure C.23: Numerically predicted deformation at $\varepsilon_{\text{applied}}^{yy} = -4\%$ (top) and -6% (bottom) of structures comprising 51×51 squares with four pinning defects arranged at the vertices of a rhombus with edge (a) $5a$ and (b) $8a$. In addition, two phase-inducing defects are located next to the top and bottom boundary to promote phase -. These defects result in the formation of a rhomboid phase + region defined by the pinning defects.

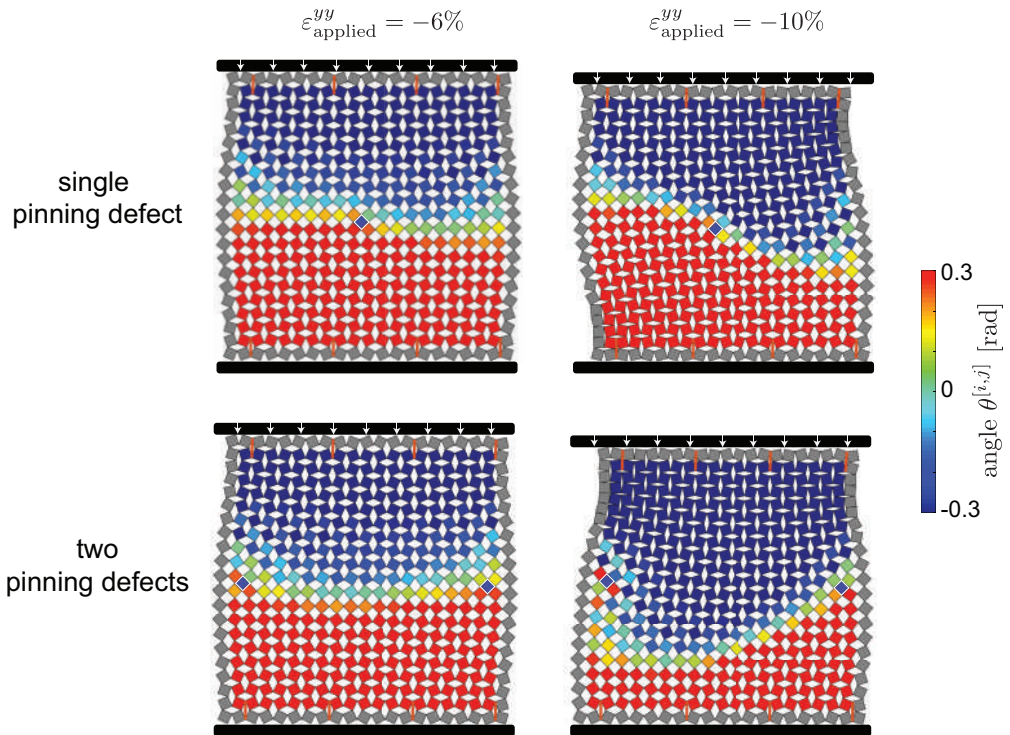


Figure C.24: Numerically predicted deformation at $\varepsilon_{\text{applied}}^{yy} = -6\%$ (left) and -10% (right) of structures comprising 21×21 squares with (a) only one pinning defect and (b) two pinning defects (in addition to phase-inducing defects arranged to generate an horizontal domain wall). Similar wavy pattern are observed for the emerged domain walls as in the wide 21×60 squares sample (see Fig. C.21).

C.4 Continuum Model

As shown in Section C.3.4, in the absence of defects the applied uniaxial loading results in an homogenous state of deformation that can be easily described analytically. By contrast, our experiments and discrete simulations indicate that the introduction of defects may lead to highly inhomogenous deformation fields and the formation of distinct domain walls. Here, we simplify the discrete equations of motions to obtain analytical solutions for a system in which the defects generate such domain walls.

We start by considering a structure that is uniaxially deformed by applying a compressive strain $\varepsilon_{\text{applied}}^{yy}$ and has a perfectly straight domain wall at an angle φ with respect to the horizontal axis and seek for an analytical solution that describes the spatially inhomogeneous deformation of the system. Towards this end, we introduce three continuous functions $u(x, y)$, $v(x, y)$ and $\theta(x, y)$ that interpolate the displacements and rotation of the $[i, j]^{\text{th}}$ square as

$$u(x = ja, y = ia) = u^{[i,j]}, \quad (\text{C.33})$$

$$v(x = ja, y = ia) = v^{[i,j]}, \quad (\text{C.34})$$

$$\theta(x = ja, y = ia) = \theta^{[i,j]}, \quad (\text{C.35})$$

where x and y are the coordinate along the x - and y -axis, respectively. Assuming that the width of the domain wall is much larger than the size of the squares, the normalized displacements u and v and the rotation θ of the $[i, j - 1]^{\text{th}}$, $[i, j + 1]^{\text{th}}$, $[i - 1, j]^{\text{th}}$ and $[i + 1, j]^{\text{th}}$ squares can then be expressed

using Taylor expansion as

$$\begin{aligned}
u^{[i,j+p]} &\approx \left[u + ap \partial_x u + \frac{(ap)^2}{2} \partial_{xx} u \right]_{x=j, y=i} \\
u^{[i+p,j]} &\approx \left[u + ap \partial_y u + \frac{(ap)^2}{2} \partial_{yy} u \right]_{x=j, y=i} \\
v^{[i,j+p]} &\approx \left[v + ap \partial_x v + \frac{(ap)^2}{2} \partial_{xx} v \right]_{x=j, y=i} \\
v^{[i+p,j]} &\approx \left[v + ap \partial_y v + \frac{(ap)^2}{2} \partial_{yy} v \right]_{x=j, y=i} \\
\theta^{[i,j+p]} &\approx \left[\theta + ap \partial_x \theta + \frac{(ap)^2}{2} \partial_{xx} \theta \right]_{x=j, y=i} \\
\theta^{[i+p,j]} &\approx \left[\theta + ap \partial_y \theta + \frac{(ap)^2}{2} \partial_{yy} \theta \right]_{x=j, y=i} \\
\cos \theta^{[i,j+p]} &\approx \left[\cos \theta + ap \partial_x \cos \theta + \frac{(ap)^2}{2} \partial_{xx} \cos \theta \right]_{x=j, y=i} \\
\cos \theta^{[i+p,j]} &\approx \left[\cos \theta + ap \partial_y \cos \theta + \frac{(ap)^2}{2} \partial_{yy} \cos \theta \right]_{x=j, y=i} \\
\sin \theta^{[i,j+p]} &\approx \left[\sin \theta + ap \partial_x \sin \theta + \frac{(ap)^2}{2} \partial_{xx} \sin \theta \right]_{x=j, y=i} \\
\sin \theta^{[i+p,j]} &\approx \left[\sin \theta + ap \partial_y \sin \theta + \frac{(ap)^2}{2} \partial_{yy} \sin \theta \right]_{x=j, y=i}
\end{aligned} \tag{C.36}$$

where $p \in \{-1, 1\}$ and $\partial_\alpha f = \partial f / \partial \alpha$. Substitution of Eqs. (C.36) into Eq. (C.3) yields the continuum governing equations of the system,

$$k_l \partial_{xx} u + k_s \partial_{yy} u - k_l \partial_x \cos \theta = 0, \tag{C.37a}$$

$$k_l \partial_{yy} v + k_s \partial_{xx} v - k_l \partial_y \cos \theta = 0, \tag{C.37b}$$

$$\begin{aligned}
&4k_\theta a^2 \nabla^2 \theta + 32k_\theta (\theta + 4\gamma \theta^3) - k_s a^4 \cos \theta \nabla^2 \sin \theta \\
&k_l a^2 \sin \theta [8 - 8 \cos \theta - a^2 \nabla^2 \cos \theta + 4(\partial_x u + \partial_y v)] = 0,
\end{aligned} \tag{C.37c}$$

where $\nabla^2 = \partial_{xx} + \partial_{yy}$. Note that in Eqs. (C.37) the inertia terms are disregarded as we are looking for quasi-static solutions. Furthermore, in deriving Eqs. (C.37) from Eqs. (C.3) we also have neglected all the terms that switch sign between each neighboring unit (i.e., the terms with coefficient $(-1)^{i+j}$), as they are intrinsically incompatible with continuous solutions and have shown to have small influence on the final solutions^[129].

The uniaxial compression loading considered in our experiments is then modeled by imposing

$$v(y = aN_y) - v(y = a) = a(N_y - 1)\varepsilon_{\text{applied}}^{yy}, \quad (\text{C.38})$$

and

$$\partial_x u + 1 - \cos \theta = 0, \quad (\text{C.39})$$

where Eq. (C.39) is obtained by requiring the longitudinal forces in all horizontal ligaments to vanish (by substituting Eqs. (C.36) into Eq. (C.9)).

C.4.1 Analytical solution

Eqs. (C.37)-(C.39) formulate a complete mathematical problem that can be solved to obtain analytical solutions. To this end, we use a third order Taylor polynomial to approximate the functions sin and cos as

$$\sin \theta \approx \theta - \frac{\theta^3}{6}, \quad \text{and} \quad \cos \theta \approx 1 - \frac{\theta^2}{2}, \quad (\text{C.40})$$

Substitution of Eq. (C.40) into Eq. (C.37) and (C.39) yields

$$k_l \partial_{xx} u + k_s \partial_{yy} u + k_l \theta \partial_x \theta = 0, \quad (\text{C.41a})$$

$$k_l \partial_{yy} v + k_s \partial_{xx} v + k_l \theta \partial_y \theta = 0, \quad (\text{C.41b})$$

$$\begin{aligned} & -a^2(k_s a^2 - 4k_\theta) \nabla^2 \theta + 32k_\theta \theta + 4(k_l a^2 + 32\gamma k_\theta) \theta^3 \\ & + 4k_l a^2(\theta - \frac{1}{6}\theta^3)(\partial_x u + \partial_y v) = 0, \end{aligned} \quad (\text{C.41c})$$

and

$$\partial_x u + \theta^2/2 = 0, \quad (\text{C.42})$$

respectively. Since Eqs. (C.41) are a set of coupled nonlinear partial differential equations, to obtain an analytical solution we want first to reduce them to a single second order differential equation. As a first step in this direction, we substitute Eq. (C.42) into Eqs. (C.41) and find that Eq. (C.41a) vanishes, whereas Eqs. (C.41b) and (C.41c) simplify to

$$k_l \partial_{yy} v + k_s \partial_{xx} v + k_l \theta \partial_y \theta = 0, \quad (\text{C.43a})$$

$$\begin{aligned} & -a^2(k_s a^2 - 4k_\theta) \nabla^2 \theta + 32k_\theta \theta + 2(k_l a^2 + 64\gamma k_\theta) \theta^3 \\ & + 4k_l a^2(\theta - \frac{\theta^3}{6}) \partial_y v = 0. \end{aligned} \quad (\text{C.43b})$$

Next, we introduce a local coordinate system, ζ - η , aligned with the domain wall

$$\zeta = x \sin \varphi + y \cos \varphi, \quad \text{and} \quad \eta = x \cos \varphi - y \sin \varphi, \quad (\text{C.44})$$

where φ is the angle between the domain wall and the horizontal axis (which is considered positive when clockwise - see Fig. C.25). Since our experiments and discrete simulations indicate that the

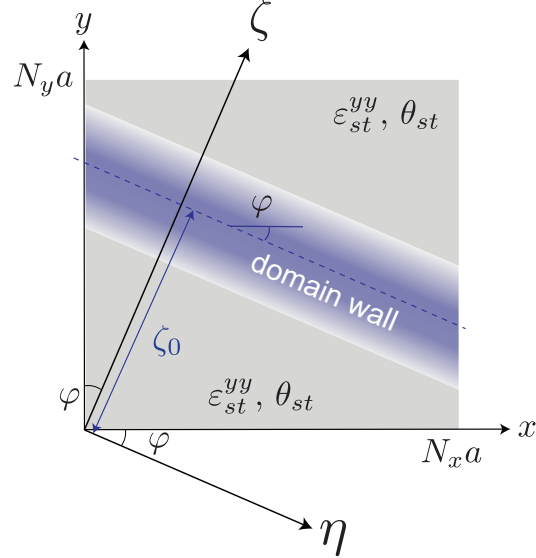


Figure C.25: Schematic of a domain wall with an orientation of φ and position ζ_0 .

variation of deformation along the domain wall are negligible (see Figs. C.13-C.18), we further assume that $\partial_\eta(\cdot) = 0$ and write the derivatives with respect of x and y as

$$\partial_x(\cdot) = \sin \varphi d_\zeta(\cdot), \quad \text{and} \quad \partial_y(\cdot) = \cos \varphi d_\zeta(\cdot). \quad (\text{C.45})$$

Substitution of Eq. (C.45) into Eqs. (C.43) yields

$$(k_l \cos^2 \varphi + k_s \sin^2 \varphi) d_{\zeta\zeta} v + k_l \cos \varphi \theta d_\zeta \theta = 0, \quad (\text{C.46a})$$

$$\begin{aligned} & -a^2(k_s a^2 - 4k_\theta)d_{\zeta\zeta}\theta + 32k_\theta\theta + 2(k_l a^2 + 64\gamma k_\theta)\theta^3 \\ & + 4k_l a^2(\theta - \frac{1}{6}\theta^3)d_\zeta v = 0 \end{aligned} \quad (\text{C.46b})$$

which are the governing equations of the system written as a function of ζ . To solve this system of differential equations we first integrate Eq. (C.46a) to obtain

$$d_\zeta v = -\frac{k_l \cos \varphi}{2(k_l \cos^2 \varphi + k_s \sin^2 \varphi)}\theta^2 + C, \quad (\text{C.47})$$

where C is an integration constant that can be determined by assuming homogeneous deformation inside each phase (i.e. far away from domain wall). Specifically, by imposing

$$\partial_y v \Big|_{phase\pm} = \varepsilon_{st}^{yy}, \quad \theta \Big|_{phase\pm} = \pm \theta_{st}, \quad (\text{C.48})$$

and using Eq. (C.11) to connect ε_{st}^{yy} and θ_{st} , C is determined as

$$C = \frac{k_l \cos \varphi}{k_l \cos^2 \varphi + k_s \sin^2 \varphi}\theta_{st}^2 - \frac{8k_\theta}{k_l a^2 \cos \varphi}(1 + 4\gamma\theta_{st}^2) - \frac{\theta_{st}^2}{2 \cos \varphi} - \frac{4k_\theta\theta_{st}^2}{3k_l a^2 \cos \varphi}. \quad (\text{C.49})$$

By introducing Eq. (C.49), Eq. (C.47) can be rewritten as

$$d_\zeta v = \frac{k_l \cos \varphi}{k_l \cos^2 \varphi + k_s \sin^2 \varphi}(\theta_{st}^2 - \theta^2) - \frac{8k_\theta}{k_l a^2 \cos \varphi}(1 + 4\gamma\theta_{st}^2) - \frac{\theta_{st}^2}{2 \cos \varphi} - \frac{4k_\theta\theta_{st}^2}{3k_l a^2 \cos \varphi}. \quad (\text{C.50})$$

We then substitute Eq. (C.50) into Eq. (C.46b) to obtain

$$a^2 d_{\zeta} \theta = \frac{1}{k_s a^2 - 4k_\theta} \left[4 \left(\frac{4}{3} + 32\gamma \right) k_\theta + \frac{2k_s k_l a^2 \sin^2 \varphi}{k_s \sin^2 \varphi + k_l \cos^2 \varphi} \right] \theta(\theta - \theta_{st})(\theta + \theta_{st}). \quad (\text{C.51})$$

Eq. (C.51) has the form of a Klein-Gordon Equation with quadratic and cubic non-linearities and admits analytic solutions in the form of

$$\theta = \theta_{st} \tanh \frac{\zeta - \zeta_0}{w} = \theta_{st} \tanh \frac{x \sin \varphi + y \cos \varphi - \zeta_0}{w}, \quad (\text{C.52})$$

where w represents the width of the domain wall and ζ_0 denotes the position of the domain wall (see Fig. C.25). Note that to determine w as a function of system parameters we substitute the solution Eq. (C.52) into Eq. (C.51) and find that the latter is identically satisfied only if

$$w = \frac{a}{\theta_{st}} \sqrt{\frac{3(k_s a^2 - 4k_\theta)}{8k_\theta(1 + 24\gamma) + \frac{3k_s k_l a^2 \sin^2 \varphi}{k_s \sin^2 \varphi + k_l \cos^2 \varphi}}}. \quad (\text{C.53})$$

Finally, the displacement solutions $u(x, y)$ and $v(x, y)$ can be obtained by integrating Eqs. (C.39) and (C.50), respectively

$$\begin{aligned} u(x, y) &= \int_0^x (\cos \theta - 1) dx' \approx \int_0^x -\frac{\theta^2}{2} dx' \\ &= -\frac{w \theta_{st}^2}{2 \sin \varphi} \left(\frac{x \sin \varphi}{w} + \frac{2}{e^{2(x \sin \varphi + y \cos \varphi - \zeta_0)/w} + 1} - \frac{2}{e^{2(y \cos \varphi - \zeta_0)/w} + 1} \right), \end{aligned} \quad (\text{C.54a})$$

$$\begin{aligned}
v(x, y) &= \int_0^\zeta \left[\frac{k_l \cos \varphi (\cos \theta - \cos \theta_{st})}{k_l \cos^2 \varphi + k_s \sin^2 \varphi} - \frac{8k_\theta \theta_{st} (1 + 4\gamma \theta_{st}^2)}{k_l a^2 \cos \varphi \sin \theta_{st}} - \frac{1 - \cos \theta_{st}}{\cos \varphi} \right] d\zeta' \\
&\approx \int_0^\zeta \left[\frac{k_l \cos \varphi (\theta_{st}^2/2 - \theta^2/2)}{k_l \cos^2 \varphi + k_s \sin^2 \varphi} - \frac{8k_\theta \theta_{st} (1 + 4\gamma \theta_{st}^2)}{k_l a^2 \cos \varphi \sin \theta_{st}} - \frac{1 - \cos \theta_{st}}{\cos \varphi} \right] d\zeta' \\
&= \frac{k_l w \cos \varphi \theta_{st}^2}{k_l \cos^2 \varphi + k_s \sin^2 \varphi} \left(\frac{1}{e^{-2\zeta_0/w} + 1} - \frac{1}{e^{2(x \sin \varphi + y \cos \varphi - \zeta_0)/w} + 1} \right) \\
&\quad - \left[\frac{8k_\theta \theta_{st} (1 + 4\gamma \theta_{st}^2)}{k_l a^2 \cos \varphi \sin \theta_{st}} + \frac{1 - \cos \theta_{st}}{\cos \varphi} \right] (x \sin \varphi + y \cos \varphi).
\end{aligned} \tag{C.54b}$$

Finally, θ_{st} at a given level of applied strain $\varepsilon_{\text{applied}}^{yy}$ is determined imposing Eq. (C.38) with $v(x, y)$ given by Eq. (C.54b).

In the special case of a structure with an horizontal domain wall (i.e. $\varphi = 0$) Eqs. (C.52), (C.53), (C.54a) and (C.54b) reduce to

$$\begin{aligned}
\theta(x, y) &= \theta_{st} \tanh \frac{y - y_0}{w}, \\
u(x, y) &= -\frac{\theta_{st}^2 x}{2} \tanh^2 \frac{y - y_0}{w}, \\
v(x, y) &= \theta_{st}^2 w \left(\frac{1}{e^{-2y_0/w} + 1} - \frac{1}{e^{2(y-y_0)/w} + 1} \right) \\
&\quad - \left[\frac{8k_\theta \theta_{st} (1 + 4\gamma \theta_{st}^2)}{k_l a^2 \sin \theta_{st}} + 1 - \cos \theta_{st} \right] y,
\end{aligned} \tag{C.55}$$

with

$$w = \frac{a}{\theta_{st}} \sqrt{\frac{(k_s a^2 - 4k_\theta)}{2(\frac{4}{3} + 32\gamma)k_\theta}}. \tag{C.56}$$

C.4.2 Position ζ_0 and orientation φ of the domain walls

To predict the position and orientation of the domain walls as a function of the applied deforma-

tion, we use Eq. (C.5) to calculate the total energy of the system for a given distribution of defects with the displacements and rotation of each square (i.e. $u^{[i,j]}$, $v^{[i,j]}$ and $\theta^{[i,j]}$) defined by interpolating the analytical solutions given by Eqs. (C.52) and (C.54),

$$\begin{aligned} u^{[i,j]} &= u(x=j, y=i), \\ v^{[i,j]} &= v(x=j, y=i), \\ \theta^{[i,j]} &= \theta(x=j, y=i). \end{aligned} \quad (\text{C.57})$$

The position ζ_0 and orientation φ of the domain walls are then obtained by minimizing E_{total} . Examples are reported in Figs. C.26, C.27 and C.28.

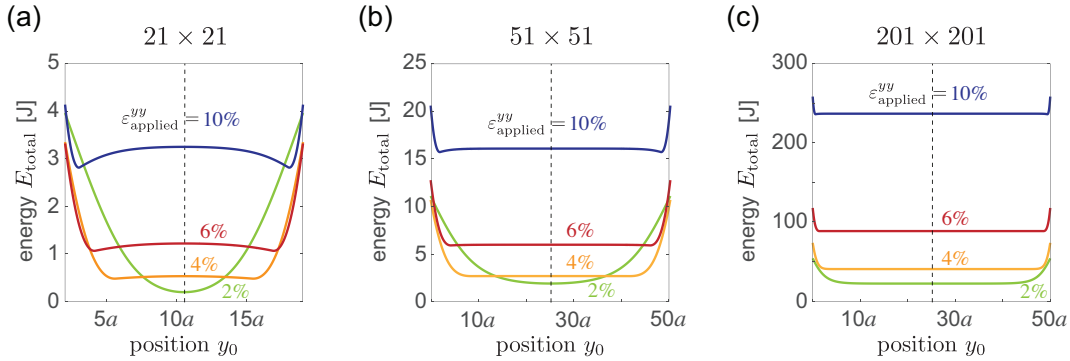


Figure C.26: Analytical predicted evolution of E_{total} as a function of domain wall position y_0 at $\varepsilon_{\text{applied}}^{yy} = -2\%$, -4% , -6% and -10% for structures with (a) 21×21 squares; (b) 51×51 squares and (c) 201×201 squares and phase-inducing defects arranged to generate an horizontal domain wall. The results indicate that, while in small structures E_{total} gradually turns into a multi-welled landscape with two minima that progressively move towards the horizontal boundaries, in larger structures present E_{total} becomes flat upon compression. As such, we expect the domain walls in large structures to remain at the center even upon compression. In other words, the shifting of domain walls observed in our samples is caused by boundary effects.

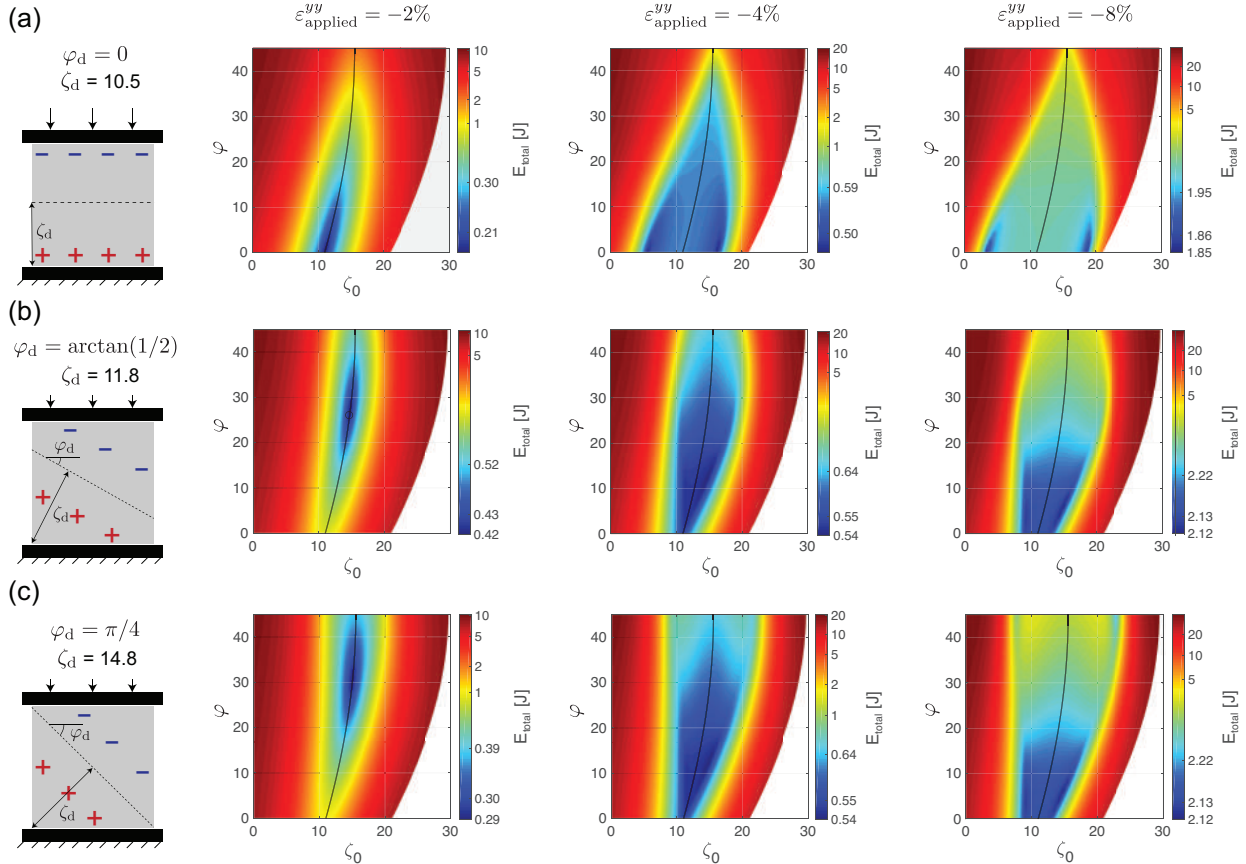


Figure C.27: Analytically predicted evolution of E_{total} as a function of ζ_0 and φ at $\varepsilon_{\text{applied}}^{yy} = -2\%$, -4% and -8% for structures comprising 21×21 squares and phase-inducing defects arranged as (a) in Fig. 4.2B-C of the main text; (b) in Fig. 4.4A of the main text ($\varphi_d = \arctan(1/2)$) and (c) in Fig. 4.4A of the main text ($\varphi_d = \pi/4$). As the applied compression increases, the local minima of E_{total} move away from the centered line between and shift towards the boundaries. Furthermore, for the cases with $\varphi_d \neq 0$ the domain walls also change their orientation as $\varepsilon_{\text{applied}}^{yy}$ increased. These results nicely explain the experimental results reported in Figs. 4A and 4C.

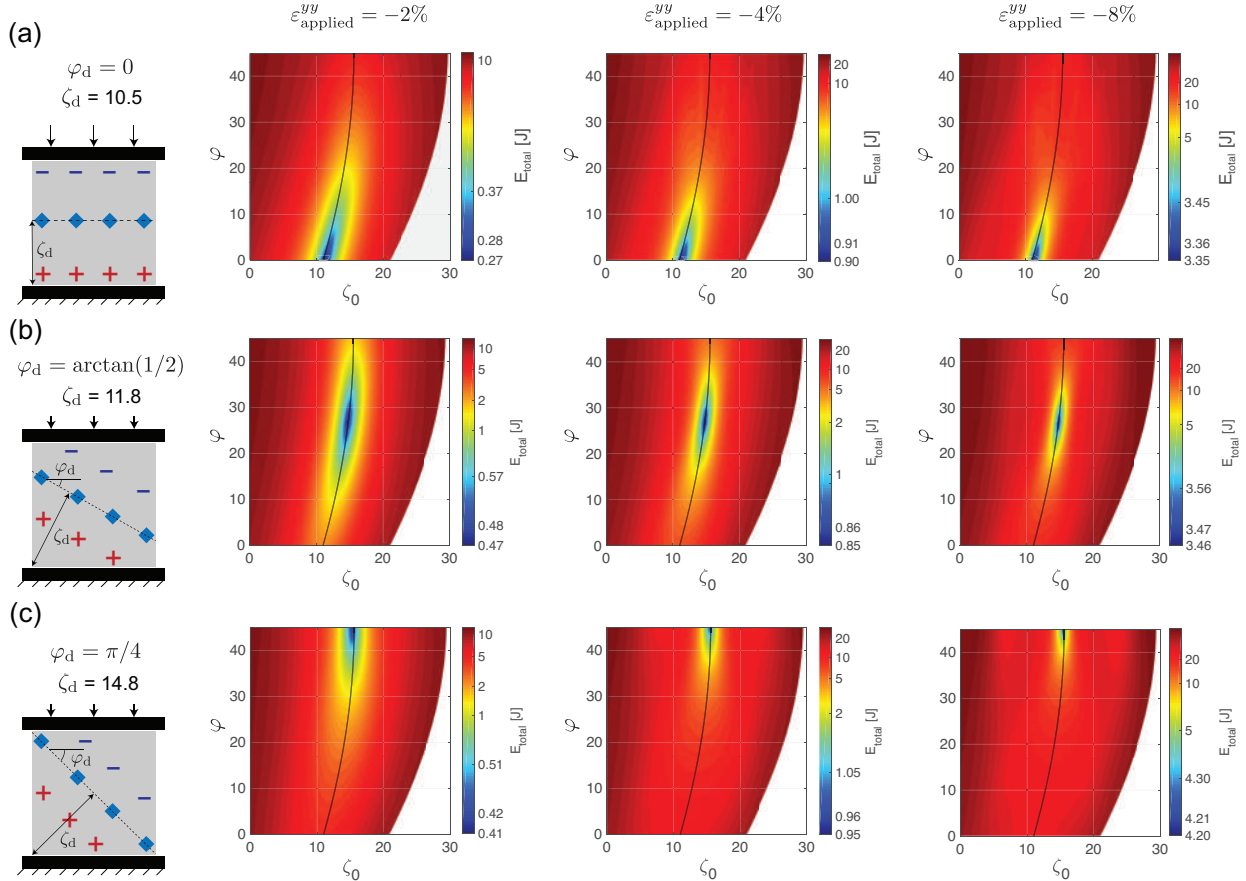


Figure C.28: Analytically predicted evolution of E_{total} at $\varepsilon_{\text{applied}}^{yy} = -2\%, -4\%$ and -8% for structures comprising 21×21 squares and phase-inducing and pinning defects arranged as (a) in Fig. 4.3A of the main text; (b) in Fig. 4.4C of the main text ($\varphi_d = \arctan(1/2)$) and (c) in Fig. 4.4C of the main text ($\varphi_d = \pi/4$).

C.4.3 Stress-strain curves

To determine the stress-strain curve of our structures and quantify the effect of the domain wall on their mechanical response, we take the continuum limit of the longitudinal forces acting on the vertical ligaments (i.e. we substitute Eqs. (C.36) into Eq. (C.14))

$$F^y = ak_l \left(\frac{\partial v}{\partial y} + \frac{\theta^2}{2} \right) \quad (\text{C.58})$$

By assuming that inside each phase (i.e., far away from domain wall) the deformation is homogeneous, we can make use of Eq. (C.48) to simplify Eq. (C.58) as

$$F^y = ak_l \left(\varepsilon_{st}^{yy} + \frac{\theta_{st}^2}{2} \right) \quad (\text{C.59})$$

Finally, the normal stress in y direction can be obtained as

$$\sigma^{yy} = \frac{F^y}{at} = \frac{k_l}{t} \left(\varepsilon_{st}^{yy} + \frac{\theta_{st}^2}{2} \right) \quad (\text{C.60})$$

Note that Eq. (C.60) can be used to calculate the stress-strain curve of samples with or without a domain wall. While for the case of homogeneous deformation $\varepsilon_{st}^{yy} = \varepsilon_{\text{applied}}^{yy}$ and θ_{st} can be determined as a function of $\varepsilon_{\text{applied}}^{yy}$ using Eq. (C.11), in the presence of a domain wall θ_{st} and ε_{st}^{yy} are simultaneously determined as a function of $\varepsilon_{\text{applied}}^{yy}$ by imposing Eqs. (C.11) and (C.38) (with v given by Eq. (C.54b)).

In Fig. C.29 we compare the stress-strain curves predicted by Eq. (C.60) with those obtained experimentally and using our discrete model for 21×21 structures without phase-inducing defects

and with phase-inducing defects arranged along two lines that form an angle $\varphi_d = 0$, $\arctan(1/2)$ and $\pi/4$ with the horizontal axis to generate a domain wall. We find that our continuum model nicely captures the mechanical response of all these structures.

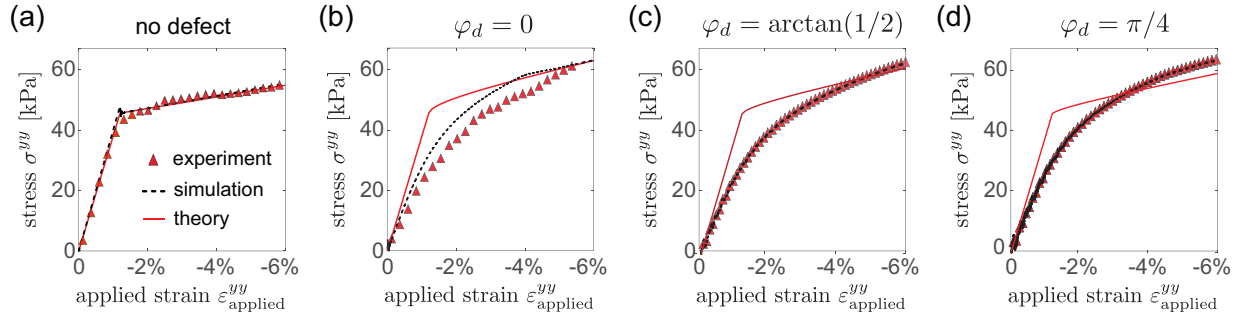


Figure C.29: Stress-strain curve measured in experiments (markers) and predicted by numerical simulations (dashed lines) and analytical solution (solid lines) for structures with 21×21 squares and (a) no phase-inducing defects; (b-d) phase-inducing and pinning defect arranged along two lines that form an angle (b) $\varphi_d = 0$, (c) $\arctan(1/2)$ and (d) $\pi/4$ with the horizontal axis to generate a domain wall.

C.4.4 Additional analytical results

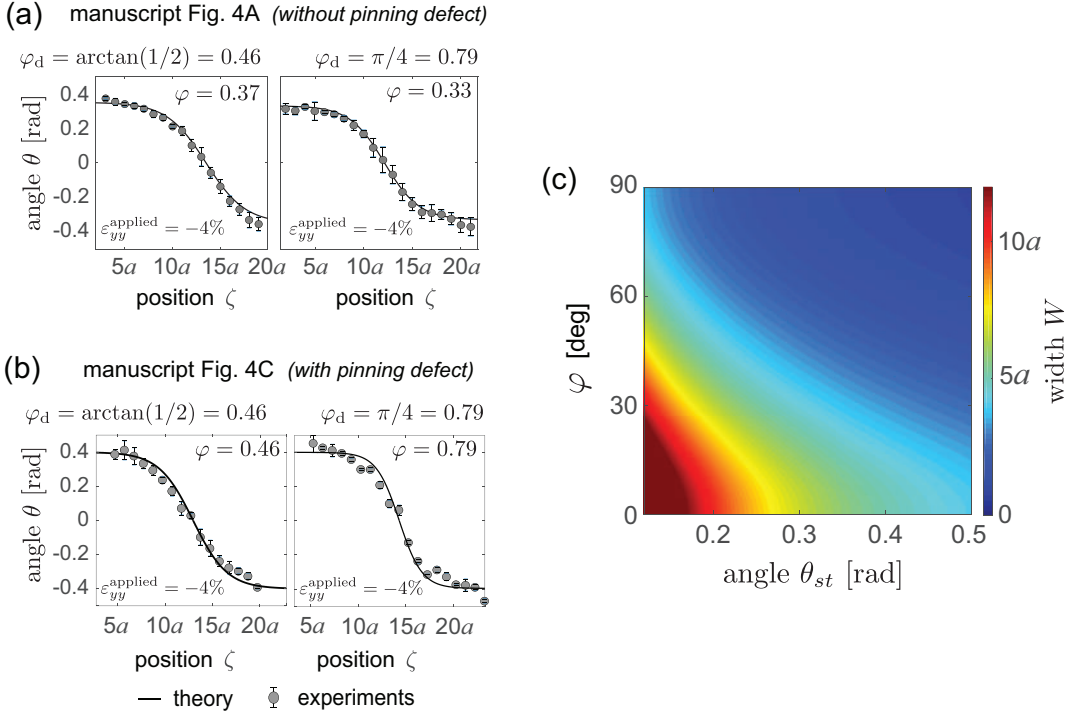


Figure C.30: (a)-(b) Comparison between analytically predicted (solid lines) and experimentally extracted (circular markers) evolution of the squares rotation θ across the sample at $\varepsilon_{yy}^{applied} = -4\%$ for a 21×21 structure with defects arranges as in (a) Fig. 4.4A of the main text and (b) Fig. 4.4C of the main text. (c) Contour plot of domain wall width w as a function of φ and θ_{st} as predicted by Eq. (C.53). As observed in experiments, our analytical solution predicts the domain walls to become thinner for increasing compression (i.e. for larger θ_{st}).

Appendix D

Supplementary Information:

Liquid-induced Topological

Transformations of Cellular

Microstructures

By: Shucong Li*, Bolei Deng*, Alison Grinthal, Alyssha Schneider-Yamamura, Jinliang Kang, Reese S. Martens, Cathy T. Zhang, Jian Li, Siqin Yu, Katia Bertoldi, Joanna Aizenberg. Published in *Nature*, on Apr. 14 2021. [doi:10.1038/s41586-021-03404-7](https://doi.org/10.1038/s41586-021-03404-7)

D.1 Materials and Methods

D.1.1 Materials

The monomer 1 4-(6-Acryloxy-hex-1-yl-oxy)phenyl 4-(hexyloxy)benzoate was purchased from Synthon Chemicals (ST03457). Photoinitiator Darocur®1173 (bis(2,4,6-trimethylbenzoyl) phenyl-phosphineoxide) was purchased from Sigma-Aldrich. 1,6-Hexanediol diacrylate (HDDA, crosslinker 2) was purchased from Sigma-Aldrich, and the inhibitor was removed prior to use. Fluorescence label for confocal microscopy Methacryloxyethyl thiocarbamoyl rhodamine B dye was purchased from Polysciences, Inc.

The monomer (4"-acryloyloxybutyl 2,5-di(4'-butyloxybenzyloxy) benzoate) used for the aligned LCP cellular structure was synthesized following a previously published procedure¹. For magnetic alignment of the liquid crystal molecules, the high-temperature neodymium magnets (NdFeB, Grade N42SH; 1" × 1/2" × 1/2" thick; BX088SH) were purchased from K&J Magnetics, Inc.

For the control experiment with very soft materials, EcoflexTM 00-10, and EcoflexTM 00-50 were purchased from Smooth-on, Inc.

The monomer 2-Hydroxyethyl methacrylate and n-butyl acrylate for synthesizing poly(2-hydroxyethyl methacrylate-co-n-butyl-acrylate) PHEMA-co-PBA were purchased from Sigma-Aldrich. 2,5-dihydroxybenzoic acid, benzyl bromide, 4-butyloxybenzoic acid, 4-hydroxybutyl acrylate, N,N'-dicyclohexylcarbodiimide (DCC), sodium bicarbonate (NaHCO₃), palladium on carbon (10 w%, matrix activated), 4-pyrrolidinopyridine, Silica gel (Davisil Grade 633, high-purity grade, pore size 60 Å, 200-425 mesh particle size), and glacial acetic acid were purchased from Sigma-Aldrich.

Organic liquids including acetone, ethanol, isopropanol, used for testing assembly behavior

were purchased from Macron. Organic liquids, including dichloromethane, toluene, dichloromethane, hexane, and toluene, were purchased from Sigma-Aldrich. Deionized water was used for aqueous systems.

4-inch Silicon wafers and 6-inch silicon-dioxide carriers were purchased from Nova Electronic Materials. Photoresist SPR220–7.0 was purchased from Microchem. Sylgard® 184 silicone kit was purchased from Ellsworth Adhesive Systems and used as 10:1 (Sylgard® base to curing agent). Microscopy glass slides (25×75 mm, 1 mm in thickness) were obtained from VWR.

D.1.2 Methods

UV-polymerization was conducted with a Dymax Model 2000 Flood UV Curing System chamber (light intensity of ~18 mW/cm²) with a custom-made steel-mesh (as neutral density filter).

Differential Scanning Calorimetry (DSC) was performed on a Thermal Analysis (TA) DSC Q200 instrument to analyze the phase behaviors of the LC mixture and LCP in the dry and wet states under a nitrogen atmosphere. The program consisted of three cycles from –5 °C to 130 °C with a 10 °C/min rate for the LC mixtures, three cycles from –5 °C to 200 °C with a 10 °C/min rate for the LCP in the dry state, and three cycles from –80 °C to 50 °C with a 10 °C/min rate for the LCP in the wet state.

Scanning electron microscopy (SEM) of the Si master and LCP cellular microstructures was performed on a Zeiss Supra55VP Field Emission Scanning Electron Microscope (FESEM). The tilted view was taken with the SEM holder tilted 30° on a Zeiss Supra55VP FESEM. LCP cellular microstructures were coated with 10 nm Pt/Pd prior to imaging for increasing the conductivity of the polymeric surface.

Atomic force microscopy (AFM) was used to measure the Young's moduli of the LCP materials on a JPK Instruments NanoWizard®AFM with 240AC-NA tips (NANOANDMORE, USA, OP240AC-NA-10, force constant 2 N/m). In this technique, the deflection of the cantilever tip is measured as it approaches and indents the surface. The Young's moduli of the LCP material were determined through analyzing the slope of the force-displacement curves that result from these measurements while LCP is in the dry state and in the saturated swollen state. Profilometer 3D profile was measured on a Veeco Dektak 6M profilometer. LCP cellular microstructures were coated with 10 nm Au prior to imaging for increased contrast.

Confocal Laser Scanning Microscopy measurements were performed on a Zeiss LSM 700 instrument with 5 \times and 10 \times objectives under bright light channel and 532 nm fluorescence channel. LCP was copolymerized with the dye methacryloxyethyl thiocarbamoyl rhodamine B for fluorescence signal. Time-series was analyzed with the Zeiss ZEN black software.

Fabrication of the microstructured silicon master. The microstructured silicon master was produced by photolithography followed by reactive ion etching (RIE). Photoresist (SPR220-7.0) patterning was performed by UV exposure at 375 nm, 470 mJ/cm², under a Heidelberg MLA150 Maskless Aligner, which later served as the mask for the anisotropic etching of a Si wafer using an STS ICP RIE System, to obtain the Si microstructures. After removal of the photoresist with oxygen plasma, the Si master was treated with trichloro(1H,1H,2H,2H-perfluoroctyl) silane to render the structure hydrophobic for molding. Silicon master with positive cellular structure was designed for fabricating LCP microstructure and with negative cellular structure (micropost with gaps) was designed for fabricating silicone-based (i.e., EcoflexTM 00-10, EcoflexTM 00-50) microstructure.

Fabrication of PDMS negative mold. The polydimethylsiloxane (PDMS) precursor (mixture of Sylgard® 184 base and the crosslinker with the ratio of 10:1 (wt:wt)) was applied on top of the Si

wafer, degassed under vacuum and cured at 70°C for 2 h. Finally, the PDMS was cooled down to room temperature and carefully peeled off from the Si wafer and used as a mold for the synthesis of LCP microstructures.

Fabrication of EcoflexTM 00-10 and EcoflexTM 00-50 microstructure. The EcoflexTM 00-10 or EcoflexTM 00-50 precursor (part A and part B 1:1 by volume) were mixed thoroughly and applied on top of the Si wafer, degassed under vacuum, cured at room temperature for 4 h, and post cured at 80 °C for 2 h and 100 °C for 1 h. Finally, the Ecoflex was cooled down to room temperature and carefully peeled off from the Si wafer.

Fabrication of free-standing cellular microstructure. The free-standing cellular microstructure was obtained by precoating the glass slides with polyvinyl alcohol (PVA) as a sacrificial layer which can be washed off in water to release the attached LCP cellular film after demolding. The coating was done by spin coating the clean glass slide with a 3wt% PVA water solution and then baking at 120°C for 2h to evaporate the residual water. After fabrication of the microstructure with such coated glass substrates and demolding from the PDMS, the sample was immersed in room temperature water overnight to dissolve off the PVA and release the cellular film from the glass (such dissolving process can be facilitated with hot water). The bottom LCP layer of the cellular film can be further etched to make it thinner for a higher deformability and compliance using oxygen plasma (Diener, Model: Femto PCCE).

Global topological transformation was done simply by adding ~50 μ L droplet of liquids with commonly used plastic pipettes onto a 1 cm \times 1 cm cellular film to immerse the structure fully and waiting for it to dry under ambient conditions. The applied liquid needs wet the structure (wetting angle > 90°) to form concave meniscus lines for the assembly to happen. For a sufficient swelling and softening of the materials, the liquid should be able to enter the cells of the microstructure

and infiltrate into the polymer matrix. Note that the size and final thickness of the solvent play a role in determining the size of the area being transformed and the speed/timing of the transformation. Localized topological transformation was done by adding small amount of liquid with a 0.5-10 μL micropipette to a large area film. Only the area that is in contact with the liquid will be assembled/disassembled.

Particle trapping is realized through topological transformation of the cellular structures to selectively trap particles with diameters that can be geometrically accommodated by the lattice compartments, while excluding particles that are larger. In particle trapping experiments, spherical particles (silica gel spherical, purchased from Sigma-Aldrich) with diameters ranging from 40 μm to 70 μm were randomly scattered on the triangular cellular surface. The triangular lattice has an edge length of 100 μm and thickness 7 μm , resulting in chambers that can accommodate spherical particles up to 50 μm in diameter. Particles with diameter $< 50 \mu\text{m}$ fell into the compartments and were then engulfed and trapped under the newly formed node upon reconfiguration. On the other hand, the particles with diameters $> 50 \mu\text{m}$ were washed away by the added liquid. The trapped particles can subsequently be released upon disassembly of the cellular structure by a liquid mixture of ethanol and DCM.

Surface resilience is characterized by the coefficient of restitution e , which is the ratio between relative velocity after and before the collision. In this work, we used the ball bouncing test to measure e . Specifically, steel balls with mass 0.027 g, 0.054 g, 0.104 g and 0.166 g are released from an initial height of $h_0 = 50$ mm. Their bouncing height was recorded as h_1 . Since the velocity of the ball before the collision is proportional to $\sqrt{h_0}$ and the velocity of the ball after the collision is proportional to $\sqrt{h_1}$, the coefficient of restitution is calculated by $e = \sqrt{h_1/h_0}$.

Band gap structures of the cellular structures before and after transformation is calculated

via finite element simulations. We focus on the representative volume element (RVE) taken from the cellular structure. We assume the elastic wave propagates in the upper part of the structure and therefore use a plane-strain model for our analysis. Commercial software COMSOL 5.3a was used to perform the Bloch-Floquet analysis with Bloch boundary conditions applied to the boundary of the RVE. We scanned wave vectors on the Γ -M-K- Γ boundary of the irreducible Brillouin zone to obtain the dispersion relation or the so-called band structure. Since band structures depend on the geometries of the considered cellular structure, one can tune the band by transforming the structure.

Water sliding angles (WAS) of the microstructured surface before and after reconfiguration were measured on a Drop Shape Analyzer (Kruss GmbH DSA100). $40\ \mu\text{L}$ of MilliQ water droplets were slowly dispensed on to the structured film. The roll-off angle was measured using a droplet size of $40\ \mu\text{L}$, and the stage was tilted at a tilt rate of $0.5^\circ/\text{s}$. The averaged roll-off angle was measured at three different positions on the sample set and were confirmed across different sets of samples. Additionally, the same experiments were performed on a flat LCP thin film before and after the solvent treatment. No noticeable changes in the roll-off angle and were observed, suggesting that the change in wettability originated from the structural change rather than the chemical nature of the polymer.

Surface friction was measured as a function of a sliding angle using an 4 mm acrylic disc, which was loaded with steel ball bearings of various masses. To measure the angle, a contact angle goniometer (Kruss GmbH DSA100) was used with the structures placed on the sample stage. The disc, with a basket and wire loop affixed using two-part epoxy, was then lowered onto the structures at a controlled rate by replacing the traditional needle with a hook. This was done to prevent additional pressure being applied, which could result in the disk becoming adhered to the surface. The stage was then tilted at $0.5^\circ/\text{s}$, until the disk slid off the sample.

D.2 Theoretical Model

D.2.1 Critical Young's modulus

To quantitatively study the reconfiguration process and provide the upper stiffness limit for the material to undergo capillary assembly, we investigate a micro-cellular structure with the base of the structure anchored to a rigid substrate (see Fig. D.1(a)). The structure is made of plates with edge length l , height h , thickness b , which are separated by an angle α . After the capillary assembly, only the upper portion with height h^* is coalesced since the bottom of the structure is always attached to the substrate and remains triangular (see Fig. D.1(a)). This upper portion deformation, including the stretching and folding of the walls, dominates the total elastic energy in comparison to the bending deformation of the lower part (this assumption fails when the height of the structure h is too small relative to the edge length l). Therefore, the total elastic energy of one edge after the reconfiguration can be approximated by that of the upper part. The elastic energy of the deformation of the upper part includes two major components: stretching and folding (extreme bending) of the walls. In Fig. D.1(b), we use the triangular-to-hexagonal transformation as an example to demonstrate the stretching and folding of a single wall and such schematic is general for structures with other angles and topologies.

Energy associated with stretching: When the liquid is added to the system, the length of the walls increases from l to $l_{wet} = l(1 + \delta)$, where δ is the swelling ratio. However, after the capillary assembly, the walls have length $l_a = l \sin \frac{\alpha}{2}$ (see Fig. D.1(b)). Therefore, the walls upon assembly are strained by $\varepsilon_S = l_a/l_{wet} - 1 = (\sec \frac{\alpha}{2} - 1 - \delta)/(1 + \delta)$, and the energy of a single wall can thus be

approximated by

$$U_1 = \frac{1}{2} E_{wet} V_S \varepsilon_S^2 = \frac{1}{2} Eh^* lb \left[\sec \frac{\alpha}{2} - 1 - \delta \right]^2 \quad (\text{D.1})$$

where E_{wet} is the Young's modulus of the material in the swollen state and $V_s = h^* bl(1 + \delta)^2$ is the volume of the swollen wall.

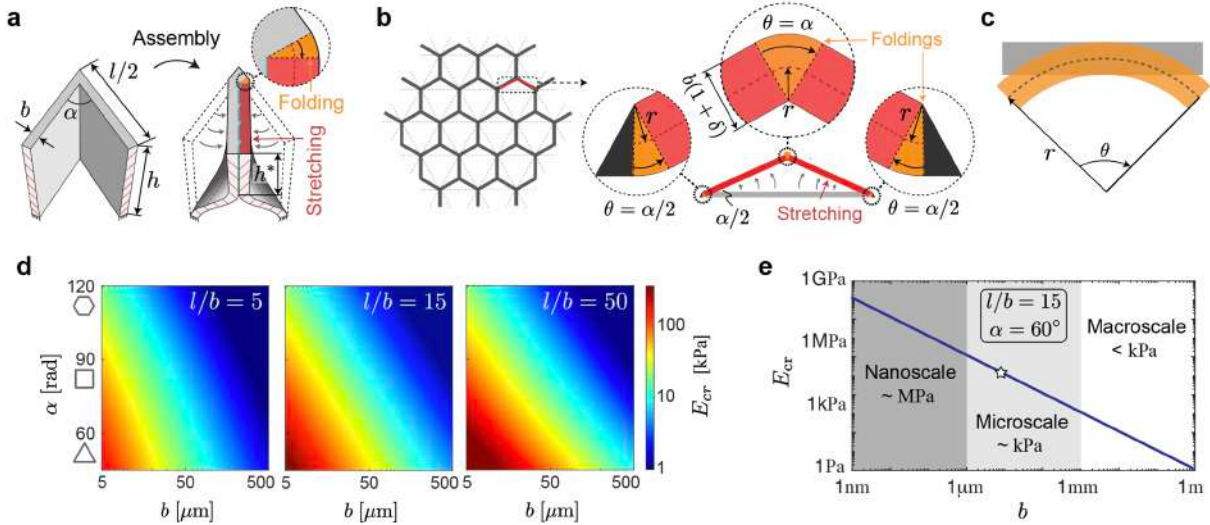


Figure D.1: Schematic presentation of the structural parameters used for a theoretical model. (a) Pre- and post-assembly configurations of a triangular compartment. (b) Components of wall deformation required for assembly. (c) Pure bending of an initially straight beam. (d) Contour plot of critical Young's modulus E_{cr} with respect to structural parameters "aand b, while the slenderness ratio is set as $l/b = 5, 15$ and 50 . (e) Relation between E_{cr} and the wall thickness b predicted by our theoretical model for triangular lattices with $\alpha = 60^\circ$. The slenderness of the lattice edges remains constant at $l/b = 15$.

Energy associated with folding: To estimate the elastic energy associated with folding we use classical beam theory. As shown in Fig. D.1(c), when an initially straight beam is deformed to an arch with radius r and opening angle θ , its elastic energy can be expressed as^[155],

$$U_{bend} = \frac{E_{wet} I \theta}{2r} \quad (\text{D.2})$$

where I is the second moment of area of the cross-section ($I = h^* b^3 (1 + \delta)^3 / 12$ in our case). As

demonstrated in the insets of Fig. D.1(b), upon assembly the wall experiences folding at both nodes (with $\theta = \alpha/2$) and at the center (with $\theta = \alpha$). Assuming that the bending radius is half of the thickness of the swelled beam (i.e., $r \approx b(1 + \delta)/2$), the total folding energy can be expressed as

$$U_2 = \frac{1}{12} E_{wet} h^* b^2 (1 + \delta)^2 \left(\frac{\alpha}{2} + \alpha + \frac{\alpha}{2} \right) = \frac{1}{6} \alpha E_{wet} h^* b^2 (1 + \delta)^2 \quad (\text{D.3})$$

Total elastic energy: The total elastic energy of a single wall can be obtained by summing the series associated with stretching and folding

$$U_e = U_1 + U_2 = \frac{1}{2} E_{wet} h^* \left[\left(\sec \frac{\alpha}{2} - 1 - \delta \right)^2 lb + \frac{1}{3} \alpha b^2 (1 + \delta)^2 \right]. \quad (\text{D.4})$$

Work done by capillarity: The work done by capillarity can be estimated by the product of the capillary forces and the distance traveled by the meniscus, and can be expressed as^[134,156,157]

$$W_c = \gamma h^* l \sec \frac{\alpha}{2}. \quad (\text{D.5})$$

where γ is the surface tension of the liquid (for a volatile liquid, such as acetone, $\gamma = 25 \times 10^{-3}$ N/m). Critical Young's modulus: For the capillary reconfiguration to occur, the capillary work W_c must overcome the elastic energy gain U_e , i.e., $W_c > U_e$. Such simplified energy argument gives a critical Young's modulus for the underlying material:)

$$E_{cr} = \frac{6\gamma l \sec \frac{\alpha}{2}}{3lb \left(\sec \frac{\alpha}{2} - 1 - \delta \right)^2 + ab^2 (1 + \delta)^2}. \quad (\text{D.6})$$

The Young's modulus of the material in the swollen state E_{wet} needs to be smaller than E_{cr} to ensure

the capillary assembly. In Fig. D.1(d), we present the contour plots of E_{cr} as functions of angle α and thickness b with respect to slenderness ratio $l/b = 5, 15$ and 50 . The proposed theoretical model connects the geometry and stiffness of the polymer network with liquid characteristics, and can guide the design of reconfigurable structures. It is worth noting that according to our model, the capillary assembly mechanism is not scale-independent. In Fig. D.1(e), we show how the critical Young's modulus changes as a function of the smallest dimension of the structure, i.e., wall thickness b , for a constant slenderness $l/b = 15$. According to Fig. D.1(e), E_{cr} changes over multiple orders of magnitude as we scale the thickness from millimeter scale down to nanometer scale — a clear indication that the behavior is not scale-independent. Specifically, at the micrometer scale E_{cr} is on the order of kPa and such a threshold can be achieved through polymer softening with properly chosen solvent. However, if the wall thickness is scaled up to millimeter scale, the polymer network needs to be softer than 1 kPa, which would normally lead to the collapse of the structure under its own weight. Moreover, since the capillary length of common liquids is around 1-3 mm, the effect of gravity would also impact the effectiveness of the capillary assembly. Therefore, the proposed capillary assembly will be less feasible for structures with their smallest dimensions beyond the micrometer scale. On the other hand, if the fabrication technique allows us to fabricate structures with nanometer scale units, the capillary assembly could work for materials with Young's moduli up to 1 GPa. This implies that for nanometer scale structures we might not need to soften the underlying material. At this scale, the capillary assembly strategy could work for more general materials that are robust against liquid, such as, plastics, carbon, or even metals.

D.2.2 Verification of the critical Young's modulus

To experimentally verify our model, the capillary assembly experiments were conducted on triangular cellular structures with varying geometrical parameters. Specifically, we fabricated four cellular structures using the same polymer material and the same unit size $l = 100 \mu\text{m}$ and height $h = 70 \mu\text{m}$, with different wall thicknesses $b = 7, 10, 13$ and $16 \mu\text{m}$. In Fig. D.2(a), we present the top view of these cellular structures after liquid evaporation. As the wall becomes thicker, it becomes more difficult for the structure to be assembled by capillary forces. To study the assembly process more quantitatively, we measure the compartment sizes A_i for the assembled structure by tracking the grayscale of the images shown in Fig. D.2(a) and use the blue-to-yellow color scale to indicate compartment sizes (see Fig. D.2(b)). In Fig. D.2(c), we plot the distribution of the compartments over different ranges of area. We find that when the structure is completely transformed to a hexagonal lattice (for example, for structures with $b= 7$ and $13 \mu\text{m}$) the compartment sizes are either very small (corresponding to the center of the newly formed nodes) or very large (corresponding to the hexagonal shapes). On the other hand, for the structures that fail to assemble, the compartment sizes are all mid-sized (for example structures for $b= 16 \mu\text{m}$). At this point, we can define an assembly index R to track the completeness of the assembly process. R is defined via the distribution of tracked compartment areas A_i as,

$$R = \frac{\text{std}[A_i]}{\text{mean}[A_i]} \quad (\text{D.7})$$

where $\text{std}[A_i]$ is the standard deviation and $\text{mean}[A_i]$ is the average of the compartment areas. For a perfect assembly, where half of the compartments are near-zero size and the other half are hexagon size, we have $R = 1$, while, for the perfect (unchanged) triangular lattice, $R= 0$. The assembly

index R deviates from 1 as the structure fails to completely assemble. To be more quantitatively, we define the structures with $R > 0.9$ successfully assembled and those with $R < 0.9$ fail to be assembled. For the four considered thicknesses $b = 7, 10, 13$ and $16 \mu\text{m}$, $R = 0.99, 0.99, 0.72$ and 0.52 respectively. Therefore, the structures with $b = 7$ and $10 \mu\text{m}$ are successfully assembled and the structures with larger thickness $b= 13$ and $16 \mu\text{m}$ fail to be assembled.

From the theoretical expression of the critical Young's modulus, we can plot E_{cr} as a function of the wall thickness b (see Fig. D.2(d)), where again theoretically $E_{wet} < E_{cr}$ is required for assembly. Since here our polymer network is fixed with a softened stiffness of $E_{wet}= 80 \text{ kPa}$ and a swelling ratio of $\delta = 10\%$, the model yields a critical thickness of $b_{cr}= 12.7 \mu\text{m}$. For structures with $b < b_{cr}$, $E_{wet} < E_{cr}$ and the assembly will happen, while for structures with $b > b_{cr}$, $E_{wet} > E_{cr}$ and the assembly will fail. In Fig. D.2(e), we compare this theoretical prediction of b_{cr} with experimental measurements via image processing. The predicted b_{cr} nicely captures the transition of the assembly index R . While the two structures with $b= 7$ and $10 \mu\text{m} < b_{cr}$ are fully assembled with $R \approx 1$, the structures with $b= 13$ and $16 \mu\text{m} > b_{cr}$ fail to assemble. The results shown in Fig. D.2(e) verify the accuracy of our theoretical model. We also verify our model by testing structures with different values of α . To this end, we fabricated two cellular structures with a square lattice ($\alpha = 90^\circ$) and hexagonal lattice ($\alpha = 120^\circ$) geometries using the same polymer material as for the triangular cellular structure. Similarly, other geometrical parameters were kept the same as for the triangular cellular structure, with edge length $l = 100 \mu\text{m}$, height $l = 70 \mu\text{m}$ and thickness $b = 7 \mu\text{m}$. The predicted critical Young's moduli for such square and hexagonal lattices are $E_{cr}= 37 \text{ kPa}$ and $E_{cr}= 7 \text{ kPa}$, respectively, which are lower than the Young's modulus of the softened polymer $E_{wet}= 80 \text{ kPa}$; that is, $E_{wet} > E_{cr}$. This indicates that for both square and hexagonal lattices, our model predicts that the capillary forces will not be strong enough to assemble the walls and therefore the recon-

Transformation for structures with different wall thickness b

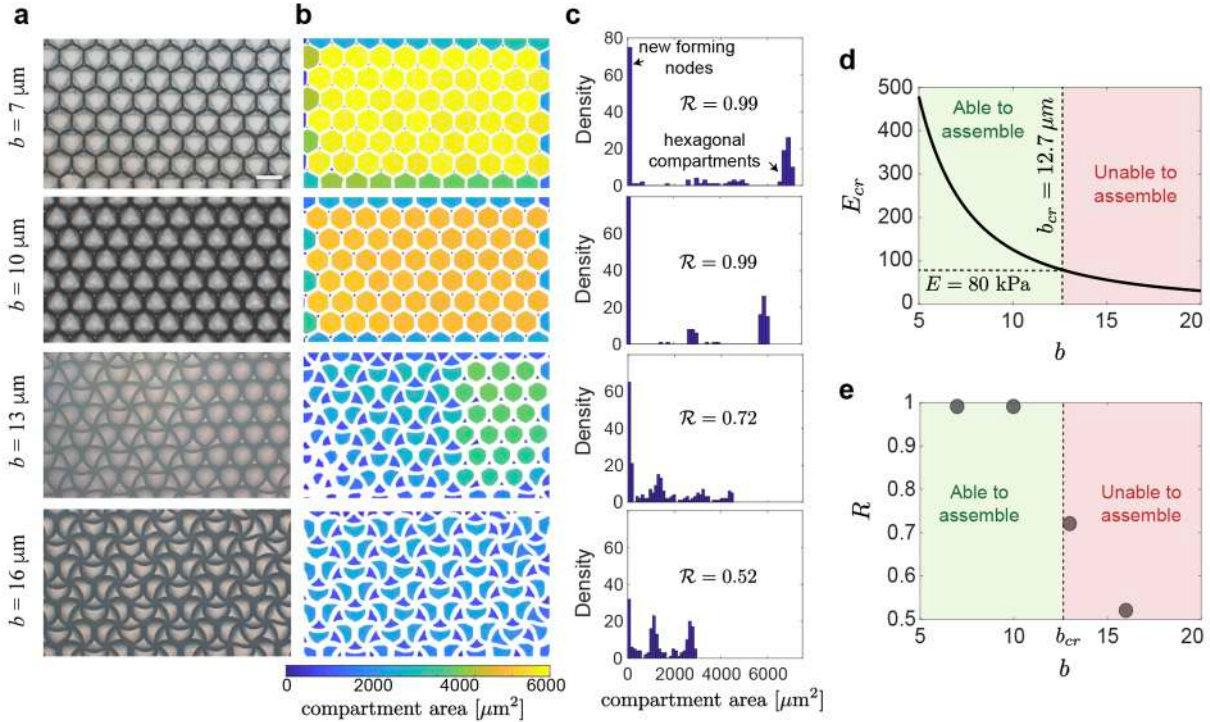


Figure D.2: Transformation of cellular structures with different wall thicknesses b and angle α . (a) Top view optical images of the liquid-treated cellular structures with thicknesses $b = 7, 10, 13$ and $16 \mu\text{m}$, respectively. (b) Image processing to track the area of each compartment. (c) Distributions of the compartment areas and the corresponding assembly index R . (d) Critical Young's modulus E_{cr} as a function of wall thickness b . For a fixed material stiffness $E = 80 \text{ kPa}$, we can derive the critical thickness $b_{cr} = 12.6 \mu\text{m}$. (e) Assembly index R with increasing thickness b . The predicted b_{cr} captures the critical thickness where R starts to deviate from 1 (perfect assembly). Cellular structures with different α after liquid treatment. (f) Square lattice; (g) hexagonal lattice. Scale bars, $100 \mu\text{m}$.

figuration will not occur. The experimental results shown in Fig. D.2(f-g) verifies the accuracy of the theoretical prediction – although the walls buckle upon swelling, the capillary forces are not

strong enough to assemble them.

D.2.3 Critical adhesion energy

Next, we estimate the required adhesion energy per area to hold the structure in its configuration after assembly. In the main manuscript, we have discussed how both adhesion between the walls and kinetic trapping of the polymer conformation contribute to maintain the reconfigured structure following fast evaporation of the liquid. Here we quantify how sticky the material would need to be for the structure to be held together solely by the adhesion energy. The adhesion energy of the coalesced walls can be expressed as

$$U_a = 1/2 J h^* l \sec \frac{\alpha}{2} \quad (\text{D.8})$$

Comparing U_a with the elastic energy of the assembled structure U_e gives the critical adhesion energy per area,

$$J_{cr} = \frac{E \left[3 \left(\sec \frac{\alpha}{2} - 1 - \delta \right)^2 lb + ab^2(1 + \delta)^2 \right]}{3l \sec \frac{\alpha}{2}} \quad (\text{D.9})$$

In the dry state, the considered LCP has a measured Young's modulus $E_{dry} = 23,000$ kPa. Since the LCP is completely dried, the swelling ratio $\delta = 0\%$. In this case, with $E = E_{dry}$, Eq. (D.9) gives an approximate critical adhesion energy per area of $J_{cr} \approx 3.3$ joule/m² that is higher than the adhesion energy of typical polymer materials. In the wet state, the LCP has $E_{wet} = 80$ kPa and $\delta = 10\%$ and therefore yields a critical adhesion energy $J_{cr} = 1.5 \times 10^{-3}$ joule/m², which is lower than that of typical polymer materials^{6,7}.

D.3 Supplemental Results & Figures

D.3.1 Cellular structures of low Young's modulus materials

Cellular structures made from EcoflexTM 00-10 (Young's modulus ~50 kPa) and EcoflexTM 00-50 (Young's modulus ~250 kPa) were fabricated following the general curing procedure for Ecoflex elastomers (SI section 1). However, for both material systems the structures were distorted after being peeled off from the negative silicon master due to insufficient rigidity and stickiness of the polymer-containing free siloxane species.

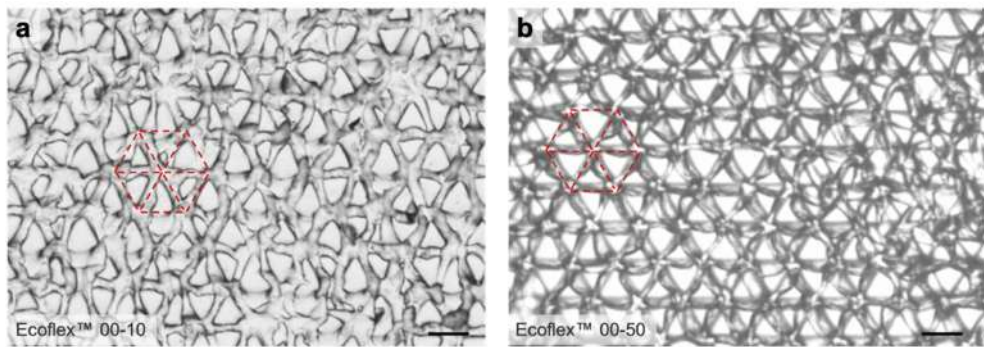


Figure D.3: Distorted triangular lattices made of (a), EcoflexTM 00-10, and (b) EcoflexTM 00-50 after being peeled off the silicon master. Scale bar, 100 μm .

D.3.2 3.2 Synthesis of liquid crystalline polymer (LCP) microstructures

The reactive LC monomer mixture was prepared by dissolving 96.5 mg of monomer 1, 1.5 mg of HDDA crosslinker 2, and 2 mg of Darocur®1173 (Fig. D.4(a)) in roughly 1 mL of anhydrous dichloromethane (DCM). The dissolved chemicals were mixed thoroughly and dried over a cleaned microscopy glass slide (washed with water, acetone, isopropanol, and then blow-dried under ni-

trogen) to yield the crystallized reactive mixture for polymerization. The phase behavior of the reactive LC monomer mixture was studied with differential scanning calorimetry (DSC) using Thermal Analysis DSC Q200 with a rate of 10 °C/min. The reactive mixture showed a melting point at 42 °C and nematic to isotropic (T_{NI}) phase transition at 62 °C, as shown in Fig. D.4(b). The polymerization temperature was set to 120 °C where the mixture is in the isotropic phase to give a polydomain material.

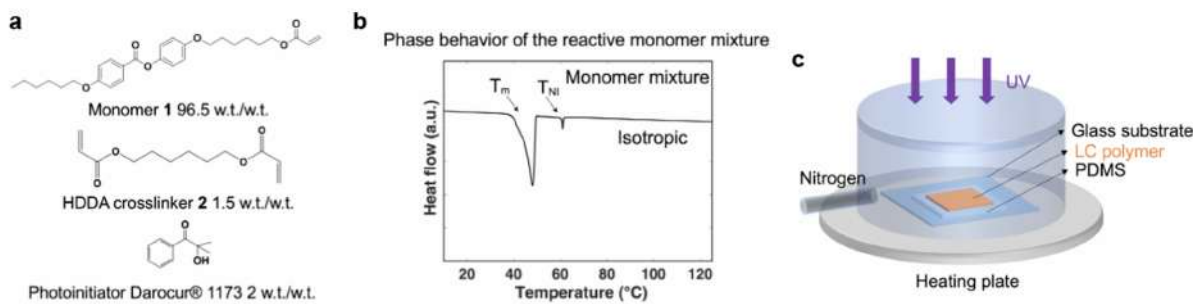


Figure D.4: Synthesis of LCP. (a) LCP chemical constituents. (b) Phase diagram of the reactive LC monomer mixture. The heating rate of the differential scanning calorimetry (DSC) was 10 °C/min. (c) Schematic of the polymerization setup.

The Si master with designed geometries (edge length $l = 100 \mu\text{m}$, height $h = 70 \mu\text{m}$ and thickness $b = 7 \mu\text{m}$) and the negative PDMS mold were fabricated following the procedure described in SI section 1 and characterized with scanning electron microscopy (SEM). To synthesize the LCP microstructures, we applied ~20 mg of the reactive mixture into a PDMS mold and covered the mixture with a glass substrate. The sample was heated to 120 °C (isotropic phase) and exposed to UV (Dymax Model 2000 Flood UV Curing System, light intensity of ~18 mW/cm²) under a nitrogen atmosphere to initiate polymerization. After 20 min of polymerization, the sample was cooled down to room temperature, and the PDMS mold was carefully peeled off from the LCP microstructures.

D.3.3 Characterization of material properties

D.3.3.1 Swelling and trapping of an LCP microplate

The swelling ratio and the kinetic trapping of the LCP were tested on a microplate with the same dimensions as the lattice structure ($l = 100 \mu\text{m}$, $h = 70 \mu\text{m}$ and $b = 7 \mu\text{m}$) to assure comparable dynamics and kinetics of evaporation. The structure was first treated with acetone and observed under an optical microscope. However, the microplates collapse upon evaporation due to the capillary force which hinders the accurate measurement of the swelling ratio of the liquid to LCP as well as the investigation of freezing dynamics. To avoid the collapse of the microplates and remove the capillary forces generated during acetone evaporation, ethanol was introduced to provide an inert liquid environment. Since ethanol does not swell the polymer, the presence of ethanol does not affect the swelling and trapping dynamics significantly and acts primarily to avoid the formation of menisci. The LCP microplate was then treated with acetone in the presence of an ethanol environment (manuscript Fig.1f): as the liquid penetrates the polymer network, the opaque glassy polymer turns clear and bright, indicating a glassy-to-rubbery transition upon swelling. The microplate was swelled to a 10% strain along the length of the top edge. After the evaporation of acetone, the plate was trapped with a 9% strain. Furthermore, when heated up to 70°C (above its $T_g = 58^\circ\text{C}$), the elongated microplate relaxed back to its initial length, confirming the kinetic nature of the trapping mechanism (Supplementary Video 10).

D.3.3.2 Glass transition temperature of LCP in the dry and wet states

The phase behavior of the LCP in the dry and wet states was studied with differential scanning calorimetry (DSC) using Thermal Analysis DSC Q200 with a rate of $10^\circ\text{C}/\text{min}$. The dry LCP

showed a glass transition temperature (T_g) of ~ 58 °C (Fig. D.5(a)). When immersed in acetone, the fully swollen wet LCP showed a drastic decrease in T_g to -30 °C (Fig. D.5(a)).

D.3.3.3 Young's moduli of LCP in the dry and wet states

The Young's moduli of the dry and wet LCP were obtained through nanoindentation measurements conducted by atomic force microscopy (AFM). By analyzing the slope of the force-displacement curves, the Young's moduli of the LCP material were determined for 4 states: (1) in its original dry state, (2) after it is fully swollen in acetone (nanoindentation measurements were conducted completely in liquid acetone environment), (3) within tens of seconds after the evaporation of acetone from the surface, and (4) after the sample was left to dry for 30 min. Fig. D.5(b) shows that the dry LCP has a Young's modulus of $\sim 23100 \pm 2400$ kPa; it softens by three orders of magnitude to 80 ± 19 kPa in the swollen state, and fully recovers its initial stiffness of 24000 ± 5500 kPa after drying. Moreover, the Young's modulus does not continue to change after drying for 30 min, suggesting that the material fully regains its stiffness within ~ 30 s after the evaporation of the liquid from the structure.

D.3.3.4 Systematic study of the swelling behavior of LCP with different liquids

Water and a range of organic liquids with different polarities, volatilities, and solution parameters were selected to study the swelling behaviors of the LCP cellular microstructures. Based on their different intermolecular interactions with the LCP matrix, these solvents can be classified as good solvents, including acetone, dichloromethane (DCM), and toluene, and poor solvents, including water, ethanol, isopropanol, and hexane. Droplets of different liquids ($\sim 50 \mu\text{L}$ for a $\sim 1 \text{ cm}^2$ sample, in excess of the amount required to swell the LCP to a saturated state) were placed on horizontally

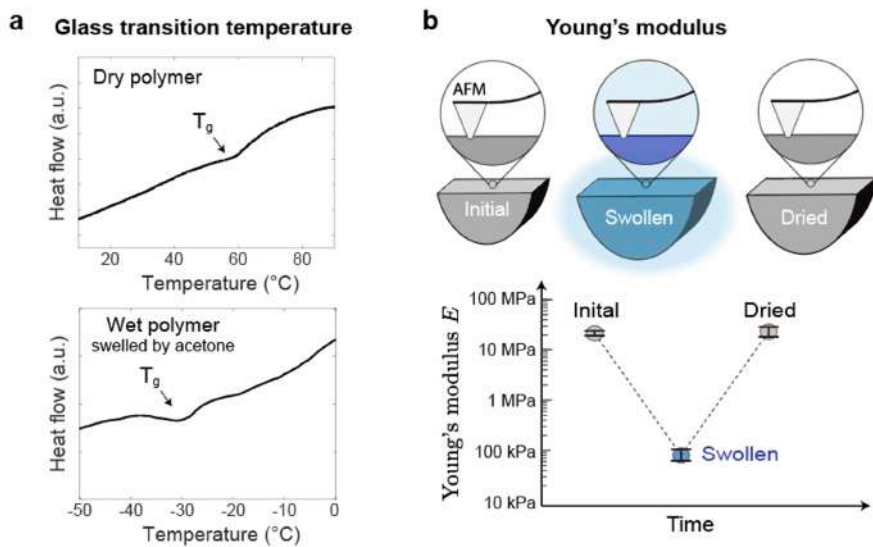


Figure D.5: Characterization of material properties of LCP. (a) Phase diagrams of the LCP polymer. Dry LCP polymer and wet LCP polymer swollen with acetone. The heating rate of the differential scanning calorimetry (DSC) was 10 °C/min. (b) Young's modulus characterization of the LCP upon swelling and drying. AFM was applied to measure the Young's moduli of the polymer on a cellular structure in the original dry state, fully swollen state, and dried state after evaporation of the liquid.

oriented substrates and allowed to evaporate under ambient conditions. The immersing, swelling, and drying of the cellular structures were monitored by optical microscopy. As the LCP material is hydrophobic, water does not wet the microstructure and cannot permeate into and swell the polymer matrix (Fig. D.6(i)). As discussed in SI section 3.3.1 for an isolated microplate, ethanol wets but does not swell the cellular microstructure; as discussed in the main text, this behavior allows it to be used as an inert solvent to enable control over the disassembly process. Isopropanol and hexane swell the structure mildly, such that the induced softening is not sufficient to trigger the assembly. DCM and toluene swell the polymer to such a large extent that the whole LCP film ruptures and delaminates from the glass substrate. It is worth noting that a mixture of different solvents can be used to trigger capillary assembly and vary the extent of the reconfiguration by controlling the swelling ratio. In addition, adjusting the crosslinking density of the polymer also offers a simple control to modify the material's mechanical properties, swelling ratio, trapping

strain, and interfacial adhesion, and thus the extent and reversibility of the lattice transformation.

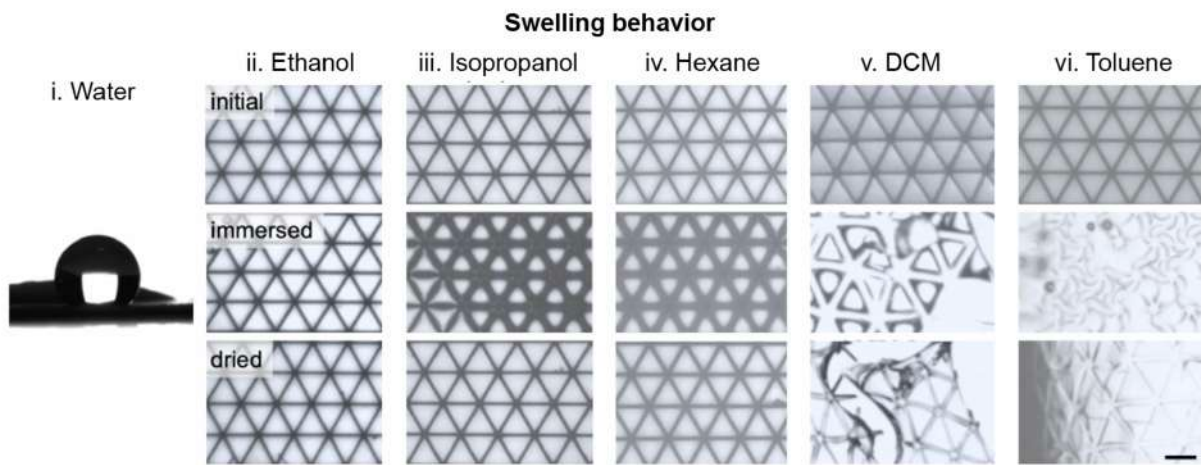


Figure D.6: Swelling behavior of LCP with different liquids. Snapshots of LCP cellular structures in the initial state, during immersing in liquids, and after evaporation of liquids. (i) Water does not wet the structure. (ii) Ethanol wets the structure but does not swell the LCP noticeably. (iii-iv), isopropanol and hexane wet and swell the structure slightly but are not sufficient to trigger assembly upon evaporation. (v-vi), Dichloromethane and toluene wet the structure, but the swelling ratio is so large that the LCP films rupture and delaminate from the glass substrate. Scale bar, $100 \mu\text{m}$.

D.3.4 Characterization of the topological transformation

D.3.4.1 3D topography of the cellular structures

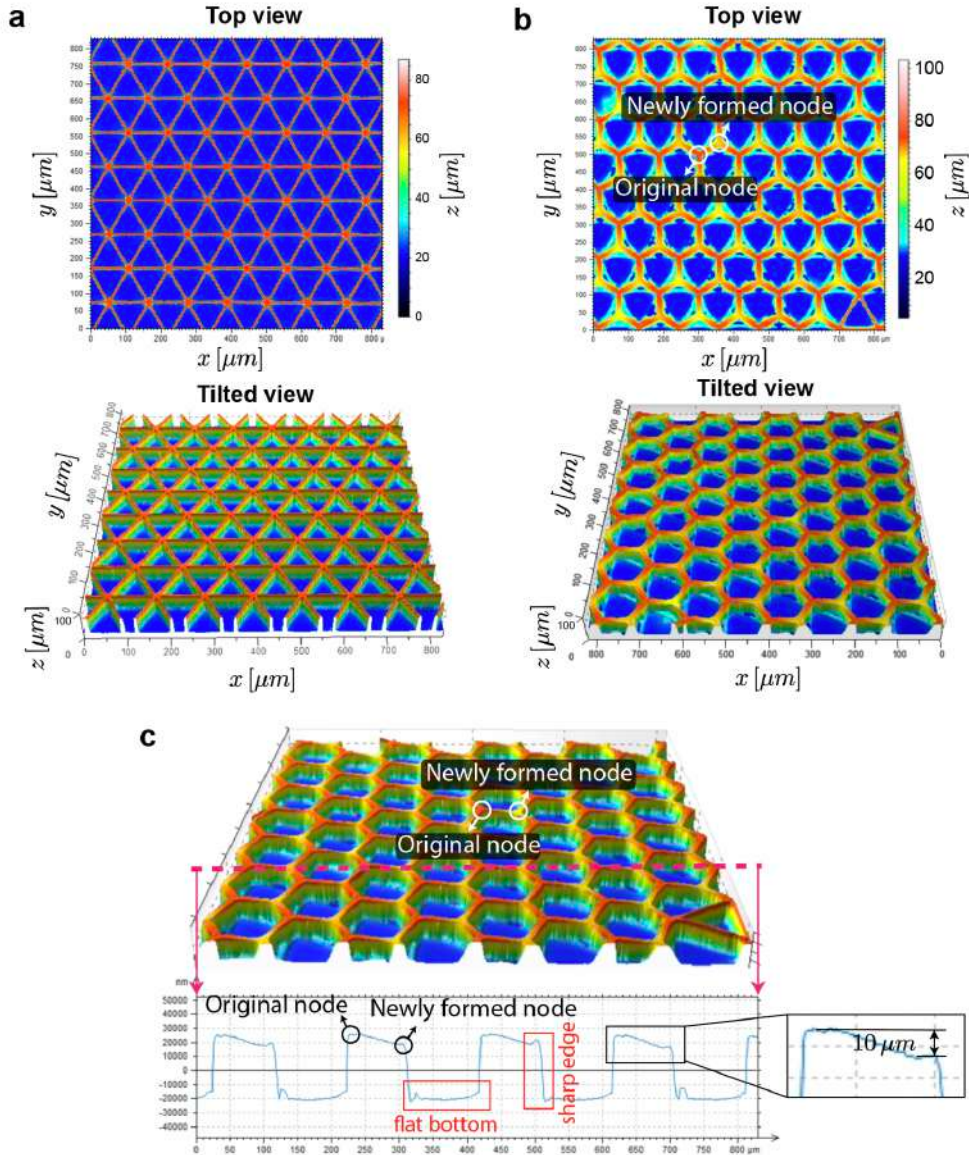


Figure D.7: 3D topography of the cellular structures. Top and tilted view of the optical profilometer measurements showing the reconfigured 3D shape of the (a) initial triangular lattice and (b) assembled hexagonal lattice. (c) The height profile of the assembled hexagonal lattice along the dashed line. The newly formed nodes are $\approx 10 \mu\text{m}$ shorter than the original nodes. Furthermore, the inset of (c) shows that the transformed hexagonal structure contains flat bottoms and sharp vertical walls, which indicates that half of the initial triangle compartments are completely closed through the transformation.

D.3.4.2 Assembly process: symmetry breaking and phase boundaries

The triangular lattices consist of nodes with connectivity six, and during the reconfiguration to hexagonal lattice the nodes are transformed to connectivity three. Let us focus on a small region around a certain node of the triangular cellular structure. Upon evaporation, six menisci form between the neighboring walls. The curved meniscus surfaces generate Laplace pressure inside the liquid. If the structure is perfect and menisci are identical, the pressures on both sides of the wall are balanced and no torque is generated (see the left inset of Fig. D.8(a)). However, such a balanced state is not stable under infinitesimal perturbation. For example, if certain walls are perturbed by a small amount due to fabrication imperfections or environmental fluctuation, the height of the liquid surfaces on two sides of the wall become different, which generate a non-zero net torque (see the right inset of Fig. D.8(a)). Such torque further increases the perturbation and the perturbation in turn further magnifies the torque. The process goes on and on until the adjacent walls are assembled. Since assembling three adjacent walls together costs a lot of energy, the walls will always be assembled pair by pair, which at the same time transforms the node from connectivity six to three. The transformation of node connectivity from six to three results in an equal probability of forming two phases of patterns, with the original nodes to transform to either the Y-shaped nodes (phase I) or inverted Y-shaped nodes (phase II, see Fig. D.8(b)). Due to the integrity of cellular structure as well as the evaporation line formed by the liquid that sequentially assemble the node (see Fig. D.8(c)), the neighboring nodes tend to select the same phase forming ordered domains. However, over large scales, the coexistence of two phases inevitably leads to phase boundaries in between (see Fig. D.8(d)).

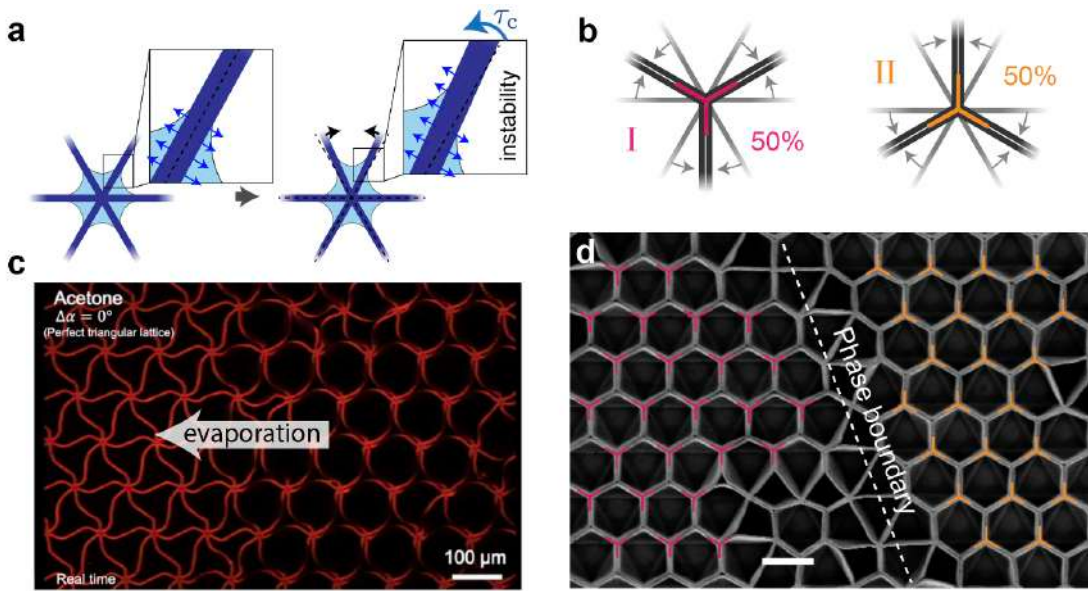


Figure D.8: Initial instability of the node and domain boundaries formation in a perfect triangular lattice after transformation. (a) A schematic demonstrating the initial instability of a triangular lattice node. (c) Two equally probable ways of transforming initial nodes leading to two different phases. (c) The evaporation line formed during transformation and the unit cells are assembled sequentially from right to left. (d) Phase boundary forms between two phases. Scale bar, 100 μm .

D.3.4.3 Stability of the assembled microstructures under harsh conditions

The reconfigured structure is maintained by both the kinetic trapping of the polymer conformation and the interfacial adhesion between the assembled walls. Such dual protection enables the robustness of the assembled microstructures under various harsh conditions. For example, the structures remain assembled when heated up to 130 °C (see Fig. D.9(a-b)). Although heating above T_g overcomes the kinetic trapping and relaxes the polymer conformation, the material becomes sticky and more importantly it becomes much softer due to increased molecular mobility – similar to the swelling-induced rubbery state (plasticizing with solvents) that has a Young's modulus of ~80 kPa. If we assume that both cases have similar Young's moduli, it then requires only an adhesion energy of 1.5 mJ to hold the reconfigured structure (see discussion in SI section 2.3). Only a slight bulging of the assembled walls was observed at 130 °C due to the thermal expansion of the LCP

materials upon heating. Furthermore, the assembled structures stay robust after being immersed in a poor solvent such as ethanol for a few days, indicating that, although ethanol may be able to decrease (but not fully eliminate) the adhesion energy between the assembled walls, it cannot enter the polymer network to alter the conformation of the polymer chains at the molecular scale, and therefore cannot disassemble the microstructure (Fig. D.9(c)).

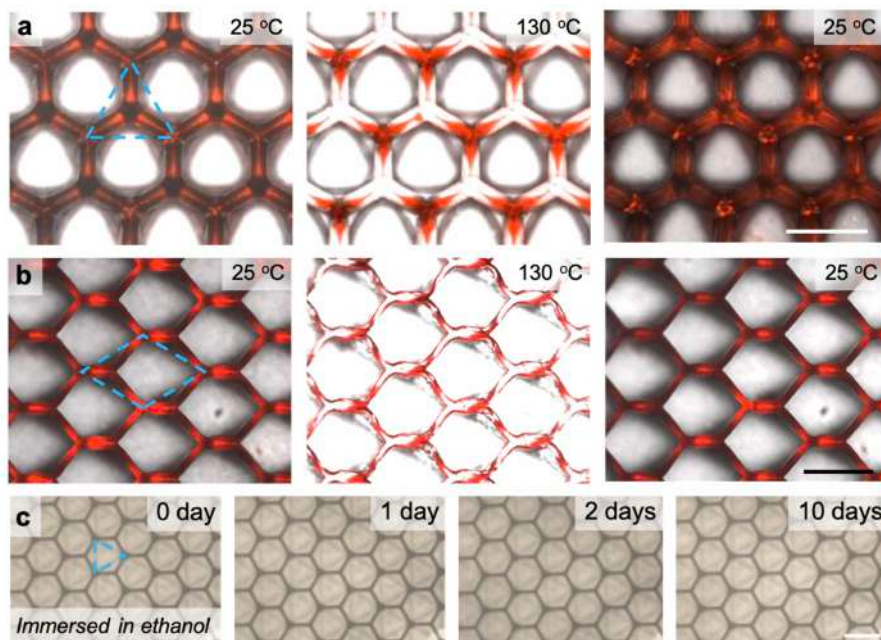


Figure D.9: Stability of the assembled microstructures under harsh conditions. Confocal microscopy images of the assembled structure for (a) a triangular-to-hexagonal system and (b) a diamond-to-hexagonal system, at room temperature (left), heated to 130 °C (middle), and cooled to room temperature (right). The structure is locked in a fully assembled configuration throughout the heating and cooling process. (c) Optical microscopy images of the assembled structure after immersion in ethanol for 0 day, 1 day, 2 days, and 10 days post assembly. Scale bar, 100 μ m.

D.3.4.4 Reversibility and fatigue test

To test the reversibility of the transformation, ten back-and-forth repeated cycles of transformation on the same cellular structure was conducted (Fig. D.10(a)). No noticeable fatigue behavior was observed. As shown in the zoomed-in image, the walls remain clearly separated around the node

after the 10th disassembly. We note that fatigue may occur with more transformation cycles, and it is expected to first show at the hinges due to large deformations near the node.

D.3.4.5 Hysteresis test

The hysteresis behavior of the reversibility of the transformation over long time breaks was tested over 3, 6, 9, and 18 days, and no noticeable hysteresis was observed (Fig. D.10(b)). Specifically, the transformed structure was kept under its hexagonal configuration for a long period (3, 6, 9, and 18 days), and then subjected to disassembly and assembly process. The structure was shown to be capable of complete disassembly and assembly over at least an 18-day break.

We note the potential ‘sticky’ problems over very long periods after transformation in systems with polymer films in close contact. The hysteresis tests showed that a slightly higher concentration of DCM might be required for a larger swelling sufficient to peel apart the assembled walls as compared to freshly assembled structures, due to an increase in the interfacial adhesion. Furthermore, different crosslinking densities of the polymer may affect the hysteresis behavior. With a lower crosslinking density, the polymer is likely to be stickier and is more vulnerable to hysteresis during repeated transformation. For the purpose of robust reversibility, we choose the crosslinking density of LCP within a range of 1.5 to 3wt

D.3.5 Generalization of the topological transformation

D.3.5.1 Other lattice geometries

Our theoretical model predicts that the capillary forces prefer to assemble edge pairs with smaller angles. Addition geometries are designed and experimentally tested based on this general principal

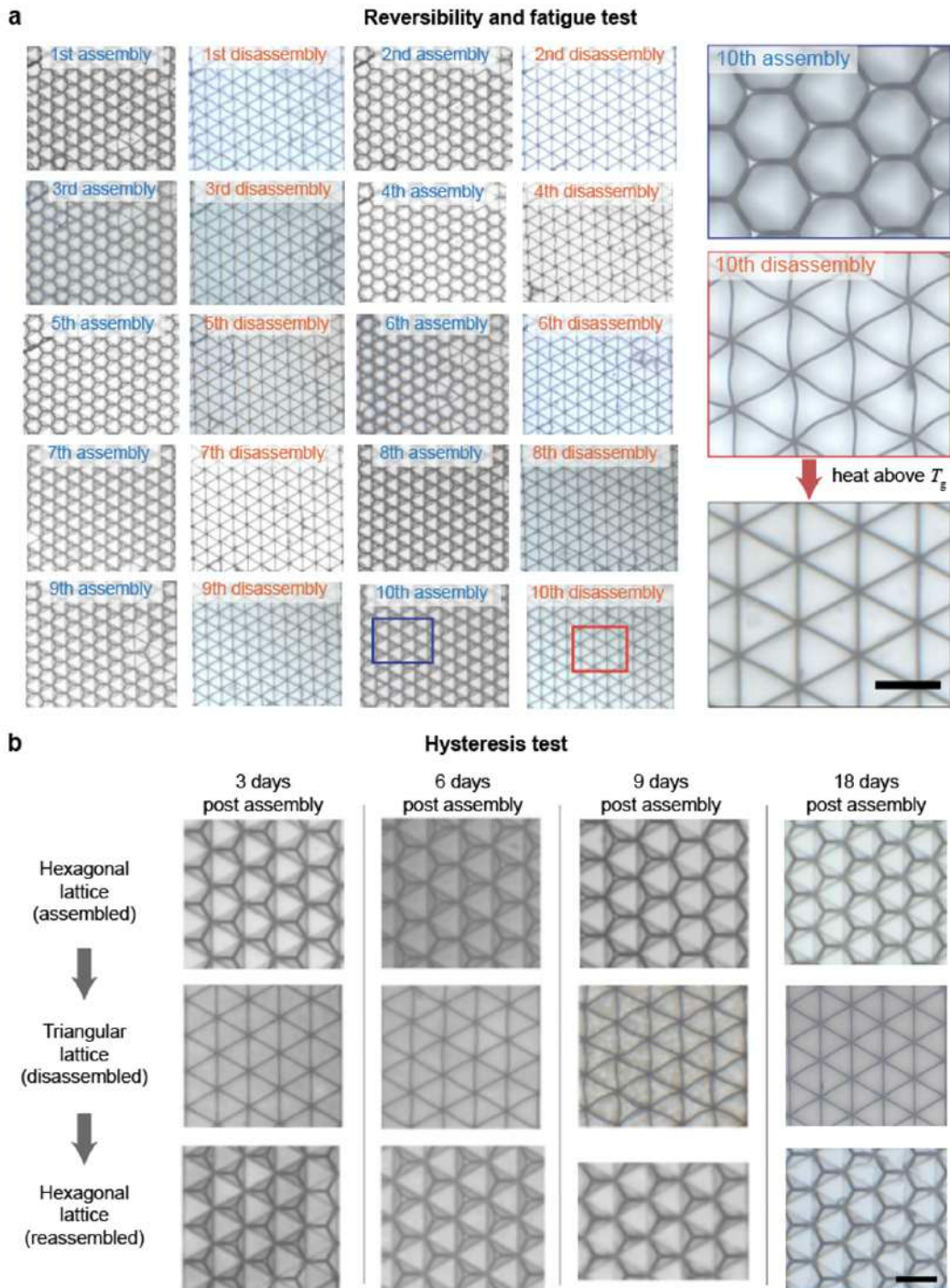


Figure D.10: Reversibility, fatigue and hysteresis test with LCP (2wt%). (a) Reversibility and fatigue test over ten cycles. (b) Hysteresis test over time breaks of 3, 6, 9 and 18 days.

(Fig. D.11). It is important to note that geometrical compatibility also needs to be taken into account when considering certain lattices, such as the diamond lattice (shown in manuscript Fig. 53a, iv). If both small angles at the rhombus nodes were closed, the transformed nodes would fail to repack into a connected lattice due to geometrical frustration. Under this circumstance, one of the smallest angles at each node has to open up to be compatible with other nodes, which results in a hexagonal lattice.

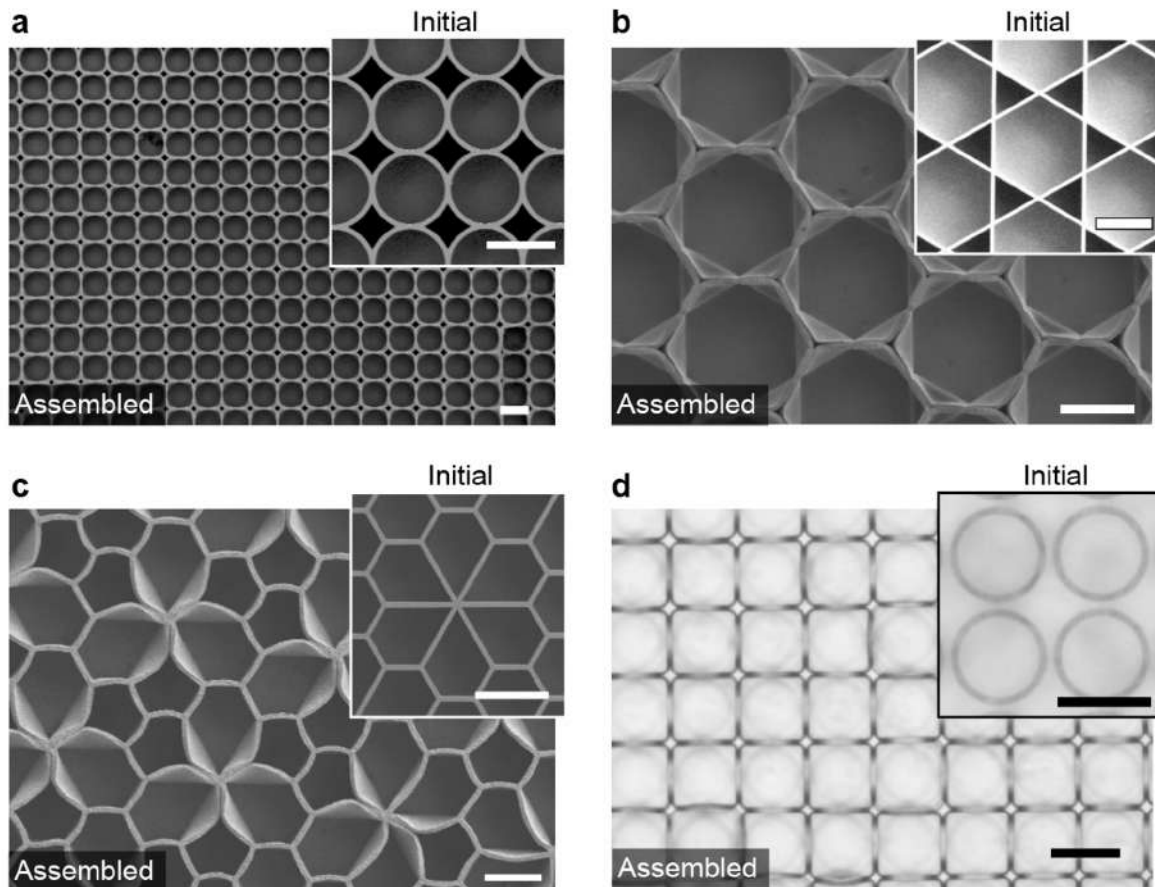


Figure D.11: Topological transformation of complex lattice geometries in large areas. (a) Circular lattice (inset) transformed to a square lattice. (b) Initial kagome lattice (inset) transformed to a hexagonal lattice. (c) Transformation of flower-patterned lattice. Scale bar, 100 μm . (d) Initial isolated rings transformed to an interconnected square lattice. When the top surface is coated with conductive materials, such transformation could be potentially used to alter the conductivity of the cellular structures. Scale bar, 30 μm .

D.3.5.2 Other structural dimensions

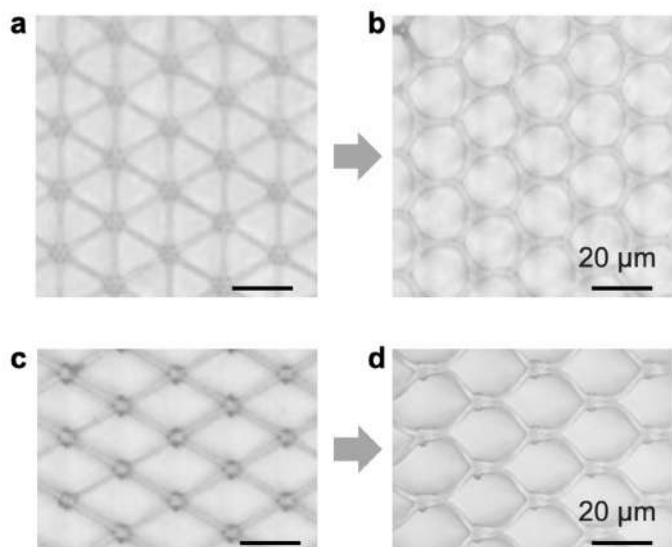


Figure D.12: Topological transformation of cellular structures with edge length $l=20\ \mu\text{m}$, $b=2\ \mu\text{m}$, and $h=10\ \mu\text{m}$. (a) Initial triangular lattice and (b) assembled hexagonal lattice. (c) Initial diamond lattice and (d) assembled hexagonal lattice. These results prove that, as predicted by our theoretical model (Fig. D.2), our strategy is applicable to smaller scales. Scale bar, $20\ \mu\text{m}$.

D.3.5.3 Other materials

PHEMA-co-PBA The generality of the transformation strategy to other materials was successfully demonstrated with poly(2-hydroxyethyl methacrylate-co-n-butyl-acrylate) (PHEMA-co-PBA) (55.4 : 44.6 mol%), as shown in Fig. D.13(a). The PHEMA-co-PBA was synthesized following a reported procedure with adjusted chemistries¹². The polymer precursor was prepared by mixing 200 mg 2-hydroxyethyl methacrylate (HEMA, Sigma-Aldrich) with 200 mg n-butyl acrylate (Sigma-Aldrich) and 10 mg Darocur®1173. The mixture was then exposed to UV light (Dymax Model 2000 Flood UV Curing System, light intensity of $\sim 18\ \text{mW/cm}^2$) under a nitrogen atmosphere for 15 s $\times 3$ to yield a prepolymer solution. Additional 4 mg of Darocur®1173 and 6 mg of 1,6-Hexanediol diacrylate (HDDA) were added to the precursor solution for the molding and polymerization fol-

lowing the same procedure described in SI section 3.2.

Molecularly aligned side-on LCP Hierarchical deformation of the cellular structures was achieved by imprinting the material with anisotropic thermal responses from aligned LCPs. Here we present the results using a different LCP material from the one described before – a side-on LCP shown in Fig. D.13(b) with LC mesogens aligned following a procedure we reported recently¹³. The reactive monomer mixture was prepared following the procedure in SI section 3.2. For the alignment and polymerization, 20 mg of the reactive mixture was applied into a PDMS mold and covered with a glass substrate. The sample was then placed in a magnetic field generated by a NdFeB-based magnet with surface field of 0.5 T (Fig. D.13(b)), heated to 80 °C (isotropic phase), cooled down to 60 °C at a rate of 1 °C/min. The UV polymerization was conducted following the same procedure described in SI section 3.2.

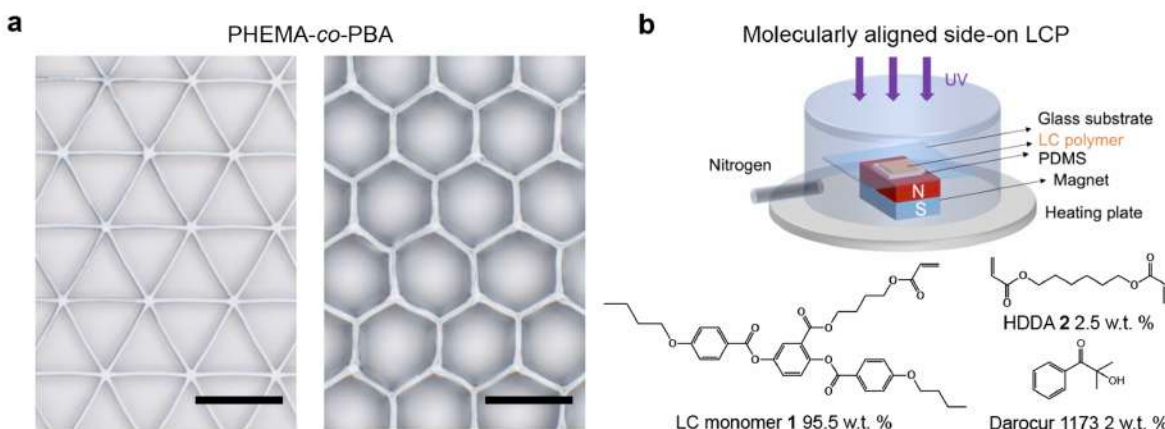


Figure D.13: Application to different polymeric materials. (a) Topological transformation of a poly(2-hydroxyethyl methacrylate-co-n-butyl-acrylate) PHEMA-co-PBA triangular cellular lattice to a hexagonal one. (b) Schematic of experimental setup and LCP chemical constituents for the synthesis of molecularly aligned nematic LCP.

D.3.6 Free-standing cellular structures

In Fig. D.14, we show the microscopic image of a free-standing cellular film with a triangular lattice. After liquid treatment, part of the initial triangular lattice is transformed to a hexagonal one. However, since the thin cellular film cannot hold any force or moment, the film is warped and curled by the liquid during the transformation. It indicates that the substrate anchoring guarantees the stability of the cellular structure so that the transformation is immune from global floppy deformations. Application-wise, a firm substrate also provides strong support to the cellular structures, which in turn possess characteristic surface properties. Additionally, without the anchoring from the substrate, floppy lattice geometries such as square and rhombic lattices will collapse or assemble chaotically (Fig. D.14(d)).

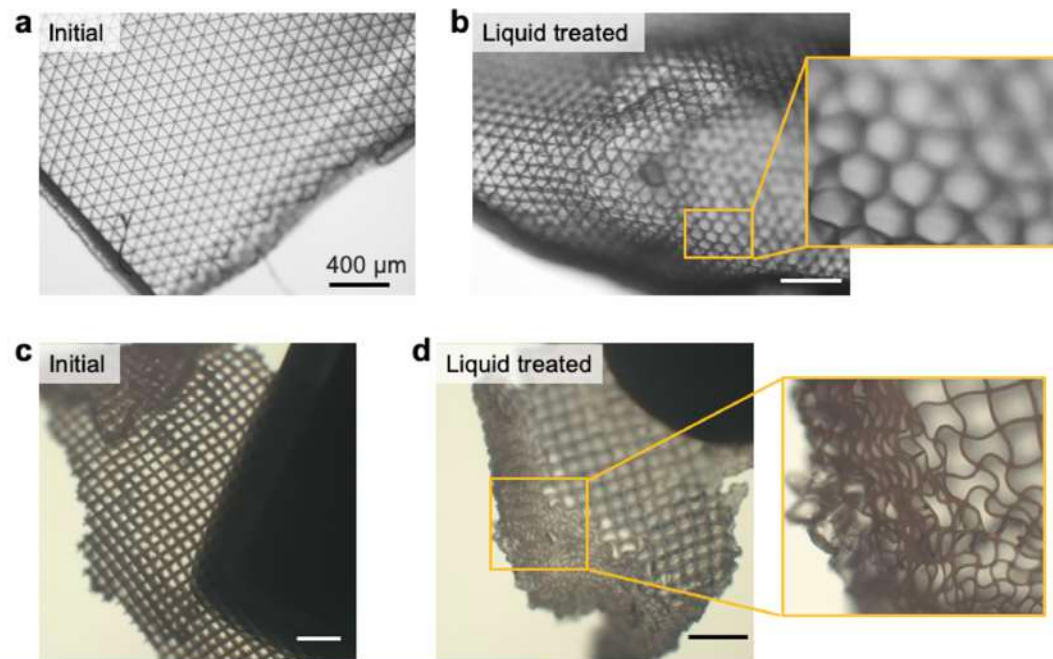


Figure D.14: (a-b) The free-standing triangular cellular mesh with soft deformable substrate: (a) initial structure upon exposure to liquid (acetone); (b) partially assembled structure after the evaporation. (c-d) The free-standing square cellular mesh with soft deformable substrate: (c) initial structure; (d) after the evaporation, the structure assembled chaotically and deformed globally due to the floppy nature of square lattice.

D.3.7 Local transformations with small droplets

Localized transformations can be achieved by applying a small amount of liquid to a large sample, such that only the area that is in contact with the liquid will be transformed (see Fig. D.15). Such localized control of transformations could be potentially used for area-specific applications. Due to the compartmentalized nature of the cellular structure, the applied liquid will tend to fully fill a certain number of cells rather than spreading to larger areas with partially filled cells. Therefore, the thickness of the applied solvent drop can be considered as no shorter than the cell height in most cases. As shown in Fig. D.15(a) albeit complete transformation in a $\sim 500 \mu\text{m} \times 500 \mu\text{m}$ area. By varying the volume of the liquid applied, local topological transformations with different feature sizes can be realized controllably (Fig. D.15(a-d)). Note that for some extreme cases where the liquid volume is far below $1 \mu\text{L}$, transformation was not observed due to insufficient swelling and capillary work.

Local disassembly can be achieved with similar procedure, which enables more sophisticated local patterns through sequential assembly and disassembly. In Fig. D.15(e), a small droplet was first applied to a uniformly assembled hexagonal lattice that disassembled a $\sim 1500 \mu\text{m} \times 1500 \mu\text{m}$ area. Then, a $\sim 500 \mu\text{m} \times 500 \mu\text{m}$ area within this disassembled region can be assembled again by a smaller droplet yielding concentric rings of assembled and disassembled lattices. Furthermore, such local control can also be integrated with the trapped intermediate configurations described in manuscript Fig. 52(g) for more complex patterns and corresponding functions (Fig. D.15(f)).

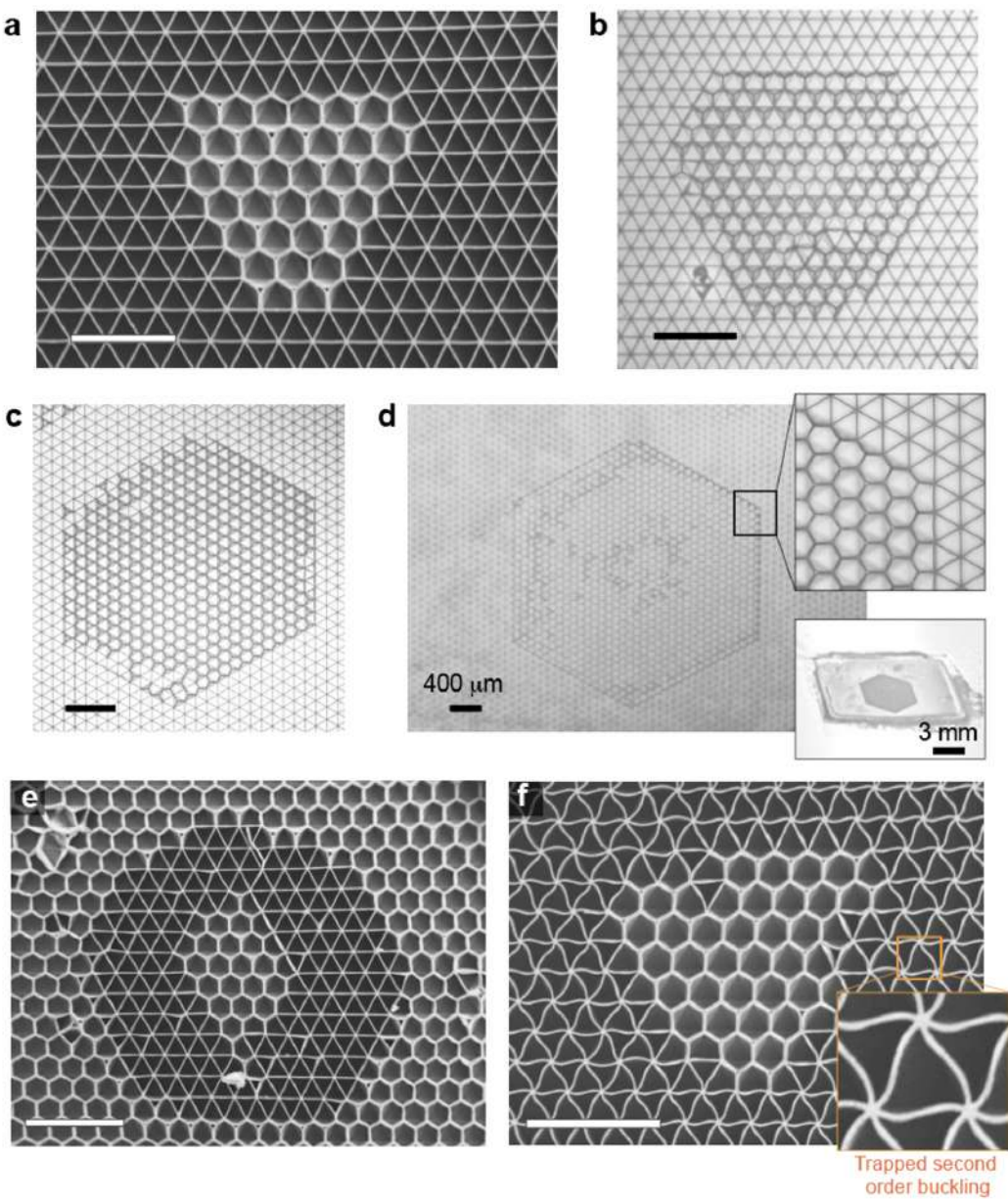


Figure D.15: Localized transformation with small droplets. (a-d) Localized transformation of the triangular lattice into a hexagonal lattice with different sizes of the applied droplets. Note that the small droplet applied tends to spread to a hexagonal shape due to the symmetry and connectivity of the initial triangular lattice. (e) Multi-step localized transformation after a sequential assembly (large area)-disassembly (medium area)-assembly (small area) process. (f) Integration of the kinetic trapping effect of buckled walls with the local transformation.

D.3.8 Phase design

D.3.8.1 Geometrical perturbations

To obtain a defect-free assembled structure, small geometrical perturbations can be introduced to the initial triangular lattice to make every node favor one phase over the other. Our theoretical model indicates that edges with smaller angles are easier to assemble than those with larger angles. Therefore, by perturbing the angles at the initial nodes by a small angle $\Delta\alpha$, we can design the structure to favor a chosen phase at every node (see Fig. D.16(a) as an example for favor phase I). Experimentally this is realized by building structures with slightly curved walls (see Fig. D.16(b)). Specifically, to design a node with its angles perturbed by $\Delta\alpha$, we fabricate curved walls with radius $\rho = l/(2 \sin \frac{\alpha}{2})$ and central angle $2\Delta\alpha$. We choose $\Delta\alpha = 2.5^\circ$ where the actual difference between a lattice with curved edges and a perfect lattice is visually indistinguishable (see Fig. D.16(c), where the inset shows the marginal difference of the curved triangle and the perfect triangle in terms of CAD design).

The indistinguishable imperfections introduced to the triangular lattice have a profound impact during the capillary assembly. As shown in Fig. D.16(d) when the lattice is swelled by the liquid, the buckling modes of the edges are altered by the imperfections in a way that favors Y shape nodes. The capillary forces then further zip up the closer walls to form a uniform hexagonal lattice. Fig. D.16(e-h) show SEM, optical, and confocal microscopic images of the assembled perfect hexagonal cellular structures in large areas. No defects or domain boundaries appear in this case, due to the controlled geometrical perturbations introduced in the structure.

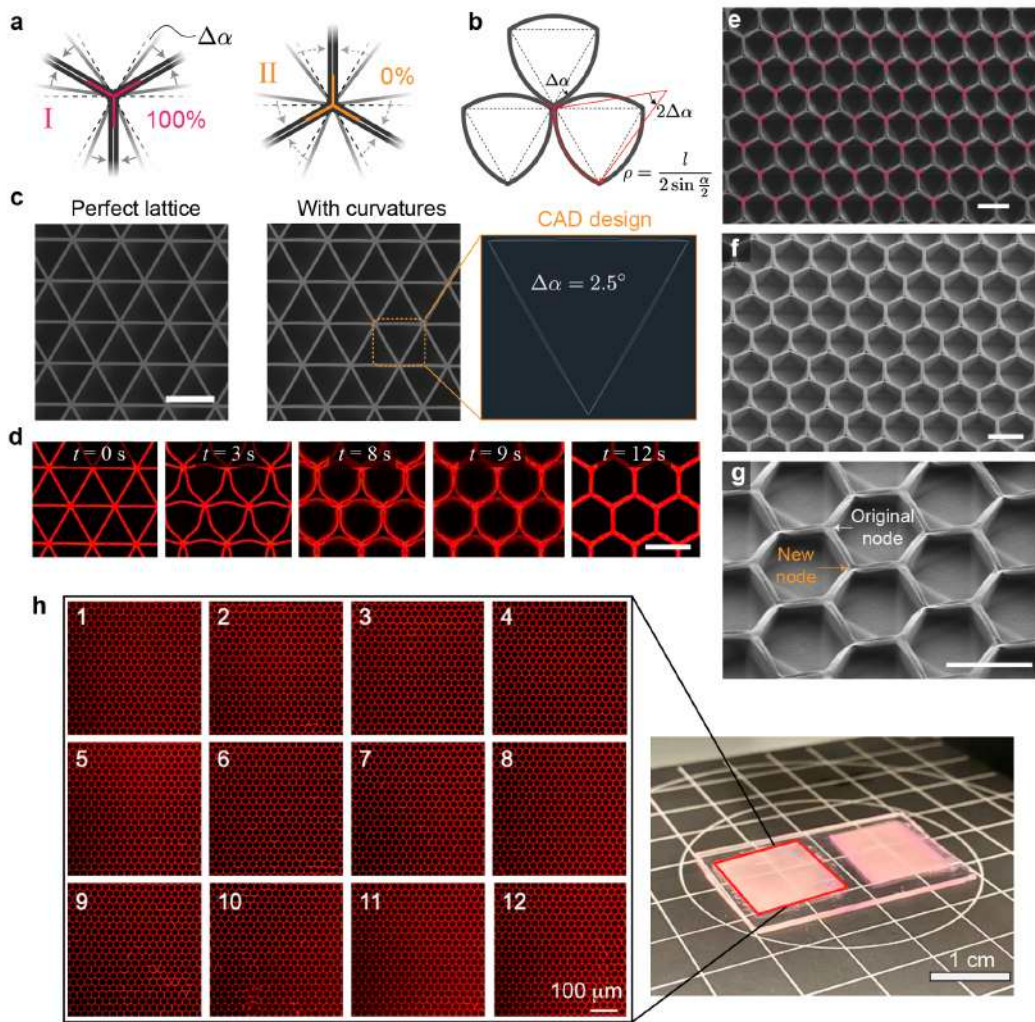


Figure D.16: Perturbation design for uniform assembly. (a) The phase selection can be controlled at each initial node by introducing a small difference in the local angles $\Delta\alpha$. (b) A schematic of the experimental design of the node to favor phase I using curved walls. The schematics exaggerate the curvature used in the experiments shown in c-f. (c) Actual structure with slightly perturbed angles $\Delta\alpha = 2.5^\circ$ (imaged by SEM). The inset shows the corresponding CAD design. The initial structure is visually indistinguishable from a perfect triangular lattice. (d) Confocal snapshots of the assembly of a perturbed triangular lattice at different time points. (e-g) Initial triangular lattice with $\Delta\alpha = 2.5^\circ$ is transformed to a perfect hexagonal lattice with a single uniform phase without phase boundaries: (e) top view, (f) tilted view and (g) zoomed-in tilted view. Scale bar, 100 μm . (h) Large-area uniformed transformed samples ($1.5\text{ cm} \times 1.5\text{ cm}$, much larger samples are readily accessible with molding) used for friction and wetting measurement. Homogeneous transformations are observed in every region as illustrated by twelve different regions of sample each containing roughly 20 by 20 compartments (2 mm by 2 mm in size).

D.3.8.2 Phase boundary design

Since designing the orientation of the wall curvature enables one to program each individual node to favor either phase I or phase II (Fig. D.17(a)), the locations of phase boundaries can be easily controlled by prescribing the distribution of the two types of angular perturbations. Fig. 17b illustrates how structures with two regions, consisting of nodes with perturbations that favor phase I or phase II, respectively, lead to an assembled lattice with domains concatenating with each other at the phase boundary, with phase I on the left and phase II on the right. Again, while the schematic in Fig. D.17(b) shows exaggerated curvatures, the actual structures are indistinguishable from a perfect triangular lattice. It is worth noting that the specific design of the edges on the boundary does not matter, because the position of the defect is determined by the phases of bulk structures rather than the specific imperfections on the boundary. Fig. D.17(c) shows the emergence of a phase boundary upon reconfiguration. The left part and the right part of the structure corresponding to different phases. Furthermore, such phase boundary design can be applied to form more complex patterns, as exemplified in Fig. D.17(d) as a heart pattern. We note that the large area SEM image is stitched from 4 small panels. Fig. D.17(e) shows that the differences between two phases are optically invisible before capillary reconfiguration and become visible afterwards. The encryption level of this method is determined by the value of perturbation curvature and the unit cell size. If a computer equipped with a high-resolution camera is able to pick up the curvature in each unit cell, then we need to increase the level of encryption by either decreasing the curvature or making the unit cells smaller. Generally, we believe that our current information encryption method cannot be easily picked up by a computer. For example, the demonstrated information encryption samples usually contain 50 by 50 unit cells. A high-resolution camera can take a picture with roughly 2000

by 2000 pixels with each unit cell described by 40 by 40 pixels. With a perturbation of 2.5 deg, the maximal deviation of the curved edge is roughly 0.01 times the unit cell length, which cannot be picked up by a 40 by 40 resolution picture. After the transformation, such subtle difference is strongly magnified by the phase boundaries that are visible even by naked eyes (see Fig. D.17(e)). Lastly, depending on the fabrication accuracy, the perturbation angle can be further decreased to ensure stronger encryption.

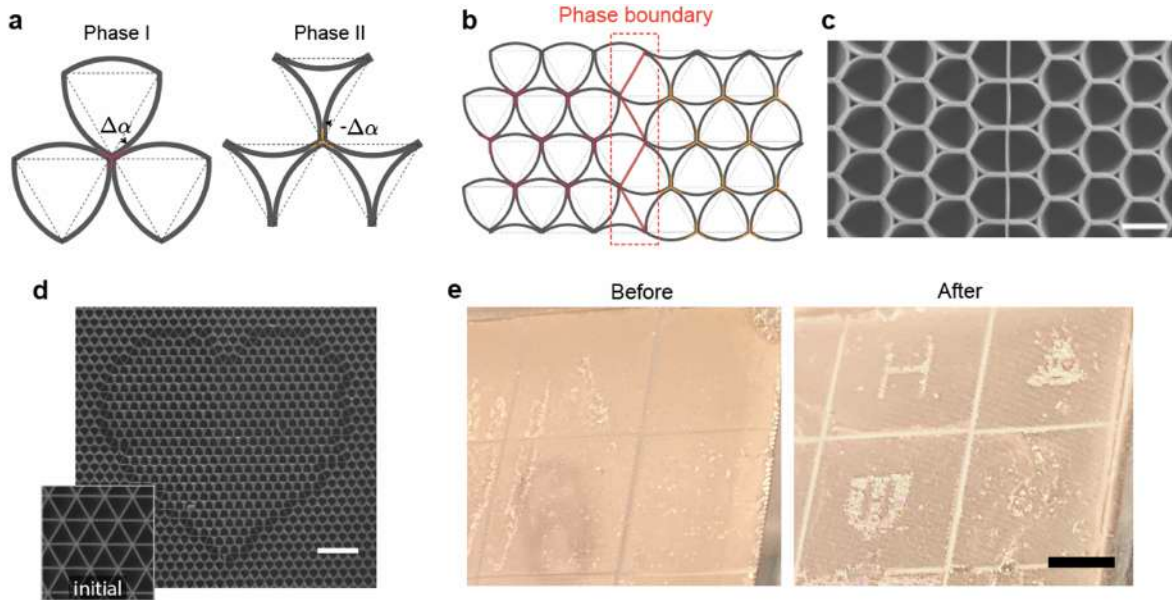


Figure D.17: Phase boundary design. (a) Schematics of two imperfection designs that lead to phase I and phase II respectively. (b) Design of a phase boundary by controlling the distribution of the two types of angular perturbations. (c) SEM image of the engineered phase boundary: the nodes on the left are designed to favor a different phase than the nodes on the right. Scale bar, 100 μm . (d) Phase designed heart pattern before and after transformation. Scale bar, 400 μm . (e) Photos of microstructures with designed phase boundaries before and after capillary reconfiguration. The boundary between the two phases is optically visible in the assembled structures. Scale bar, 5 mm.

References

- [1] Shim, J., Shan, S., Košmrlj, A., Kang, S. H., Chen, E. R., Weaver, J. C., and Bertoldi, K. (2013). Harnessing instabilities for design of soft reconfigurable auxetic/chiral materials. *Soft Matter*, 9(34):8198–8202.
- [2] Hereman, W. (2013). Shallow water waves and solitary waves. *arXiv preprint arXiv:1308.5383*.
- [3] Kang, S. H., Shan, S., Noorduin, W. L., Khan, M., Aizenberg, J., and Bertoldi, K. (2013). Buckling-induced reversible symmetry breaking and amplification of chirality using supported cellular structures. *Advanced Materials*, 25(24):3380–3385.
- [4] Boley, J. W., Van Rees, W. M., Lissandrello, C., Horenstein, M. N., Truby, R. L., Kotikian, A., Lewis, J. A., and Mahadevan, L. (2019). Shape-shifting structured lattices via multimaterial 4D printing. *Proceedings of the National Academy of Sciences of the United States of America*, 116(42):20856–20862.
- [5] Xia, X., Afshar, A., Yang, H., Portela, C. M., Kochmann, D. M., Di Leo, C. V., and Greer, J. R. (2019). Electrochemically reconfigurable architected materials. *Nature*, 573(7773):205–213.
- [6] Bertoldi, K., Vitelli, V., Christensen, J., and van Hecke, M. (2017). Flexible mechanical metamaterials. *Nature Reviews Materials*, 2(11):17066.
- [7] Engheta, N. and Ziolkowski, R. W. (2006). *Metamaterials: physics and engineering explorations*. John Wiley & Sons.
- [8] Cui, T. J., Smith, D. R., and Liu, R. (2010). *Metamaterials*. Springer.
- [9] Soukoulis, C. M. and Wegener, M. (2011). Past achievements and future challenges in the development of three-dimensional photonic metamaterials. *Nature photonics*, 5(9):523–530.
- [10] Cummer, S. A., Christensen, J., and Alù, A. (2016). Controlling sound with acoustic metamaterials. *Nature Reviews Materials*, 1(3):1–13.

- [11] Maldovan, M. (2013). Narrow low-frequency spectrum and heat management by thermocrystals. *Phys Rev Lett*, 110(2):025902.
- [12] Lakes, R. (1987). Foam structures with a negative Poisson's ratio. *Science*, 235:1038–1041.
- [13] Bertoldi, K., Reis, P. M., Willshaw, S., and Mullin, T. (2010). Negative Poisson's ratio behavior induced by an elastic instability. *Advanced materials*, 22(3):361–366.
- [14] Baughman, R. H., Stafström, S., Cui, C., and Dantas, S. O. (1998). Materials with negative compressibilities in one or more dimensions. *Science*, 279(5356):1522–1524.
- [15] Wang, Q., Jackson, J. A., Ge, Q., Hopkins, J. B., Spadaccini, C. M., and Fang, N. X. (2016). Lightweight mechanical metamaterials with tunable negative thermal expansion. *Physical Review Letters*, 117(17):175901.
- [16] Boatti, E., Vasilos, N., and Bertoldi, K. (2017). Origami metamaterials for tunable thermal expansion. *Advanced Materials*, 29(26):1700360.
- [17] Hussein, M. I., Leamy, M. J., and Ruzzene, M. (2014). Dynamics of phononic materials and structures: Historical origins, recent progress, and future outlook. *Applied Mechanics Reviews*, 66(4):040802.
- [18] Huber, S. D. (2016). Topological mechanics. *Nature Physics*, 12(7):621–623.
- [19] Wang, P., Lu, L., and Bertoldi, K. (2015). Topological phononic crystals with one-way elastic edge waves. *Phys Rev Lett*, 115(10):104302.
- [20] Zhang, S., Xia, C., and Fang, N. (2011). Broadband acoustic cloak for ultrasound waves. *Physical Review Letters*, 106(2):024301.
- [21] Elser, D., Andersen, U., Korn, A., Glöckl, O., Lorenz, S., Marquardt, C., and Leuchs, G. (2006). Reduction of guided acoustic wave Brillouin scattering in photonic crystal fibers. *Physical Review Letters*, 97(13):133901.
- [22] Elnady, T., Elsabbagh, A., Akl, W., Mohamady, O., Garcia-Chocano, V. M., Torrent, D., Cervera, F., and Sánchez-Dehesa, J. (2009). Quenching of acoustic bandgaps by flow noise. *Applied Physics Letters*, 94(13):134104.
- [23] Casadei, F., Dozio, L., Ruzzene, M., and Cunefare, K. A. (2010). Periodic shunted arrays for the control of noise radiation in an enclosure. *Journal of sound and vibration*, 329(18):3632–3646.
- [24] Wang, P., Casadei, F., Shan, S., Weaver, J. C., and Bertoldi, K. (2014). Harnessing buckling to design tunable locally resonant acoustic metamaterials. *Phys Rev Lett*, 113(1):014301.

- [25] Florijn, B., Coulais, C., and van Hecke, M. (2014). Programmable mechanical metamaterials. *Physical Review Letters*, 113(17):175503.
- [26] Haghpanah, B., Salari-Sharif, L., Pourrajab, P., Hopkins, J., and Valdevit, L. (2016). Multistable Shape-Reconfigurable Architected Materials. *Advanced Materials*, 28(36):7915–7920.
- [27] Rafsanjani, A., Jin, L., Deng, B., and Bertoldi, K. (2019). Propagation of pop ups in kirigami shells. *Proceedings of the National Academy of Sciences*, 116(17):8200–8205.
- [28] Raney, J. R., Nadkarni, N., Daraio, C., Kochmann, D. M., Lewis, J. A., and Bertoldi, K. (2016). Stable propagation of mechanical signals in soft media using stored elastic energy. *Proceedings of the National Academy of Sciences*, 113(35):9722–9727.
- [29] Drazin, P. and Johnson, R. (1989). *Solitons: An Introduction*. Cambridge Texts in Applied Mathematics. Cambridge University Press.
- [30] Russell, J. S. (1844). Report on Waves. *Report of the fourteenth meeting of the British Association for the Advancement of Science*, pages 311–390.
- [31] Stegeman, G. and Segev, M. (1999). Optical Spatial Solitons and Their Interactions: Universality and Diversity. *Science*, 286(5444):1518–1523.
- [32] Radhakrishnan, R., Lakshmanan, M., and Hietarinta, J. (1997). Inelastic collision and switching of coupled bright solitons in optical fibers. *Phys. Rev. E*, 56:2213–2216.
- [33] Tsuboi, T. (1989). Phase shift in the collision of two solitons propagating in a nonlinear transmission line. *Phys. Rev. A*, 40:2753–2755.
- [34] Shen, Y., Kevrekidis, P. G., Sen, S., and Hoffman, A. (2014). Characterizing traveling-wave collisions in granular chains starting from integrable limits: The case of the Korteweg–de Vries equation and the Toda lattice. *Phys. Rev. E*, 90:022905.
- [35] Malik, H. K., Kumar, R., Lonngren, K. E., and Nishida, Y. (2015). Collision of ion acoustic solitary waves in a magnetized plasma: Effect of dust grains and trapped electrons. *Phys. Rev. E*, 92:063107.
- [36] Nguyen, J. H. V., Dyke, P., Luo, D., Malomed, B. A., and Hulet, R. G. (2014). Collisions of matter-wave solitons. *Nature Physics*, 10:918–922.
- [37] Ibañez, J. and Verdaguer, E. (1983). Soliton Collision in General Relativity. *Phys. Rev. Lett.*, 51:1313–1315.

- [38] Sen, S., Hong, J., Bang, J., Avalos, E., and Doney, R. (2008). Solitary waves in the granular chain. *Physics Reports*, 462(2):21–66.
- [39] Santibanez, F., Munoz, R., Caussarieau, A., Job, S., and Melo, F. (2011). Experimental evidence of solitary wave interaction in Hertzian chains. *Phys. Rev. E*, 84:026604.
- [40] Manciu, M., Sen, S., and Hurd, A. J. (2000). Crossing of identical solitary waves in a chain of elastic beads. *Phys. Rev. E*, 63:016614.
- [41] Nesterenko, V. (2013). *Dynamics of heterogeneous materials*. Springer Science & Business Media.
- [42] Theocharis, G., Boechler, N., and Daraio, C. (2013). Nonlinear periodic phononic structures and granular crystals. In *Acoustic Metamaterials and Phononic Crystals*, pages 217–251. Springer.
- [43] Forsbergh Jr, P. W. (1949). Domain structures and phase transitions in barium titanate. *Physical Review*, 76(8):1187.
- [44] Catalan, G., Seidel, J., Ramesh, R., and Scott, J. F. (2012). Domain wall nanoelectronics. *Reviews of Modern Physics*, 84(1):119.
- [45] Merz, W. J. (1954). Domain formation and domain wall motions in ferroelectric bati o 3 single crystals. *Physical Review*, 95(3):690.
- [46] LaBonte, A. (1969). Two-dimensional Bloch-type domain walls in ferromagnetic films. *Journal of Applied Physics*, 40(6):2450–2458.
- [47] Yamanouchi, M., Chiba, D., Matsukura, F., and Ohno, H. (2004). Current-induced domain-wall switching in a ferromagnetic semiconductor structure. *Nature*, 428(6982):539–542.
- [48] Sapriel, J. (1975). Domain-wall orientations in ferroelastics. *Physical Review B*, 12(11):5128.
- [49] Massad, J. E. and Smith, R. C. (2003). A domain wall model for hysteresis in ferroelastic materials. *Journal of Intelligent Material Systems and Structures*, 14(7):455–471.
- [50] Paul, D., Marquiss, J., and Quattrochi, D. (2003). Theory of magnetization: Twin boundary interaction in ferromagnetic shape memory alloys. *Journal of applied physics*, 93(8):4561–4565.
- [51] MacLennan, J. and Seul, M. (1992). Novel stripe textures in nonchiral hexatic liquid-crystal films. *Physical Review Letters*, 69(14):2082.

- [52] Allwood, D. A., Xiong, G., Faulkner, C., Atkinson, D., Petit, D., and Cowburn, R. (2005). Magnetic domain-wall logic. *Science*, 309(5741):1688–1692.
- [53] Parkin, S. S., Hayashi, M., and Thomas, L. (2008). Magnetic domain-wall racetrack memory. *Science*, 320(5873):190–194.
- [54] Barkley, J., Brixner, L., Hogan, E., and Waring Jr, R. (1972). Control and application of domain wall motion in gadolinium molybdate. *Ferroelectrics*, 3(1):191–197.
- [55] Yang, D., Jin, L., Martinez, R. V., Bertoldi, K., Whitesides, G. M., and Suo, Z. (2016). Phase-transforming and switchable metamaterials. *Extreme Mechanics Letters*, 6:1–9.
- [56] Nadkarni, N., Arrieta, A. F., Chong, C., Kochmann, D. M., and Daraio, C. (2016). Unidirectional transition waves in bistable lattices. *Physical Review Letters*, 116(24):244501.
- [57] Frazier, M. J. and Kochmann, D. M. (2017). Atomimetic mechanical structures with non-linear topological domain evolution kinetics. *Advanced Materials*, 29(19):1605800.
- [58] Jin, L., Khajehtourian, R., Mueller, J., Rafsanjani, A., Tournat, V., Bertoldi, K., and Kochmann, D. M. (2020). Guided transition waves in multistable mechanical metamaterials. *Proceedings of the National Academy of Sciences*, 117(5):2319–2325.
- [59] Zareei, A., Deng, B., and Bertoldi, K. (2020). Harnessing transition waves to realize deployable structures. *Proceedings of the National Academy of Sciences*, 117(8):4015–4020.
- [60] Kang, S. H., Shan, S., Noorduin, W. L., Khan, M., Aizenberg, J., and Bertoldi, K. (2013). Buckling-induced reversible symmetry breaking and amplification of chirality using supported cellular structures. *Advanced materials*, 25(24):3380–3385.
- [61] Paulose, J., Meeussen, A. S., and Vitelli, V. (2015). Selective buckling via states of self-stress in topological metamaterials. *Proceedings of the National Academy of Sciences*, 112(25):7639–7644.
- [62] Yasuda, H., Korpas, L., and Raney, J. (2020). Transition Waves and Formation of Domain Walls in Multistable Mechanical Metamaterials. *Physical Review Applied*, 13(5):054067.
- [63] Khan, M., Shan, S., Aizenberg, J., Noorduin, W. L., Bertoldi, K., and Kang, S. H. (2013). Buckling-Induced Reversible Symmetry Breaking and Amplification of Chirality Using Supported Cellular Structures. *Advanced Materials*, 25(24):3380–3385.
- [64] Zhang, H., Guo, X., Wu, J., Fang, D., and Zhang, Y. (2018). Soft mechanical metamaterials with unusual swelling behavior and tunable stress-strain curves. *Science advances*, 4(6):eaar8535.

- [65] Kim, Y., Yuk, H., Zhao, R., Chester, S. A., and Zhao, X. (2018). Printing ferromagnetic domains for untethered fast-transforming soft materials. *Nature*, 558(7709):274–279.
- [66] Fu, H., Nan, K., Bai, W., Huang, W., Bai, K., Lu, L., Zhou, C., Liu, Y., Liu, F., Wang, J., Han, M., Yan, Z., Luan, H., Zhang, Y., Zhang, Y., Zhao, J., Cheng, X., Li, M., Lee, J. W., Liu, Y., Fang, D., Li, X., Huang, Y., Zhang, Y., and Rogers, J. A. (2018). Morphable 3D mesostructures and microelectronic devices by multistable buckling mechanics. *Nature Materials*, 17(3):268–276.
- [67] Coulais, C., Teomy, E., de Reus, K., Shokef, Y., and van Hecke, M. (2016). Combinatorial design of textured mechanical metamaterials. *Nature*, 535(7613):529–532.
- [68] Gibson, L., Ashby, M., and Harley, B. (2010). *Cellular materials in nature and medicine*.
- [69] Gibson, L. J. and Ashby, M. F. (1999). *Cellular Solids: Structure, Properties and Applications*. Cambridge University Press.
- [70] Ruzzene, M., Scarpa, F., and Soranna, F. (2003). Wave beaming effects in two-dimensional cellular structures. Technical report.
- [71] He, H., Qiu, C., Ye, L., Cai, X., Fan, X., Ke, M., Zhang, F., and Liu, Z. (2018). Topological negative refraction of surface acoustic waves in a Weyl phononic crystal. *Nature*, 560(7716):61–64.
- [72] Kang, S., Hong, S. Y., Kim, N., Oh, J., Park, M., Chung, K. Y., Lee, S. S., Lee, J., and Son, J. G. (2020). Stretchable Lithium-Ion Battery Based on Re-entrant Micro-honeycomb Electrodes and Cross-Linked Gel Electrolyte. *ACS Applied Materials and Interfaces*.
- [73] Shirman, E., Shirman, T., Shneidman, A. V., Grinthal, A., Phillips, K. R., Whelan, H., Bulger, E., Abramovitch, M., Patil, J., Nevarez, R., et al. (2018). Modular design of advanced catalytic materials using hybrid organic–inorganic raspberry particles. *Advanced Functional Materials*, 28(27):1704559.
- [74] Kim, O. H., Cho, Y. H., Kang, S. H., Park, H. Y., Kim, M., Lim, J. W., Chung, D. Y., Lee, M. J., Choe, H., and Sung, Y. E. (2013). Ordered macroporous platinum electrode and enhanced mass transfer in fuel cells using inverse opal structure. *Nature Communications*, 4:1–9.
- [75] Muth, J. T., Dixon, P. G., Woish, L., Gibson, L. J., and Lewis, J. A. (2017). Architected cellular ceramics with tailored stiffness via direct foam writing. *Proceedings of the National Academy of Sciences of the United States of America*, 114(8):1832–1837.

- [76] Christensen, R. M. (1986). Mechanics of low density materials. *Journal of the Mechanics and Physics of Solids*, 34(6):563–578.
- [77] Gan, Z., Turner, M. D., and Gu, M. (2016). Biomimetic gyroid nanostructures exceeding their natural origins. *Science Advances*, 2(5):e1600084.
- [78] Maloney, K. J., Fink, K. D., Schaedler, T. A., Kolodziejska, J. A., Jacobsen, A. J., and Roper, C. S. (2012). Multifunctional heat exchangers derived from three-dimensional micro-lattice structures. *International Journal of Heat and Mass Transfer*, 55(9-10):2486–2493.
- [79] Khan, M. I. H., Farrell, T., Nagy, S. A., and Karim, M. A. (2018). Fundamental Understanding of Cellular Water Transport Process in Bio-Food Material during Drying. *Scientific Reports*, 8(1):1–12.
- [80] Zhang, R., Hao, P., Zhang, X., and He, F. (2016). Dynamics of high Weber number drops impacting on hydrophobic surfaces with closed micro-cells. *Soft Matter*, 12(26):5808–5817.
- [81] Kim, E., Martínez, A. J., Phenisee, S. E., Kevrekidis, P. G., Porter, M. A., and Yang, J. (2017). Direct measurement of superdiffusive and subdiffusive energy transport in disordered granular chains.
- [82] Dauxois, T. and Peyrard, M. (2006). *Physics of solitons*. Cambridge University Press.
- [83] Porter, M. A., Kevrekidis, P. G., and Daraio, C. (2015). Granular crystals: Nonlinear dynamics meets materials engineering. *Phys Today*, 68(11):44–50.
- [84] Chong, C., Porter, M. A., Kevrekidis, P., and Daraio, C. (2017). Nonlinear coherent structures in granular crystals. *J Phys-Condens Mat*, 29(41):413003.
- [85] Vega-Flick, A., Duncan, R., Wallen, S., Boechler, N., Stelling, C., Retsch, M., Alvarado-Gil, J., Nelson, K., and Maznev, A. (2017). Vibrational dynamics of a two-dimensional microgranular crystal. *Phys Rev B*, 96(2):024303.
- [86] Hiraiwa, M., Wallen, S., and Boechler, N. (2017). Acoustic wave propagation in disordered microscale granular media under compression. *Granul Matter*, 19(3):62.
- [87] Burgoyne, H. A., Newman, J. A., Jackson, W. C., and Daraio, C. (2015). Guided impact mitigation in 2D and 3D granular crystals. *Procedia Engineering*, 103:52–59.
- [88] Donahue, C. M., Anzel, P. W., Bonanomi, L., Keller, T. A., and Daraio, C. (2014). Experimental realization of a nonlinear acoustic lens with a tunable focus. *Appl Phys Lett*, 104(1):014103.

- [89] Li, F., Anzel, P., Yang, J., Kevrekidis, P. G., and Daraio, C. (2014). Granular acoustic switches and logic elements. *Nat Commun*, 5:5311.
- [90] Singhal, T., Kim, E., Kim, T.-Y., and Yang, J. (2017). Weak bond detection in composites using highly nonlinear solitary waves. *Smart Mater Struct*, 26(5):055011.
- [91] Skryabin, D., Luan, F., Knight, J., and Russell, P. (2003). Soliton Self-Frequency Shift Cancellation in Photonic Crystal Fibers. *Science*, 301(5640):1705–1708.
- [92] Ouzounov, D., Ahmad, F., Müller, D., Venkataraman, N., Gallagher, M., Thomas, M., Silcox, J., Koch, K., and Gaeta, A. (2003). Generation of Megawatt Optical Solitons in Hollow-Core Photonic Band-Gap Fibers. *Science*, 301(5640):1702–1704.
- [93] Ma, G., Fu, C., Wang, G., Del Hougne, P., Christensen, J., Lai, Y., and Sheng, P. (2016). Polarization bandgaps and fluid-like elasticity in fully solid elastic metamaterials. *Nat Commun*, 7:13536.
- [94] Deng, B., Raney, J. J., Tournat, V., and Bertoldi, K. (2017). Elastic Vector Solitons in Soft Architected Materials. *Phys Rev Lett*, 118(20):204102.
- [95] Celli, P. and Gonella, S. (2015). Manipulating waves with LEGO® bricks: A versatile experimental platform for metamaterial architectures. *Appl Phys Lett*, 107(8):081901.
- [96] Polyanin, A. and Zaitsev, V. (2011). *Handbook of Nonlinear Partial Differential Equations, Second Edition*. Chapman and Hall/CRC.
- [97] Geniet, F. and Leon, J. (2002). Energy Transmission in the Forbidden Band Gap of a Non-linear Chain. *Phys Rev Lett*, 89:134102.
- [98] Yang, J., Dunatunga, S., and Daraio, C. (2012). Amplitude-dependent attenuation of compressive waves in curved granular crystals constrained by elastic guides. *Acta Mechanica*, 223:549–562.
- [99] Nesterenko, V. F. (2001). *Dynamics of Heterogeneous Materials*. Springer Verlag.
- [100] Kivshar, Y. S. (1990). Soliton stability in birefringent optical fibers: analytical approach. *J Opt Soc Am B*, 7(11):2204–2209.
- [101] Cao, X. D. and McKinstry, C. J. (1993). Solitary-wave stability in birefringent optical fibers. *J Opt Soc Am B*, 10(7):1202–1207.
- [102] Turner, M., Saba, M., Zhang, Q., Cumming, B., Schröder-Turk, G., and Gu, M. (2013). Miniature chiral beamsplitter based on gyroid photonic crystals. *Nat Photonics*, 7:801.

- [103] Job, S., Santibanez, F., Tapia, F., and Melo, F. (2009). Wave localization in strongly nonlinear Hertzian chains with mass defect. *Phys Rev E*, 80:025602.
- [104] Fleury, R., Sounas, D., Haberman, M., and Alu, A. (2015). Nonreciprocal acoustics. *Acoustics Today*, 11:14–21.
- [105] Liang, B., Guo, B., Tu, J., Zhang, D., and Cheng, J. (2010). An acoustic rectifier. *Nat Mater*, 9:989–992.
- [106] Boechler, N., Theocharis, G., and Daraio, C. (2011). Bifurcation-based acoustic switching and rectification. *Nat Mater*, 10:665–668.
- [107] Wu, Y., Yang, M., and Sheng, P. (2018). Perspective: Acoustic metamaterials in transition. *J Appl Phys*, 123(9):090901.
- [108] Devaux, T., Tournat, V., Richoux, O., and Pagneux, V. (2015). Asymmetric acoustic propagation of wave packets via the self-demodulation effect. *Phys Rev Lett*, 115:234301.
- [109] Wehmeyer, G., Yabuki, T., Monachon, C., Wu, J., and Dames, C. (2017). Thermal diodes, regulators, and switches: Physical mechanisms and potential applications. *Appl Phys Rev*, 4(4):041304.
- [110] Ma, G. and Sheng, P. (2016). Acoustic metamaterials: From local resonances to broad horizons. *Sci Adv*, 2(2):e1501595.
- [111] Chaunsali, R., Li, F., and Yang, J. (2016). Stress Wave Isolation by Purely Mechanical Topological Phononic Crystals. *Sci Rep*, 6:30662.
- [112] Tol, S., Xia, Y., Ruzzene, M., and Erturk, A. (2017). Self-bending elastic waves and obstacle circumventing in wireless power transfer. *Appl Phys Lett*, 110(16):163505.
- [113] Matlack, K. H., Serra-Garcia, M., Palermo, A., Huber, S. D., and Daraio, C. (2018). Designing Perturbative Metamaterials from Discrete Models. *Nat Mater*, 104(1):014103.
- [114] Ganesh, R. and Gonella, S. (2015). From modal mixing to tunable functional switches in nonlinear phononic crystals. *Phys Rev Lett*, 114(5):054302.
- [115] Bilal, O. R., Foehr, A., and Daraio, C. (2017). Bistable metamaterial for switching and cascading elastic vibrations. *P Natl Acad Sci USA*, 114(18):4603–4606.
- [116] Krödel, S., Thomé, N., and Daraio, C. (2015). Wide band-gap seismic metastructures. *Extreme Mechanics Letters*, 4:111–117.
- [117] Yasuda, H., Chong, C., Charalampidis, E. G., Kevrekidis, P. G., and Yang, J. (2016). Formation of rarefaction waves in origami-based metamaterials. *Phys Rev E*, 93(4):043004.

- [118] Mei, J., Chen, Z., and Wu, Y. (2016). Pseudo-time-reversal symmetry and topological edge states in two-dimensional acoustic crystals. *Sci Rep*, 6:32752.
- [119] Zabusky, N. J. and Kruskal, M. D. (1965). Interaction of "Solitons" in a Collisionless Plasma and the Recurrence of Initial States. *Phys. Rev. Lett.*, 15:240–243.
- [120] Makhankov, V. G. (1989). *Soliton Phenomenology*. Kluwer Academic.
- [121] Deng, B., Wang, P., He, Q., Tournat, V., and Bertoldi, K. (2018a). Metamaterials with amplitude gaps for elastic solitons. *Nature Communications*, 9:3410.
- [122] Deng, B., Tournat, V., and Bertoldi, K. (2018b). Effect of predeformation on the propagation of vector solitons in flexible mechanical metamaterials. *Physical Review E*, 98(5):053001.
- [123] Coulais, C., Kettenis, C., and van Hecke, M. (2017). A characteristic lengthscale causes anomalous size effects and boundary programmability in mechanical metamaterials. *Nature Physics*, page 1708.04643.
- [124] Tabor, M. (1989). *Chaos and integrability in nonlinear dynamics: an introduction*. Wiley-Interscience publication. Wiley.
- [125] Onuki, A. (2002). *Phase transition dynamics*. Cambridge University Press.
- [126] Fiebig, M., Lottermoser, T., Meier, D., and Trassin, M. (2016). The evolution of multiferroics. *Nature Reviews Materials*, 1(8):16046.
- [127] Coulais, C., Kettenis, C., and van Hecke, M. (2018). A characteristic length scale causes anomalous size effects and boundary programmability in mechanical metamaterials. *Nature Physics*, 14(1):40–44.
- [128] Deng, B., Tournat, V., Wang, P., and Bertoldi, K. (2019a). Anomalous collisions of elastic vector solitons in mechanical metamaterials. *Physical Review Letters*, 122(4):044101.
- [129] Deng, B., Mo, C., Tournat, V., Bertoldi, K., and Raney, J. R. (2019b). Focusing and Mode Separation of Elastic Vector Solitons in a 2D Soft Mechanical Metamaterial. *Physical Review Letters*, 123(2):024101.
- [130] Kleinert, H. and Schulte-Frohlinde, V. (2001). *Critical Properties of [Greek Letter Phi] 4-theories*. World Scientific.
- [131] Bico, J., Roman, B., Moulin, L., and Boudaoud, A. (2004). Elastocapillary coalescence in wet hair. *Nature*, 432(7018):690.

- [132] Pokroy, B., Kang, S. H., Mahadevan, L., and Aizenberg, J. (2009). Self-organization of a mesoscale bristle into ordered, hierarchical helical assemblies. *Science*, 323(5911):237–240.
- [133] Kang, S. H., Pokroy, B., Mahadevan, L., and Aizenberg, J. (2010). Control of shape and size of nanopillar assembly by adhesion-mediated elastocapillary interaction. *ACS Nano*, 4(11):6323–6331.
- [134] Roman, B. and Bico, J. (2010). Elasto-capillarity: Deforming an elastic structure with a liquid droplet. *Journal of Physics Condensed Matter*, 22(49).
- [135] Cai, L. H., Kodger, T. E., Guerra, R. E., Pegoraro, A. F., Rubinstein, M., and Weitz, D. A. (2015). Soft Poly(dimethylsiloxane) Elastomers from Architecture-Driven Entanglement Free Design. *Advanced Materials*, 27(35):5132–5140.
- [136] Jeong, S. H., Zhang, S., Hjort, K., Hilborn, J., and Wu, Z. (2016). PDMS-Based Elastomer Tuned Soft, Stretchable, and Sticky for Epidermal Electronics. *Advanced materials (Deerfield Beach, Fla.)*, 28(28):5830–5836.
- [137] Matsunaga, M., Aizenberg, M., and Aizenberg, J. (2011). Controlling the stability and reversibility of micropillar assembly by surface chemistry. *Journal of the American Chemical Society*, 133(14):5545–5553.
- [138] Flory, P. J. (1953). *Principles of Polymer Chemistry*. Cornell University Press, Ithaca, NY, 1st edition.
- [139] Rubinstein, M. and Colby H. Ralph (2003). *Polymer Physics*. Oxford Univerisity Press, New York.
- [140] Dimarzio, E. A. and Gibbs, J. H. (1963). Molecular interpretation of glass temperature depression by plasticizers. *Journal of Polymer Science Part A: General Papers*, 1(4):1417–1428.
- [141] Lin, H., Zhang, S., Xiao, Y., Zhang, C., Zhu, J., Dunlop, J. W., and Yuan, J. (2019). Organic Molecule-Driven Polymeric Actuators. *Macromolecular Rapid Communications*, 40(7).
- [142] Du, H. and Zhang, J. (2010). Solvent induced shape recovery of shape memory polymer based on chemically cross-linked poly(vinyl alcohol). *Soft Matter*, 6(14):3370–3376.
- [143] Gu, Y., Zhao, J., and Johnson, J. A. (2020). Polymer Networks: From Plastics and Gels to Porous Frameworks. *Angewandte Chemie - International Edition*, 59(13):5022–5049.
- [144] Chow, T. S. (1980). Molecular Interpretation of the Glass Transition Temperature of Polymer-Diluent Systems. *Macromolecules*, 13(2):362–364.

- [145] Rath, A., Geethu, P. M., Mathesan, S., Satapathy, D. K., and Ghosh, P. (2018). Solvent triggered irreversible shape morphism of biopolymer films. *Soft Matter*, 14(9):1672–1680.
- [146] Zhu, X., Wu, G., Dong, R., Chen, C. M., and Yang, S. (2012). Capillarity induced instability in responsive hydrogel membranes with periodic hole array. *Soft Matter*, 8(31):8088–8093.
- [147] Myshkin, N. and Kovalev, A. (2018). Adhesion and surface forces in polymer tribology—A review. *Friction*, 6(2):143–155.
- [148] Israelachvili, J. N. (2011). *Intermolecular and surface forces*. Academic press.
- [149] White, T. J. and Broer, D. J. (2015). Programmable and adaptive mechanics with liquid crystal polymer networks and elastomers. *Nature materials*, 14(11):1087–1098.
- [150] Ohm, C., Brehmer, M., and Zentel, R. (2010). Liquid crystalline elastomers as actuators and sensors. *Advanced materials*, 22(31):3366–3387.
- [151] Ramakrishnan, V. and Frazier, M. J. (2020). Transition waves in multi-stable metamaterials with space-time modulated potentials. *Applied Physics Letters*, 117(15):151901.
- [152] Nassar, H., Yousefzadeh, B., Fleury, R., Ruzzene, M., Alù, A., Daraio, C., Norris, A. N., Huang, G., and Haberman, M. R. (2020). Nonreciprocity in acoustic and elastic materials. *Nature Reviews Materials*, 5(9):667–685.
- [153] Senn, M. (2016). MATLAB central file exchange: Digital Image Correlation and Tracking. <https://www.mathworks.com/matlabcentral/fileexchange/50994-digital-image-correlation-and-tracking>.
- [154] Horowitz, P. and Hill, W. (1989). *The Art of Electronics*. Cambridge low price editions. Cambridge University Press.
- [155] Beer, F. P., Johnston, E., DeWolf, J., and Mazurek, D. (1992). Mechanics of materials. *New York*.
- [156] Holmes, D. P., Brun, P. T., Pandey, A., and Protier, S. (2016). Rising beyond elastocapillarity. *Soft Matter*, 12(22):4886–4890.
- [157] Wei, Z., Schneider, T. M., Kim, J., Kim, H.-Y., Aizenberg, J., and Mahadevan, L. (2015). Elastocapillary coalescence of plates and pillars. *Proceedings of the Royal Society A: Mathematical, Physical and Engineering Sciences*, 471(2175):20140593.

List of Publications

Peer Reviewed Journals

1. **Bolei Deng**, Jordan R. Raney, Vincent Tournat, Katia Bertoldi (2017). Elastic Vector Solitons in Soft Architected Materials. *Physical Review Letters*, Volume 118, Issue 20, 204102. [doi:10.1103/PhysRevLett.118.204102](https://doi.org/10.1103/PhysRevLett.118.204102)
2. **Bolei Deng**, Pai Wang, Qi He, Vincent Tournat, Katia Bertoldi (2018). Metamaterials with amplitude gaps for elastic solitons. *Nature Communications*, Volume 9, 3410. [doi:10.1038/s41467-018-05908-9](https://doi.org/10.1038/s41467-018-05908-9)
3. **Bolei Deng**, Vincent Tournat, Katia Bertoldi (2018). Effect of predeformation on the propagation of vector solitons in flexible mechanical metamaterials. *Physical Review E*, Volume 98, Issue 5, 053001. [doi:10.1103/PhysRevE.98.053001](https://doi.org/10.1103/PhysRevE.98.053001)
4. **Bolei Deng**, Vincent Tournat, Pai Wang, Katia Bertoldi (2019). Anomalous collisions of elastic vector solitons in mechanical metamaterials. *Physical Review Letters*, Volume 122, Issue 4, 044101. [doi:10.1103/PhysRevLett.122.044101](https://doi.org/10.1103/PhysRevLett.122.044101)
5. **Bolei Deng***, Chengyang Mo*, Vincent Tournat, Katia Bertoldi, Jordan R. Raney (2019). Focusing and Mode Separation of Elastic Vector Solitons in a 2D Soft Mechanical Metamaterial. *Physical Review Letters*, Volume 123, Issue 2, 024101. [doi:10.1103/PhysRevLett.123.024101](https://doi.org/10.1103/PhysRevLett.123.024101)
6. **Bolei Deng**, Yuning Zhang, Qi He, Vincent Tournat, Pai Wang, Katia Bertoldi (2019). Propagation of elastic solitons in chains of pre-deformed beams. *New Journal of Physics*, Volume 21, 073008. [doi:10.1088/1367-2630/ab2810](https://doi.org/10.1088/1367-2630/ab2810)
7. Xinxin Guo, Vitalyi E Gusev, Vincent Tournat, **Bolei Deng**, Katia Bertoldi (2019). Frequency-doubling effect in acoustic reflection by a nonlinear, architected rotating-square metasurface. *Physical Review E*, Volume 99, Issue 5, 052209. [doi:10.1103/PhysRevE.99.052209](https://doi.org/10.1103/PhysRevE.99.052209)

8. Ahmad Rafsanjani*, Lishuai Jin*, **Bolei Deng**, Katia Bertoldi (2019). Propagation of pop ups in kirigami shells. *Proceedings of the National Academy of Sciences, Volume 116*, 8200-8205. [doi:10.1073/pnas.1817763116](https://doi.org/10.1073/pnas.1817763116)
9. **Bolei Deng**, Pai Wang, Vincent Tournat, Katia Bertoldi (2020). Nonlinear Transition Waves in Free-standing Bistable Chains. *Journal of the Mechanics and Physics of Solids, Volume 136*, 103661. [doi:10.1016/j.jmps.2019.07.004](https://doi.org/10.1016/j.jmps.2019.07.004)
10. Ahmad Zareei, **Bolei Deng**, Katia Bertoldi (2020). Harnessing transition waves to realize deployable structures. *Proceedings of the National Academy of Sciences, Volume 117*, 4015–4020. [doi:10.1073/pnas.1917887117](https://doi.org/10.1073/pnas.1917887117)
11. **Bolei Deng**, Liyuan Chen, Donglai Wei, Vincent Tournat, Katia Bertoldi (2020). Pulse-driven robot: Motion via solitary waves. *Science Advances, Volume 6, Issue 18*. [doi:10.1126/sciadv.aaz1166](https://doi.org/10.1126/sciadv.aaz1166)
12. Lishuai Jin, Antonio Elia Forte, **Bolei Deng**, Ahmad Rafsanjani, Katia Bertoldi (2020). Kirigami-inspired Inflatables with Programmable Shapes. *Advanced Materials, Volume 32, Issue 33*, 2001863. [doi:10.1002/adma.202001863](https://doi.org/10.1002/adma.202001863)
13. **Bolei Deng***, Siqin Yu*, Antonio E Forte, Vincent Tournat, Katia Bertoldi (2020). Characterization, stability, and application of domain walls in flexible mechanical metamaterials. *Proceedings of the National Academy of Sciences, Volume 117, Issue 49*, 31002. [doi:10.1073/pnas.2015847117](https://doi.org/10.1073/pnas.2015847117)
14. Nikolaos Vasios, **Bolei Deng**, Benjamin Gorissen, Katia Bertoldi (2021). Universally bistable shells with nonzero Gaussian curvature for two-way transition waves. *Nature communications, Volume 12, Issue 1*, 1-9. [doi:10.1038/s41467-020-20698-9](https://doi.org/10.1038/s41467-020-20698-9)
15. **Bolei Deng***, Jian Li*, Vincent Tournat, Prashant K Purohit, Katia Bertoldi (2021). Dynamics of mechanical metamaterials: A framework to connect phonons, nonlinear periodic waves and solitons. *Journal of the Mechanics and Physics of Solids, Volume 147*, 104233. [doi:10.1016/j.jmps.2020.104233](https://doi.org/10.1016/j.jmps.2020.104233)
16. Shucong Li*, **Bolei Deng***, Alison Grinthal, Alyssa Schneider-Yamamura, Jinliang Kang, Reese S. Martens, Cathy T. Zhang, Jian Li, Siqin Yu, Katia Bertoldi, Joanna Aizenberg (2021). Liquid-induced topological transformations of cellular microstructures. *Nature, Volume 592, Issue 33*, 386-391. [doi:10.1038/s41586-021-03404-7](https://doi.org/10.1038/s41586-021-03404-7)
17. **Bolei Deng**, Jordan R. Raney, Katia Bertoldi, Vincent Tournat (2021). Nonlinear waves in flexible mechanical metamaterials. *Journal of Applied Physics, Volume 130, Issue 4*, 040901. [doi:10.1063/5.0050271](https://doi.org/10.1063/5.0050271)